ORDRE:40099

THÈSE

Présentée à

Université Lille1- Sciences et Technologies

(Ecole Doctorale des Sciences de la Matière, du Rayonnement et de l'Environnement)

pour l'obtention du

Docteur

(Discipline : Molécules et Matière Condensée)

par

Bingwen HU

Manipulations des interactions dipole-dipole en RMN de l'état solide

(The manipulations of dipolar-dipolar interactions in Solid-State NMR)

Soutenue le 23 novembre 2009

Membres du Jury :

Directeur de Thèse : Jean-Paul Amoureux, Professeur, Université Lille1

Rapporteurs :

(1)Christian Fernandez, Professeur, Ecole Nationale Supérieure des Ingénieurs de CAEN et Université de Caen

(2)Francis Taulelle, Directeur de Recherche CNRS, Université de Versailles St-Quentin

Membres :

(3)Lionel Montagne, Professeur, Université Lille1

Remerciements

Je souhaite remercier en premier lieu, Prof. Jean-Paul AMOUREUX, mon directeur de thèse, pour la formation de qualité qu'il m'a transmise, pour ses conseils, son regard critique et constructif sur mes travaux. Merci pour sa disponibilité et merci pour m'avoir permis de participer à de nombreux congrès.

Merci à Julien Trébosc, qui m'a enseigné les arcanes de l'utilisation du spectromètre RMN Bruker ainsi que les recettes concernant la manipulation des noyaux quadripolaire.

Je ne peux évidemment pas manquer de remercier toutes les personnes qui m'ont aidé au cours de ma thèse: Elodie CRETON, Gregory TRICOT, Laurent DELEVOYE, Olivier LAFON, Qiang WANG, Rong Li, Weiting XU, Filipe VASCONCELOS, Daniel COILLOT, Nina FORLER, François MEAR, Xavier TRIVELLI, Zhenmian SHAO, Chanapa KONGMARK, Prof. Marek PRUSKI, Prof. Zhehong GAN, Olivier MENTRE, Prof. Rose-Noelle VANNIER, et Prof. Lionel MONTAGNE.

Je remercie Prof. Ping ZHOU qui m'a mis en contact avec Jean-Paul AMOUREUX et m'encourage continuellement.

Ce travail a été effectué dans le laboratoire d'Unité de Catalyse et de Chimie du Solide. Donc, un grand merci à toutes les personnes de l'UCCS qui m'ont accueilli chaleureusement et qui m'ont aidé. Merci aux étudiants de l'UCCS pour la vie dans le laboratoire.

Et je finirai par mes parents et ma femme qui toujours m'encouragent et me soutiennent.

Contents

Introduction

Despite its short existence, Nuclear Magnetic Resonance (NMR) has become a powerful technique of investigation used for research in a wide range of domains: biology, physics, chemistry, *etc*, due to its ability to probe the local environment of a specific nucleus through the characterizations of its interactions.

One of the main interests in material science and biology science is to obtain information about the structure of the sample correlated with spatial distribution of the neighboring nuclei. For determining distances between atoms and the orientation of their connecting vectors, measurement of the dipolar interaction (including homonuclear and heteronuclear dipole-dipole couplings) can be used. Usually, dipolar interactions are cancelled by the MAS (Magic Angle Spinning) rotation. Consequently recoupling of the dipolar coupling is necessary.

Another important issue of solid-state NMR is to obtain the spectra in high resolution. In solid-state NMR, fast MAS are usually applied to eliminate the homonuclear dipolar interactions and then narrow the line widths. However, MAS alone does not generally achieve enough resolution in some cases, such as protonated systems. Due to very strong homo-nuclear ^{1}H-^{1}H dipolar interactions the ^{1}H spectra are typically broad and featureless. Thus, one of the critical remaining challenges in NMR is to develop homonuclear decoupling techniques to narrow ^{1}H spectra of solids and recover chemical shift and *J*-coupling information.

The aim of this thesis is to develop new decoupling techniques to obtain the ^{1}H spectra in high resolution and to devise new heteronuclear and homonuclear recoupling techniques in order to obtain the structural information.

The first chapter concerns the theoretical basics of NMR. The principles of the MQMAS and STMAS are described in detail. Besides, Continuous-Wave Cross-Polarization in MAS (CW-CPMAS) for quadrupolar nuclei is also explained.

In chapter 2, a new CPMAS method, named as Multiple-Pulse CPMAS (MP-CPMAS) is introduced. It allows the acquisition of through-space 2D HETCOR spectra between spin-1/2 nuclei and half-integer quadrupolar nuclei in the solid state. It uses rotor-synchronized selective pulses on the quadrupolar nucleus and continuous-wave RF irradiation on the spin-1/2 nucleus to create hetero-nuclear dipolar coherences. The method is more robust, more efficient, and easier to set up than the standard CW-CPMAS transfers. However, both CW-CPMAS and MP-CPMAS are sensitive to the C_Q values and offsets.

In chapter 3, *D*-HMQC is introduced to create through-space 2D HETCOR spectra between spin-1/2 nuclei and half-integer quadrupolar nuclei. These methods use recoupling concept to create hetero-nuclear coherences through the dipolar interaction instead of scalar coupling into the HMQC for spin n/2 (n > 1). Compared to those based on the cross-polarization transfer to quadrupolar nuclei, the methods are *less sensitive to the C_Q values and offsets* because only two CT-selective pulses are sent in the quadrupolar channel. In this chapter, several important recoupling methods

are also compared. When homo-nuclear interactions are negligible, SFAM is the best one; on the contrary, $SR4_1^2$ is preferred.

In chapter 4, a new smooth amplitude-modulated (SAM) method that allows observing highly resolved ^1H spectra in solid-state NMR is presented. This method, which works mainly at fast or ultra-fast MAS speed (ν_R > 25 kHz) is complementary to previous methods, such as DUMBO, FSLG/PMLG or symmetry-based sequences. We demonstrated that SAM could work on both t_1 and t_2 dimensions. Theoretical explanations are also described. It should be pointed out that SAM is *rotor-synchronized* decoupling sequence (which is important for t_1 decoupling under MAS condition) while PMLG and DUMBO are not.

In chapter 5, a novel symmetry-based method SPIP, using inversion elements bracketed by spin locks, for exciting double-quantum (DQ) coherences between spin-1/2 nuclei, such as protons, are presented. Compared to previous ^1H DQ-recoupling techniques, this new pulse sequence requires moderate rf field, even at ultra-fast MAS speeds. Furthermore, it is easy to implement and it displays higher robustness to both chemical shift anisotropy and to spreads in resonance frequencies.

In chapter 6, a numerical method, called covariance method, is presented. Covariance method can be employed in solid state NMR to get homo-nuclear correlation (HOMCOR) 2D spectra, without any previous knowledge of the positions and line-widths of the resonances, in a much faster way than the usual 2D-FT data treatment. Besides, covariance methods can be applied to HETCOR NMR data to generate two HOMCOR indirect-covariance spectra.

In chapter 7, we will introduce SAM decoupling techniques into *D*-HQMC experiment, and apply them into ^{14}N systems.

In chapter 8, SPIP and its variations, which can be applied to study ^{19}F (large homo-nuclear interactions, large chemical shift and large CSA), ^{31}P (large CSA) and quadrupolar nuclei, will be discussed.

In the appendix, the super-cycling of RN_n^v sequences is described and this super-cycling is pivotal to understand $SR4_1^2$ and SPIP sequences.

The main contributions of different people in our papers are summarized below following the suggestions of Prof. Taulelle. Massive efforts have been made by Prof. Amoureux and Olivier Lafon (if involved) to write the papers and ameliorate the papers. Julien Trébosc helps me a lot in the SIMPSON simulations.

Paper List

1. Hu, B.; Amoureux, J. P.; Trébosc, J.; Hafner, S., Through-space MP-CPMAS experiments between spin-1/2 and half-integer quadrupolar nuclei in solid-state NMR. *Journal of Magnetic Resonance* **2008,** 192, (1), 8.

   Prof. Amoureux → original idea of MP-CPMAS

   Hu → simulations & experiments.

2. Trebosc, J.; Hu, B.; Amoureux, J. P.; Gan, Z., Through-space R^3-HETCOR experiments between spin-1/2 and half-integer quadrupolar nuclei in solid-state NMR. *Journal of Magnetic Resonance* **2007,** 186, (2), 220.

   Trebosc & Hu → original idea of R^3 *D*-HMQC for quadrupolar nuclei

   Trebosc → Experiments

3. Hu, B.; Trebosc, J.; Amoureux, J. P., Comparison of several hetero-nuclear dipolar recoupling NMR methods to be used in MAS HMQC/HSQC. *Journal of Magnetic Resonance* **2008,** 192, (1), 112.

   Hu → original idea to introduce the SFAM and RN_n^v sequences into *D*-HMQC to replace R^3 & Simulations & Experiments

4. Amoureux, J. P.; Trebosc, J.; Hu, B.; Halpern-Manners, N.; Antonijevic, S., High-resolution ^{14}N-edited ^{1}H-^{13}C correlation NMR experiment to study biological solids. *Journal of Magnetic Resonance* **2008**.

   Prof. Amoureux & Antonijevic → original idea of ^{14}N-filtered *D*-HMQC experiment

   Trebosc → Experiments

5. Amoureux, J. P.; Wang, Q.; Hu, B.; Lafon, O.; Trebosc, J.; Deng, F., Rapid analysis of isotopically unmodified amino acids by high-resolution ^{14}N-edited ^{1}H-^{13}C correlation NMR spectroscopy. *Chemical Communications* **2008**, (48), 6525-6527.

   Prof. Amoureux → original idea of ^{14}N-filtered *D*-HMQC experiment with saturation pulse

   Hu → first experimental test in histidine

   Wang → improve the performance & experiment of glutamine

6. Amoureux, J. P.; Hu, B.; Trebosc, J., Enhanced resolution in proton solid-state NMR with very-fast MAS experiments. *Journal of Magnetic Resonance* **2008,** 193, (2), 305.

   Prof. Amoureux → sine x-rotation SAM line-shape for t_1 decoupling

   Hu → cosine z-rotation SAM line-shape & simulations & experiments

7. Amoureux, J. P.; Hu, B.; Trebosc, J.; Wang, Q.; Lafon, O.; Deng, F., Homonuclear dipolar decoupling schemes for fast MAS. *Solid State Nuclear Magnetic Resonance* **2009,** 35, (1), 19-24.

Hu → cosine SAM line-shape for t_2 decoupling & simulations & experiments

8. Lafon, O.; Wang, Q.; Hu, B.; Trebosc, J.; Deng, F.; Amoureux, J. P., Proton-proton homonuclear dipolar decoupling in solid-state NMR using rotor-synchronized z -rotation pulse sequences. *Journal of Chemical Physics* **2009,** 130, (1).

Lafon → theoretical treatment

Wang → experiments & simulations

9. Hu, B.; Wang, Q.; Lafon, O.; Trebosc, J.; Deng, F.; Amoureux, J. P., Robust and efficient spin-locked symmetry-based double-quantum homonuclear dipolar recoupling for probing 1H-1H proximity in the solid-state. *Journal of Magnetic Resonance* **2009**.

Wang & Hu → original idea of SPIP for ^{1}H & experiments

10. Wang, Q.; Hu, B.; Lafon, O.; Trebosc, J.; Deng, F.; Amoureux, J. P., Double-quantum homonuclear NMR correlation spectroscopy of quadrupolar nuclei subjected to magic-angle spinning and high magnetic field. *Journal of Magnetic Resonance* **2009,** 200, (2), 251-260.

Wang & Hu → original idea of $BR2_2^1$ for quadrupolar nuclei & experiments

11. Hu, B.; Delevoye, L.; Lafon, O.; Trebosc, J.; Amoureux, J. P., Double-quantum NMR spectroscopy of 31P species submitted to very large CSAs. *Journal of Magnetic Resonance* **2009,** 200, (2), 178-188.

Delevoye & Hu → Original idea to apply $wBR2_2^1$ in the ^{31}P system & experiments

12. Amoureux, J. P.; Trebosc, J.; Delevoye, L.; Lafon, O.; Hu, B.; Wang, Q., Correlation NMR spectroscopy involving quadrupolar nuclei. *Solid State Nuclear Magnetic Resonance* **2009,** 35, (1), 12-18.

Prof. Amoureux → review

13. Wang, Q.; Hu, B.; Fayon, F.; Trébosc, J.; Legein, C.; Lafon, O.; Deng, F.; Amoureux, J.P.; Double-quantum 19F-19F dipolar recoupling at ultra-fast magic

angle spinning NMR: application to the assignment of 19F NMR spectra of inorganic fluorides, *PCCP*, 2009, 11

Prof. Amoureux & Hu → original idea of SPIP for ^{19}F system

Hu → simulations & first experimental test on $Ba_3Al_2F_{12}$

Wang → simulations & experiments

14. Hu, B.; Amoureux, J. P.; Trébosc, J., Indirect covariance NMR spectroscopy of through-bond homo-nuclear correlations for quadrupolar nuclei in solids under high-resolution. *Solid State Nuclear Magnetic Resonance* **2007,** 31, (4), 163.

Prof. Amoureux → original idea of indirect covariance

Hu → data treatment

15. Hu, B.; Amoureux, J. P.; Trébosc, J.; Deschamps, M.; Tricot, G., Solid-state NMR covariance of homonuclear correlation spectra. *Journal of Chemical Physics* **2008,** 128, (13), 134502.

Prof. Amoureux → original idea to explorer the details of covariance

Hu → data treatment

16. Lafon O.; Wang, Q.; Hu, B.; Vasconcelos, F.; Trebosc, J.; Cristol, S.; Deng, F; Amoureux, J.P.; Indirect detection via spin-1/2 nuclei in solid state NMR spectroscopy: application to the observation of proximities between protons and quadrupolar nuclei, *The Journal of Physical Chemistry*, 2009, in press.

Lafon → theoritical treatment

Lafon & Wang → HMQC/HSQC comparison

Hu → employ SAM in *D*-HMQC & D-HSQC

17. Wang, Q.; Hu, B.; Fayon, F.; Trébosc, J.; Legein, C.; Lafon, O.; Deng, F.; Amoureux, J.P.; Comparison of several double-quanta single-quanta solid-state NMR recoupling methods that can be applied at ultra-fast MAS to nuclei submitted to large homo-nuclear dipolar interactions, such as 1H and 19F. Submitted.

Wang → simulations & experiments

Hu → experiments

18. Chen, L.; Wang, Q.; Hu, B.; Lafon, O.; Deng, F.; Amoureux, J.P.; Measurement of hetero-nuclear distances using a symmetry-based pulse sequence in solid-state NMR. Submitted.

Chen → original idea of S-REDOR & Experiments & Simulations

Hu → Simulations

19. Trebosc, J.; Lafon, O.; Hu, B.; Wang, Q.; Deng, F.; Amoureux, J.P. D-HMQC-ST in quadrupolar system. In preparation.

Trebosc → idea of D-HMQC-ST & experiments

Chapter 1. The basics of solid-state NMR involving half-integer quadrupolar nuclei

The purpose of this chapter is to present the theory necessary to describe nuclear spins in solid-state NMR experiments. The concepts of nuclear spin, density operator, NMR interactions (including the quadrupolar interaction), rotations of the tensor, and some other important concepts are introduced to describe NMR experiments. The details can be found in several references[1-6].

1.1 Density operator[3, 5]

The phenomenon of nuclear magnetic resonance results from the coupling of a spin of a magnetic particle with a strong magnetic field B_0.

Consider a spin with angular quantum number I in a static external magnetic field B_0 along the z direction. According to quantum mechanics, the component along the z-axis of the spin angular moment will take values of the form $m\hbar$, where the magnetic quantum number m = -I, -I+1, … +I. Thus this spin has 2I+1 states. The magnetic moment $\hat{\mu}$ is related to the spin, by:

$$\hat{\mu} = \gamma\hbar\hat{I} \tag{1.1}$$

Where $\hbar$ is the reduced Planck constant and γ is the gyromagnetic ratio. Thus the energy of the spin system can be expressed by

$$E = -\hat{\mu}\cdot\hat{B} = -\mu_z B_0 = -\gamma\hbar I_z B_0 \tag{1.2}$$

Therefore, a particle with spin I has 2I+1 energy states when a strong magnetic field is applied.

In quantum mechanics, the state of a system is described by a wave-function. In NMR, we are only concerned by nuclear spin states and thus, the wave-function $|\psi(t)\rangle$ is the nuclear spin wave-function, which describes the spin state of the N different nuclei. The wave-function can be described by a vector in an N-dimensional vector space (Hilbert space):

$$|\psi(t)\rangle = \sum_{i=1}^{N} C_i(t)|\phi_i\rangle \tag{1.3}$$

Here, the $|\phi_i\rangle$ are orthogonal basis-functions that span the Hilbert space.

An operator $\hat{A}$ transforms the wave-function into another wave-function in the same Hilbert space:

$$|\psi'(t)\rangle = \hat{A}|\psi(t)\rangle \tag{1.4}$$

The matrix elements $A_{i,j}$ in the basis spanned by the set of $|\phi_i\rangle$ are obtained through:

$$A_{i,j} = \langle\phi_i|\hat{A}|\phi_j\rangle \tag{1.5}$$

The time evolution of a wave-function in a closed quantum system is described by the time-dependent Schrödinger equation:

$$\hat{H}|\psi(t)\rangle = i\hbar\frac{\partial|\psi(t)\rangle}{\partial t} \tag{1.6}$$

where $\hat{H}$ is the Hamilton operator.

The measurements made on a quantum system do not always lead to reproducible results because quantum theory only allows probabilistic predictions. The quantity A to be measured is represented by an operator $\hat{A}$. The expectation value of an observable, denoted by $\langle\hat{A}\rangle$, is defined by:

$$\langle\hat{A}\rangle = \frac{\langle\psi(t)|\hat{A}|\psi(t)\rangle}{\langle\psi(t)|\psi(t)\rangle} \tag{1.7}$$

If we insert the expansion of Eq.(1.3) into the definition of an expectation value Eq.(1.7), we can get that

$$\langle\hat{A}\rangle = \sum_i\sum_j C_i^* C_j \langle\phi_i|\hat{A}|\phi_j\rangle \tag{1.8}$$

Here we have used the convention $\langle\psi(t)|\psi(t)\rangle$=1.

We see that the information we need to know about the state of a system to calculate an observable is contained in the product of expansion coefficients $C_i^* C_j$. This suggests constructing an operator $\hat{\rho}(t)$ that contains these products as the elements of its matrix representation:

$$\langle \phi_1 | \hat{\rho}(t) | \phi_2 \rangle = C_1 C_2^* \tag{1.9}$$

We call this operator the density operator and its corresponding matrix the density matrix. Formally we can write

$$\hat{\rho}(t) = |\psi(t)\rangle\langle\psi(t)| = \sum_i \sum_j C_i(t) C_j^*(t) |\phi_i\rangle\langle\phi_j| \tag{1.10}$$

By inserting Eq. (1.10) into the expression of the expectation value Eq. (1.7), we find:

$$\begin{aligned} \langle \hat{A} \rangle &= \sum_i \sum_j C_i^*(t) C_j(t) \langle \phi_i | \hat{A} | \phi_j \rangle \\ &= \sum_i \sum_j \langle \phi_j | \hat{\rho}(t) | \phi_i \rangle \langle \phi_i | \hat{A} | \phi_j \rangle \\ &= \mathrm{tr}\{\hat{\rho}(t)\hat{A}\} \end{aligned} \tag{1.11}$$

Because the density operator is a function of the state function, we are able to re-formulate the time-dependent Schrödinger equation to its equivalent equation as follows:

$$\frac{d}{dt}\hat{\rho}(t) = -\frac{i}{\hbar}[\hat{H}, \hat{\rho}] = -\frac{i}{\hbar}[\hat{H}\hat{\rho} - \hat{\rho}\hat{H}] \tag{1.12}$$

Its solution is, for time-independent Hamiltonians, easily found to be

$$\hat{\rho}(t) = \exp(-\frac{i}{\hbar}\hat{H}t)\hat{\rho}(0)\exp(\frac{i}{\hbar}\hat{H}t) \tag{1.13}$$

With this equation, we can formulate the general result for the expectation of any time-independent operator as

$$\langle \hat{A} \rangle = \mathrm{tr}\{\exp(-\frac{i}{\hbar}\hat{H}t)\hat{\rho}(0)\exp(\frac{i}{\hbar}\hat{H}t)\hat{A}\} \tag{1.14}$$

In NMR, the initial density operator of a nucleus is often used in a simplified version: $\hat{\rho}(0) = \hat{I}_z$, and the observation operator is $\hat{A} = I_x - iI_y$.

1.2 Rotations and MAS [5]

All NMR Hamiltonians can be written as a summation of product of spin and spatial tensors as shown below:

$$\hat{H}_\lambda = W_\lambda \sum_{l=0}^{2} \sum_{m=-l}^{l} (-1)^m A^\lambda_{l,-m} \hat{T}^\lambda_{l,m} \tag{1.15}$$

where W_λ is a constant and the tensor components $A^\lambda_{l,-m}$ and $\hat{T}^\lambda_{l,m}$ are the spatial and spin tensor components of the λ interaction, respectively. The rotations in each space only affect the variables in that space. Thus, by writing the Hamiltonians in the above form, the spin and real spaces are decoupled and handled separately. These tensors, such as A^λ, can then be rotated from coordinate system (X, Y, Z) into another coordinate system (x, y, z) by a rotation R

$$A^\lambda(\mathrm{x, y, z}) = RA^\lambda(\mathrm{X, Y, Z})R^{-1} \tag{1.16}$$

The rotation is often specified by three Euler angles (α,β,γ) between the two reference frames, before and after rotation, as shown in Fig. 1.1.

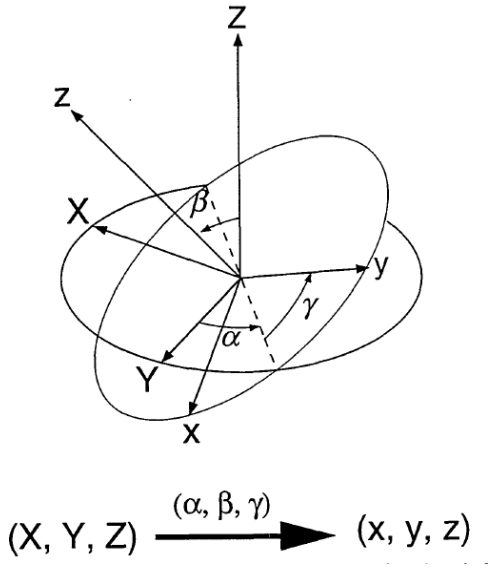

Fig. 1.1. Euler angle definitions. The first rotation is defined by an angle α about the Z axis of the original coordinate system. This changes the positions of the X and Y axes. The second rotation is defined by the angle β about the newly-rotated Y axis, and it changes the positions of the X and Z axes. The third rotation is defined by the angle γ about the newly-rotated Z axis. The final positions of the axes are given by the labels x, y, and z.

If we call the coordinate system (X,Y, Z) as PAS (Principal Axis System) and (x, y, z) as LAB (LABoratory system), Eq.(1.16) can be written as

$$\begin{aligned} A^{\lambda}_{l,m}(LAB) &= R(\alpha,\beta,\gamma)A^{\lambda}_{l,m}(PAS)R^{-1}(\alpha,\beta,\gamma) \\ &= \sum_{m'=-l}^{l} A^{\lambda}_{l,m'}(PAS)D^{(l)}_{m',m}(\alpha,\beta,\gamma) \end{aligned} \tag{1.17}$$

Where $R(\alpha,\beta,\gamma) = R_z(\alpha)R_y(\beta)R_z(\gamma)$, $R_\chi(\theta) = \exp(-i\theta I_\chi)$ ($\chi = x, y, z$) and the functions $D^{(l)}_{m',m}(\alpha,\beta,\gamma)$ are called Wigner rotation matrices. This expression may be numerically simplified by expressing $D^{(l)}_{m',m}(\alpha,\beta,\gamma)$ in terms of exponentials and reduced Wigner rotation matrix elements $d^{(l)}_{m',m}(\beta)$.

$$D^{(l)}_{m',m}(\alpha,\beta,\gamma) = e^{-im'\alpha}d^{(l)}_{m',m}(\beta)e^{-im\gamma} \tag{1.18}$$

The second-order (l = 2) reduced Wigner rotation matrix elements $d^{(2)}_{m',m}(\beta)$ can be found in Table 1.1.

Table 1.1. Reduced Wigner rotation matrix elements $d^{(2)}_{m',m}(\beta)$ in terms of the Eulerian angle β.

m' \ m	2	1	0	-1	-2
2	$\frac{(1+\cos\beta)^2}{4}$	$-\sin\beta\left(\frac{1+\cos\beta}{2}\right)$	$\sqrt{\frac{3}{8}}\sin^2\beta$	$-\sin\beta\left(\frac{1-\cos\beta}{2}\right)$	$\frac{(1-\cos\beta)^2}{4}$
1	$\sin\beta\left(\frac{1+\cos\beta}{2}\right)$	$\cos^2\beta-\left(\frac{1-\cos\beta}{2}\right)$	$-\sqrt{\frac{3}{8}}\sin 2\beta$	$\left(\frac{1+\cos\beta}{2}\right)-\cos^2\beta$	$-\sin\beta\left(\frac{1-\cos\beta}{2}\right)$
0	$\sqrt{\frac{3}{8}}\sin^2\beta$	$\sqrt{\frac{3}{8}}\sin 2\beta$	$\frac{3\cos^2\beta-1}{2}$	$-\sqrt{\frac{3}{8}}\sin 2\beta$	$\sqrt{\frac{3}{8}}\sin^2\beta$
-1	$\sin\beta\left(\frac{1-\cos\beta}{2}\right)$	$\left(\frac{1+\cos\beta}{2}\right)-\cos^2\beta$	$\sqrt{\frac{3}{8}}\sin 2\beta$	$\cos^2\beta-\left(\frac{1-\cos\beta}{2}\right)$	$-\sin\beta\left(\frac{1+\cos\beta}{2}\right)$
-2	$\frac{(1-\cos\beta)^2}{4}$	$\sin\beta\left(\frac{1-\cos\beta}{2}\right)$	$\sqrt{\frac{3}{8}}\sin^2\beta$	$\sin\beta\left(\frac{1+\cos\beta}{2}\right)$	$\frac{(1+\cos\beta)^2}{4}$

In solid state NMR, magic-angle spinning (MAS, Fig. 1.2) is the most important way to remove the spatial tensors. In MAS experiments, the sample is rotated rapidly

about an axis oriented at the angle $\theta_M = \cos^{-1}(1/\sqrt{3}) = 54.736°$ with respect to the magnetic field B_o. For a general spinning angle θ, this introduces a time-dependence to the spatial tensors $A^{\lambda}_{l,m}$ as follows:

$$A^{\lambda}_{l,m} = \sum_{n=-l}^{l} a^{\lambda}_{l,n} D^{(l)}_{n,m}(\omega_r t, \theta, 0)$$
$$a^{\lambda}_{l,n} = \sum_{m'=-l}^{l} \rho^{\lambda}_{l,m'} D^{(l)}_{m',n}(\alpha, \beta, \gamma) \qquad (1.19)$$

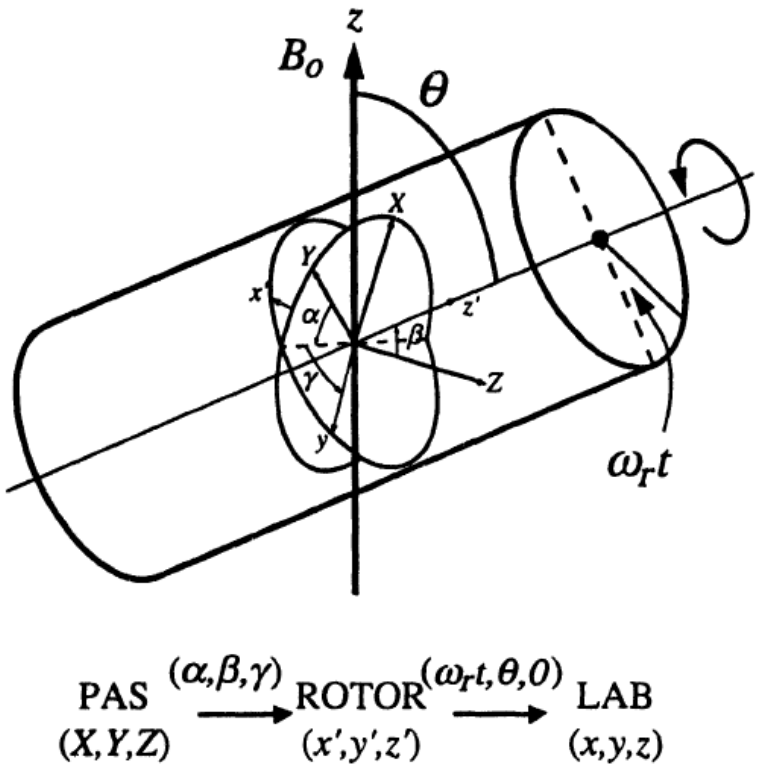

Fig. 1.2. Rotations from PAS to ROTOR and from ROTOR to LAB frames. The Euler angles used in moving from a sample fixed PAS coordinate system to the laboratory system are indicated. This involves multiple rotations. There is no need to use a third Euler angle, with $\omega_r t$ and θ, because it corresponds to a rotation about the magnetic field.

1.3 Nuclear Spin interactions

The nuclei interact with the surrounding magnetic and electric (if they have a non-spherical electric charge distribution) microscopic interactions, so that with the macroscopic electric rf-fields. Here we describe the most important interactions which will be used in the following.

1.3.1 Zeeman interaction

When a sample is placed in the external magnetic field $\hat{B} = B_0 \vec{e}_z$, the nuclear magnetic moment interacts with this field as follows:

$$\hat{H}_Z = -\hat{\mu} \cdot \hat{B} = -\mu_z B_0 = -\gamma \hbar B_0 I_z = -\hbar \omega_0 I_z \tag{1.20}$$

This is the so-called nuclear Zeeman interaction. This equation tells that the spin rotates around the z-axis at a so-called Larmor frequency $\omega_0 = \gamma B_0$.

1.3.2 Chemical shift

The magnetic field at the nucleus is equal to the external magnetic field B_0 only for a naked atomic nucleus. Actually, B_0 induces magnetic moments in the electron distribution surrounding the nuclei, which leads to a local magnetic field B_{loc} that can be written as the sum of the external field B_0 and the induced chemical-shift field $B_{\text{cs:}}$

$$\begin{aligned} B_{\text{loc}} &= B_0 + B_{\text{CS}} \\ &= (1+\sigma)\, B_0 \end{aligned} \tag{1.21}$$

The chemical shielding tensor σ describes the orientation dependent chemical shielding interaction of a spin *I*. This contribution is dependent on the electronic environment of the nuclear spin and by this carries information about chemical bonding and structure. The spin Hamiltonian of this chemical shielding interaction can be written as

$$\hat{H}_{CS} = \gamma \hbar \hat{I} \cdot \sigma \cdot \vec{B}_0 \tag{1.22}$$

Thus the chemically-shielded Zeeman Hamiltonian can be written as

$$\hat{H}_0^{'} = \hat{H}_Z + \hat{H}_{CS} = -\gamma \hbar \hat{I} \cdot (1-\sigma) \cdot \vec{B}_0 = -\omega_0^{'} \hat{I} \tag{1.23}$$

The tensor σ can be described first in its principal axis system (PAS). The isotropic

part σ_{iso} does not depend on the orientation of the applied field and can be defined from the principal values of the tensor ($\sigma_{xx}^{PAS}, \sigma_{yy}^{PAS}, \sigma_{zz}^{PAS}$) as follows:

$$\sigma_{iso} = \frac{1}{3}(\sigma_{xx}^{PAS} + \sigma_{yy}^{PAS} + \sigma_{zz}^{PAS}) \tag{1.24}$$

The assignment of $\sigma_{xx}^{PAS}, \sigma_{yy}^{PAS}, \sigma_{zz}^{PAS}$ needs to fulfill the following condition $\left|\sigma_{xx}^{PAS} - \sigma_{iso}\right| \le \left|\sigma_{yy}^{PAS} - \sigma_{iso}\right| \le \left|\sigma_{zz}^{PAS} - \sigma_{iso}\right|$.

Then, the anisotropy δ_{CS} and the asymmetry η_{CS} of the tensor can be defined as:

$$\begin{aligned} \delta_{CS} &= \sigma_{zz}^{PAS} - \sigma_{iso} \\ \eta_{CS} &= \frac{\sigma_{yy}^{PAS} - \sigma_{xx}^{PAS}}{\delta_{CS}} \end{aligned} \tag{1.25}$$

Using high-temperature approximation, the Hamiltonian of the chemical shielding interaction becomes

$$\hat{H}^{CS} = \hbar\omega_0\sigma_{iso}\hat{I}_z + \hbar\omega_0\delta_{CS}\left(\frac{3\cos\beta_{CS} - 1}{2} + \frac{\eta_{CSA}}{2}\sin\beta_{CS}^2\cos 2\alpha_{CS}\right) \tag{1.26}$$

1.3.3 Direct dipolar-dipolar coupling

Another important interaction in solid-state NMR is the through-space interaction between the magnetic moments of two nuclei. Since each nuclear spin possesses a magnetic moment, it generates a magnetic field looping around its surrounding space, according to the direction of the spin magnetic moment. A second nucleus in this surrounding space will thus interact with this "local" magnetic field. This interaction is called the direct dipolar-dipolar interaction and it can be described by the following Hamiltonian

$$\hat{H}_D = -2\gamma_j\gamma_k\hbar^2\left(\frac{\mu_0}{4\pi}\right)\hat{I}_j \cdot D \cdot \hat{I}_k \tag{1.27}$$

Where D is the dipolar-dipolar coupling tensor which describes how the interaction varies with the orientation of the internuclear vector in the applied field.

Most NMR studies are conducted at high magnetic fields where $\left\|\hat{H}_Z\right\| >> \left\|\hat{H}_D\right\|$, and the chemically-shielded Zeeman Hamiltonian is $\hat{H}_0' = -\hbar\omega_1\hat{I}_{z1} - \hbar\omega_2\hat{I}_{z2}$, where $\omega_1 = -\gamma_1 B_0(1 - \sigma_1^{zz})$ and $\omega_2 = -\gamma_2 B_0(1 - \sigma_2^{zz})$. The secular approximation (a first-order perturbation theory treatment) keeps only the part of $\hat{H}_D$ that commutes

with $\hat{H}_0^{'}$.

If the two spins are of the same isotopic species (homo-nuclear case), the secular Hamiltonian is given by

$$\hat{H}_D^{HOMO} = -\frac{\mu_0}{4\pi}\frac{\gamma^2\hbar^2}{r_{jk}^3}(3\cos^2\beta_D - 1)\left(\hat{I}_{jz}\hat{I}_{kz} - \frac{1}{2}(\hat{I}_{jx}\hat{I}_{kx} + \hat{I}_{jy}\hat{I}_{ky})\right) \tag{1.28}$$

If the two spins are of different isotopic species (hetero-nuclear case), the secular part of the Hamiltonian is given by

$$\hat{H}_D^{HETERO} = -\frac{\mu_0}{4\pi}\frac{\gamma_j\gamma_k\hbar^2}{r_{jk}^3}(3\cos^2\beta_D - 1)\hat{I}_{jz}\hat{I}_{kz} \tag{1.29}$$

1.3.4 Indirect dipolar-dipolar coupling (J-coupling)

Nuclear magnetic moments interact not only by means of the direct (through space) dipolar coupling. They are also influenced by dipolar interactions mediated by the electrons involved in the chemical bond between the two corresponding atoms. This interaction, called J coupling or indirect dipolar-dipolar coupling, is B_0 field independent.

$$\hat{H}_J = 2\pi\hat{I}_j \cdot J \cdot \hat{I}_k \tag{1.30}$$

The anisotropic part of the J-coupling tensor is usually small and often ignored.

In the homonuclear case, the secular form of the interaction can be written:

$$\hat{H}_J^{HOMO} = 2\pi J_{jk}\hat{I}_j \cdot \hat{I}_k \tag{1.31}$$

In the heteronuclear case, the secular form of the interaction can be written:

$$\hat{H}_J^{HETERO} = 2\pi J_{jk}\hat{I}_{jz}\hat{I}_{kz} \tag{1.32}$$

1.3.5 Quadrupolar coupling

It's important to realize that while some nuclei (I = 1/2) have a spherical electric charge distribution and thus do not possess electric quadrupole moments, most nuclei (I > 1/2) have a non-spherical electric charge distribution and hence possess electric quadrupole moments that can couple to local electric field gradients.

The corresponding bilinear Hamiltonian reads

$$\begin{aligned}\hat{H}_Q &= \frac{eQ}{2I(2I-1)}\hat{I}\cdot V\cdot\hat{I} \\ &= \frac{e^2qQ}{4I(2I-1)}[3\hat{I}_z^2-\hat{I}^2+\eta_Q(\hat{I}_x^2-\hat{I}_y^2)]\end{aligned} \tag{1.33}$$

Where V is the electric field gradient (EFG) tensor, and eQ is the electric quadrupole moment. The quadrupolar coupling constant C_Q and the asymmetry parameter η_Q are defined from the principal values of EFG tensor $V_{xx}^{\mathrm{PAS}}, V_{yy}^{\mathrm{PAS}}, V_{zz}^{\mathrm{PAS}}$, where $V_{zz}^{\mathrm{PAS}}=eq$:

$$C_Q = \frac{e^2qQ}{h} \tag{1.34}$$

$$\eta_Q = \frac{V_{yy}^{\mathrm{PAS}}-V_{xx}^{\mathrm{PAS}}}{V_{zz}^{\mathrm{PAS}}} \tag{1.35}$$

Here C_Q is given in Hz unit and $\left|V_{zz}^{\mathrm{PAS}}\right|\geq\left|V_{yy}^{\mathrm{PAS}}\right|\geq\left|V_{xx}^{\mathrm{PAS}}\right|$. It's convenient to define another parameter as follows:

$$\Omega_Q = \frac{C_Q}{2I(2I-1)} = \frac{e^2qQ}{2I(2I-1)\hbar} \tag{1.36}$$

Ω_Q has unit of rad.s^{-1}. Often, another notation is used in the literature, which gives

$$\omega_Q = \frac{3\Omega_Q}{2\pi} = \frac{3e^2qQ}{2I(2I-1)h} \tag{1.37}$$

This quantity has unit of Hz and it corresponds to the distance between resonance lines in a zero-field experiment or in a high-field experiment with $\eta_Q = 0$.

In the laboratory frame, the first order secular Hamiltonian for the quadrupolar interaction of static sample is

$$\hat{H}_Q^{(1)} = \frac{C_Q}{8I(2I-1)}(3\cos^2\beta_Q-1-\eta_Q\sin^2\beta_Q\cos 2\alpha_Q)(3\hat{I}_z^2-\hat{I}^2) \tag{1.38}$$

Where $(\alpha_Q, \beta_Q, \gamma_Q)$ are the Euler angles defining the orientation of the principal axis system of the EFG tensor in the laboratory frame.

For convenience in the future, we will omit the ^ at the top of the density operator and $\hbar$ in the representation of the Hamiltonian.

1.4 MQMAS and STMAS

1.4.1 Quadrupolar interactions in MAS

All microscopic interactions can be described in terms of irreducible tensors[5]

$$H_Q = \Omega_Q \sum_{m=-2}^{2} (-1)^m V_{2,-m}^Q T_{2,m}^Q \tag{1.39}$$

For spin I > 1/2, the pre-factor of the quadrupolar interaction is equal to Ω_Q, and the spin elements are given by:

$$\begin{aligned} T_{2,0}^Q &= \frac{1}{\sqrt{6}}(3I_z^2 - I(I+1)) \\ T_{2,\pm1}^Q &= \mp\frac{1}{2}(I_z I_\pm + I_\pm I_z) \\ T_{2,\pm2}^Q &= \frac{1}{2} I_\pm^2 \end{aligned} \tag{1.40}$$

The spatial elements $V_{2,m}^Q$ are obtained by transforming the elements $\rho_{2,m'}^Q$ of the EFG tensor in their Principal Axis System to the laboratory system:

$$\begin{aligned} V_{2,m}^Q &= \sum_{m'=-2}^{2} \rho_{2,m'}^Q D_{m',m}^{(2)}(\alpha,\beta,\gamma) \\ &= \sum_{m'=-2}^{2} \sum_{n=-2}^{2} \rho_{2,m'}^Q D_{m',n}^{(2)}(\alpha_Q,\beta_Q,\gamma_Q) D_{n,m}^{(2)}(\omega_r t, \theta_M, 0) \end{aligned} \tag{1.41}$$

The spatial elements $\rho_{2,m'}^Q$ are given by

$$\begin{aligned} \rho_{2,0}^Q &= \sqrt{\frac{3}{2}} \\ \rho_{2,\pm1}^Q &= 0 \\ \rho_{2,\pm2}^Q &= \frac{1}{2}\eta_Q \end{aligned} \tag{1.42}$$

If we only consider the Zeeman Effect and the quadrupole interaction, we obtain

$$H = H_Z + H_Q = -\omega_0 I_z + H_Q \tag{1.43}$$

The quadrupolar interaction can be treated as a perturbation to the Zeeman field using average Hamiltonian theory. This is done by transforming H_Q to the Zeeman interaction frame by applying the rotation to the spin elements $T_{2,k}^Q$.

$$\begin{aligned}\tilde{H}_Q &= e^{iH_0t}H_Qe^{-iH_0t} = (-1)^m\Omega_Q\sum_m V_{2,-m}^Q\sum_k T_{2,k}^Q D_{k,m}^{(2)}(-\omega_0 t,0,0)\\ &= (-1)^m\Omega_Q\sum_m V_{2,-m}^Q\sum_k T_{2,k}^Q e^{ik\omega_0 t}\delta_{k,m}\\ &= (-1)^m\Omega_Q\sum_m V_{2,-m}^Q T_{2,m}^Q e^{im\omega_0 t}\end{aligned} \tag{1.44}$$

Averaging over the Larmor period $\tau_c=2\pi/\omega_0$ is performed by taking the zero and first order Magnus expansion[7] terms. They are marked as $\tilde{H}_Q^{(1)}$ and $\tilde{H}_Q^{(2)}$ in order to stress their equivalence to the first and second order terms of standard perturbation theory:

$$\tilde{H}_Q^{(1)} = \frac{\omega_0}{2\pi}\int_0^{2\pi/\omega_0}\tilde{H}_Q(t)\mathrm{d}t = (-1)^0\Omega_Q V_{2,0}^Q T_{2,0}^Q = \frac{\Omega_Q}{\sqrt{6}}V_{2,0}^Q[3I_z^2 - I^2] \tag{1.45}$$

Thus we can obtain the corresponding energy levels in MAS:

$$\begin{aligned}\left\langle m\left|\tilde{H}_Q^{(1)}\right|m\right\rangle &= \frac{\Omega_Q}{\sqrt{6}}V_{2,0}^Q[3m^2 - I(I+1)]\\ &= \omega_Q^{(1)}(\alpha_Q,\beta_Q,\eta_Q)[3m^2 - I(I+1)]d_{0,0}^{(2)}(\theta_M)\end{aligned} \tag{1.46}$$

Accordingly, we get

$$\begin{aligned}\tilde{H}_Q^{(2)} &= -\frac{i\omega_0}{4\pi}\int_0^{2\pi/\omega_0}\mathrm{d}t\int_0^t\mathrm{d}t'[\tilde{H}_Q(t),\tilde{H}_Q(t')]\\ &= \frac{\Omega_Q^2}{4\pi}\int_0^{2\pi/\omega_0}\mathrm{d}t(-1)^{m+n}\left[\sum_m V_{2,-m}^Q T_{2,m}^Q,\sum_n\frac{1}{n}V_{2,-n}^Q T_{2,n}^Q\right]e^{i(m+n)\omega_0 t}\\ &= \frac{\Omega_Q^2}{\omega_0}\{V_{2,1}^Q V_{2,-1}^Q\left[T_{2,-1}^Q,T_{2,1}^Q\right] + \frac{1}{2}V_{2,2}^Q V_{2,-2}^Q\left[T_{2,-2}^Q,T_{2,2}^Q\right]\}\end{aligned} \tag{1.47}$$

The products of Wigner matrices are expanded using the Clebsch-Gordon coefficients[8]:

$$T_{2,m}T_{2,-m} = \sum_{j=0}^{4}C(2,m,2,-m\,|\,j,0)T_{j,0} \tag{1.48}$$

Thus we obtain

$$\tilde{H}_Q^{(2)} = \frac{\Omega_Q^2}{2\omega_0}I_Z[(8I_Z^2 - 4I(I+1)+1)V_{2,1}^Q V_{2,-1}^Q + (2I_Z^2 - 2I(I+1)+1)V_{2,2}^Q V_{2,-2}^Q] \tag{1.49}$$

The corresponding energy levels are

$$\langle m|\tilde{H}_Q^{(2)}|m\rangle = \frac{\Omega_Q^2}{2\omega_0} m[(8m^2 - 4I(I+1)+1)V_{2,1}^Q V_{2,-1}^Q + (2m^2 - 2I(I+1)+1)V_{2,2}^Q V_{2,-2}^Q] \quad (1.50)$$

The elements $V_{2,n}V_{2,-n}$ can be written explicitly as

$$V_{2,n}^Q V_{2,-n}^Q = \sum_{k,k'=-2}^{2}\sum_{r,r'=-2}^{2} \rho_{2,k}\rho_{2,k'} D_{k,r}^{(2)}(\alpha_Q,\beta_Q,\varphi_r) D_{k',r'}^{(2)}(\alpha_Q,\beta_Q,\varphi_r) d_{r,n}^{(2)}(\theta_M) d_{r',-n}^{(2)}(\theta_M) \quad (1.51)$$

Where the rotor phase and the γ angle are combined by $\phi_r = \gamma_Q + \omega_r t$. The products of Wigner matrices D are also expanded using the Clebsch-Gordon coefficients:

$$D_{k,r}^{(2)}(\alpha_Q,\beta_Q,\varphi_r) D_{k',r'}^{(2)}(\alpha_Q,\beta_Q,\varphi_r) = \sum_{j=0}^{4} D_{k+k',r+r'}^{(j)} C(2,k,2,k'|j,k+k') C(2,r,2,r'|j,r+r') \quad (1.52)$$

The value of j takes only even values since for odd k $C(2,k,2,k'|j,k+k') = -C(2,k',2,k|j,k'+k)$ and it implies the summations for odd k will be zero. Thus we can rewrite the Eq. (1.50) as

$$\langle m|\tilde{H}_Q^{(2)}|m\rangle = \frac{\Omega_Q^2}{2\omega_0}\sum_{j=0}^{2}\sum_{n=-j}^{j} A^{(2j)}(I,m) B_{2n}^{(2j)}(\eta_Q) \sum_{k=-j}^{j} D_{2n,k}^{(2j)}(\alpha_Q,\beta_Q,\varphi_r(t)) d_{k,0}^{(2j)}(\theta_M) \quad (1.53)$$

With the following values:

$$\begin{aligned} A^{(0)}(I,m) &= m(I(I+1) - 3m^2) \\ A^{(2)}(I,m) &= m(8I(I+1) - 12m^2 - 3) \\ A^{(4)}(I,m) &= m(18I(I+1) - 34m^2 - 5) \end{aligned} \quad (1.54)$$

$$\begin{aligned} B_0^{(0)} &= -(3+\eta_Q^2)/5 \\ B_0^{(2)} &= (\eta_Q^2 - 3)/14 \\ B_0^{(4)} &= -(18+\eta_Q^2)/140 \\ B_{\pm 2}^{(2)} &= \eta_Q\sqrt{1.5}/7 \\ B_{\pm 2}^{(4)} &= 3\eta_Q\sqrt{2.5}/70 \\ B_{\pm 4}^{(4)} &= \eta_Q^2/4/\sqrt{70} \end{aligned} \quad (1.55)$$

Under very fast MAS condition, time dependent terms ($k \neq 0$) can be dropped, and thus Eq.(1.53) becomes

$$\left\langle m\left|\tilde{H}_Q^{(2)}\right|m\right\rangle = \frac{\Omega_Q^2}{2\omega_0}\left\{\begin{array}{l} A^{(0)}(I,m)B_0^{(0)}(\eta_Q) \\ +\sum_{n=-1}^{1} A^{(2)}(I,m)B_{2n}^{(2)}(\eta_Q)D_{2n,0}^{(2)}(\alpha_Q,\beta_Q,0)d_{0,0}^{(2)}(\theta_M) \\ +\sum_{n=-2}^{2} A^{(4)}(I,m)B_{2n}^{(4)}(\eta_Q)D_{2n,0}^{(4)}(\alpha_Q,\beta_Q,0)d_{0,0}^{(4)}(\theta_M) \end{array}\right\} \quad (1.56)$$

$$\begin{aligned} &= \omega_Q^{(0)}(\eta_Q)A^{(0)}(I,m) \\ &+\omega_Q^{(2)}(\alpha_Q,\beta_Q,\eta_Q)A^{(2)}(I,m)d_{0,0}^{(2)}(\theta_M) \\ &+\omega_Q^{(4)}(\alpha_Q,\beta_Q,\eta_Q)A^{(4)}(I,m)d_{0,0}^{(4)}(\theta_M) \end{aligned}$$

1.4.2 MQMAS[4, 9-13]

For symmetric transitions, (-m↔m), the contribution from the first-order perturbation (Eq. (1.46)) vanishes as:

$$\nu_{-m\leftrightarrow m}^{(1)} = -\left\langle -m\left|\tilde{H}_Q^{(1)}\right|-m\right\rangle + \left\langle m\left|\tilde{H}_Q^{(1)}\right|m\right\rangle = 0 \quad (1.57)$$

Thus for the symmetric transitions, only the second-order perturbation will be considered.

Thus we then only consider the second-order effects (Eq. (1.56)). First, the $d_{0,0}^2(\theta_M)$ vanishes because the system spins at the MAS angle. Second, the isotropic part (j = 0) can be ignored since it does not contribute to phase dispersion and only induces an isotropic quadrupolar-induced shift. Thus only the terms resulting from j = 2 remain and we obtain

$$\begin{aligned} \nu_{-m\leftrightarrow m}^{(2)} &= -\left\langle -m\left|\tilde{H}_Q^{(2)}\right|-m\right\rangle + \left\langle m\left|\tilde{H}_Q^{(2)}\right|m\right\rangle \\ &= 2\omega_Q^{(4)}(\alpha_Q,\beta_Q,\eta_Q)A^{(4)}(I,m)d_{0,0}^{(4)}(\theta_M) \end{aligned} \quad (1.58)$$

In MQMAS, one uses RF pulses to create (-m↔m) multiple quantum coherences, one lets these coherences evolve for a time t_1, and then one convert them to detectable (t_2) coherences (-1/2 ↔1/2). The observable part of the density matrix will take the following global phase:

$$\phi(t) = 2\omega_Q^{(4)}(\alpha_Q,\beta_Q,\eta_Q)d_{0,0}^{(4)}(\theta_M)\{A^{(4)}(I,m)t_1 + A^{(4)}(I,\frac{1}{2})t_2\} \quad (1.59)$$

$\phi(t)$ becomes zero for all crystallites simultaneously when the following equation

holds:

$$t_2 = -\frac{A^{(4)}(I,m)}{A^{(4)}(I,\frac{1}{2})} t_1 = R(I,m)t_1 \tag{1.60}$$

The values $R(I,m)$ for various spins I is shown in Table 1.2.

Table 1.2. The values $R(I, m)$ for various half-integer quadrupolar spins

	m=3/2	5/2	7/2	9/2
I=3/2	-7/9			
5/2	19/12	-25/12		
7/2	101/45	11/9	-161/45	
9/2	91/36	95/36	7/18	-31/6

1.4.3 STMAS[14-17]

In a reference frame rotating at the Larmor frequency ω_0, the frequency of an observable (m-1) ↔ m transition can be written for a rapidly spinning sample as the sum of two terms arising from the first- and second-order quadrupolar interactions, respectively:

$$\nu^{(1)}_{m-1\leftrightarrow m} = -\langle m-1|\tilde{H}^{(1)}_Q|m-1\rangle + \langle m|\tilde{H}^{(1)}_Q|m\rangle = (2m-1)A^{(1)}_Q(\alpha,\beta,\eta)d^{(2)}_{0,0}(\theta_M) \tag{1.61}$$

$$\begin{aligned}\nu^{(2)}_{m-1\leftrightarrow m} &= -\langle m-1|\tilde{H}^{(2)}_Q|m-1\rangle + \langle m|\tilde{H}^{(2)}_Q|m\rangle \\ &= \omega^{(0)}_Q(\eta_Q)C^{(0)}(I,m-1,m) \\ &+\omega^{(2)}_Q(\alpha_Q,\beta_Q,\eta_Q)C^{(2)}(I,m-1,m)d^{(2)}_{0,0}(\theta_M) \\ &+\omega^{(4)}_Q(\alpha_Q,\beta_Q,\eta_Q)C^{(4)}(I,m-1,m)d^{(4)}_{0,0}(\theta_M)\end{aligned} \tag{1.62}$$

Where

$$C^{(2j)}(I,m-1,m) = A^{(2j)}(I,m) - A^{(2j)}(I,m-1) \tag{1.63}$$

Thus

$$C^{(0)}(I,m-1,m) = I(I+1) - 9m^2 + 9m - 3$$
$$C^{(2)}(I,m-1,m) = 8I(I+1) - 36m^2 + 36m - 15 \quad (1.64)$$
$$C^{(4)}(I,m-1,m) = 18I(I+1) - 102m^2 + 102m - 39$$

If the system spins at magic angle, $d^{(2)}_{0,0}(\theta_M) = 0$. Furthermore, if we ignore the isotropic part ($j = 0$) of the second order effect, we obtain

$$\nu^{(2)}_{m-1\leftrightarrow m} = \omega^{(4)}_Q(\alpha_Q,\beta_Q,\eta_Q)C^{(4)}(I,m-1,m)d^{(4)}_{0,0}(\theta_M) \quad (1.65)$$

In STMAS, one uses RF pulses to create (m-1↔m) multiple quantum coherences, one lets these coherences evolve for a time t_1, and then convert them with RF pulses to detectable (t_2) coherences (-1/2 ↔1/2). The observable part of the density matrix will take the following global phase:

$$\phi(t) = \omega^{(4)}_Q(\alpha_Q,\beta_Q,\eta_Q)d^{(4)}_{0,0}(\theta_M)\{C^{(4)}(I,m-1,m)t_1 + C^{(4)}(I,-\frac{1}{2},\frac{1}{2})t_2\} \quad (1.66)$$

$\phi(t)$ becomes zero for all crystallites simultaneously when the following equation holds:

$$t_2 = -\frac{C^{(4)}(I,m-1,m)}{C^{(4)}(I,-\frac{1}{2},\frac{1}{2})}t_1 = R'(I,m-1,m)t_1 \quad (1.67)$$

The values $R'(I,m\text{-}1,m)$ for various spins I is shown in Table 1.3.

Table 1.3. The values $R'(I, m\text{-}1, m)$ for various half-integer quadrupolar spins

	m=3/2	5/2	7/2	9/2
I=3/2	-8/9			
5/2	7/24	-11/6		
7/2	28/45	-23/45	-12/5	
9/2	55/72	1/18	-9/8	-25/9

1.5 Principle of 1D and 2D NMR experiments[1]

One-dimensional (1D) spectra are those where the signal intensity is plotted versus a single frequency axis. r.f. pulses are used to disturb the spin system from its equilibrium. Just after that perturbation, the system evolves under the influence of local interactions, giving an electric signal known as FID (*free induction decay*), $S(t_2)$, during time t_2. Fourier transformation of $S(t_2)$ converts the time-domain signal into a frequency domain spectrum $S(\omega_2)$.

So far, the relaxation of the time-domain signal has not yet been considered. Including it into the FID leads to a broadening of the spectrum lines. Fourier transformation (FT) of such a damping signal leads to the spectrum which can be written in terms of absorptive (A) and dispersive (D) components

$$S(t_2) \xrightarrow{\text{FT}} S(\omega_2) = A(\omega_2) + iD(\omega_2) \tag{1.68}$$

In most of the cases, only the absorptive part of the signal, $A(\omega_2)$, is interesting. With short rf-pulses, it is composed of positive resonances. Dispersive line-shape, $D(\omega_2)$, exhibits anti-symmetry and always consists of positive and negative parts, which superimpose in a complicated way. Thus, due to the anti-symmetry, the integral over the dispersive lineshape always vanishes. In addition, a dispersive signal has always broader wings than the corresponding absorption component, resulting in a worse resolution.

In most of the cases, in liquids, as well as in solids, the 1D spectrum is so complicated that lines of different nuclear species overlap and that the targeted information cannot be obtained. To overcome this difficulty a second time period, t_1, between preparation and detection periods can be included. During this period, called evolution, microscopic interactions influencing the spins may be different from those influencing the spins during the detection (t_2), leading to quite informative 2D spectra.

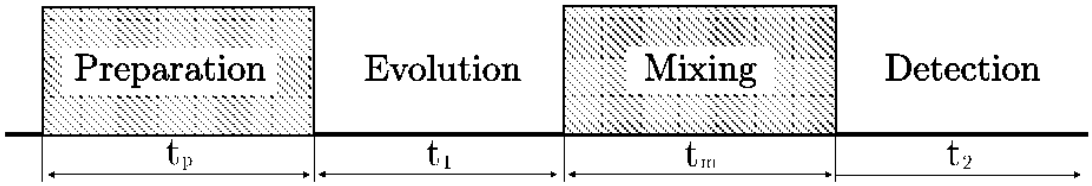

Fig. 1.3. Schematic representation for two-dimensional experiment.

An intuitive scheme of two-dimensional (2D) experiment is shown in Fig. 1.3. It consists of four periods in general: preparation, evolution, mixing and detection. The mixing period is not mandatory. The preparation period may be formed by a series of r.f. pulses to convert the system to the desired state. It can also consist of a delay long enough to allow the nuclei to reach equilibrium. During evolution time t_1 the system propagates under the influence of some internal Hamiltonians. To manipulate the spin system after the evolution period the mixing period can be included. In the last period a signal is detected for each increment of t_1 separately, thus a 2D free induction decay signal $S(t_1, t_2)$ is obtained. Double Fourier transformation of $S(t_1, t_2)$ will lead to the two-dimensional spectrum $S(\omega_1, \omega_2)$.

In 2D spectroscopy it is often necessary to have purely absorptive spectrum $A(\omega_1)A(\omega_2)$, in short A_1A_2, in order to have optimum resolution and no spectral distortions. However, two successive complex Fourier transformations, over t_2 (FT_2) and t_1 (FT_1), from the 2D time-domain signal $S(t_1, t_2)$ give the spectrum

$$S(t_1,t_2) \xrightarrow{FT_2} S(t_1,\omega_2) \xrightarrow{FT_1} S(\omega_1,\omega_2) = (A_1A_2 - D_1D_2) + i\,(D_1A_2 - A_1D_2) \quad (1.69)$$

which contains a mixture of absorptive and dispersive parts. To obtain pure absorptive spectrum the data processing has to be modified. It is often required to acquire a real (cosine), S_c, and an imaginary (sine), S_s, part of the time-domain signal with respect to t_1. This can be written shortly as

$$\begin{aligned} S_c(t_1,t_2) &= \cos(\tilde{\omega}_1 t_1)\exp(i\tilde{\omega}_2 t_2) \\ S_s(t_1,t_2) &= \sin(\tilde{\omega}_1 t_1)\exp(i\tilde{\omega}_2 t_2) \end{aligned} \quad (1.70)$$

Where $\tilde{\omega}_1$ and $\tilde{\omega}_2$ represent schematically all components present. S_c and S_s are called amplitude-modulated (with respect to t_1) spectra. When only one amplitude modulated spectrum is acquired, after the Fourier transformation, one observes a

symmetrization of the spectrum along F_1, with respect to the carrier frequency.

Performing separately for both S_c and S_s Fourier transformation and setting the dispersive parts to zero, $D_2 = 0$, the real part of the spectrum corresponds to

$$\begin{aligned} \mathrm{Re}[S_c(\omega_1,\omega_2)] &= \frac{1}{2}(A(\omega_1-\tilde{\omega}_1)+A(\omega_1+\tilde{\omega}_1))A_2 \\ \mathrm{Re}[S_s(\omega_1,\omega_2)] &= \frac{1}{2}(A(\omega_1-\tilde{\omega}_1)-A(\omega_1+\tilde{\omega}_1))A_2 \end{aligned} \qquad (1.71)$$

Adding both $S_c(\omega_1,\ \omega_2)$ and $S_s(\omega_1,\ \omega_2)$, a full absorption spectrum ($A_1.A_2$) is obtained. This technique is usually encountered in modern NMR instruments. It requires measuring of both amplitude-modulated spectra, $S_c(t_1,\ t_2)$ and $S_s(t_1,\ t_2)$, which together represent a *hypercomplex or States*[1, 7] dataset.

On the other hand an equivalent absorption spectrum, without F_1 symmetrization, can be obtained by TPPI (*time-proportional phase incrementation*)[8] acquisition and data treatment of a single amplitude-modulated spectrum. The data $S(t_1,\ t_2)$ contains two different signals from two coherence orders $\pm p$, which will overlap and give out the dispersion lineshape. Thus TPPI scheme is applied to either the excitation or reconversion pulse sequence to create an artificial offset which separates the different coherence orders, by phase-shifting the r.f. pulses of the excitation period or reconversion period synchronically with incrementing of time t_1. This frequency offset is given by $\Delta\omega = \Delta\phi/\Delta t_1$, where $\Delta\phi$ is the phase increment. A coherence of order p is then offset from the spectral center by $p\Delta\omega$, resulting in a spectrum in which all excited coherence orders can be observed without any folding or symmetrization. In this case, and with respect to States, there is a single experiment not two, but the t_1 step is divided by two to double the spectral-width.

Another way to obtain the absorption spectrum is echo/anti-echo method, which utilize the symmetry properties of the time-domain signals and their complex Fourier transformations. Normally $S(t_1,t_2) = f(t_1)e^{-\lambda t_2}e^{i\omega t_2}u(t_2)$, $f(t_1)$ is a function of t_1 and $u(t)$ is a step function, which is defined as

$$u(t) = \begin{cases} 1, & t \geq 0 \\ 0, & t < 0 \end{cases} \qquad (1.72)$$

In the echo/anti-echo method, the signal $S'(t_1,t_2)$ is symmetrized and defined as

$$S'(t_1,t_2) = f(t_1)[e^{-\lambda t_2}e^{i\omega t_2}u(t_2) + e^{\lambda t_2}e^{i\omega t_2}u(-t_2)] \quad (1.73)$$

The complex Fourier transformation of the two halves of a suitably phased symmetrical NMR echo is real. Each half yields the absorption components with the same phase and the dispersion components with opposite phases, which thus cancel. Thus two successive complex Fourier transformations give out an absorption 2D spectrum, which shows below:

$$S'(t_1,t_2) \xrightarrow{FT_2} A_2 * S'(t_1,\omega_2) \xrightarrow{FT_1} S'(\omega_1,\omega_2) = A_2(A_1 + iD_1)$$

1.6 Through-space correlation: Continuous-wave cross-polarization

Continuous-wave cross-polarization (CW-CP)[18, 19] has played an instrumental role in extending the analytical capabilities of solid-state nuclear magnetic resonance (NMR) to the studies of what were once considered 'difficult' nuclei, such as ^{13}C, ^{15}N, ^{29}Si. Nuclear polarization is usually transferred from abundant spins I with large gyromagnetic ratio γ_I and short longitudinal relaxation time T_{1I} to diluted spins S with small γ_S or long T_{1S}, in order to increase the magnetization of S and the repetition rate of the experiment. For resolution enhancement, this transfer is very often combined with magic-angle spinning (MAS), leading to the CW-CPMAS method.[20, 21] The widespread use of this method is not limited to signal enhancement, but also includes spectral editing and various two-dimensional (2D) techniques, such as hetero-nuclear correlation (HETCOR) experiments. These experiments can provide detailed information about complex structures in chemistry, biology and materials science by identifying atoms in local 'proximity' to one another. HETCOR methods have been well established for spin-1/2 nuclei using CW-CPMAS.[22]

CW-CP between spin I = 1/2 and S = 1/2 systems is a relatively simple and well-understood process. For a static sample and under on-resonance conditions there is a unique 'Hartmann-Hahn' matching condition[18], at which polarization is transferred between the two sets of nuclei, given by:

$$\nu_{1S} = \nu_{1I} \tag{1.74}$$

where $\nu_{1I} = -\gamma_I B_{1I}$ and $\nu_{1S} = -\gamma_S B_{1S}$ are the strengths (or the nutation rates) of the radiofrequency fields B_{1I} and B_{1S} applied to the *I* and *S* nuclei, respectively, during the spin-locking period.

The rotation of the sample that occurs during MAS introduces a modulation of the dipolar interaction between spins *I* and *S* and, consequently, a modification of the Hartmann-Hahn matching condition. Under fast MAS, optimum transfer of CW-CPMAS is observed at the modified Hartmann- Hahn condition given by[21]:

$$\nu_{1S} = \varepsilon\nu_{1I} \pm j\nu_R \qquad (j = 0, 1, 2, 3..) \tag{1.75}$$

where ν_R is the spinning frequency and *j* is an integer. In the case of very fast MAS, the $j = 1$ and 2 conditions are the two most efficient. Depending on the CP transfer, ε is equal to +1 or –1, corresponding to flip-flop or flop-flop terms, respectively. It is important to note that these two types of transfers give signals of opposite signs.

CW-CPMAS can be applied to half-integer quadrupolar nuclei (spin: 3/2, 5/2, 7/2, 9/2). In powdered samples, these CP dynamics are strongly anisotropic with respect to crystallite orientation and they depend on numerous experimental parameters.[23, 24] As a result, in most cases, CW-CPMAS transfers become much less sensitive than with spin-1/2 nuclei only, especially when two different quadrupolar nuclei are involved.[25, 26] In the standard CW-CPMAS method performed under fast MAS with weak CT-selective irradiation of the quadrupolar *I* nucleus, the two rf-fields are related each other by the following rule: [21, 23, 24, 27]

$$\nu_{1S} = \varepsilon(I + \frac{1}{2})\nu_{1I} \pm j\nu_R \qquad (j = 0, 1, 2, 3..) \tag{1.76}$$

Cross polarization involving quadrupolar nuclei presents additional challenges due to the convoluted spin dynamics involved in the spin-locking of these nuclei and polarization transfer. The efficiency of spin locking under MAS depends on the amplitude and frequency of the spin-locking rf field, the MAS rotation frequency and the magnitude of the quadrupolar interaction. Magic angle spinning complicates the polarization transfer by making the quadrupole splitting time dependent. The central transition can no longer be treated as an isolated fictitious spin-1/2 system, which

affects both spin locking and polarization transfer.

The effect of MAS on spin locking of spin *I* magnetization can be categorized based on the magnitude of the adiabaticity parameter[23, 24]

$$\alpha = \frac{\nu_{1I}^2}{\nu_Q \nu_R} \tag{1.77}$$

The efficiency of spin locking increases when $\alpha >> 1$ or when $\alpha << 1$, whereas the intermediate case $\alpha \approx 1$ results in a loss of spin locked state. For $\alpha << 1$, referred to as sudden passage, the spins remain in their initial eigenstates during MAS. When the condition $\alpha >> 1$ (referred as adiabatic passage) holds, the level populations of *I* spins continuously follow the eigenstates of the Hamiltonian. Under typical conditions of ν_Q = 1 MHz and ν_R =10 kHz, the sudden passage condition requires that $\nu_{1I} << 100$ kHz. To be efficient in practice, RF fields of a few kHz are often used, which leads to a large sensitivity to off-resonance irradiation. This is the reason why CW-CPMAS HETCOR spectra are often recorded with several complementary experiments performed with different irradiation offsets, especially at high magnetic field.

Moreover, the RF matching curves show numerous dips related to level crossings[27] or rotary resonance phenomenon[28] (Fig. 1.4), which means that setting up the CW-CPMAS transfer is not easy, especially with samples of low sensitivity. Moreover, the efficiency of this transfer decreases largely with increasing second-order quadrupole interactions[27], and hence sites with large C_Q values are often hardly observable. As a result, methods based on CW-CPMAS transfer to or from half-integer quadrupolar nuclei are subject to many important experimental and theoretical limitations and are thus not commonly used.

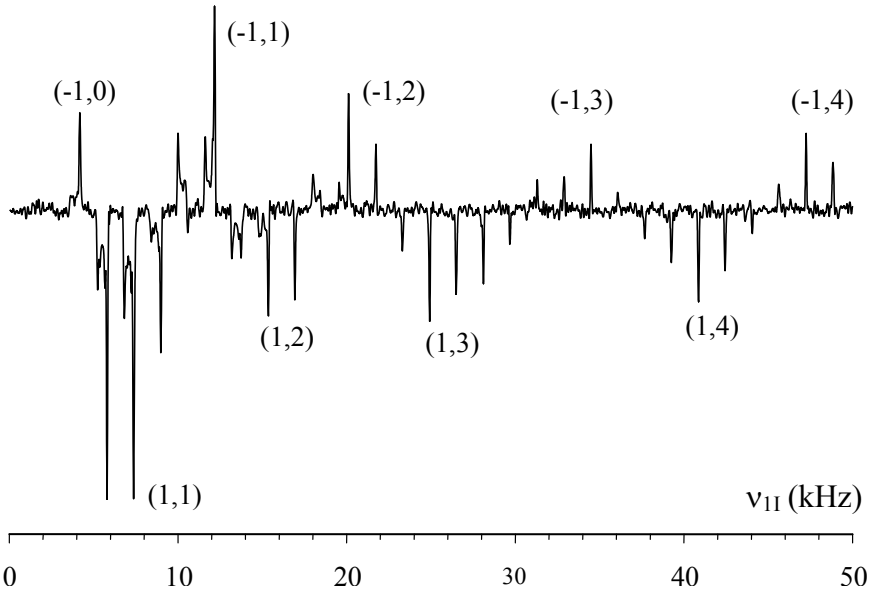

Fig. 1.4. Efficiency of $^{1}H \rightarrow ^{11}B$ CW-CPMAS in borax as a function of ν_{1I} (Hartmann-Hahn matching curve). The spectra were acquired on-resonance, using ν_{1S}= 6 kHz, CT=300 ms (which favors the sidebands with j=1) and ν_R = 20 kHz. The match at ν_{1I} = 3 kHz corresponds to an (ε, j) pair of (-1, 0).

1.7 Through-bond correlation

Indirect dipolar–dipolar coupling constants, *J* couplings, are widely used in liquid-state NMR to provide through-bond information about molecular structure.[1] However in the solid state *J* couplings are more difficult to observe directly, as they are obscured by the much stronger dipolar, chemical shift and quadrupolar contributions to the line-width. Typical isotropic values of *J*-coupling constants between light nuclei are in the range of a few tens of Hertz, while dipolar couplings are in the range of kHz, chemical shift anisotropy in the range of several or tens of kHz, and quadrupolar couplings in the range of MHz.

Recent results on spin 1/2 nuclei in solid state materials have shown that the measurement and utilization of *J* couplings are nevertheless possible in cases that the other line broadening interactions could be sufficiently reduced[29-33]. Thus it is possible to transpose liquid sequences based on scalar coupling like *J*-Resolved ,[29-31] *J*-HMQC [32], or *J*-HSQC[33] experiments into solid state NMR.

When considering inorganic compounds involving quadrupolar nuclei bonded to I=1/2 nuclei, it is also possible to accurately measure *J*-couplings, using *J*-Resolved

experiments[34], and to transpose the *J*-HMQC[34] or *J*-RINEPT[35, 36] heteronuclear correlation experiment.

The *J*-Resolved pulse sequence used to measure the *J*-coupling is shown in Fig. 1.5. First it is possible to measure the spin-echo decay time $T_2^{'}$ of the selectively irradiated central transition of ^{27}Al ($\pi/2 - \tau - \pi - \tau$ -acquire), which corresponds to a non-refocusable line-width under the current experimental conditions. Although this value is currently referred to as "T_2 relaxation time", it is better to name it $T_2^{'}$ which clearly states its experimental nature and makes no hypothesis on its underlying mechanism. Fig. 1.5 shows the spin-echo decay (b1) and its Fourier transform (c1). They can be modeled with a close to perfect mono-exponential decay in time domain or a Lorentzian line in frequency domain, leading to $T_2^{'}$ = 14.1 ± 0.5 ms.

The application of a π pulse on the ^{31}P channel simultaneously with the ^{27}Al π pulse of the echo sequence (Fig. 1.5a) introduces a modulation of the obtained signal by the heteronuclear Al–O–P J-coupling, which can be modeled as:

$$S(\tau) = \prod_n \cos(2\pi J_n t) \exp(-2\tau / T_2^{'}) \qquad (1.78)$$

where *n* are the different coupled nuclei with their coupling J_n and $T_2^{'}$ corresponds to the non-refocusable line-width under this experiment. Because the berlinite structure involves two slightly different O sites (O_a and O_b) and thus two different Al–O–P bonds, a two *J*-coupling model is used here. Then we obtain a good fit of *J*-Resolved spectrum, resulting in $J_a = J_{Al–Oa–P}$ = 26.0 ± 1 Hz, $J_b = J_{Al–Ob–P}$ = 19.5 ± 1 Hz, and $T_2^{'}$(*J*-Resolved) = $T_2^{'}$(spin-echo) (Fig. 1.5 b2 and c2).

Thus *J*-Resolved experiment allows us to experimentally evidence the presence of the two non-equivalent O sites translating into their different scalar *J*-couplings.

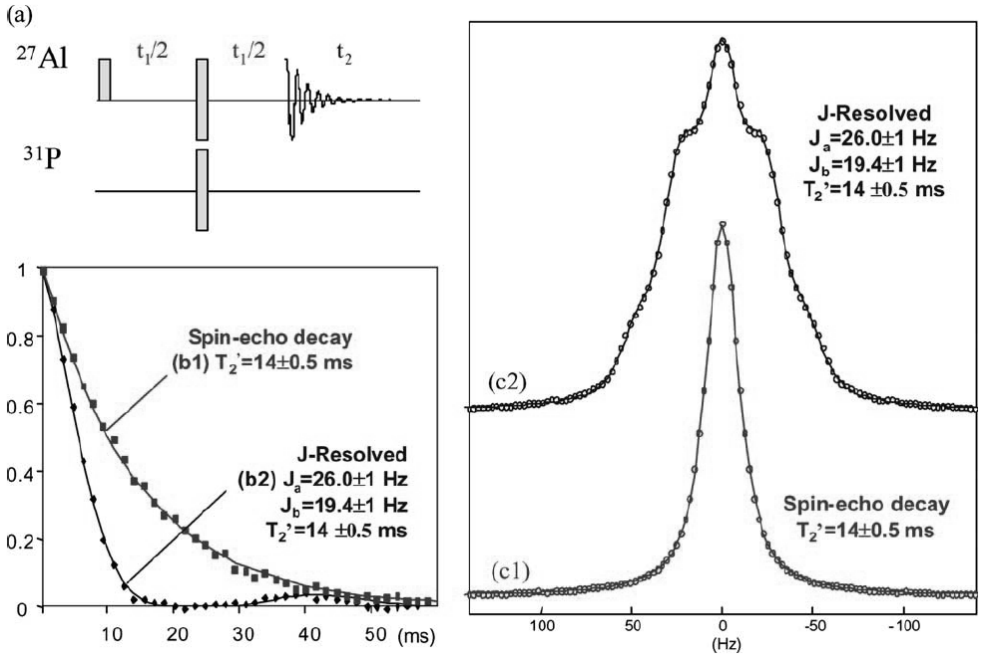

Fig. 1.5. (^{31}P)-^{27}Al *J*-Resolved experiment on $AlPO_4$ berlinite, acquired with ν_R =13 kHz: (a) Pulse sequence of the *J*-Resolved experiment, (b1, c1) time and frequency domains of the ^{27}Al spin-echo spectra (no 31P pulse); (b2, c2) time and frequency domains of the (^{31}P)-^{27}Al *J*-Resolved spectra (symbols) with their modeling (continuous line).

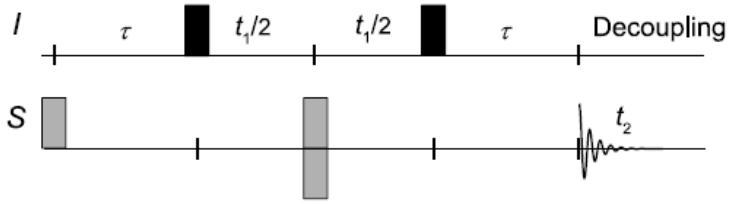

Fig. 1.6. *J*-HMQC pulse sequences under MAS

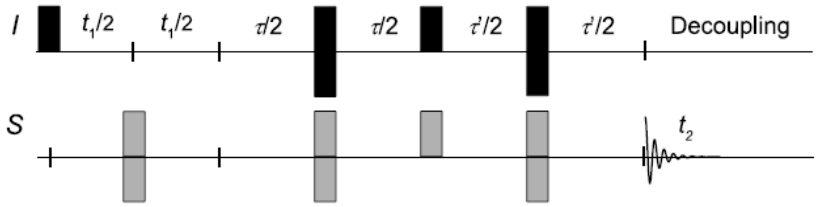

Fig. 1.7. *J*-RINEPT pulse sequences under MAS

J-HMQC directly derives from the *J*-Resolved experiment, by splitting the ^{31}P π pulse into two π/2 pulses placed on both sides of the central ^{27}Al π pulse and

separated by an incremented $t_1/2$ evolution encoding the indirect dimension of the two-dimensional spectrum (see Fig. 1.6). The other useful *J*-RINEPT pulse sequence is shown in Fig. 1.7.

References

1. Ernst, R. R.; Bodenhausen, G.; Wokaun, A., *Principles of Nuclear Magnetic Resonance in One and Two Dimensions*. Oxford University Press: 1990.

2. Slichter, C. P., *Principles of Magnetic Resonance*. Springer: 1996.

3. Cowan, B., *Nuclear Magnetic Resonance and Relaxation*. Cambridge University Press: 1997.

4. Charpentier, T., *Résonance magnetique nucléaire haute-résolution sur les noyaux quadripolaires dans les solides* PhD Thesis, University of Paris XI Orsay: 1998.

5. Duer, M. J., *Solid-State NMR Spectroscopy: Principles and Applications*. Blackwell Science: 2002.

6. Levitt, M. H., *Spin Dynamics: Basics of Nuclear Magnetic Resonance* Wiley: 2002.

7. Magnus, W., On the exponential solution of differential equations for a linear operator. *Com. Pure. Appl. Math.* **1954,** 7, 649.

8. Edmonds, A. R., *Angular Momentum in Quantum Mechanics*. Princeton University Press: Princeton, 1957.

9. Medek, A.; Harwood, J. S.; Frydman, L., Multiple-quantum magic-angle spinning NMR: A new method for the study of quadrupolar nuclei in solids. *Journal of the American Chemical Society* **1995,** 117, (51), 12779.

10. Brown, S. P.; Wimperis, S., Two-Dimensional Multiple-Quantum MAS NMR of Quadrupolar Nuclei: A Comparison of Methods. *Journal of Magnetic Resonance* **1997,** 128, (1), 42.

11. Amoureux, J. P.; Pruski, M., Advances in MQMAS NMR *Encyclopædia of NMR (2nd edition)* **2002**, 54-90.

12. Amoureux, J. P.; Fernandez, C.; Frydman, L., Optimized multiple-quantum magic-angle spinning NMR experiments on half-integer quadrupoles. *Chemical Physics Letters* **1996,** 259, (3-4), 347.

13. Frydman, L.; Harwood, J. S., Isotropic spectra of half-integer quadrupolar spins from bidimensional magic-angle spinning NMR. *Journal of the American Chemical*

Society **1995,** 117, (19), 5367.

14. Gan, Z., Isotropic NMR spectra of half-integer quadrupolar nuclei using satellite transitions and magic-angle spinning. *Journal of the American Chemical Society* **2000,** 122, (13), 3242.

15. Gan, Z., Satellite transition magic-angle spinning nuclear magnetic resonance spectroscopy of half-integer quadrupolar nuclei. *Journal of Chemical Physics* **2001,** 114, (24), 10845.

16. Ashbrook, S. E.; Wimperis, S., Satellite-transition MAS NMR of spin I = 3/2, 5/2, 7/2, and 9/2 nuclei: Sensitivity, resolution, and practical implementation. *Journal of Magnetic Resonance* **2002,** 156, (2), 269.

17. Ashbrook, S. E.; Wimperis, S., High-resolution NMR of quadrupolar nuclei in solids: The satellite-transition magic angle spinning (STMAS) experiment. *Progress in Nuclear Magnetic Resonance Spectroscopy* **2004,** 45, (1-2), 53.

18. Hartmann, S. R.; Hahn, E. L., Nuclear double resonance in the rotating frame. *Phys. Rev.* **1962,** 128 2042-2053.

19. Pines, A.; Gibby, M. G.; Waugh, J. S., Proton-enhanced NMR of dilute spins in solids. *J. Chem. Phys.* **1973,** 59, 569-590.

20. Schaefer, J.; Stejskal, E. O., Carbon-13 nuclear magnetic resonance of polymers spinning at the magic angle *Journal of the American Chemical Society* **1976,** 98, (4), 1031.

21. Stejskal, E. O.; Schaefer, J.; Waugh, J. S., Magic-Angle Spinning and Polarization Transfer in Proton-Enhanced NMR. *J. Magn. Reson.* **1977,** 28, 105-112.

22. Caravatti, P.; Bodenhausen, G.; Ernst, R. R., Heteronuclear Solid-State Correlation Spectroscopy *Chem. Phys. Lett.* **1982,** 89, 363-367.

23. Vega, A. J., CP/MAS of quadrupolar S = 3/2 nuclei. *Solid State NMR* **1992,** 1, 17-32.

24. Vega, A. J., MAS NMR spin-locking of half-integer quadrupolar nuclei. *J. Magn. Reson.* **1992,** 96 50-68.

25. Eastman, M. A., Examples of Hartmann-Hahn match conditions for CW-CPMAS between two half-integer quadrupolar nuclei. *J. Magn. Reson.* **1999,** 139 98-108.

26. Chan, J. C. C., High-resolution hetero-nuclear correlation between quadrupolar nuclei. *J. Magn. Reson.* **1999,** 140, 487-490.

27. Amoureux, J. P.; Pruski, M., Theoretical and experimental assessment of single- and multiple-quantum cross-polarization in solid-state NMR. *Molec. Phys.* **2002,** 100, 1595-1613.

28. Oas, T. G.; Griffin, R. G.; Levitt, M. H., Rotary resonance recoupling of dipolar interactions in solid-state nuclear magnetic resonance spectroscopy. *J. Chem. Phys.* **1988,** 89, 692–695.

29. Kubo, A.; McDowell, C. A., One- and two-dimensional 31P crosspolarization magic-angle-spinning nuclear magnetic resonance studies on two-spin systems with homonuclear dipolar and J coupling,. *J. Chem. Phys.* **1990,** 92, 7156–7170.

30. Wu, G.; Wasylishen, R. E., Homonuclear 31P J-resolved 2D spectra of rhodium(I) phosphine complexes in the solid state. *Inorganic Chemistry* **1992,** 31, (1), 145.

31. Brown, S. P.; Perez-Torralba, M.; Sanz, D.; Claramunt, R. M.; Emsley, L., The direct detection of a hydrogen bond in the solid state by NMR through the observation of a hydrogen-bond mediated 15N-15N J coupling. *Journal of the American Chemical Society* **2002,** 124, (7), 1152.

32. Fayon, F.; Le Saout, G.; Emsley, L.; Massiot, D., Through-bond phosphorus-phosphorus connectivities in crystalline and disordered phosphates by solid-state NMR. *Chemical Communications* **2002**, (16), 1702.

33. Lesage, A.; Emsley, L., Through-bond heteronuclear single-quantum correlation spectroscopy in solid-state NMR, and comparison to other through-bond and through-space experiments. *Journal of Magnetic Resonance* **2001,** 148, (2), 449.

34. Massiot, D.; Fayon, F.; Alonso, B.; Trebosc, J.; Amoureux, J. P., Chemical bonding differences evidenced from J-coupling in solid state NMR experiments involving quadrupolar nuclei. *Journal of Magnetic Resonance* **2003,** 164, (1), 160.

35. Wiench, J. W.; Pruski, M., Probing through bond connectivities with MQMAS NMR. *Solid State NMR* **2004,** 26, 51–55.

36. Amoureux, J. P.; Trebosc, J.; Wiench, J.; Pruski, M., HMQC and refocused-INEPT experiments involving half-integer quadrupolar nuclei in solids.

Journal of Magnetic Resonance **2007,** 184, (1), 1.

Chapter 2. Through-space Correlation experiments between spin-1/2 and half-integer quadrupolar nuclei: Multiple-Pulse CPMAS

In chapter 1, we mentioned that the RF-fields in the quadrupolar nuclei channel of CW-CPMAS must then be very weak, which leads to a large sensitivity to off-resonance irradiation. Moreover, the RF matching curves of CW-CPMAS show numerous dips related to level crossings[1] or rotary resonance phenomenon.[2]

Recently a sequence, named MP-CPMAS (Multiple-Pulse CPMAS) has been presented.[3] It is composed of a CW irradiation on one channel and rotor synchronized pulses on the other channel. The sequence was originally designed to reduce ^{1}H RF power in ^{1}H-^{13}C CP at ultra-fast MAS speed. The authors made a comparison on alanine under $\nu_R = 60$ kHz MAS between CW-CPMAS with proton RF amplitude of $\nu_{1H} = 4$ kHz and MP-CPMAS using short and strong pulses (0.35 μs and $\nu_{1H} = 280$ kHz) leading to the same averaged 4kHz RF field on ^{1}H. In both cases, the ^{13}C RF-field (ν_{1C}) was close to either ν_R or $2\nu_R$. The signal to noise ratio under MP-CPMAS conditions was approximately 50% larger than that obtained with a CW-CPMAS experiment performed with either low (4 kHz) or high (100 kHz ramped) ^{1}H power. As it utilizes a weak average RF field, this method is close to that used for quadrupolar nuclei where RF field is most of the time smaller than ν_R. Here we adapt the MP-CPMAS method to avoid the previously described limitations observed with CW-CPMAS transfers between spin-1/2 and half-integer quadrupolar nuclei.

2.1 Theory

Our MP-CPMAS experiment is based on the conventional CPMAS sequence where one replaces the CW spin-lock pulse on the quadrupolar nucleus by low RF rotor-synchronized multiple pulses using the same phase (Oy) shifted by 90° relative to the initial pulse (Ox). Here, low RF means that one wants to manipulate only the central transition (CT), which thus behaves as a fictitious spin ½. Indeed, a low RF field in the order of a few kHz does not affect satellite transitions and avoids uncontrollable transfer to satellite coherences.[4-6] We will call these pulses CT-selective. Fig. 2.1 shows the sequence when transferring magnetization from the quadrupolar nucleus. We will also show results for the opposite transfer (from spin ½ to quadrupolar nucleus) in Fig. 2.9.

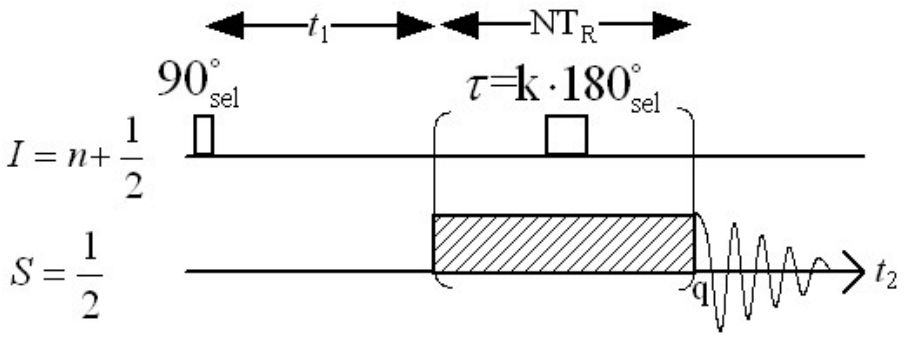

Fig. 2.1. Pulse-sequence for the acquisition of MP-CPMAS 2D HETCOR spectra, starting from the quadrupolar nucleus (the subscript *sel* stands for CT selective). Phases follow the conventional CPMAS sequence.

During the multiple CT-selective train pulses the first-order anisotropic interactions are averaged by MAS over full rotor periods and rotary resonance conditions are avoided, while the series of rotor-synchronized RF pulses acts as a spin-lock. Indeed, the pulses make the magnetization rotate around the "spin-lock" axis keeping it close to it, as long as dephasings due to offsets are not too strong. Of course, this is true only as long as the non-refocusable transverse ($T_2^{'}$) relaxation time (instead of $T_{1\rho}$ in CW-CPMAS) is long enough to avoid signal decay during the spin-lock period.

In the following, the observed nucleus will always be denoted S and the non-observed I. In the standard CW-CPMAS method performed under fast MAS with weak CT-selective irradiation of the quadrupolar I nucleus, the two effective RF fields (ν_{1S} , ν_{1I}^{eff}) are related each other by the extended Hartman-Hahn conditions: [4-7]

$$\nu_{1S} = \varepsilon \nu_{1I}^{eff} \pm j\nu_R \tag{2.1}$$

with j = 0, **1, 2,** 3... and $\varepsilon = \pm 1$. In the case of very fast MAS only the j = 1 and 2 conditions are efficient. ε corresponds to flip-flop (+1) or flop-flop (-1) terms leading to CP transfer of opposite signs. For quadrupolar CT-selective RF field we have $\nu_{1I}^{eff} = (I+1/2)\nu_{1I}$, where ν_{1I} is the field measured in the absence of the quadrupolar coupling, for example on a liquid.

Following the treatment in S-AMCP,[8-10] in MP-CPMAS one must consider the averaged effective field ($\overline{\nu}_{1I}^{eff}$) instead of ν_{1I}^{eff} . For one pulse every N rotor periods (NT_R) one has :

$$\overline{\nu}_{1I}^{eff} = \nu_{1I}^{eff}\tau / NT_R = \nu_{1I}^{eff} k\tau_{\pi sel}\nu_R / N = k\nu_R / 2N \tag{2.2}$$

where the pulse-length (τ) has been scaled by the factor k with respect to that of a CT-selective π pulse ($\tau_{\pi sel}$) using the same effective RF-field. As example, for a spin 5/2 nucleus, if the RF pulse specifications are: τ= 8.333 μs and ν_{1I}=10kHz ($\tau_{\pi sel}$= 50/3=16.667 μs), then k=0.5. Let us introduce the duty-cycle parameter p equal to the ratio between the pulse length and the rotor period:

$$p = \tau / T_R = k\tau_{\pi sel} / T_R = 0.5k\nu_R / \nu_{1I}^{eff} \tag{2.3}$$

Eq. (2.2) assumes that one pulse fits into N rotor periods**,** that is :

$$k\pi_{\pi sel} < N / \nu_R \quad \text{or} \quad k / 2N < (I+1/2)\nu_{1I} / \nu_R \quad \text{or} \quad p < N \tag{2.4}$$

By replacing the I RF-field by its time average, one can re-write Eq. (2.1) as:

$$\nu_{1S} = (\varepsilon k / 2N \pm j)\nu_R, j = 0, \mathbf{1}, \mathbf{2}, 3... \tag{2.5}$$

As already discussed before, for quadrupolar nuclei one must use weak RF fields. One may also wish to spin very fast in order to enhance proton resolution or to drive the sidebands out of the spectral range or to get sufficiently large indirect spectral width in rotor-synchronized 2D experiments. Therefore, the factor $k/2N$ is usually smaller than 1, and hence Eq.(2.5) can be simplified as:

$$\nu_{1S} = (\varepsilon k / 2N + j)\nu_R, j = 0, \mathbf{1}, \mathbf{2}, 3... \quad (2.6)$$

In the case of very fast MAS mainly the j = 1 and 2 conditions are efficient, which gives rise to four main resonances, with ν_{1S} frequencies pair-wise symmetrical with respect to ν_R and $2\nu_R$: two with flip-flop and two with flop-flop transfers ($\varepsilon = +1$ or -1, respectively). When the pulse-length is short, as in the $^{1}H \rightarrow {}^{13}C$ experiment previously described (k = 0.19),[3] two matching fields are close to ν_R and the two others to $2\nu_R$.

A partial signal cancellation occurs at $\nu_{1S} = 1.5\ \nu_R$ when the condition $k = N$ is fulfilled on the quadrupolar channel, e.g. one CT-selective π pulse every rotor period. This partial cancellation is related to coinciding matching conditions of flip-flop ($\varepsilon = +1, j$ = 1) and flop-flop ($\varepsilon = -1, j$ = 2) transfers, which are of opposite signs.

2.2 Experimental parameters

In preparation for the experiments, simulations were run on SIMPSON.[11] The system used for the simulations is a ^{27}Al nucleus (C_Q=3MHz, η_Q=0) coupled to ^{31}P with a dipolar coupling of 400Hz aligned with the electric field gradient tensor. Powder averaging was performed using 168 crystallites following the REPULSION algorithm.[12] RF fields, spinning speed and static field are given in figure captions.

The experiments were performed on a wide bore 9.4 T and narrow bore 18.8 T Bruker Avance-II spectrometers equipped with triple resonance 3.2mm MAS probes. We have tested

the MP-CPMAS experiments on four different samples: $AlPO_4$-berlinite, $AlPO_4$-VPI5, $AlPO_4$-14, and $Na_7(AlP_2O_7)_4PO_4$.

The structure of berlinite $AlPO_4$ (space group $P3_121$) involves only one Al and one P crystallographic sites.[13] Aluminum and phosphorus atoms occupy tetrahedrally coordinated positions, Al–$(OP)_4$ and P–$(OAl)_4$, cross-linked by two different bridging oxygen atoms, O_1 and O_2. This leads to a single gaussian line for the ^{31}P MAS NMR spectrum and a single second-order quadrupolar line-shape for the ^{27}Al MAS spectrum (C_Q = 4.07 MHz, and η_Q = 0.34).[14]

Microporous hydrated aluminophosphate $AlPO_4$-VPI5 contains three equally populated sites for Al and P, which are coordinated with each other through one bridging oxygen.[15] Under MAS, the ^{31}P resonances are well resolved, but only two ^{27}Al peaks are observable at 9.4 T. The resonance which is labeled Al_1 represents a site between the fused four-membered rings. Two water molecules complete an octahedral coordination sphere for Al_1 and render inequivalent the tetrahedrally coordinated Al_2 and Al_3 sites, as well as the phosphorus sites P_2 and P_3 in the six-membered rings. The specific connectivities between various nuclei are as follows: Al_1 ($2P_1$, P_2, P_3), Al_2 (P_1, $2P_2$, P_3) and Al_3 (P_1, P_2, $2P_3$). The quadrupolar coupling constants C_Q for the aluminum sites are 3.95 MHz (Al_1), 1.3 MHz (Al_2), and 2.8 MHz (Al_3).[16, 17]

We have also tested our sequences on a powder sample of $AlPO_4$-14, templated using isopropylamine. Its structure consists of 4-, 6-, and 8-rings pores. Its space group is $P\bar{1}$ with an inversion center.[18] The unit cell composition corresponds to $Al_8P_8O_{32}(OH)_2^-$ for the framework, plus two protonated isopropylamine $(C_3H_{10}N)^+$ ions and two water molecules[18] that undergo motions on the microsecond timescale in the 8-ring channels.[19] This AFN-type material forms a 3D channel system, made of alternating AlO_x (x = 4, 5, 6) and PO_4 polyhedrons, with 8-ring pores containing four different P and four different Al sites. The

quadrupolar coupling constants C_Q and asymmetry parameters η_Q of $Al_{1,2,3,4}$ are equal to 5.58, 4.08, 1.74 and 2.57 MHz and 0.97, 0.82, 0.63 and 0.7, respectively.[20, 21]

As for the sample of $Na_7(AlP_2O_7)_4PO_4$, there are one aluminum species, three phosphorus species and three sodium species.[22, 23] The phosphate network is made of one $(P_2O_7)^{4-}$ unit where the two Q_1 phosphorous sites are close to all three Na sites and one isolated $(PO_6)^{3-}$ unit where the Q_0 phosphorous site is close to only two Na sites.

2.3 Results

Synchronization

First we have verified experimentally on $AlPO_4$-berlinite that the rotor-synchronization of the pulses is mandatory (Fig. 2.2).

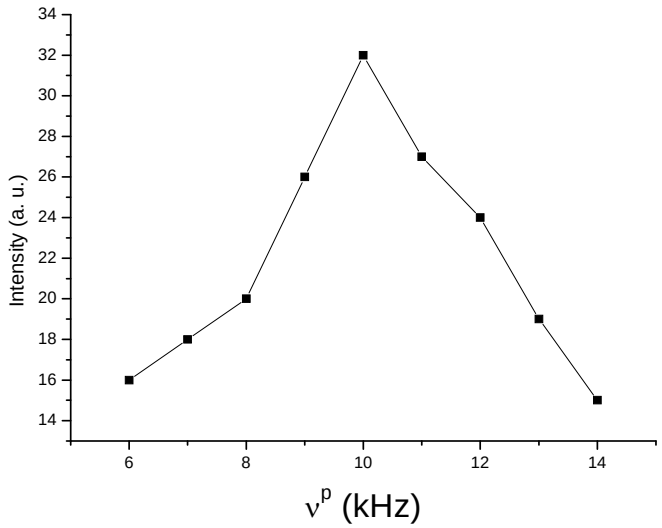

Fig. 2.2. ^{31}P signal observed on the $^{27}Al \rightarrow {}^{31}P$ MP-CPMAS spectrum of $AlPO_4$-berlinite (t_1 = 0), versus the repeat frequency of the pulses (ν^P), which are applied to the aluminum channel. B_0 = 9.4T, ν_R = 10kHz, $k = N = 1$, ν_{1Al} = 8kHz. ν_{1P} is optimized after every change of the frequency. The signal is maximal when rotor synchronization is achieved: $\nu^P = \nu_R$.

It is important to note that, in contrast to CW-CPMAS,[6] for MP-CPMAS of quadrupolar nuclei we have never observed any dip in the matching curve. The reason for this

is that the RF-sequence applied to the quadrupolar nucleus consists of short selective pulses and thus the anti-level crossing and rotary resonance effects encountered with CW-CPMAS are avoided. This is very important when optimizing the RF-conditions on an insensitive sample. The CW RF-field applied to the spin-1/2 nucleus on the other hand is easy to optimize as its value is known in advance from Eq.(2.6).

Matching curves

In Fig. 2.3 we have simulated the absolute value of the signal versus ν_{1S}.

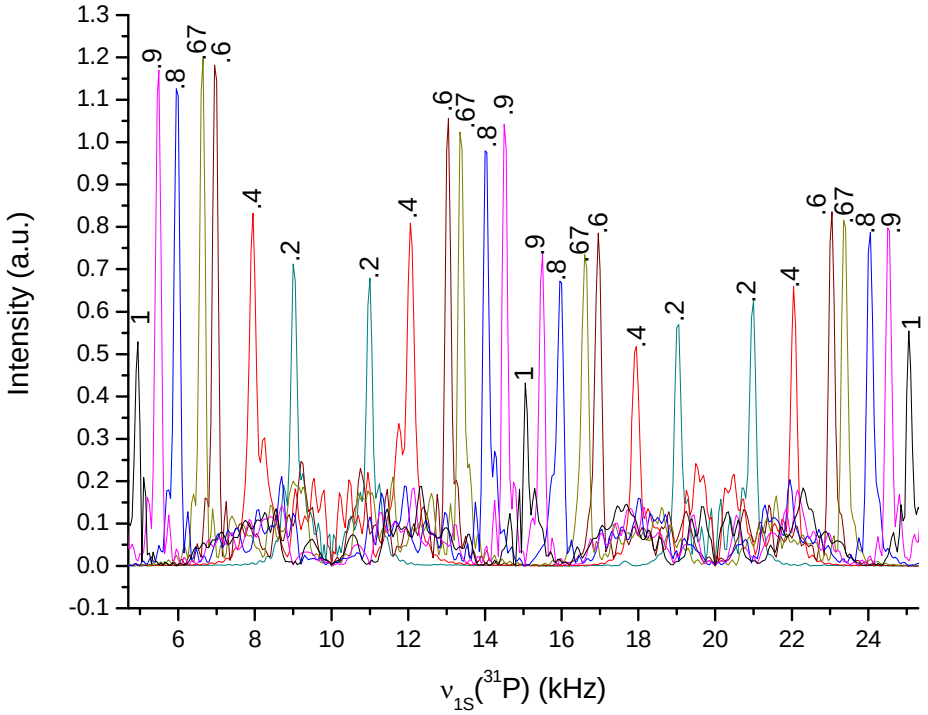

Fig. 2.3. ^{27}Al-^{31}P MP-CPMAS HETCOR absolute-value of the signal ($t_1 = 0$) versus ν_{1S}, simulated with SIMPSON. $B_0 = 9.4$T, on-resonance irradiation, $\nu_{1Al} = \nu_R = 10$kHz, $C_Q = 3$MHz, $\eta_Q = 0$, $D_{IS} = 400$Hz aligned with the largest component of the aluminum electric-field gradient tensor, one rotor-synchronized pulse every rotor-period ($N = 1$). The k value is indicated for each matching condition. The duty-cycle parameter is equal to $p = 0.033$, 0.067, 0.100, 0.133, 0.167 for $k = 0.2$, 0.4, 0.6, 0.8, 1.0, respectively.

One can see that equation (2.6) is fulfilled. For example, for $k = 0.5$ the best matching field is achieved for 7.5 kHz ($\varepsilon = -1$, $j = 1$), 12.5 kHz ($\varepsilon = +1$, $j = 1$), 17.5 kHz ($\varepsilon = -1$, $j = 2$)

and 22.5 kHz ($\varepsilon = +1$, $j = 2$). For very short pulse-lengths ($0 < k < 0.5$) the transfer efficiency remains poor; but when k increases, the spin-locking of the I nucleus becomes more efficient. It reaches a maximum for $0.5 \leq k \leq 0.9$, and then decreases for k equal to 1, for which only three matching conditions (ν_{1S}/ν_R = 0.5, 1.5, 2.5) are observable. In the latter case (k = 1), resonances are much less efficient than those observed for $0.5 \leq k \leq 0.9$. This decrease of the signal is related to a partial signal cancellation due to overlap of flip-flop ($\varepsilon = +1$) and flop-flop ($\varepsilon = -1$) transfers, which are of opposite signs. As an example, the resonance observed at ν_{1S} = 15kHz, results from an overlap of flip-flops with j = 1, and flop-flops with j = 2. When the CP transfer is made to, not from, the quadrupolar nucleus the matching curves are exactly the same, except that ν_{1S} is exchanged with ν_{1I}.

CT-selective pulses

With moderate or large quadrupole interactions, only the central transition (CT) is observable on powder samples, and most of the time ($C_Q >> 100$ kHz) soft CT-selective RF pulses must be used in order to control the evolution of the density matrix during the dipolar transfer. Indeed, when this is not the case the coherences will spread all over the density matrix after a few pulses, instead of remaining localized within the +1/2 ↔ -1/2 one-quantum coherences, as it is the case when using weak RF-fields. Simulations have shown that for $\nu_{1I} \geq$ 20 kHz, most of the time ($C_Q >> 100$ kHz), the signal decreases considerably in the same way as for CW-CPMAS.[6] This fact has been experimentally confirmed on our test sample, $AlPO_4$-berlinite (C_Q = 4.07 MHz, η_Q = 0.34).[14] Indeed, in Fig. 2.4, one can observe a decrease in efficiency of approximately a factor of 2 when increasing the RF-field from 5 to 20 kHz.

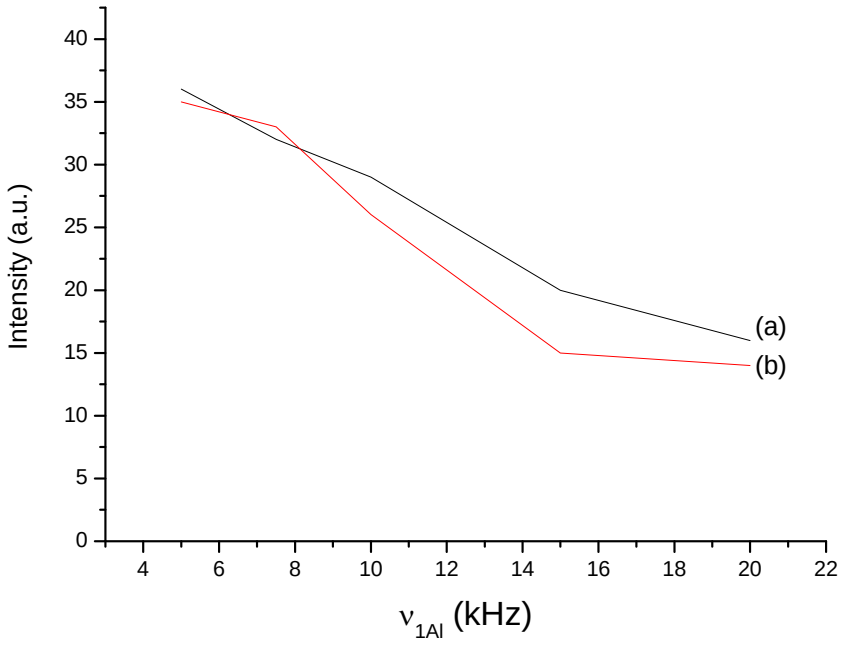

Fig. 2.4. ^{31}P experimental signal intensity versus the ν_{1Al} RF-field amplitude, observed on the ^{27}Al→^{31}P MP-CPMAS spectrum of $AlPO_4$-berlinite (t_1 = 0), k = N = 1, on-resonance irradiations. (a) B_0 = 9.4T, ν_{1P} = 5 kHz, ν_R = 10kHz. (b) B_0 = 18.8T, ν_{1P} = 10 kHz, ν_R = 20kHz. The duty-cycle parameter p varies from 0.333 (ν_{1Al} = 5kHz) to 0.083 (ν_{1Al} = 20kHz), or from 0.666 (ν_{1Al} = 5kHz) to 0.167 (ν_{1Al} = 20kHz), according to B_0 is equal to 9.4T or 18.8T, respectively.

Non-uniform CT excitation

We have also checked the effect of non-uniform CT excitation by RF pulses. Fig. 2.5 shows a simulation made for two field-strengths, B_0 = 9.4T (a) and 18.8T (b). For each, we have simulated for several C_Q the efficiencies that can be obtained with different flip-angles 180°_{sel} (k = 1, $\nu_{1S} = 0.5\nu_R$), 120°_{sel} (k = 2/3, $\nu_{1S} = 2\nu_R/3$), and 90°_{sel} (k = 0.5, $\nu_{1S} = 0.75\ \nu_R$). The curves corresponding to 180°_{sel} pulses are only shown to remind that this case, which is subject to a partial canceling of the flip-flop and flop-flop signals, is always the least efficient. For increasing quadrupole interactions the behavior of the other curves is identical: for weak C_Q the signal first increases, then it follows a plateau and finally it decreases for large C_Q. For small quadrupole interactions (c.a. $C_Q \leq$ 2-3 MHz), the RF excitation is too strong and hence

not fully CT-selective and the evolution of the density matrix is not perfectly controlled. Taking into account the RF and quadrupolar specifications introduced in the simulations, the total static CT line-width is $\Delta = 3 \cdot 10^{-10} C_Q^2$ (Δ = 1.2 kHz to 19.2 kHz for C_Q = 2 MHz to 8 MHz, respectively) at B_0 = 9.4 T and $\Delta = 1.5 \cdot 10^{-10} C_Q^2$ (Δ = 600 Hz to 9.6 kHz for C_Q = 2 MHz to 8 MHz, respectively) at 18.8 T, respectively. For large C_Q values the RF-field ν_{1I} becomes insufficient to irradiate uniformly the whole CT line-width and the signal decreases. This occurs if C_Q is larger than c.a. 3 MHz or 4.5-5 MHz for B_0 = 9.4 and 18.8 T, respectively. Fig. 2.5 also confirms that the CP efficiency decreases when 2nd order quadrupolar interaction ($\propto C_Q^2 / B_0$) increases; hence higher static magnetic fields are useful when observing sites with larger C_Q. The evolution of the three-fold and four-fold rotation efficiencies are very similar, however the first ones are always slightly larger than the seconds.

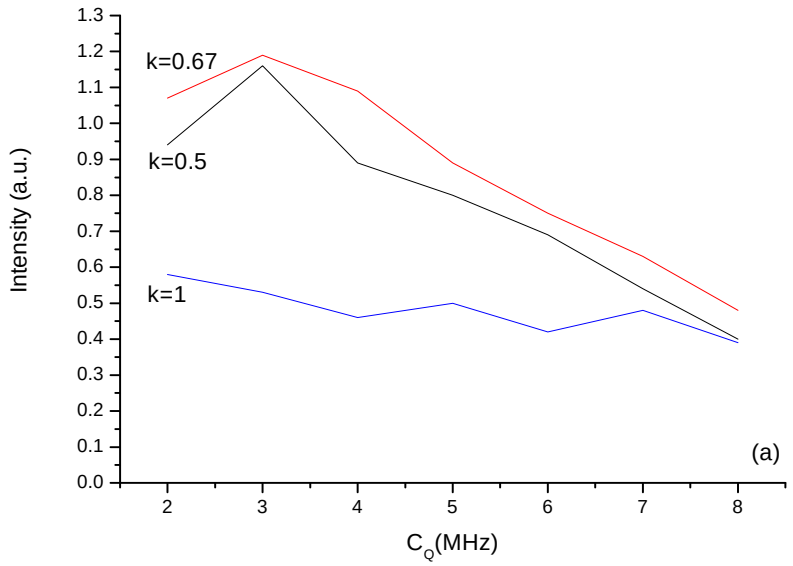

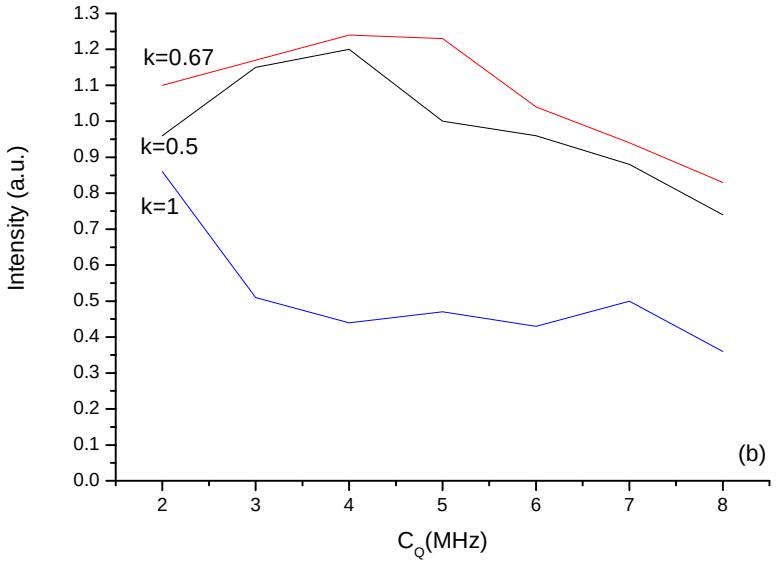

Fig. 2.5. ^{27}Al-^{31}P MP-CPMAS signal ($t_1 = 0$) versus C_Q, simulated with SIMPSON. The conditions are: on-resonance irradiation, $\nu_{1Al} = \nu_R = 10$kHz, $\eta_Q = 0$, $D_{IS} = 400$Hz aligned with the largest component of the aluminum electric-field gradient tensor, one rotor-synchronized pulse every rotor-period ($N = 1$), $B_0 = 9.4$T (a), or 18.8T (b). The three k values corresponding to the simplest r-fold rotation about Oy are indicated: $k = 1$ ($r = 2$, 180°_{sel}), 0.67 ($r = 3$, 120°_{sel}), and 0.5 ($r = 4$, 90°_{sel}). The duty-cycle parameter is equal to $p = 0.167$, 0.111, and 0.083, according to k is equal to 1, 0.67, and 0.5, respectively.

Pulse flip angle effect

In Fig. 2.6 is represented the ^{27}Al →^{31}P signal that have been observed on $AlPO_4$-berlinite at $B_0 = 9.4$ and 18.8 T. The RF amplitude was fixed to $\nu_{1Al} = 7.5$ kHz, but the pulse length τ was changed to cover a flip angle varying between 36°_{sel} and 180°_{sel}. For small flip angles the magnetization is not rotated fast enough to remain close to the spin-lock axis, while a flip angle of 180°_{sel} ($k = 1$) leads to destructive overlap of flip-flop and flop-flop transfers. In between, one observes a broad maximum. Experimentally, maximum signal occurs for pulse flip-angles close to 120°_{sel} and this optimum condition leads to a larger sensitivity than the CW-CPMAS transfer.

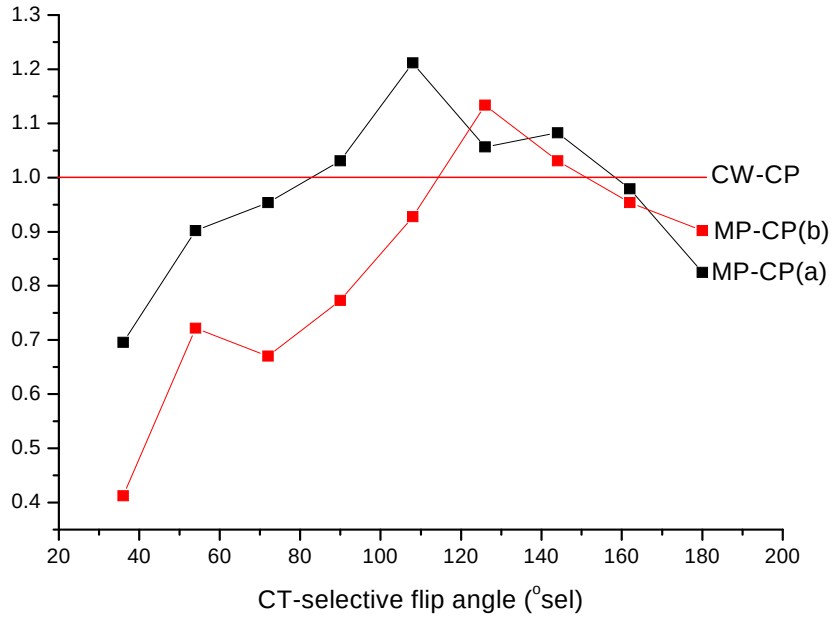

Fig. 2.6. ^{31}P MP-CPMAS signal ($t_1 = 0$) versus the flip angle expressed in CT-selective flip angles ($^{\circ}_{sel}$), observed on the ^{27}Al→^{31}P spectrum of $AlPO_4$-berlinite. The parameters are ν_{1Al} = 7.5 kHz, $N = 1$, ν_{1P} is optimized after the change of pulse-length. (a) B_0 = 9.4T, ν_R = 10kHz. (b) B_0 = 18.8T, ν_R = 20kHz. Both signals have been scaled with respect to the optimum CW-CPMAS signals observed for the same ν_R and ν_{1Al} values. The duty-cycle parameter p varies from 0.049 (40°_{sel}) to 0.222 (180°_{sel}), or from 0.098 (40°_{sel}) to 0.444 (180°_{sel}), according to B_0 is equal to 9.4T (a) or 18.8T (b), respectively. It is equal to 1 for CW-CPMAS.

Offsets

It is well-known that using a very weak RF-field leads to a large offset sensitivity. Thus another limitation for standard CW-CPMAS transfers involving quadrupolar nuclei is the attenuation due to the RF offset. Indeed, this attenuation is often very important due to the use of weak CW RF-fields during a relatively long time (≈ $1/D_{IS}$) resulting in very narrow offset line-widths.[6] In the case of MP-CPMAS experiments, the RF is applied in a completely different way, which thus leads to a different offset sensitivity, especially on the quadrupolar channel where the multiple-pulses are applied. This can be observed in Fig. 2.7, where the aluminum offset effects are shown that are observed on $AlPO_4$-berlinite with standard CW-CPMAS (Fig. 2.7a), or with MP-CPMAS using either 180°_{sel} (Fig. 2.7b) or 120°_{sel} (Fig. 2.7c)

pulses. CW-CPMAS has a quite narrow response to offset irradiation while MP-CPMAS exhibits an unusual behavior with strong inverted off resonance signals. Thus we can imagine 2D HETCOR experiments on samples with very large chemical shift offsets in a single shot. However, some of the through-bond cross-peaks may then appear with a negative sign.

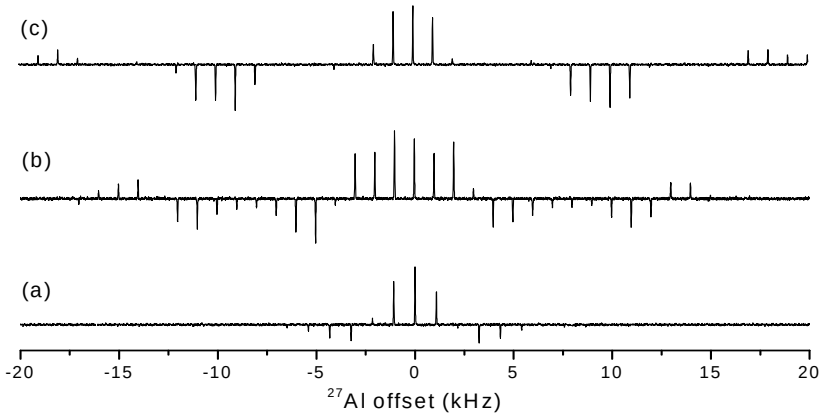

Fig. 2.7. ^{27}Al offset sensitivity observed on the ^{27}Al→^{31}P spectrum of $AlPO_4$-berlinite. ν_R = 10kHz, ν_{1Al} = 7.5kHz, B_0 = 9.4T, (a) CW-CPMAS, (b) MP-CPMAS with k = 1, (c) MP-CPMAS with k = 0.67. The duty-cycle parameter is equal to p = 1 (a), 0.222 (b), 0.148 (c), respectively.

The offset sensitivity on the side of the spin-1/2 nucleus is similar to that observed in standard CW-CPMAS experiments. However, the RF-amplitude on spin-1/2 nucleus is proportional to the spinning speed (e.g. $\nu_{1S} = 2\nu_R/3$ if k = 2/3), and thus the offset sensitivity would be small with very fast MAS.

Very fast spinning

An important issue with modern solid-state NMR methods is how easily they can be adapted to the very fast spinning speeds (of up to 80 kHz) that have recently become available. Indeed, for reasons of resolution and sensitivity, experiments are performed at increasingly high magnetic fields, which often require very fast MAS rates to minimize the appearance of spinning sidebands due to chemical-shift anisotropy. At these very fast speeds, the main problem encountered when manipulating quadrupolar nuclei is related to the length

of the CT-selective pulses with respect to the rotor period. As an example, for a spin-3/2 nucleus with an RF-field of 10 kHz (classical value for a CT-selective irradiation: Fig. 2.4) the CT-selective π pulses can last up to *two* rotor periods for very fast spinning speeds such as ν_R = 80 kHz, and thus the selective pulses must then be separated by several (N) rotor periods. We have analyzed with SIMPSON the optimum value of rotor periods (N_{opt}) versus the spinning speed, for two different RF-fields (ν_{1I}) (Table 2.1). For spinning speeds faster than 40 kHz, the signal is negligible for N = 1, it becomes maximum for a few rotor periods (N_{opt}), and then decreases to zero for very long delays. For a fixed RF-field (ν_{1I}), the optimum signal slowly decreases with increasing spinning speed except for very small ν_{1I} values.

Table 2.1. Optimum number of rotor periods (N_{opt}) between two consecutive pulses, and related signal, that can be observed for different spinning speeds and two ν_{1I} values.

ν_{1I}	5 kHz		8 kHz	
ν_R (kHz)	N_{opt}	signal (a.u)	N_{opt}	signal (a.u)
10	1	1.02	1	1.15
30	3	0.98	3	0.90
50	5	0.90	5	0.88
70	7	0.64	7	0.76

B_0 = 9.4T, $S = {}^{31}$P, $I = {}^{27}$Al, pulse length : 120°_{sel} (k = 2/3), C_Q = 3 MHz, D_{IS} = 400Hz aligned with the quadrupolar tensor (η_Q = 0), on-resonance irradiations. For ν_{1I} = 5kHz and ν_R = 70kHz, the pulse lasts 1.6 rotor periods, and hence the signal decreases considerably. This effect is less important for ν_{1I} = 8kHz, where the pulse lasts only 1 rotor-period.

It can be observed in Table 2.1 that for a given RF-field, the optimum number of rotor periods is approximately proportional to the spinning speed, thus corresponding to a constant

averaged RF-field $\overline{\nu}_{1I}$. This is exactly what has been observed for $^{1}H \rightarrow ^{13}C$ MP-CPMAS transfers: the optimum transfer was observed with approximately the same ^{1}H averaged RF-field: 4kHz with CW-CPMAS and 5.9kHz (280kHz*0.35/16.667) with MP-CPMAS.[3] This constant $\overline{\nu}_{1I}$ value can be obtained in two ways: one soft pulse every N_{opt} rotor periods, or one soft pulse N_{opt} times shorter every rotor period. However, simulations and experiments have shown that the first case is slightly better because fewer pulses are used. Another explanation may be that shorter pulses do not rotate properly all crystallite magnetizations within the quadrupolar line-width, while longer pulses benefit from crystallite sweep due to the rotation. As an example, on $AlPO_4$-berlinite with ν_R = 20kHz, the experimental signal was 13% larger with one pulse of 15.4μs ($\approx 120^{o}_{sel}$) every two rotor periods than with one pulse of 7.7μs ($\approx 60^{o}_{sel}$) every rotor period (ν_{1Al} = 7.5 kHz, B_0 = 9.4T, ν_{1P} = 13.3 kHz, $qN_{opt}T_R$ = 5 ms).

HETCOR spectra

The $^{27}Al \rightarrow ^{31}P$ MP-CPMAS HETCOR spectrum of $AlPO_4$-VPI5, recorded at 9.4T, is displayed in Fig. 2.8. Due to much more favorable relaxation times, we started the experiments from the aluminum nuclei. The resolution along the phosphorus axis has been enhanced by introducing an aluminum decoupling pulse sequence optimized for quadrupolar nuclei.[24] It can be observed that, in agreement with the structure, all aluminum atoms are spatially close to all phosphorus atoms.

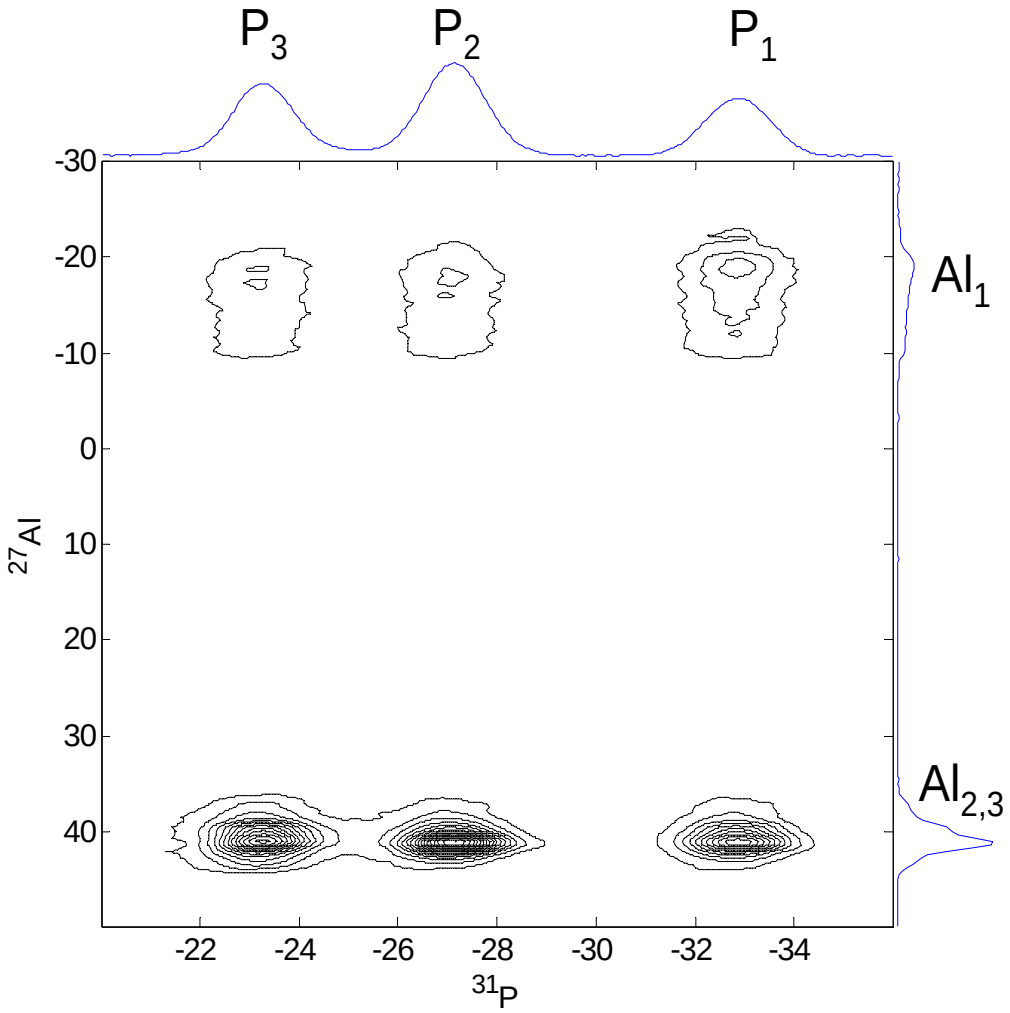

Fig. 2.8. $AlPO_4$ VPI5 $^{27}Al \rightarrow {}^{31}P$ MP-CPMAS HETCOR spectrum. ν_R = 10kHz, B_0 = 9.4T. 320 scans per row and recycling delay of 2 sec. Total experimental time = 18 hrs. ν_{1Al} = 7kHz, ν_{1P} = 14.3kHz, k = 0.9 and N = 1.

The $^{1}H \rightarrow {}^{27}Al$ HETCOR spectrum of $AlPO_4$-14 shown in Fig. 2.9 has been recorded also at 9.4 T. Due to its larger C_Q value, and the moderate field, cross peaks with Al_1 species are hardly visible. The correlations observed are equivalent to those described in Fig.3 of reference 25.

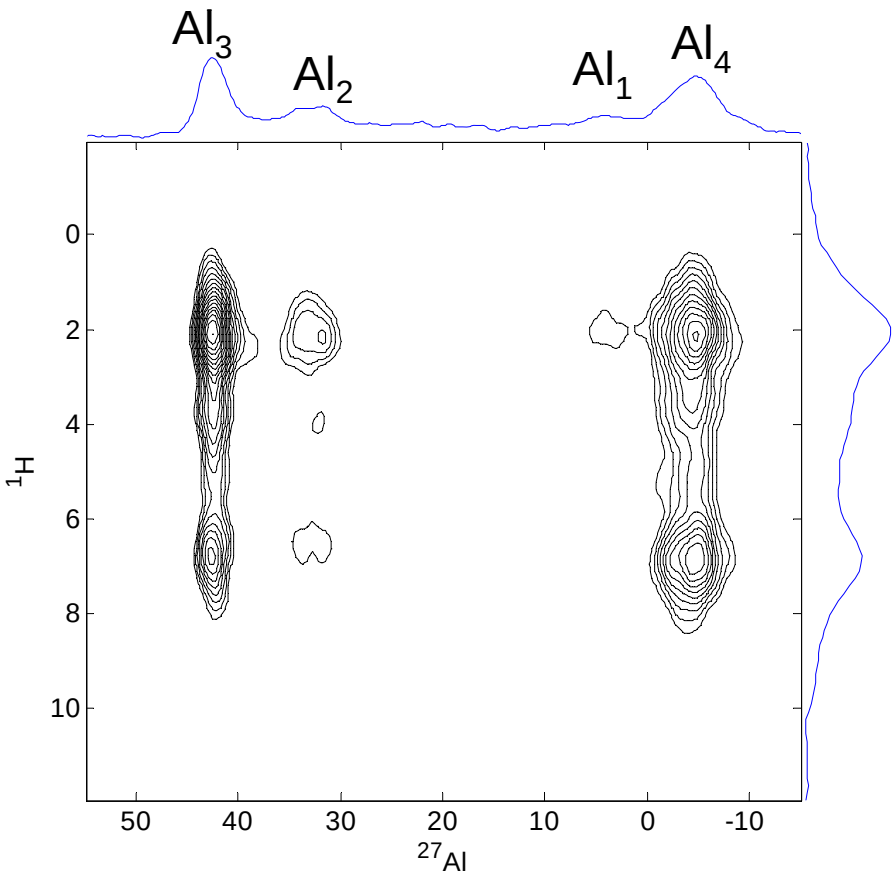

Fig. 2.9. $AlPO_4$-14, $^{1}H \rightarrow {}^{27}Al$ MP-CPMAS HETCOR spectrum. ν_R = 10kHz, B_0 = 9.4T. 200 scans per row and recycling delay of 1 sec. Total experimental time = 4.5 hrs. ν_{1Al} = 6.4kHz, ν_{1P} = 14.6kHz, k = 0.9 and N = 1.

Finally, MP-CPMAS has been tested on a spin 3/2 system and on a larger magnetic field. The $^{23}Na \rightarrow {}^{31}P$ MP-CPMAS HETCOR experiment was performed at 18.8T on $Na_7(AlP_2O_7)_4PO_4$. We can observe in Fig. 2.10 that the P_2 (Q_0) site is only correlating with Na_1 and Na_2 sites, which is in agreement with the structure.

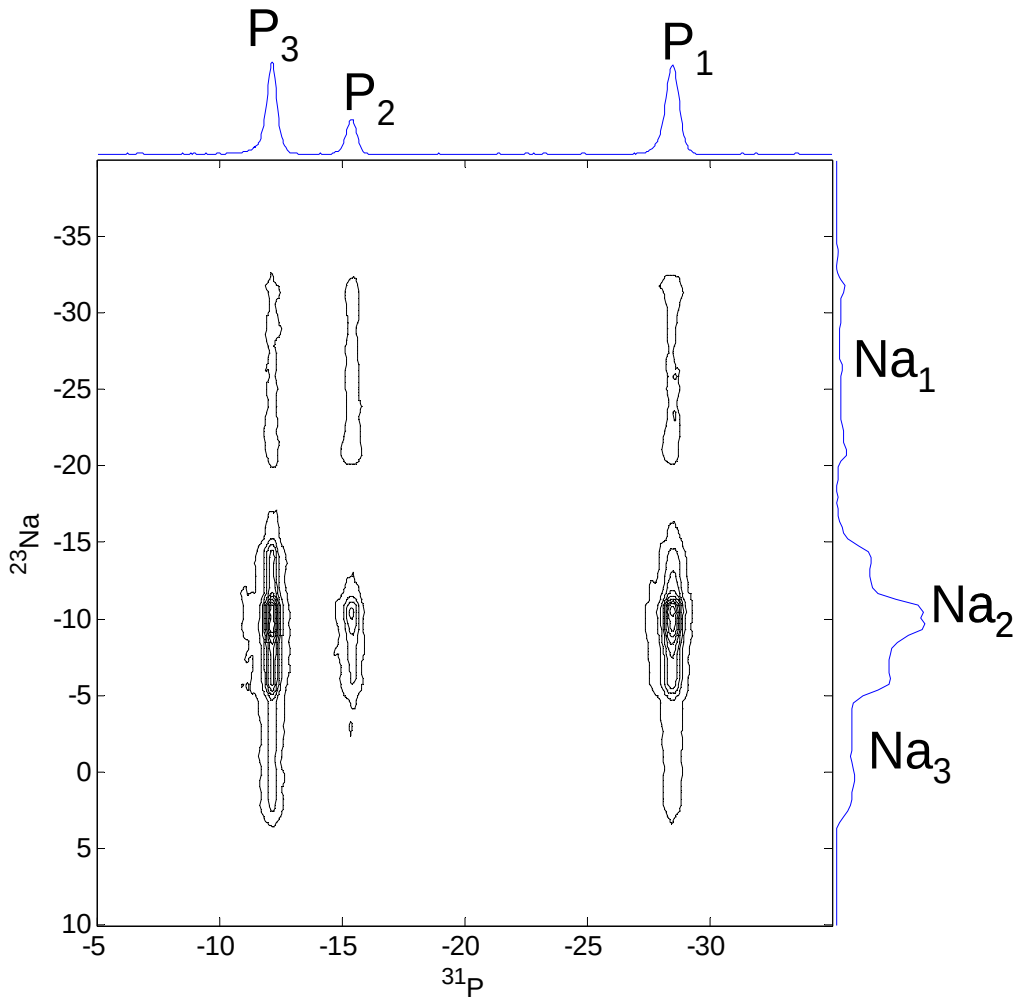

Fig. 2.10. $Na_7(AlP_2O_7)_4PO_4$. $^{23}Na \rightarrow {}^{31}P$ MP-CPMAS HETCOR spectrum. $\nu_R = 20kHz$, $B_0 = 18.8T$. 32 scans per row and recycling delay of 3 sec. Total experimental time : 128 min. $\nu_{1Al} = 7.8kHz$, $\nu_{1P} = 16.6kHz$, $k = 0.7$ and $N = 2$.

2.4 Conclusion

We have shown that the continuous-wave spin-locking of quadrupolar nuclei can be replaced by rotor-synchronized multiple-pulse spin-locking. In this case, one must consider the average RF field produced by the pulses in order to fulfill the Hartman-Hahn matching equation. MP-CPMAS is more efficient, more robust and less sensitive to offsets on the side of the quadrupolar nucleus than standard CW-CPMAS. It is thus particularly useful for 2D HETCOR experiments. The experiment is quite broad-banded with respect to the pulse-length

which must be between 0.5 and 0.9 times that of a CT selective π pulse. We find that using rotor-synchronized selective 2π/3 pulses seems to be the most efficient way to perform MP-CPMAS experiments.

References

1. Amoureux, J. P.; Pruski, M., Advances in MQMAS NMR *Encyclopædia of NMR (2nd edition)* **2002**, 54-90.

2. Oas, T. G.; Griffin, R. G.; Levitt, M. H., Rotary resonance recoupling of dipolar interactions in solid-state nuclear magnetic resonance spectroscopy. *J. Chem. Phys.* **1988,** 89, 692–695.

3. Hafner, S.; Palmer, A.; Cormos, M., Ultra-Fast Magic-Angle Spinning. In *13th National Indian NMR Meeting*, Pune, India, 2007.

4. Vega, A. J., MAS NMR spin-locking of half-integer quadrupolar nuclei. *J. Magn. Reson.* **1992,** 96 50-68.

5. Vega, A. J., CP/MAS of quadrupolar S = 3/2 nuclei. *Solid State NMR* **1992,** 1, 17-32.

6. Amoureux, J. P.; Pruski, M., Theoretical and experimental assessment of single- and multiple-quantum cross-polarization in solid-state NMR. *Molec. Phys.* **2002,** 100, 1595-1613.

7. Stejskal, E. O.; Schaefer, J.; Waugh, J. S., Magic-Angle Spinning and Polarization Transfer in Proton-Enhanced NMR. *J. Magn. Reson.* **1977,** 28, 105-112.

8. Hediger, S.; Meier, B. H.; Ernst, R. R., Cross polarization under fast magic angle sample spinning using amplitude-modulated spin-lock sequences. *Chem. Phys. Lett.* **1993,** 213 627-635.

9. Hediger, S.; Meier, B. H.; Ernst, R. R., Rotor-synchronized amplitude-modulated nuclear magnetic resonance spin-lock sequences for improved cross polarization under fast magic angle sample spinning. *J. Chem. Phys.* **1995,** 102, 4000.

10. Raya, J.; Hirschinger, J., Application of rotor-synchronized amplitude-modulated cross-polarization in a 13C-1H spin pair under fast MAS. *J. Magn. Reson.* **1998,** 133, 341-351.

11. Bak, M.; Rasmussen, J. T.; Nielsen, N. C., SIMPSON: A General Simulation Program for Solid-State NMR Spectroscopy. *Journal of Magnetic Resonance* **2000,** 147, (2), 296.

12. Bak, M.; Nielsen, N. C., Repulsion, A Novel Approach to Efficient Powder Averaging in Solid-State NMR. *Journal of Magnetic Resonance* **1997,** 125, (1), 132-139.

13. Goiffon, A.; Jumas, J. C.; Maurin, M.; Philippot, E., Etude comparée à diverses températures (173, 293 et 373°K) des structures de type quartz α des phases $M^{III}X^{V}O_4$ (M^{III} = Al, Ga et X^{V} = P, As). *Journal of Solid State Chemistry* **1986,** 61, (3), 384-396.

14. Huguenard, C.; Taulelle, F.; Knott, B.; Gan, Z., Optimizing STMAS. *Journal of Magnetic Resonance* **2002,** 156, (1), 131.

15. McCusker, L. B.; Baerlocher, C.; Jahn, E.; Bülow, M., The triple helix inside the large-pore aluminophosphate molecular sieve VPI-5. *Zeolites* **1991,** 11, 308-313.

16. Rocha, J.; Kolodziejski, W.; He, H.; Klinowski, J., Solid-state NMR studies of hydrated porous aluminophosphate VPI-5. *J. Am. Chem. Soc.* **1992,** 114, 4884-4888.

17. Fernandez, C.; Morais, C. M.; Rocha, J.; Pruski, M., High-resolution hetero-nuclear correlation spectra between ^{31}P and ^{27}Al in Microporous Aluminophosphates. *Solid State NMR* **2002,** 21, 61-70.

18. Broach, R. W.; Wilson, S. T.; Kirchner, R. M., Corrected crystallographic tables and figure for as-synthesized AlPO4-14. *Microporous Mesoporous Mater* **2003,** 57, 211-214.

19. Antonijevic, S.; Ashbrook, S. E.; Biedasek, S.; Walton, R. I.; Wimperis, S.; Yang, H., Dynamics on the microsecond timescale in microporous aluminophosphate AlPO4-14 as evidenced by 27Al MQMAS and STMAS NMR spectroscopy. *J. Am. Chem. Soc.* **2006,** 128, 8054-8062.

20. Fernandez, C.; Amoureux, J. P.; Chezeau, J. M.; Delmotte, L.; Kessler, H., 27Al MAS NMR characterization of AlPO4-14. Enhanced resolution and information by MQMAS. *Micropor. Mat.* **1996,** 6, 331-340.

21. Fyfe, C. A.; Altenschildesche, H. M. z.; Wong-Moon, K.; Grondey, H.; Chezeau, J. M., 1D and 2D solid state NMR investigations of the framework structure of As-synthesized AlPO4-14. *Solid. State. NMR* **1997,** 9, 97-106.

22. Tricot, G.; Delevoye, L.; Palavit, G.; Montagne, L., Phase identification and quantification in a devitrified glass using homo- and heteronuclear solid-state NMR. *Chem. Commun.* **2005,** 42, 5289-5291.

23. Rochère, M. d. l.; Kahn, A.; d'Yvoire, F.; Bretey, E., Crystal structure and cation transport properties of the ortho-diphosphates $Na_7(MP_2O_7)_4PO_4$. *Materials research bulletin* **1985,** 20, 27-34.

24. Delevoye, L.; Tre?bosc, J.; Gan, Z.; Montagne, L.; Amoureux, J. P., Resolution enhancement using a new multiple-pulse decoupling sequence for quadrupolar nuclei. *Journal of Magnetic Resonance* **2007,** 186, (1), 94.

25. Trébosc, J.; Hu, B.; Amoureux, J. P.; Gan, Z., Through-space R3-HETCOR experiments between spin-1/2 and half-integer quadrupolar nuclei in solid-state NMR. *Journal of Magnetic Resonance* **2007,** 186, (2), 220.

Chapter 3. Through-space *D*-HMQC experiments

In liquid-state, hetero-nuclear multiple- (*J*-HMQC)[1] or single- (*J*-HSQC)[2] quantum coherence through-bond *J*-coupling methods, which will be denoted *J*-H-M/S-QC when considered together, have been designed to enhance the signal by inverse detection.

In solids, nuclei are submitted to several anisotropic interactions, which lead to broad resonances and thus very poor signal to noise ratios. To enhance the resolution and increase the signal to noise ratio, sample-rotation at the magic-angle (MAS: magic-angle spinning)[3] is used. To further enhance the low sensitivity of NMR in solids, cross-polarization (CP) is also often used.[4] Nuclear polarization is then usually transferred through the dipolar interaction from 'strong' abundant spins I to 'weak' diluted spins S, to increase the magnetization of S and the repetition rate of the experiment. Nowadays, CP is often combined with MAS for resolution enhancement, leading to CP-MAS experiments.[5] Another way to enhance the sensitivity is to combine the indirect detection methods with MAS, leading to MAS *J*-HMQC[6] and MAS *J*-HSQC[7] experiments, to obtain through-bond hetero-nuclear correlation (MAS *J*-HETCOR) 2D spectra under high-resolution.

Recently, it has been shown that with a very slight change of the pulse sequences these methods can be adapted to observe through-space MAS *D*-HETCOR 2D spectra, leading to MAS *D*-H-M/S-QC experiments.[8] Usually, dipolar interactions are cancelled by the MAS rotation. Several different methods exist for hetero-nuclear recoupling purposes. This re-introduction has been performed first with the rotary-resonance recoupling (R^3) method,[9] and then several symmetry-based sequences have been proposed: e.g $R12_3^1$, $R12_3^5$, and $R20_5^9$.[10,11] Another symmetry-based sequence, $SR4_1^2$, has been recently introduced in the context of measuring the OH distances in samples with numerous protons, but its application to hetero-

nuclear recoupling is quite general.[12] Very recently, Cavadini *et* al published the application of the $R20_5^9$ sequence to the ^{14}N-^{1}H dipolar recoupling.[13]

Here we would like to compare the advantages and limitations of these dipolar recoupling methods in the context of MAS *D*-H-M/S-QC experiments : the R^3 continuous irradiation, the previous three symmetry-based sequences ($SR4_1^2$, $R12_3^5$, $R20_5^9$) as well as $R2_1^1$ sequence,[10,14] the standard REDOR (Rotational Echo DOuble Resonance),[15] and the SFAM (Simultaneous Frequency and Amplitude Modulation) concept,[16] which has been proposed to overcome REDOR limitations at very fast MAS. The comparison of these hetero-nuclear dipolar recoupling methods will be made in the case of nuclei also submitted or not to large homo-nuclear dipolar-interactions. A special attention will be given to the behavior of these sequences at ultra fast MAS (ν_R > 40kHz).

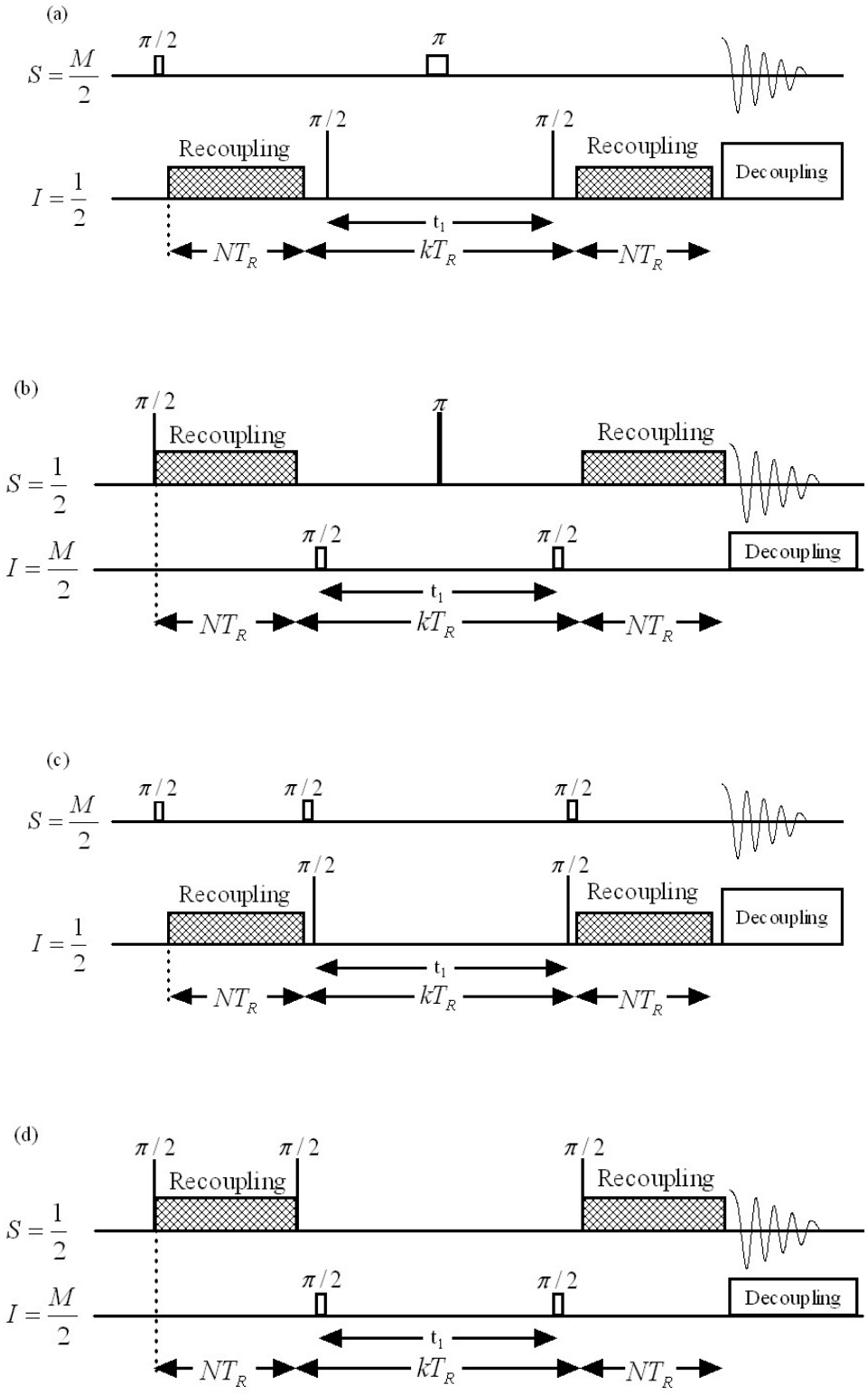

Fig.3.1. HMQC pulse-sequence with recoupling on I (a) (non-observed) or S (b) (observed) spin-1/2 nuclei. HSQC pulse-sequence with recoupling on I (c) or S (d) spin-1/2 nuclei. Pulses with large rectangle are CT (centre transition) selective pulses used for spins M/2. Phases of π and π/2 pulses follow the regular *J*-HMQC ones. The phase for R^3 is zero and the phases for other recoupling sequences are calculated according its correspondent definition.

3.1 Dipolar recoupling pulse sequences

Our purpose is to apply these *D*-H-M/S-QC methods in between spin-1/2 and quadrupolar nuclei. The spin value of the quadrupolar nuclei is larger than ½, and these systems thus present more than two Zeeman energy levels. Manipulation of the quadrupolar nucleus density matrix is thus difficult and in order to increase the efficiency of the methods, the number of pulses sent on quadrupolar nuclei must be minimized. Therefore, in the following, the dipolar recoupling sequences will always be applied to a single channel, which will be that of the spin-1/2 nucleus in case of *D*-HETCOR experiments involving quadrupolar nuclei.

Most hetero-nuclear dipolar recoupling sequences with rf field applied to a single channel automatically reintroduce the chemical shift anisotropy (CSA) on this channel because of identical rotation properties under the rf and MAS of these two interactions. In *D*-H-M/S-QC experiments, the CSA of the S observed nucleus (CSA_S) is refocused, but only at the very end of the sequence. To avoid any effect of CSA_S, its evolution must thus be perfectly identical during the two recoupling periods. One can thus anticipate that the defaults of each particular recoupling sequence will be emphasized by the re-introduction of CSA_S, when this sequence will be performed on the observed channel, particularly in case of strong CSA_S. In **Fig.3.1** we have represented the pulse-sequences corresponding to MAS *D*-HMQC **(Fig.3.1a,b)** and MAS *D*-HSQC **(Fig.3.1c,d)** in case of a spin-1/2 and a half-integer quadrupolar nucleus. In case of two spin-1/2 nuclei, the recoupling sequences can be sent on any channel. It must be noted that to add constructively the dipolar dephasings related to the two recoupling sequences (for non γ-encoded sequences, see section 3.1d), the delay between these sequences must be rotor-synchronized (kT_R), and the π pulse (HMQC) on the S channel must be in the middle of this delay. Of course, the t_1 time should be also rotor-synchronized if spinning sidebands are to be avoided (e.g. for ^{14}N indirect detection).[13,17]

(a) REDOR

The rotational echo double resonance (REDOR) sequence applies evenly spaced π-pulses (two per rotor cycle) for dipolar recoupling. The π-pulses alternate the sign of hetero-nuclear dipolar dephasings modulated under MAS, hence preventing their complete averaging. REDOR is a very simple and efficient method when only hetero-nuclear interactions are taken into account. Unfortunately, when REDOR pulses are applied to the observed channel, the remaining value of CSA_S at the beginning of acquisition depends critically on the rotor position with respect to the multiple π-pulse sequence. Small MAS frequency drifts and fluctuations accumulate timing error over the long transfer periods and consequently result in incomplete and unstable CSA_S refocusing. The phases of these π pulses can be calculated to compensate partly for the flip angle error, the off-resonance effect, and the fluctuation of rf-field, leading to sequences $REDOR_{XYk}$ (k = 4, 8, 16).[18] However, it has been shown in case of weak dipolar recoupling, that even with these compensated sequences, a very tiny 0.1 Hz change of MAS frequency can attenuate signal intensities if all REDOR pulses are sent on the observed channel.[19] In any case, it has been shown that the hetero-nuclear dipolar recoupling decreases at very fast spinning speed when the fraction of the rotor period occupied by the two π pulses increases, especially in homo-nuclear systems.[20] REDOR presents the advantage of a longitudinal two-spin-order (I_zS_z) recoupling of the hetero-nuclear dipolar interactions between I and S spins in first order, which means that this interaction commutes for different spin pairs. Non-commuting dipolar interactions on the other hand lead to 'dipolar truncation', i.e. the measurement of a weak dipolar coupling between two spins is prevented if one or both spins are also strongly dipolar coupled to other spins.[21] When REDOR pulses are applied to the non-observed I channel, REDOR recouples simultaneously the CSA_I, but this commutes with the hetero-nuclear dipolar interaction, and thus, in practice the hetero-nuclear recoupling is not influenced by CSA_I. REDOR also then recouples the I-

spin homo-nuclear dipolar couplings, and the size of the recoupled terms depends on the ratio of the duration of the π pulses with respect to the period of the sample rotation. Hence, only in the limit of short pulses with respect to the rotation period, homo-nuclear I-spin decoupling is achieved, while under very fast MAS substantial recoupling of the I-spin homo-nuclear dipolar interactions occurs.[22] It must be noted that $REDOR_{XYk}$ (k = 4, 8, 16) sequences can also be viewed as RN_n^v sequences (see section 3.1d).[10]

(b) R^3

Rotary resonance recoupling (R^3) has been shown to recover various anisotropic spin interactions under MAS with resonance conditions described by a number $q = \nu_1/\nu_R$ (where ν_1 is the rf-strength).[9] For CSA and hetero-nuclear dipolar coupling, the re-introduction occurs without 'dipolar truncation' at q = 1 and 2. For homo-nuclear dipolar coupling it occurs at q = ½ and 1 due to the bilinear nature of the spin operator in the dipolar Hamiltonian. The q = ½ resonance affects only the homo-nuclear dipolar interaction and is known as the HORROR condition.[23] It is well-known that the q = 2 condition reintroduces the hetero-nuclear dipolar coupling under MAS, but not the homo-nuclear interaction.[17] This condition should thus be used in case of nuclei submitted to strong homo-nuclear dipolar interaction. In other cases, the q = 1 condition should be preferred, because of its better experimental efficiency. R^3 can also be seen as symmetry based sequences $R2_1^0$ (q = 1) or $R4_1^0$ (q = 2) (see section 3.1d).

(c) SFAM

At very fast spinning speeds (up to $\nu_R \approx 100$ kHz, presently), which are necessary to suppress CSA in high static magnetic fields (up to $B_o = 23.5$T), REDOR suffers from artifacts because of the finite π pulse lengths, which represent a non negligible fraction of the rotational period. To overcome this limitation a method with 'simultaneous frequency and amplitude modulation' (SFAM) has been proposed.[16] The carrier frequency ($\nu_0 + \Delta\nu_0(t)$) of the rf field is modulated cosinusoidally, while its amplitude ($\nu_1(t)$) is modulated sinusoidally.

It has been shown that the best efficiency for the hetero-nuclear dipolar recoupling is observed when the modulation frequency of this rf field is equal to the spinning speed leading to the $SFAM_1$ method:

$$SFAM_1 \qquad \Delta\nu_0(t) = \Delta\nu_0^{max}\cos(2\pi\nu_R t) \qquad \nu_1(t) = \nu_1^{max}\sin(2\pi\nu_R t) \qquad (3.1)$$

It has also been shown that, with respect to hetero-nuclear dipolar interaction, continuous $SFAM_1$ behaves exactly the same as REDOR with ideal π pulses.[16] However, $SFAM_1$ also recouples the homo-nuclear dipolar interactions, and thus should not be used when these are not negligible. In this case, in a similar way as with R^3 to eliminate homo-nuclear dipolar interactions, the modulation frequency should be twice the spinning speed, leading to the $SFAM_2$ method :

$$SFAM_2 \qquad \Delta\nu_0(t) = \Delta\nu_0^{max}\cos(4\pi\nu_R t) \qquad \nu_1(t) = \nu_1^{max}\sin(4\pi\nu_R t) \qquad (3.2)$$

In both cases, the best efficiency is observed when the depth of the frequency modulation ($\Delta\nu_0^{max}$) and the maximum amplitude of the rf field (ν_1^{max}) are of sufficient amplitude. It has been shown that SFAM methods do not suffer from 'dipolar truncation'.[16]

(d) Symmetry-based sequences

The nuclear spin interactions may be classified in terms of their properties under rotations by the quantum numbers {l, m, λ, μ}, where {l, m} and {λ, μ} denote the rank and component with respect to sample spatial rotation and spin-rotation, respectively. Selection rules have been derived, which predict if a certain interaction with the quantum numbers {l, m, λ, μ} is present (symmetry-allowed) in the first-order average Hamiltonian derived under a sequence RN_n^ν (N even) or CN_n^ν with the set of numbers : N, n, ν.[10,14] The basic bloc of these sequences extends over n rotor periods and is composed of N rotor-synchronized π (2π for CN_n^ν) rotation elements : single-, composite-, or smoothly-modulated rf-pulses. The sequences are called 'γ-encoded' when only the *phase* of the average Hamiltonian depends on

the Euler angle γ_{MR}, which is one of the three angles defining the molecular orientation with respect to the rotor-frame. 'γ-encoding' generally leads to a low sensitivity to synchronization of delays, high efficiency in a powder and good discrimination of the recoupled interactions.[24] On the other-hand, non-γ-encoded sequences are generally more robust as regard to rf missettings and inhomogeneity, and superior for long-range distance estimations.[25] In their simplest forms, RN_n^ν sequences are composed of π pulses with alternate phases ± πν/N**.** In this case, when $N = 2\nu$, the pulse phases are ± 90° and hence the phase shift in between two consecutive pulses is equal to 180°. The $RN_n^{N/2}$ sequences are then called 'amplitude modulated' and are compensated for rf-inhomogeneity.[26] Another advantage of these sequences is that ± 90° phases are easy to obtain accurately and with a fast commutation time in between them, even on old consoles. But they are not 'γ-encoded'.

Here we are interested by hetero-nuclear dipolar recoupling RN_n^ν sequences. This recoupling can be accomplished either with single-quantum coherences or with longitudinal two-spin-order. This leads to dipolar 'truncated' or 'not truncated' sequences, respectively. When the recoupling sequence is sent on the non-observed channel, CSA_I and hetero-nuclear dipolar interactions are always recoupled simultaneously, because they have the same ranks l = 2, λ = 1. If these two interactions commute, hetero-nuclear dipolar recouplings are then insensitive to CSA_I.

We have chosen to only use RN_n^ν sequences which have been designed: (i) to use only π pulses, (ii) to prevent 'dipolar truncation', to provide: (iii) hetero-nuclear, but (iiii) not homo-nuclear dipolar recoupling, and (v) to be uncorrelated to the irradiated-spin CSA. As we wish these sequences working at very fast MAS, we have added a last criterion: to only select RN_n^ν sequences requiring a limited rf-field amplitude : $\nu_1/\nu_R = N/2n \leq 2$.

We have chosen to investigate the $R12_3^5$ and $R20_5^9$ sequences that have been proposed for this purpose.[10,13,14] These sequences correspond to π pulses with ± 75° and ± 81° phases, for $R12_3^5$ and $R20_5^9$, respectively. However, the duration of the whole RN_n^v bloc is given by nT_R, and it may be useful to use a shorter one in case of large hetero-nuclear dipolar interactions and/or slow spinning speed. The eight π-pulse ($\pi_x\pi_{-x}\pi_x\pi_{-x}\pi_{-x}\pi_x\pi_{-x}\pi_x$) $SR4_1^2$ sequence, only lasts two rotor-periods. It has been recently proposed to measure ^{17}O-^{1}H distances in protonated samples, but with a better discrimination of simultaneous long and short O-H distances than $R12_3^5$.[12] Another advantage of $SR4_1^2$ is that it is an 'amplitude-modulated' sequence which means compensated for rf-inhomogeneity, as $R12_3^5$ and $R20_5^9$ sequences.[10] In the Levitt symmetry-based analytical calculations, these three non 'γ-encoded' recoupling sequences ($SR4_1^2$, $R12_3^5$ and $R20_5^9$) require the rf-field strength to be only twice the spinning frequency: $\nu_1 = 2\nu_R$. It can be noticed that the plain $R4_1^2$ sequence can be considered as a simplified version of $SFAM_2$. Indeed, $R4_1^2$ is composed of four pulses with alternating phases (± 90°) per rotor period, which can be developed as a Fourier-series expansion ($\pm 2\nu_R$, $\pm 6\nu_R$, $\pm 10\nu_R$,..), with the first term ($\pm 2\nu_R$) being the largest. For each crystallite, the resonance frequency is always sweeping in a rotor-synchronized way due to the MAS rotation and anisotropic interactions. However, $SFAM_2$ also introduces an additional frequency sweep of the irradiation through the resonance frequency. This analogy is similar to that in between FAM[27] and DFS[28] for signal enhancement of quadrupolar nuclei. In the same way, the analogous of $SFAM_1$ is the $R2_1^1$ sequence, which also recouples the homo- and hetero-nuclear dipolar interactions and is composed of two π pulses of opposite phases per rotor period with $\nu_1 = \nu_R$ with the Levitt's calculations.[10,14]

3.2 Simulations

(a) Hetero-nuclear recoupling

We have chosen to calculate with SIMPSON[29] the efficiency of a MAS *D*-HMQC experiment in between two spin-1/2 nuclei, with D_{IS} = 1000 Hz. Pulses other than those in recoupling sequences are ideal pulses (pulseid statement in SIMPSON). We have chosen to do the calculations for two very different spinning speeds that are both presently accessible with commercially available probes: ν_R = 20 and 70 kHz. For each recoupling sequence, and each rf-field strength, the recoupling times ($\tau = NT_R$) have always been optimized. The efficiency has been normalized with respect to that obtained with a classical echo experiment ($\pi/2$ - τ - π - τ - Acq). For the RN_n^ν sequences, we have fixed the lengths and phases of the pulses to their theoretical values (e.g. $T_R/4$, and $\pm$ 75° for $R12_3^5$).[10,14] In SFAM sequences, we fixed the depth of the frequency modulation $\Delta\omega_0^{max}$ to 60 kHz in $SFAM_1$ and 15 kHz in $SFAM_2$, but its optimal value span over a very broad range.

In **Fig.3.2 and 3.3**, we simulated the sequence of **Fig.3.1a**, plotting efficiencies, without any CSA (except **Fig.3.2.b and 3.3.b**) or homo-nuclear dipolar interactions, versus the rf-field strength for ν_R = 20 and 70 kHz, respectively. The maximum of efficiency is always of c.a. 70%, and only the optimum rf-field and broadness of the best matching condition is changing from method to method. One observes first that the two main R^3 resonances are observed at the q = 1 and 2 conditions **(Fig.3.2a and 3.3a)**, as described previously. The q = 2 resonance is slightly narrower than that observed for q = 1, which leads experimentally to a smaller efficiency when taking into account the rf-field inhomogeneity of the coil. This is one of the reason why experimentally the q = 1 condition should be preferred in case of weak homo-nuclear interactions. We observed that CSA of the irradiated nuclei broadens these R^3 resonances, as shown in **Fig.3.2b and 3.3b**. However, this broadening is small, especially when R^3 irradiation is sent on ^{1}H nuclei whose CSA is limited to c.a. 10-12

ppm. All other matching curves are much broader and should thus lead experimentally to a larger signal. $R12_3^5$ and $R20_5^9$ sequences present similar theoretical behaviors and hence should give similar experimental results **(Fig.3.2d,e and Fig.3.3d,e)**. As predicted by Levitt's calculations,[10,14] the main broad resonance of $R2_1^1$ **(Fig.3.2c and Fig.3.3c)** and that of $R12_3^5$ and $R20_5^9$ sequences is observed for an rf-field equal to ν_R and $2\nu_R$, respectively. This is not the case with the $SR4_1^2$ sequence for which only a large plateau is observed in between $1.5\nu_R$ and $3\nu_R$, whereas the 'analytical' optimum value corresponds to $2\nu_R$. Similar very good results are obtained with the SFAM sequences, whose efficiencies are constant over a large range **(Fig.3.2g,h and Fig.3.3g,h)**. However, $SFAM_1$ requires less rf-field ($\nu_1 > \nu_R$) than $SFAM_2$ ($\nu_1 > 2\nu_R$), which thus should be mainly used in case of large homo-nuclear dipolar interactions. In the case of these very broad rf-matching curves (**Fig.3.2c-h** and **Fig.3.3c-h**), we have found that CSA of the recoupled nucleus has little effect on the efficiency if this CSA is smaller than the spinning speed. Up to now, we have calculated the theoretical efficiency of the RN_n^v sequences that may be obtained with an 'ideal' probe, which means without any rise or fall time and without any phase glitches. These effects, which increase with the spinning speed, do not exist with the constant R^3 rf-field, and they are weak with the continuous SFAM irradiation where they mainly appear as a delay of the rf-field with respect to the amplifier voltage. To mimic these experimental limitations, we have redone the previous calculations, but introducing for the four previous RN_n^v sequences a delay in between the pulses. With respect to the previous results, the efficiency of these sequences is slightly decreased and the maximum of efficiency is shifted to larger rf-fields (not shown). The scaling rf-field factor is equal to the inverse of the proportion φ during which the rf-field is sent. As an example, the optimum rf-field is multiplied by 2.3 if the delay is of 2μs, if ν_R = 70 kHz. Obviously, the SFAM sequences still appear more appealing with respect to all other sequences when taking

into account these pulse limitations. The REDOR efficiency always decreases with longer pulses (lower rf-field), and with the XY_4 phase cycling its value is proportional to $\cos(\pi\varphi/2)/(1-\varphi^2)$.[20]

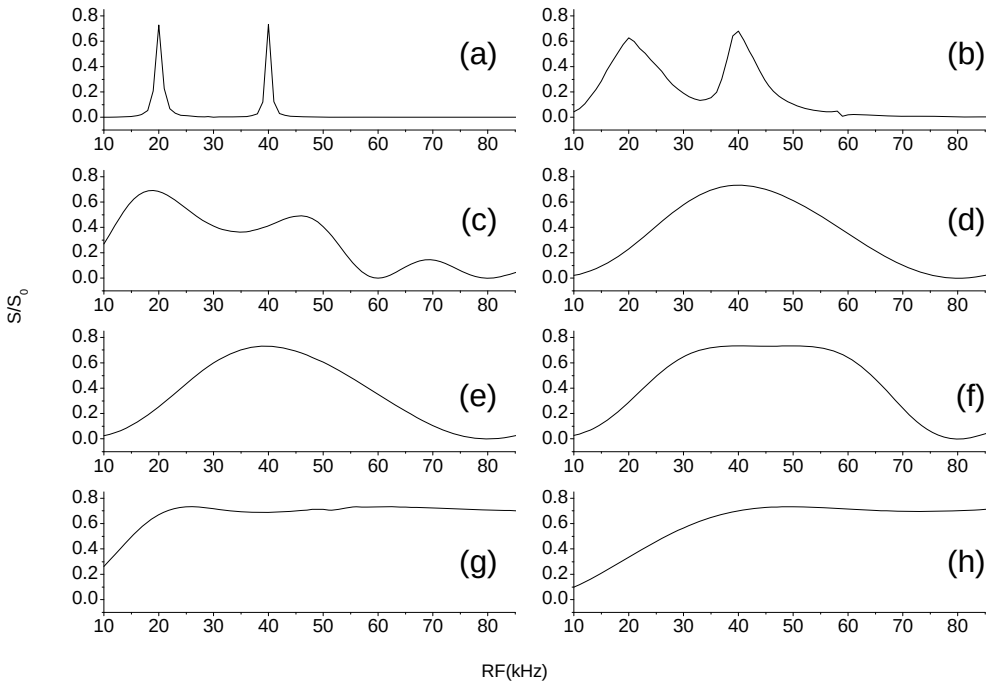

Fig.3.2. Calculated optimum ^{13}C-^{15}N-^{13}C MAS *D*-HMQC efficiency with D_{IS} = 1kHz at ν_R = 20 kHz, using sequence shown figure 1a, with ideal pulses (other than recoupling sequence), versus the rf-field amplitude (ν_1^{max} for SFAM). R^3 without (a) and with (b) CSA (10kHz), $R2_1^1$ (c), $R12_3^5$ (d), $R20_5^9$ (e), $SR4_1^2$ (f), $SFAM_1$ ($\Delta\nu_0^{max}$ = 60 kHz) (g), $SFAM_2$ (ν_0^{max} = 15 kHz) (h). Efficiencies are normalized with respect to that observed with an echo. The same results are obtained for the simulation of ^{27}Al-^{31}P-^{27}Al MAS D-HMQC using the sequence in Fig.3.1a.

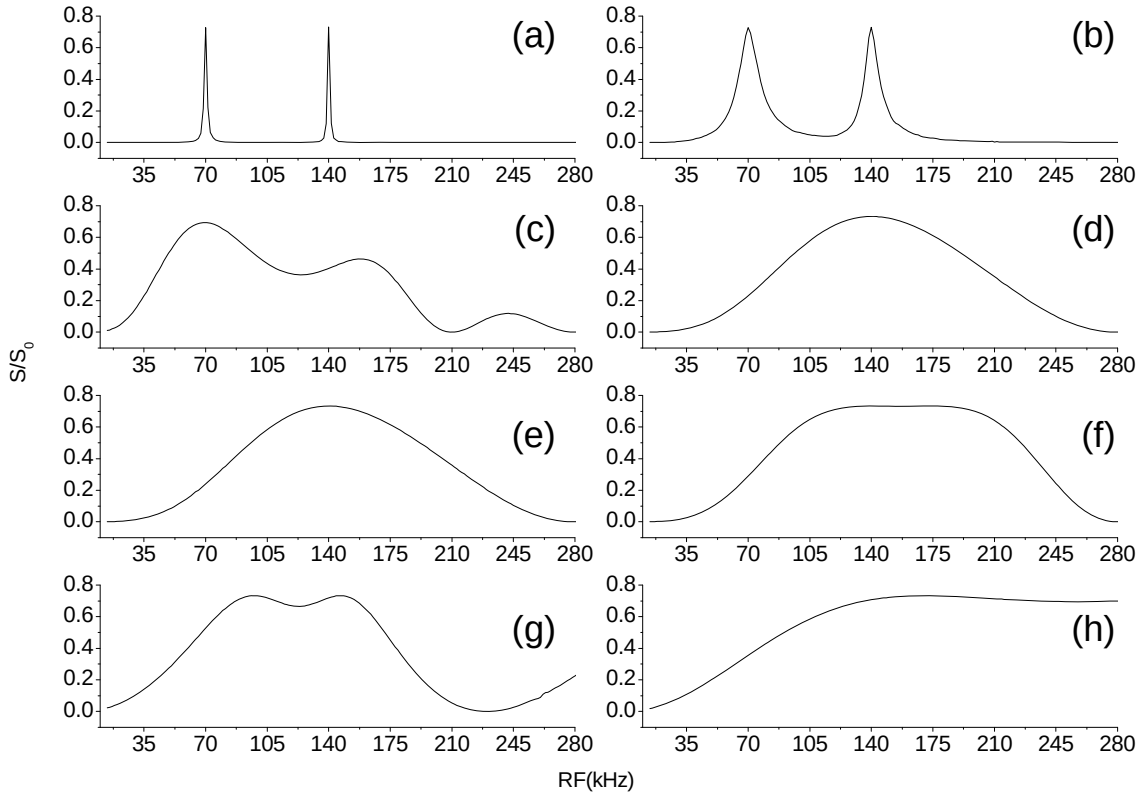

Fig.3.3. Calculated optimum ^{13}C-^{15}N-^{13}C MAS *D*-HMQC efficiency with D_{IS} = 1kHz at ν_R = 70 kHz, using sequence shown figure 1a with ideal pulses (other than recoupling sequence), versus the rf-field amplitude (ν_1^{max} for SFAM). R^3 without (a) and with (b) CSA (10kHz), $R2_1^1$ (c), $R12_3^5$ (d), $R20_5^9$ (e), $SR4_1^2$ (f), $SFAM_1$ ($\Delta\nu_0^{max}$ = 60 kHz) (g), $SFAM_2$ ($\Delta\nu_0^{max}$ = 15 kHz) (h). Efficiencies are normalized with respect to that observed with an echo. The same results are obtained for the simulation of ^{27}Al-^{31}P-^{27}Al MAS D-HMQC using the sequence in Fig.3.1a.

Another important parameter is the scaling factor of the recoupled hetero-nuclear dipolar interaction which drives the optimum length for the dipolar recoupling. Remarkably its value only depends on the fact the recoupling sequence decouples or not homo-nuclear interactions :

$SFAM_1$, $R^3_{q=1}$, $R2_1^1$, REDOR $\quad \tau_{opt} = 0.84/D$ (3.3)

$SFAM_2$, $R^3_{q=2}$, $SR4_1^2$, $R12_3^5$, $R20_5^9$ $\quad \tau_{opt} = 0.84\sqrt{2}/D$ (3.4)

In addition to previous simulations **(Fig.3.2,3.3)**, the experimental signal is decreased due to irreversible losses acting during the recoupling periods. These losses increase with the

recoupling time. Except when homo-nuclear interactions cannot be neglected, these losses are thus another reason to prefer sequences described in **Eq.3.3**, and especially $SFAM_1$ and REDOR.

(b) Homo-nuclear decoupling

In a second step, we have calculated the signal that can be obtained with a three spin system: two S nuclei strongly (25 kHz) dipolar coupled together, and simultaneously weakly (1 kHz) dipolar coupled with one I nucleus.

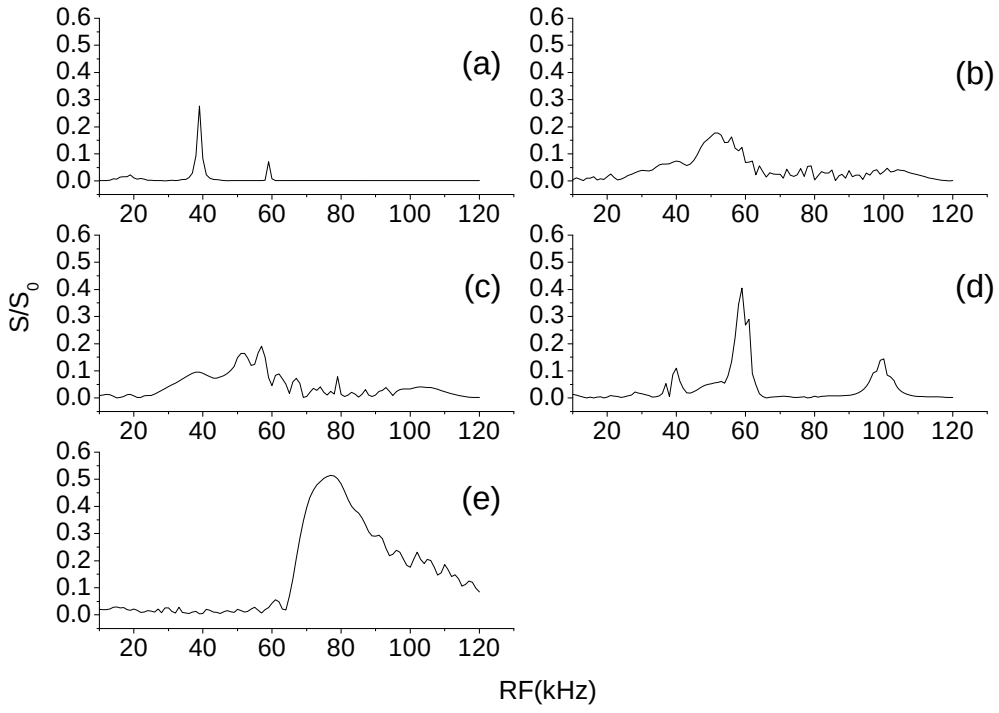

Fig.3.4. Calculated optimum ^{1}H-^{15}N-^{1}H MAS *D*-HMQC efficiency in the case of strong homo-nuclear dipolar interaction with $D_{1H\text{-}1H}$ = 25 kHz and $D_{1H\text{-}15N}$ = 1kHz, with no CSA, at ν_R = 20 kHz, using sequence of figure 1b: with R^3 (a), $R12_3^5$ (b), $R20_5^9$ (c), $SR4_1^2$ (d), $SFAM_2$ ($\Delta\nu_0^{max}$ = 15 kHz) (e).

$R2_1^1$ and $SFAM_1$ do allow homo- and hetero-nuclear dipolar recoupling, hence leading to cancellation of all available magnetization. Thus they will not be considered in the following. Only one main resonance is now observed on the R^3 matching curves (**Fig.3.4a and Fig.3.5a**), which corresponds to the q = 2 condition. The $R12_3^5$ and $R20_5^9$ efficiencies again have a very similar behavior, but much less efficient than without homo-nuclear dipolar interactions, especially at low spinning speed where this interaction is weakly MAS averaged (**Fig.3.4b,c and Fig.3.5b,c**). The $SR4_1^2$ matching curve is now split into three narrow resonances corresponding to ν_1/ν_R = 2, 3 and 5. In any case, the most efficient method is $SFAM_2$, especially when introducing the previous delay between the RN_n^ν pulses (not shown). The $SFAM_2$ matching curve is less flat than before and a broad maximum is observed for $\nu_1 = 4\nu_R$. Of course, the efficiency of all methods increases with spinning speed, as homo-nuclear interactions are then more and more averaged. The REDOR efficiency is decreased by the introduction of the homo-nuclear interactions, especially with weak rf-fields.[22]

It must be noted that in order to compare the rf-power dissipated into the coil for the various methods, the rf values indicated for SFAM are peak values **(Fig.3.2g,h and Fig.3.3g,h)** and should thus be divided by $\sqrt{2}$ to get RMS values, because they correspond to sinusoidal modulations. It is also important to note that simulations including half-integer quadrupolar nuclei (not shown), gave very similar results to those shown in **Figs.3.2-3.5**.

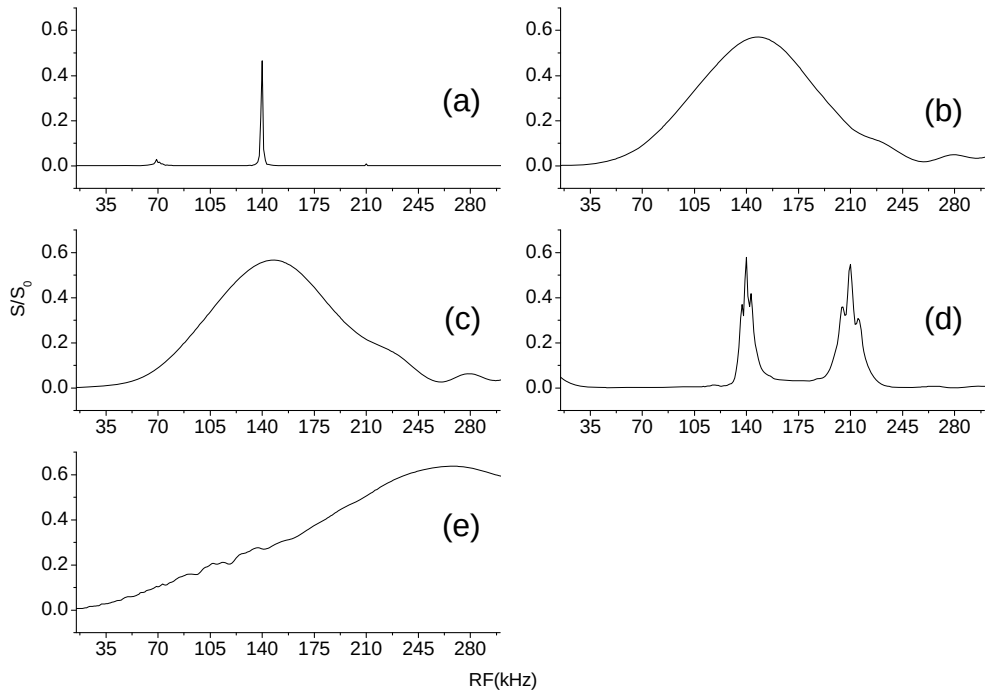

Fig.3.5. Calculated optimum ^{1}H-^{15}N-^{1}H MAS *D*-HMQC efficiency in the case of strong homo-nuclear dipolar interaction with $D_{1H\text{-}1H}$ = 25 kHz and $D_{1H\text{-}15N}$ = 1k, with no CSA at ν_R = 70 kHz, using sequence of figure 1b: with R^3 (a), $R12_3^5$ (b), $R20_5^9$ (c), $SR4_1^2$ (d), $SFAM_2$ ($\Delta\nu_0^{max}$ = 15 kHz) (e).

3.3 Experiments

(a) Verifications on ^{13}C-^{15}N-^{13}C *D*-HMQC of glycine

We have first started to verify previous calculations in between two spin-1/2 nuclei, by recording ^{13}C-^{15}N-^{13}C *D*-HMQC HETCOR spectra of fully ^{13}C and ^{15}N enriched glycine at B_o = 9.4T and ν_R = 20kHz. There are two carbons, at 42 and 180 ppm, and a single nitrogen in this amino-acid. However, the ^{13}C-^{13}C homo-nuclear interactions are weak in glycine. In **Fig.3.6** is represented the optimum first slice (t_1 = 0) spectrum for the ^{13}C resonance at 42 ppm, for the various dipolar recoupling sequences. We have used a ^{1}H TPPM decoupling sequence during the acquisition of this first slice.[30]

When the recoupling is performed indirectly on the ^{15}N channel all sequences perform similarly **(Fig.3.6)**, except mainly the two R^3 sequences, which give a very weak signal due to their narrow matching curves with respect to the coil rf-inhomogeneity. As said before, the q

= 2 resonance efficiency is still weaker than that for q = 1, due to narrower resonance and longer τ_{opt} value. The $R2_1^1$ sequence is intermediate between the R^3 sequences and the six other sequences.

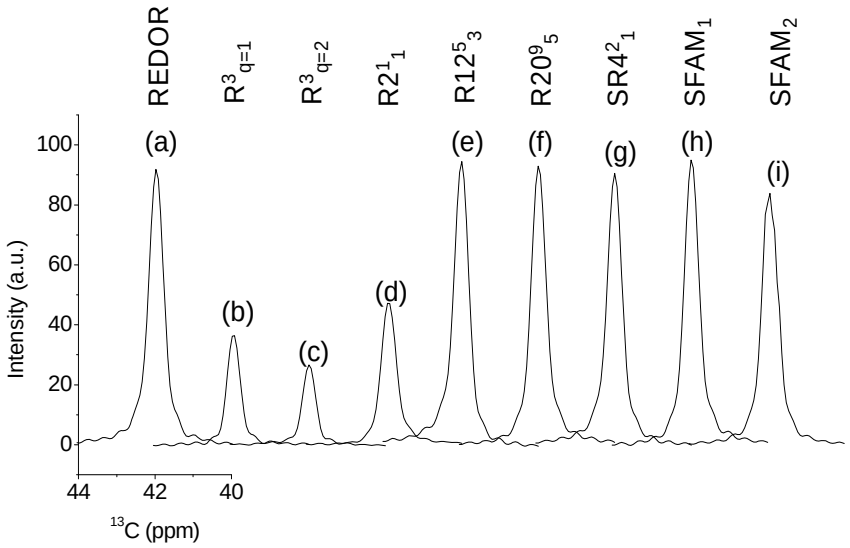

Fig.3.6. Experimental ^{13}C-^{15}N-^{13}C MAS *D*-HMQC of glycine with recoupling sequence on the ^{15}N channel (sequence figure 1a). Only the resonance at 42 ppm is shown. B_o = 9.4T, ν_R = 20 kHz, RF_C = 50 kHz, RF_N = 55 kHz, number of scan is 4, recycle time is 2s, recoupling pulse length is around 1000us. (a) $REDOR_{XY4}$, (b) R^3 (q = 1), (c) R^3 (q = 2), (d) $R2_1^1$, (e) $R12_3^5$, (f) $R20_5^9$, (g) $SR4_1^2$, (h) $SFAM_1$ (ν_1^{max} = 64 kHz, $\Delta\nu_0^{max}$ = 60 kHz), (i) $SFAM_2$ (ν_1^{max} = 26 kHz, $\Delta\nu_0^{max}$ = 15 kHz). Intensities are normalized to the same arbitrary reference.

When the ^{13}C-^{15}N dipolar recoupling is performed directly on the ^{13}C observed channel **(Fig.3.7)**, results are completely different, as all pulses defects of the recoupling sequence (rising and falling times, phase glitches and errors, rf-field strength and spinning speed instability) are then emphasized, and prevent ^{13}C CSA refocusing. One striking example of this effect is the REDOR signal, which is quite decreased with respect to **Fig.3.6**, as shown previously by Gan.[8] The normalized optimum signal intensity we achieved is : (6) REDOR, (25) $R^3_{q=2}$, (43) $R^3_{q=1}$, (47) $R2_1^1$ and $R20_5^9$, (52) $SFAM_2$, (57) $R12_3^5$, (66) $SR4_1^2$ and (80) $SFAM_1$.

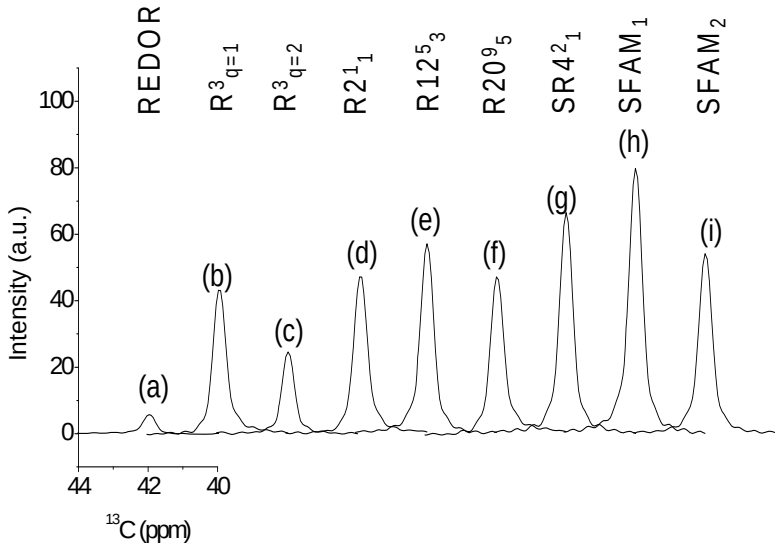

Fig.3.7. Experimental ^{13}C-^{15}N-^{13}C MAS *D*-HMQC of glycine with recoupling sequence on the ^{13}C channel (sequence figure 1b). Only the resonance at 42 ppm is shown. B_o = 9.4T, ν_R = 20 kHz, RF_C = 50 kHz, RF_N = 55 kHz, number of scan is 4, recycle time is 2s, recoupling pulse length is around 1000us. (a) $REDOR_{XY4}$, (b) R^3 (q = 1), (c) R^3 (q = 2), (d) $R2_1^1$, (e) $R12_3^5$, (f) $R20_5^9$, (g) $SR4_1^2$, (h) SFAM $_1$ (ν_1^{max} = 42 kHz, $\Delta\nu_0^{max}$ = 60 kHz), (i) $SFAM_2$ (ν_1^{max} = 22 kHz, $\Delta\nu_0^{max}$ = 15 kHz). Intensities are normalized to the same arbitrary reference as in Fig.3.6.

(b) Verifications on ^{27}Al-^{31}P-^{27}Al *D*-HMQC of $AlPO_4$ VPI5

We have performed the same type of verifications in between ^{27}Al and ^{31}P in microporous hydrated aluminophosphate $AlPO_4$-VPI5. This sample contains three equally populated sites for Al and P, which are coordinated with each other through one bridging oxygen.[31] Under MAS, the ^{31}P resonances are well resolved, but only two ^{27}Al peaks are observable. The resonance labeled Al_1 (≈ -20 ppm) represents a site between the fused four-membered rings. Two water molecules complete an octahedral coordination sphere for Al_1 and render inequivalent the tetrahedrally coordinated Al_2 and Al_3 sites (≈ 42 ppm), as well as the phosphorus sites P_2 and P_3 in the six-membered rings. The specific connectivities between various nuclei are as follows: Al_1 ($2P_1$, P_2, P_3), Al_2 (P_1, $2P_2$, P_3) and Al_3 (P_1, P_2, $2P_3$). The quadrupolar coupling constants C_Q for the aluminum sites are 3.95 MHz (Al_1), 1.3 MHz (Al_2),

and 2.8 MHz (Al_3).[32] Because we deal now with one quadrupolar nucleus with spin-5/2, the dipolar recoupling sequence must be sent onto the phosphorus channel. Due to very long phosphorus relaxation times, we have started the experiment from the aluminum channel **(Fig.3.1a)** and thus recorded the first t_1 slice of ^{27}Al-^{31}P-^{27}Al *D*-HMQC experiments. This means that the large phosphorus CSA do not intervene in the indirect refocusing of the ^{31}P-^{27}Al dipolar coupling. The results for the $Al_{2,3}$ resonances represented in **Fig.3.8** are very similar to those previously obtained in case of two spin-1/2 nuclei **(Fig.3.6)**. The $R2_1^1$ and $SFAM_2$ efficiencies are intermediate between those very small observed with R^3 and the large ones observed for REDOR, $R12_3^5$, $R20_5^9$, $SR4_1^2$ and $SFAM_1$. Simultaneously, for three methods ($R^3_{q=1}$, $SFAM_1$, $SR4_1^2$), we have calculated the efficiency versus the delay (**Fig.3.1**: $\approx kT_R$) in between the two recoupling sequences.

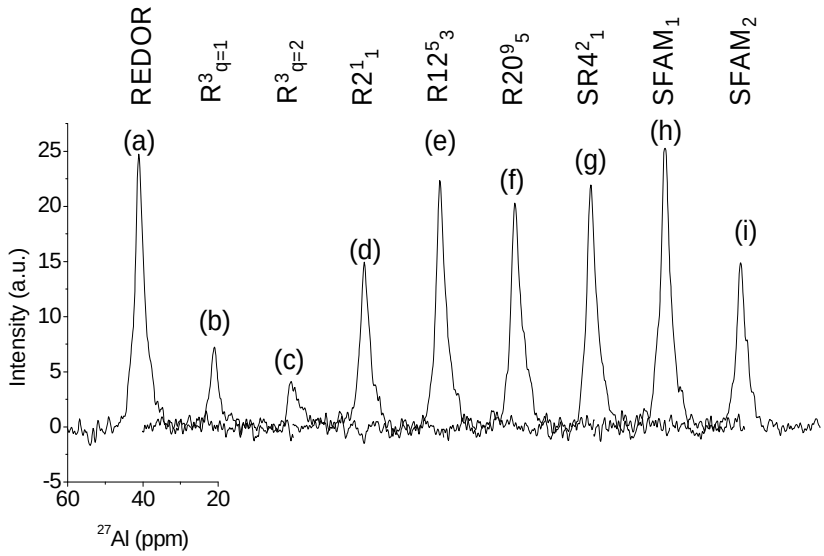

Fig.3.8. Experimental ^{27}Al-^{31}P-^{27}Al MAS *D*-HMQC of $AlPO_4$-VPI5 with recoupling sequence on the ^{31}P channel (sequence figure 1a). Only the $Al_{2,3}$ resonance at 40 ppm is shown. B_o = 9.4T, ν_R = 10 kHz, , RF_{Al} = 7 kHz, RF_P = 62 kHz, number of scan is 8, recycle time is 1s, recoupling pulse length is around 800us. (a) $REDOR_{XY4}$, (b) R^3 (q = 1), (c) R^3 (q = 2), $R2_1^1$ (d), $R12_3^5$ (e), $R20_5^9$ (f), $SR4_1^2$ (g), (h) $SFAM_1$ (ν_1^{max} = 55 kHz, $\Delta\nu_0^{max}$ = 50 kHz), (i) $SFAM_2$ (ν_1^{max} = 42 kHz, $\Delta\nu_0^{max}$ = 50 kHz).

It can be observed that the rotor-synchronization of this delay is more critical for $SR4_1^2$ than for $R^3_{q=1}$ and $SFAM_1$ **(Fig.3.9A)**. This timing is still more critical when the recoupling sequences are sent on the observed channel **(Fig.3.9B).** The experimental measured efficiencies (not shown) have verified results shown in **Fig.3.9.**

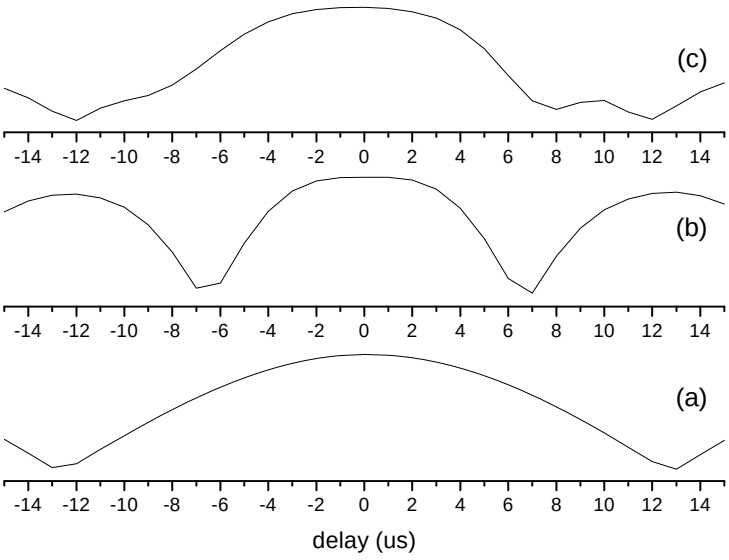

(A)

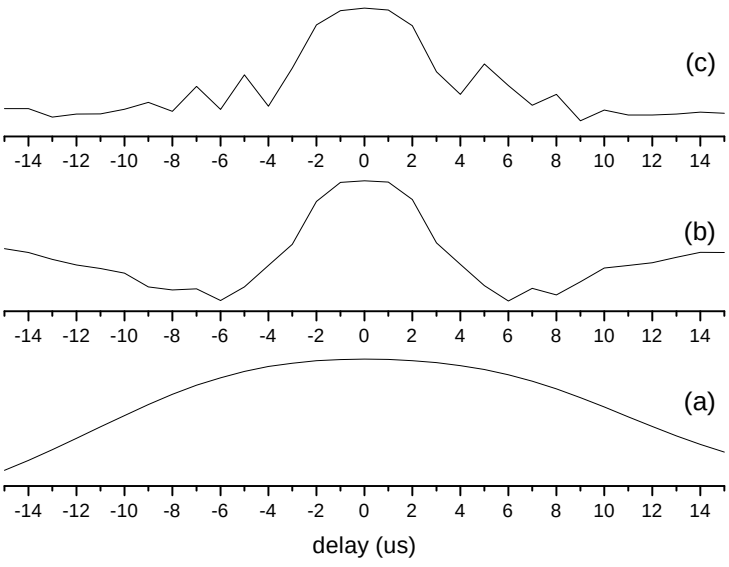

(B)

Fig.3.9 Calculated synchronization effects of the delay, with respect to kT_R, between the two recoupling periods for the R^3 (q = 1) (a), $SR4_1^2$ (b), and $SFAM_1$ (c) ($\Delta\nu_0^{max}$ = 60 kHz) sequences. B_o = 9.4T, ν_R = 10 kHz. The recoupling sequence is either sent on the non-observed (A) or the observed (B) channel.

(c) Verifications on ^{1}H-^{15}N-^{1}H *D*-HMQC of histidine

There are three different types of protons in histidine, but only two resonances are observed at 8 and 12ppm, with the spinning speed (ν_R = 20 kHz) and static field (B_o = 9.4 T) we have used. In this case, it is mandatory using a recoupling sequence that also decouples the ^{1}H-^{1}H dipolar interactions, and therefore the signal observed with REDOR, $R^3_{q=1}$, and $SFAM_1$ sequences was always very small (not shown). In **Fig.3.10**, we have thus only represented the first slice observed with the five sequences ($R^3_{q=2}$, $SR4^2_1$, $R12^5_3$, $R20^9_5$, $SFAM_2$) described in Eq.3.4 with the recoupling sequence sent on the ^{15}N channel. The optimum recoupling periods for these sequences were always similar and approximately 1.4 longer than that observed with REDOR, $R^3_{q=1}$, and $SFAM_1$. Except for the $R^3_{q=2}$ recoupling scheme, which behaves poorly due to the narrowness of its resonance, the four other sequences present approximately the same efficiency at this spinning speed. However, we believe that, in opposite to $SFAM_2$, the efficiency of RN^{ν}_{n} recoupling sequences will largely decrease at very fast spinning speed, due to pulse imperfections.

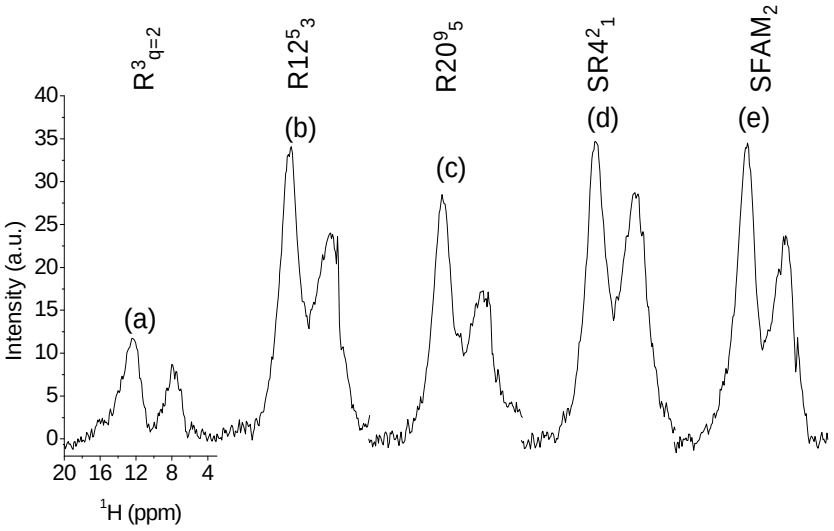

Fig.3.10. Experimental ^{1}H-^{15}N-^{1}H MAS *D*-HMQC of histidine with B_o = 9.4T, ν_R = 20 kHz, RF_H =113 kHz, RF_N = 65 kHz, number of scan is 8, recycle time is 3s, recoupling pulse length is around 200us. (a) R^3 (q = 2), (b) $R12^5_3$, (c) $R20^9_5$, (d) $SR4^2_1$, (e) $SFAM_2$ (ν_1^{max} = 71 kHz, $\Delta\nu_0^{max}$ = 15 kHz).

3.4 Conclusions

We have compared several hetero-nuclear dipolar recoupling sequences to be used with indirectly detected MAS *D*-H-M/S-QC experiments in between a spin-1/2 and a quadrupolar nucleus. In any cases, it must be noted that R^3 methods behave very poorly due to the narrowness of their rf-matching curves.

When homo-nuclear interactions are negligible, and when the recoupling sequence is sent on the non-observed channel, most of the sequences present approximately the same efficiency. However, three sequences should be preferred because of their shorter minimum length, REDOR, $SFAM_1$ (one rotor-period) and $SR4_1^2$ (two rotor-periods), which allows for a better optimization of the contact times. Indirect $SFAM_1$ is very robust, as rotor synchronization of the delay between the two recoupling periods is not critical, and also because its associated losses are smaller than with $SR4_1^2$, due to a shorter contact time. When the recoupling sequence is sent on the observed channel, only two methods emerge: $SR4_1^2$ and especially $SFAM_1$. The advantage of the method $SR4_1^2$, is that it can be done with old consoles, as it requires only pulses with phases ± 90°. However, $SFAM_1$ is still more efficient, especially at very high spinning speed.

When homo-nuclear interactions are not negligible, the most interesting recoupling sequences are $R12_3^5$, $R20_5^9$, $SR4_1^2$ and $SFAM_2$. However, the experimental comparisons have been performed at ν_R = 20kHz, and it is predictable that the advantage of $SFAM_2$ with respect to all other sequences will increase with the spinning speed. Indeed, $SFAM_2$ uses continuous modulations of frequency and amplitude, and is thus very little subject to classical pulse-limitations (rise and fall times, phase glitches..), which is not the case with the RN_n^v recoupling sequences.

We have always observed similar optimum recoupling periods for all methods that decouple homo-nuclear dipolar interactions ($R^3_{q=2}$, $SR4_1^2$, $R12_3^5$, $R20_5^9$, $SFAM_2$), and this optimum length was approximately 1.4 longer than that observed with sequences that do not decouple these interactions ($R^3_{q=1}$, REDOR, $SFAM_1$). This is one of the reasons why $SFAM_1$ should be preferred in case of weak homo-nuclear dipolar interactions, especially at very fast spinning speeds.

The robustness of RN_n^v sequences with respect to chemical shielding, rf-inhomogenity, and instrumental errors in phase setting can be improved by supercycling.[33-35] However, we anticipate that SFAM methods, which are very simple and robust, will become very fast the methods of choice, especially at very fast MAS. Moreover, the robustness of the SFAM methods may still be increased also by supercycling.

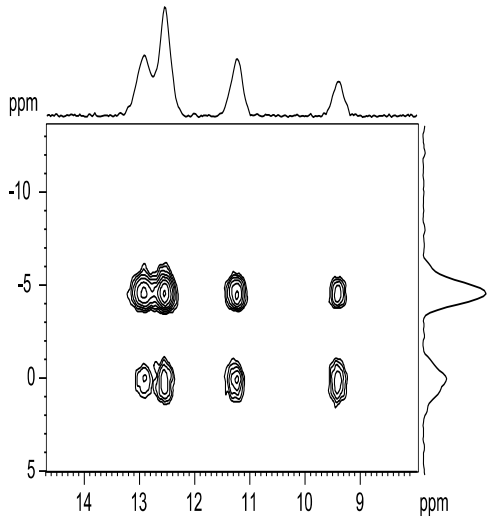

Fig. 3.11. *D*-HMQC with $SFAM_1$. NaH_2PO_4. 18.8T. ν_1^{max} = 180 kHz, $\Delta\nu_0^{max}$ = 20 kHz. ν_R = 60 kHz (Courtesy of Julien Trebosc, data unpublished).

Finally, we emphasize here that *D*-HMQC is less sensitive to C_Q values and offsets compared to MP-CPMAS or CW-CPMAS because only two CT selective pulses is sent on quadrupolar channel in *D*-HMQC. In CW-CPMAS, continuous long pulse with low rf-power

is sensitive to offset effects, while in MP-CPMAS, too many discrete pulses are sent in quadrupolar channel. Normally the pulse will not only operate on center transitions, but also on satellite transitions, therefore, too many pulses will dissipate the signals to ST. Above all, it's better to send less pulses in quadrupolar channel. At last we will show a *D*-HMQC spectrum with $SFAM_1$ to show that *D*-HMQC can be used at high magnetic field (18.8T) and fast-MAS (60kHz).

References

1. L. Müller, Sensitivity enhanced detection of weak nuclei using heteronuclear multiple quantum coherence, *J. Am. Chem. Soc*. 101, 448-4484 **(1979).**

2. G. Bodenhausen, D.J. Ruben, Natural abundance nitrogen-15 NMR by enhanced heteronuclear spectroscopy, *Chem. Phys. Lett*. 69, 185-189 **(1980).**

   A.A. Maudsley, R.R. Ernst, Indirect detection of magnetic resonance by heteronuclear two-dimensional spectroscopy, *Chem. Phys. Lett.* 50, 368-372 **(1977).**

3. E.R. Andrew, A. Bradbury, R.G. Eades, Nuclear magnetic resonance spectra from a crystal rotated at high speed, *Nature*. 182, 1659 **(1958).**

4. S.R. Hartmann, E.L. Hahn, Nuclear double resonance in the rotating frame, *Phys. Rev.* 128, 2042-2053 **(1962).**

5. A. Pines, M.G. Gibby, J.S. Waugh, Proton-enhanced NMR of dilute spins in solids, *J. Chem. Phys*. 59, 569-590 **(1973)**.

6. A. Lesage, D. Sakellariou, S. Steuernagel, L. Emsley, Carbon-proton chemical shift correlation in solid-state NMR by through-bond multiple-quantum spectroscopy, *J. Am. Chem. Soc*. 120, 13194-13201 **(1998).**

D. Massiot, F. Fayon, B. Alonso, J. Trébosc, J.P. Amoureux, Chemical bonding differences evidenced from J-coupling in solid-state NMR experiments involving quadrupolar nuclei, *J. Magn. Reson.* 164, 160-164 **(2003).**

J.P. Amoureux, J. Trébosc, J. Wiench, M. Pruski, HMQC and refocused-INEPT experiments involving half-integer quadrupolar nuclei, *J. Magn. Reson.* 184, 1-14 **(2006).**

7. A. Lesage, L. Emsley, Through-bond heteronuclear single-quantum correlation spectroscopy in solid-state NMR, and comparison to other through-bond and through-space experiments, *J. Magn. Reson*. 148, 449-454 **(2001).**

8. Z. Gan, $^{13}C/^{14}N$ heteronuclear multiple-quantum correlation with rotary resonance and REDOR dipolar recoupling, *J. Magn. Reson*. 184, 39-43 **(2006).**

J. Trébosc, B. Hu, J.P. Amoureux, Z. Gan, Through-space R^3 HETCOR experiments between spin-1/2 and half-integer quadrupolar nuclei in solid-state NMR, *J. Magn. Reson.* 186, 220-227 **(2007).**

9. M.H. Levitt, T.G. Oas, R.G. Griffin, Rotary resonance recoupling in heteronuclear spin pair systems, *Israel J. Chem*. 28, 271 **(1988).**

T.G. Oas, R.G. Griffin, M.H. Levitt, Rotary resonance recoupling of dipolar interactions in solid-state nuclear magnetic resonance spectroscopy, *J. Chem. Phys*. 89, 692-695 **(1988).**

Z. Gan, D.M. Grant, Rotational resonance in a spin-lock field for solid state NMR, *Chem. Phys. Lett*. 168, 304-308 **(1990).**

Z. Gan, D.M. Grant, R.R. Ernst, NMR chemical shift anisotropy measurements by RF driven rotary resonance, *Chem. Phys. Lett*. 254, 349-357 **(1996).**

10. A. Brinkmann, M.H. Levitt, Symmetry principles in the nuclear magnetic resonance of spinning solids: Heteronuclear recoupling by generalized Hartmann-Hahn sequences, *J. Chem. Phys*. 115, 357-384 **(2001).**

11. A. Brinkmann, A.P.M. Kentgens, Sensitivity enhancement and heteronuclear distance measurements in biological ^{17}O solid-state NMR, *J. Phys. Chem. B*. 110, 16089-16101 **(2006).**

12. A. Brinkmann, A.P.M. Kentgens, Proton-selective ^{17}O-^{1}H distance measurements in fast MAS solid-state NMR spectroscopy for the determination of hydrogen bond lengths, *J. Am. Chem. Soc.* 128, 14758-14759 **(2006)**.

13. S. Cavadini, A. Abraham, G. Bodenhausen, Proton-detected ^{14}N NMR by recoupling of heteronuclear dipolar interactions using symmetry-based sequences, *Chem. Phys. Lett*. 445, 1-5 **(2007)**.

14. M. Carravetta, M. Eden, X. Zhao, A. Brinkmann, M.H. Levitt, Symmetry principles for the design of radiofrequency pulse sequences in the nuclear magnetic resonance of rotating solids, *Chem. Phys. Lett*. 321, 205-215 **(2000)**.

X. Zhao, M. Eden, M.H. Levitt, Recoupling of heteronuclear dipolar interactions in solid-state NMR using symmetry-based pulse sequences. *Chem. Phys. Lett*. 342, 353-361 **(2001).**

M.H. Levitt, Symmetry-based pulse sequences in MAS solid-state NMR, *Encyclopedia of NMR*; D.M. Grant, R.K. Harris, Eds; Wiley: Chichester, England, Vol.9 **(2002).**

15. T. Gullion, J. Schaefer, Rotational-echo double resonance NMR, *J. Magn. Reson*. 81, 196-200 **(1989)**.

16. R. Fu, S.A. Smith, G. Bodenhausen, Recoupling of heteronuclear dipolar interactions in solid-state MAS NMR by simultaneous frequency and amplitude modulation, *Chem. Phys. Lett*. 272, 361-369 **(1997)**.

K. Nishimura, R. Fu, T.A. Cross, The effect of RF-inhomogeneity on heteronuclear dipolar recoupling in solid-state NMR: practical performance of SFAM and REDOR, *J. Magn. Reson*. 152, 227-233 **(2001)**.

17. Z. Gan, J.P. Amoureux, J. Trébosc, Proton-detected ^{14}N MAS NMR using homonuclear decoupled rotary resonance, *Chem. Phys. Lett*. 435, 163-169 **(2007).**

18. T. Gullion, D.B. Baker, M.S. Conradi, New compensated Carr-Purcell sequences, *J. Magn. Reson.* 89, 479-484 **(1990).**

T. Gullion, J. Schaefer, Elimination of resonance offset effects in rotational-echo double-resonance NMR, *J. Magn. Reson*. 92, 439-442 **(1991).**

19. L. Chopin, R. Rosanske, T. Gullion, Simple improvements in spinning-speed control for MAS experiments, *J. Magn. Reson*. A122, 237-239 **(1996).**

T. Gullion, A.J. Vega, Measuring heteronuclear dipolar couplings for I = ½, S > 1/2 spin pairs by REDOR and REAPDOR NMR, *Prog. Nucl. Mag. Res*. Spec. 47, 123-136 **(2005).**

20. C.P. Jaroniec, B.A. Tounge, C.M. Rienstra, J. Herzfeld, R.G. Griffin, Recoupling of heteronuclear dipolar interactions with REDOR at high-MAS frequencies, *J. Magn. Reson*. 146, 132-139 **(2000)**.

21. M. Baldus, B.H. Meier, Broadband polarization transfer under Magic-Angle Spinning: application to total through-space-correlation NMR spectroscopy, *J. Magn. Reson*. 128, 172-193 **(1997)**.

22. R. Tycko, G. Dabbagh, Measurement of nuclear magnetic dipole-dipole couplings in magic angle spinning NMR, *Chem. Phys. Lett*. 173, 461-465 **(1990).**

23. N.C. Nielsen, H. Bildsoe, H.J. Jakobsen, Double-quantum homonuclear rotary resonance: Efficient dipolar recovery in magic-angle spinning nuclear magnetic resonance, *J. Chem. Phys*. 101, 1805-1812 **(1994).**

R. Verel, M. Baldus, M. Ernst, A homonuclear spin-pair filter for solid-state NMR based on adiabatic-passage techniques, *Chem. Phys. Lett.* 287, 421-428 **(1998).**

24. N.C. Nielsen, H. Bildsoe, H.J. Jakobsen, M.H. Levitt, Double-quantum homonuclear rotary resonance: Efficient dipolar recovery in magic-angle spinning nuclear magnetic resonance, *J. Chem. Phys.* 101, 1805-1812 **(1994)**.

Y.K. Lee, N.D. Kurur, M. Helmle, O.G. Johannessen, N.C. Nielsen, M.H. Levitt, Efficient dipolar recoupling in the NMR of rotating solids. A sevenfold symmetric radiofrequency pulse sequence, *Chem. Phys. Lett.* 242, 304-309 **(1995)**.

25. A. Brinkmann, J. Schmedt auf der Günne, M.H. Levitt, Homonuclear zero-quantum recoupling in fast Magic-Angle Spinning Nuclear Magnetic Resonance, *J. Magn. Reson*. 156, 79-96 **(2002)**.

T. Karlsson, J.M. Popham, J.R. Long, N. Oyler, G.P. Drobny, A study of homonuclear dipolar recoupling pulse sequences in solid-state nuclear magnetic resonance, *J. Am. Chem. Soc*. 125, 7394-7407 **(2003)**.

P.E. Kristiansen, M. Carravetta, W.C. Lai, M.H. Levitt, A robust pulse sequence for the determination of small homonuclear dipolar couplings in magic-angle spinning NMR, *Chem. Phys. Lett*. 390, 1-7 **(2004).**

26. P.K. Madhu, X. Zhao, M.H. Levitt, High-resolution ^{1}H NMR in the solid-state using symmetry-based pulse sequences; *Chem. Phys. Lett*. 346, 142-148 **(2001).**

27. P.K. Madhu, A. Goldbourt, L. Frydman, S. Vega, Sensitivity enhancement of the MQMAS NMR experiments by fast amplitude modulation of the pulses, *Chem. Phys. Lett.* 307, 41-47 **(1999).**

P.K. Madhu, A. Goldbourt, L. Frydman, S. Vega, Fast radio-frequency amplitude modulation in multiple-quantum magic-angle spinning nuclear magnetic resonance: theory and experiments, *J. Chem. Phys.* 112, 2377-2391 **(2000).**

28. E. van Veenendaal, B.H. Meier, A.P.M. Kentgens, Frequency steeped adiabatic passage excitation of half-integer quadrupolar spin system. *Mol. Phys.* 93, 195-213 **(1998).**

A.P.M. Kentgens, R. Verhagen, Advantages of double-frequency sweep in static, MAS, and MQMAS NMR of spin I = 3/2 nuclei, *Chem. Phys. Lett.* 300, 435-443 **(1999).**

29. M. Bak, N.C. Nielsen, SIMPSON : a general simulation program for solid-state NMR pectroscopy, *J. Magn. Reson*. 147, 296-330 **(2000).**

30. A.E. Bennet, C.M. Rienstra, M. Auger, K.V. Lakshmi, R.G. Griffin, Hetero-nuclear decoupling in rotating solids, *J. Chem. Phys.* 103 **(1995)** 6951-6958.

31. L.B McCusker, Ch. Baerlocher, E. Jahn and M. Bülow, The triple helix inside the large-pore aluminophosphate molecular sieve VPI-5, *Zeolites.* 11, 308-313 **(1991).**

32. J. Rocha, W. Kolodziejski, H. He, J. Klinowski**,** Solid-state NMR studies of hydrated porous aluminophosphate VPI-5, *J. Am. Chem. Soc.* 114, 4884-4888 **(1992)**.

C. Fernandez, C.M. Morais, J. Rocha, M. Pruski, High-resolution hetero-nuclear correlation spectra between ^{31}P and ^{27}Al in Microporous Aluminophosphates, *Solid State Nucl. Magn. Reson.* 21, 61-70 **(2002).**

33. M. Carravetta, M. Eden, O.G. Johannessen, H. Luthman, P.J.E. Verdegem, J. Sebald, A. Sebald, M.H. Levitt, Estimation of carbon-carbon bond lengths and medium-range internuclear distances by solid-state nuclear magnetic resonance, *J. Am. Chem. Soc.* 123, 10628-10638 **(2001).**

34. A. Brinkmann, J. Schmedt auf der Günne, M.H. Levitt, Homonuclear zero-quantum recoupling in fast Magic-Angle Spinning Nuclear Magnetic Resonance, *J. Magn. Reson*. 156, 79-96 **(2002).**

35. M. Eden, Order-selective multiple-quantum excitation in magic-angle spinning NMR: creating triple-quantum coherences with a trilinear hamiltonian, *Chem. Phys. Lett*. 366, 469-476 **(2002).**

Chapter 4. ^{1}H homonuclear decoupling

Proton nuclear magnetic resonance (^{1}H NMR) spectroscopy is widely used to characterize the structure and dynamics of molecules in the liquid state. Due to its high NMR receptivity, the proton is potentially an attractive nucleus for probing the molecular structure of solid materials. Unfortunately, strong homo-nuclear dipolar interactions typically result in a broad featureless ^{1}H NMR peak void of chemical shift and *J*-coupling information. Thus, one of the critical remaining challenges in NMR is to develop techniques to narrow ^{1}H spectra of solids and recover chemical shift and *J*-coupling information.

There are currently three distinct ways to approach high-resolution ^{1}H spectra of solids: (i) isotopic dilution with deuterium,[1] (ii) fast magic angle spinning (MAS),[2] and (iii) radio-frequency (rf) multi-pulse irradiation.[3] The first method is tedious and expensive. MAS alone does not generally achieve enough resolution due to the homogeneous character of ^{1}H-^{1}H interactions. Multi-pulse spin-space narrowing is effective in averaging homo-nuclear dipolar interactions, but does not average broadening resulting from chemical shift anisotropy (CSA ≈ 10-15 ppm).

An obvious remedy is to apply the last two strategies simultaneously, which leads to the combined rotation and multiple pulse spectroscopy (CRAMPS).[4] Almost all CRAMPS sequences use a quasi-static approximation, in which low spinning frequencies (ν_R = 2-5 kHz) ensure an approximately static sample on the cycle time (τ_c) of the rf pulse sequence.[5-9] However, due to the development of very large B_0 magnetic fields, these slow spinning speeds are nowadays unable to average the ^{1}H CSA.

To overcome this problem, two CRAMPS methods: DUMBO and PMLG, have been developed recently. Both methods use a continuous irradiation of fixed amplitude (ν_1), only the phase being changed during τ_c. Two different DUMBO sequences exist, in which the

phase is described by a Fourier series of either 12 ($DUMBO_1$),[10] or 6 (eDUMBO)[11] coefficients. In the PMLG sequence,[12] the ramped phase of the original FSLG[3,13-15] is replaced by 3, 5, 7, or 9 discrete phase steps. Another method has also been proposed for fast spinning speeds, which uses a very short semi-windowless CRAMPS scheme ($swWWH_4$).[16] One of the successes of these schemes is their short cycle times: $\tau_c\nu_1 = 3$, $\sqrt{8/3}$, and 1.25 for DUMBO, FSLG/PMLG, and $swWHH_4$, respectively. However, these pulse sequences have been developed in the quasi-static approximation and MAS interferes with the averaging scheme if the rotor period T_R is not much larger than τ_c. Only one method has been proposed up to now, that is not based on a quasi-static approximation.[17] This method uses rotor synchronized pulse sequences (CN_ν^p and RN_ν^p) that exploit selection rules generated by appropriate synchronization of the rf pulses and the sample rotation.[18] All these previous methods, which are limited to c.a. $\nu_R = 25$ kHz, are also submitted to several distortions: image and zero-frequency peaks, non constant scale factor λ over the spectra, off-resonance frequency irradiation that must be optimized for optimal resolution, and rotor and radio-frequency (RRF)[19] extra lines for DUMBO, FSLG/PMLG and $swWWH_4$. All these distortions, except the RRF lines, are related to pulse transients[19] and the fact the effective Hamiltonian of the sequences does not correspond to an Oz rotation[9]. Indeed, all four methods are submitted to large sudden changes in rf phase and amplitude (for $swWHH_4$). Two very detailed analysis of the pulse transient effects have been published,[20,21] which have lead to a very elegant new PMLG sequence with Oz rotation, which is freed from pulse transient distortions, but that nevertheless still presents RRF lines.[22]

An important challenge of modern solid-state NMR methods is to take benefit of indirect proton detection at high MAS rates and/or magnetic fields, especially in biology. Recently, such kind of techniques were successfully applied in the case of biopolymers and proteins, which were either ^{1}H spin diluted[23,24] or fully protonated.[25,26] For isotopically

unmodified samples, proton resolution and signal enhancement were then achieved from the spinning speed alone (up to 40 kHz[26]). However, even at ultra-fast MAS speeds currently commercially available (up to ν_R = 70 kHz), strong ^{1}H-^{1}H interactions are only partially cancelled leading to ^{1}H spectra with a resolution lower than that obtained with swWHH$_4$, PMLG or DUMBO at much slower speed. Very fast spinning speeds present many advantages, especially at large magnetic fields. Indeed, (1) it increases the rotor-synchronized indirect dimension of most experiments, (2) it allows an efficient proton decoupling with weak ^{1}H rf-field, (3) it increases the T'$_2$ constant times, and (4) it allows using strong rf-fields due to the small rotor diameter used.

Therefore, we have designed our sequence with the following point in mind: we focus on improving resolution at fast spinning speeds as below such speeds, efficient techniques already exist. Our design can not rely on a quasi-static approximation with such short rotor periods (14 to 33 μs for 30 kHz ≤ ν_R ≤ 70 kHz). To avoid any risk of interference between MAS decoupling and rf effect, only rotor-synchronised sequences are envisaged here. It has been shown that CN_ν^p sequences described in ref.17 with the basic C element corresponding to a 2π rotation, lead to a null scale factor (λ = 0), and thus can not be used for our purpose.[27]

We have therefore developed a new class of symmetry-adapted sequences ($CN_n^{N/2}$), which correspond to an Oz rotation.[28] These sequences are based on 0° rotation elements, and they use an amplitude-modulated basic element that is made of two identical subsequent pulses with opposite phases (±x).[28] Among these new possible sequences, we have selected those that decouple the homo-nuclear dipolar interaction, but recouple the chemical shift. However, these sequences are composed of numerous pulses every rotor period, which may be difficult to realize at ultra-fast MAS. Experimentally, this would introduce a large proportion of pulse transients, which would lead to very large spectral distortions.

In order to avoid these phase transients, we have 'smoothed' the $CN_n^{N/2}$ pulses, and our recoupling sequence thus consists in a cosine amplitude modulation, rotor-synchronized with n rf periods fitting in one rotor period T_R. This approach has already been successful in the case of hetero-nuclear dipolar re-introduction under MAS using $SFAM_{1,2}$.[29,30] We name this sequence SAMn after Smooth Amplitude Modulation.

SAM_1 and SAM_2 re-introduce CSA, homo- and hetero-nuclear dipolar interactions and thus cannot be used to get ^1H improved resolution, while sequences with $n > 2$ decouple CSA and homo- and hetero-nuclear dipolar interactions. One can thus expect improved resolution with SAMn methods, if n is larger than 2. In this communication we present preliminary results obtained with integer n values.

4.1 Description of SAM homo-nuclear decoupling sequence

SAM is a rotor-synchronized smooth version of one subclass of the $CN_n^{N/2}$ symmetry-based pulse sequence.[18] As a general rule, the basic element of the CN_n^{ν} sequences must be an rf cycle that in the absence of other spin interaction induces a rotation of the nuclear spins through an integer multiple of 360°, *including* 0°. $CN_n^{N/2}$ sequences which use a 2π rotation basic element, are known to scale the chemical shift to zero, and are therefore not suitable for ^1H high-resolution.[27] In contrast, the implementation of $CN_n^{N/2}$ subclass, using a zero rotation basic element, does not cancel the isotropic chemical shift.

The most simple basic element of this $CN_n^{N/2}$ subclass with zero rotation is composed of two identical square pulses, nutating magnetization by an angle α with opposite phases. This basic element is repeated N times per n rotor periods (Fig.4.1). We will call this sequence $CN_n^{N/2}\left(\alpha\overline{\alpha}\right)$ hereafter. This sequence is amplitude modulated, and hence the rf phases of subsequent basic elements are shifted with respect to each other by the angle π. So,

globally, $CN_n^{N/2}(\alpha\bar{\alpha})$ sequences are composed of (N–1) 2α pulses sandwiched by two α pulses, all with alternating ± x phase, extending over n rotor periods, and then repeated. However, experimentally, $CN_n^{N/2}(\alpha\bar{\alpha})$ sequences are affected by square pulse phase transients that occupy a large proportion of the time at ultra-fast spinning speeds. These transients, which may lead to line-shape distortions and false peaks, are largely reduced by 'smoothing' the $CN_n^{N/2}(\alpha\bar{\alpha})$ pulse amplitude, in such way that the irradiation corresponds to a rotor-synchronized cosine shape, with p = N/2n rf modulation periods fitting in one rotor period:

$$\nu_1(t) = \nu_{1peak} \cos(\nu_{mod} t) = \nu_{1peak} \cos(p\nu_R t) \qquad (4.1)$$

To simplify the notation, we have christened this $CN_n^{N/2}(\cos)$ sequence, SAM_p, for Smooth Amplitude Modulation.

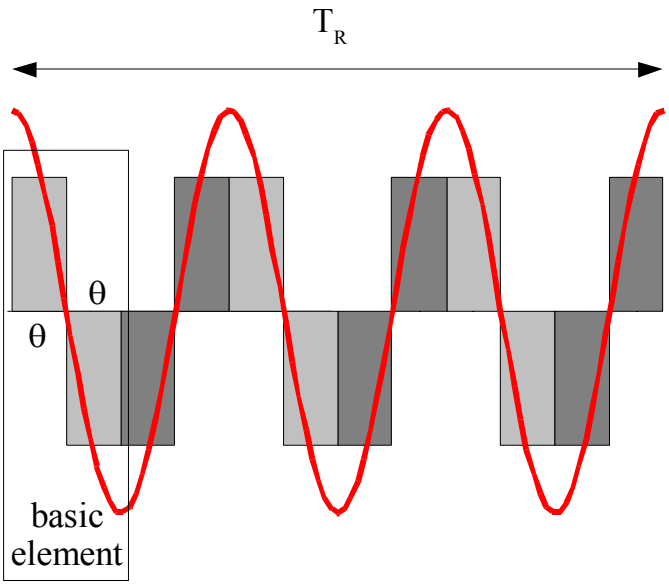

Fig.4.1 $C6_1^3(\alpha\bar{\alpha})$ (squares) and SAM_3 (cosine) basic sequences.

$C6_1^3(\alpha\bar{\alpha})$, $C8_1^4(\alpha\bar{\alpha})$ or $C14_2^7(\alpha\bar{\alpha})$ square pulse sequences and their corresponding smoothed versions, SAM_3, SAM_4 or $SAM_{3.5}$, are some examples of sequences suitable for high-resolution ^1H spectra. Conversely, $C2_1^1(\alpha\bar{\alpha})$, $C4_1^2(\alpha\bar{\alpha})$, SAM_1 and SAM_2 pulse

sequences do not average out CSA and dipolar interactions. In the first-order (Levitt's convention) average Hamiltonian theory (AHT), the isotropic chemical shift term of $CN_n^{N/2}\left(\alpha\bar{\alpha}\right)$ and SAM_p sequences corresponds to an effective field along the *z* axis that makes the technique free of image or zero frequency artifacts and simplifies the experimental setup. In the case of an *IS* spin system, the first-order average Hamiltonian of both sequences is

$$\bar{H}^{(1)}/2\pi = \kappa\left(\nu_I^0 I_z + J_{IS}\, I_z S_z\right) + \nu_S^0 S_z \qquad (4.2)$$

where ν_I^0 and J_{IS} denote respectively the isotropic chemical shift (off-resonance) values of *I*-spin and hetero-nuclear isotropic *J*-coupling, and ν_S^0 the isotropic chemical shift of *S*-spins. The chemical shift scaling factor κ depends on the basic element nutation angle α, i.e. the rf-field amplitude and shape (square or cosine for example). The experimental setup is then reduced to the choice of the $CN_n^{N/2}\left(\alpha\bar{\alpha}\right)$ or SAM_p sequence, and only the rf-field amplitude has to be optimized in order to get optimal resolution. Indeed, there is a competition between the line narrowing effect and the scaling factor, which both decrease with increasing rf-field amplitude. As an example, to the 1st-order AHT, the scaling factor is equal to:

$$\kappa = \mathrm{sinc}(\alpha) \text{ with } \alpha = n\pi\nu_1/N\nu_R \quad \text{for } CN_n^{N/2}\left(\alpha\bar{\alpha}\right) \qquad (4.3)$$

$$\kappa = J_0(2\alpha/\pi) \text{ with } \alpha = \pi\nu_{1peak}/2p\nu_R = n\pi\nu_{1peak}/N\nu_R \quad \text{for } SAM_p. \qquad (4.4)$$

Thereby, there are optimal rf-field and nutation angle values in term of resolution. Simulations using SIMPSON program[31] allow inferring an optimal rf-field of:

$$\nu_1^{opt} \approx N\nu_R/2n \qquad \text{for } CN_n^{N/2}\left(\alpha\bar{\alpha}\right) \qquad (4.5)$$

$$\nu_{1\,peak}^{opt} \approx 1.15p\nu_R = 1.15N\nu_R/2n \quad \text{for } SAM_p, \qquad (4.6)$$

4.2 SAM implemented in t_1 dimension

The pulse sequence incorporating SAM with ^{1}H-X (X = ^{13}C or ^{31}P) CP-MAS HETCOR is shown in Fig. 4.2a. Spectra presented in Fig. 4.2b have been obtained with standard Bruker AVANCE II console, preamplifiers and commercial 1.3 mm and 2.5 mm probes at 14 T and 9.4 T respectively. First, we have acquired at 9.4 T ^{1}H-^{31}P spectra of NaH_2PO_4, which contains three ^{1}H and two ^{31}P different species, using SAMn decoupling sequences with various n during t_1. Only those corresponding to small integer n values (n = 3 and 4) gave the best results, except those with n = 1 and 2 that re-introduce the CSA, homo- and hetero-nuclear dipolar interactions.[28] The best resolution was always observed for the largest rf-field (ν_{1peak} = 85 kHz) available on our old 2.5 mm probe, and with the SAM_3 sequence which provided peaks resolved to the baseline (Fig.4.2b). With this rf-field, the experimental scale factor was λ_{exp} = 0.72, 0.83, 0.90, and 0.94, for n = 3, 4, 5, 6, respectively.

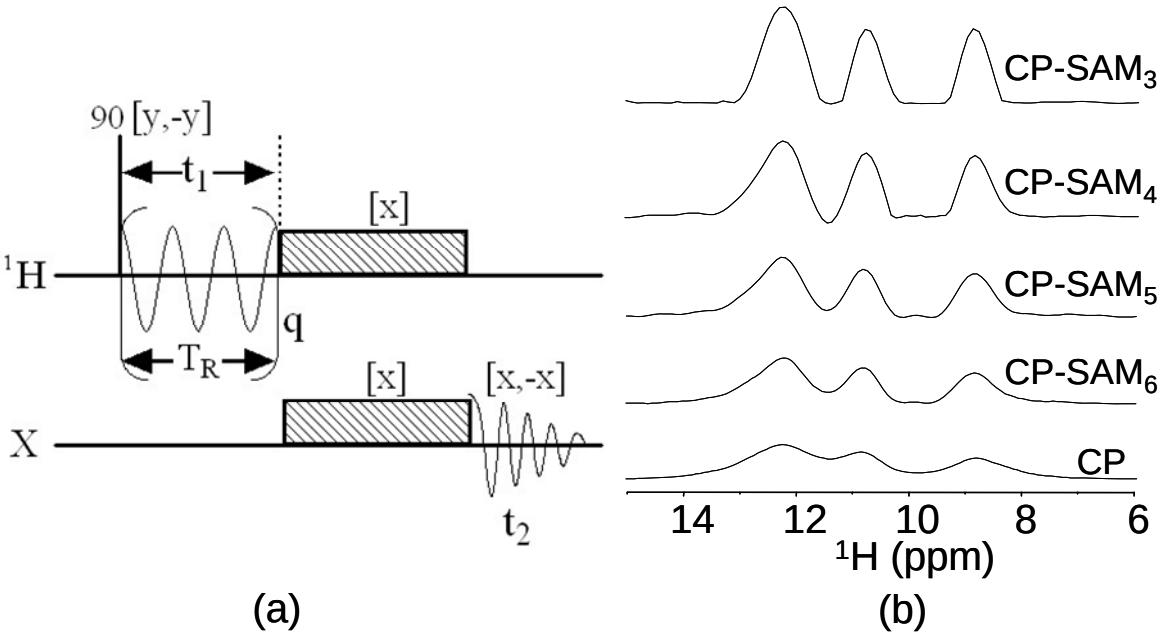

Fig. 4.2 (a) Pulse scheme of ^{1}H-X CP-MAS HETCOR with SAM_3 decoupling during t_1. (b) ^{1}H projection of the ^{1}H-^{31}P CP-MAS 2D spectrum of NaH_2PO_4. B_0 = 9.4 T, ν_R = 30 kHz, ν_{1peak} = 85 kHz. Phase cycling, shown in brackets, follow the normal CP with States method for 2D hypercomplex acquisition while the SAM_3 shape pulse keeps a constant phase throughout the experiments.

The better decoupling efficiency of SAM_3, with respect to other SAMn sequences (n integer), was confirmed by recording ^1H-^{13}C spectra of histidine.HCl.H_2O, at B_0 = 9.4 T, ν_R = 30 kHz and ν_{1peak} = 85 kHz (Fig.4.3a,b). We also did experiments on a 1.3 mm probe at ultra-fast MAS recording ^1H-^{13}C spectra of histidine.HCl. H_2O at B_0 = 14 T, ν_R = 65 kHz, and ν_{1peak} = 210 kHz. We observed a ^1H resolution enhancement mainly on the CH_2 resonance submitted to the largest ^1H-^1H broadening (Fig.4.3c,d). Other ^1H resonances such as COOH, for which homo-nuclear dipolar interaction was already fully removed by MAS alone, only slightly suffered from SAM irradiation as they exhibited 70% of the intensity of regular CP-HETCOR. Moreover, it must be noted that experiments at ν_R = 65 kHz were affected by phase transients as 350 ns steps were used to define the cosine line-shape, meaning less than four discrete steps to alter rf between 0 and ν_{1peak}. It is important to mention that observed SAMn spectra could be more resolved with larger rf-fields. Actually, the optimum rf-field for SAMn methods is equal to $\nu_{1peak}^{opt} = 1.15n\nu_R$ and the optimum scaling factor is then $\lambda_{opt} = 0.70$.[28]

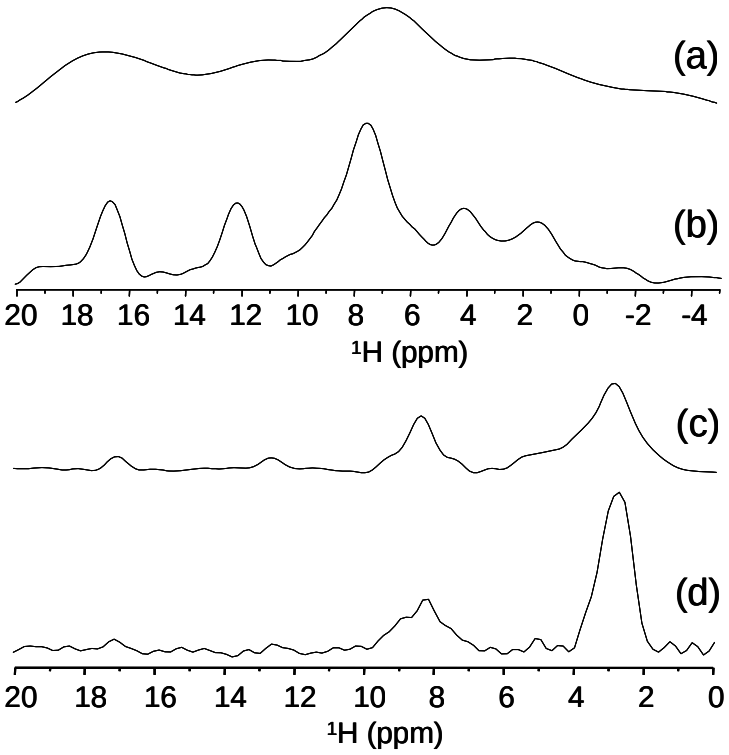

Fig.4.3 Slices of ^{1}H-^{13}C CP-MAS spectra of histidine.HCl.H_2O. (a,b) $B_0 = 9.4$ T, $\nu_R = 30$ kHz, $\nu_{1peak} = 85$ kHz, $\delta_{13C} = 173$ ppm (COOH site). (c,d) $B_0 = 14$ T, $\nu_R = 65$ kHz, $\nu_{1peak} = 210$ kHz, $\delta_{13C} = 57$ ppm (CH_2 site). Spectra (b,d) and (a,c) are acquired respectively with and without SAM_3 decoupling during t_1.

4.3 wSAM implemented in t_2 dimension

The main question is how to sample the signal in the 1D $wCN_n^{N/2}\left(\alpha\bar{\alpha}\right)$ and $wSAM_p$ experiments. Indeed, while in windowless experiments all units are consecutive, we must insert observation windows between them in 1D experiments. We have chosen to keep rotor-synchronized rf cycles, hence leading to a sampling that is not rotor-synchronized. Fig.4.4 depicts the $wSAM_3$ pulse sequence as implemented on our spectrometer. SAM_3 modulation is then lasting $t_d = qT_R$ and a short time t_w (typically 5 to 8 μs, depending on the Larmor frequency, the console and the probe) is used to switch to acquisition mode, wait for probe dead time, acquire a few points and switch back to excitation mode.

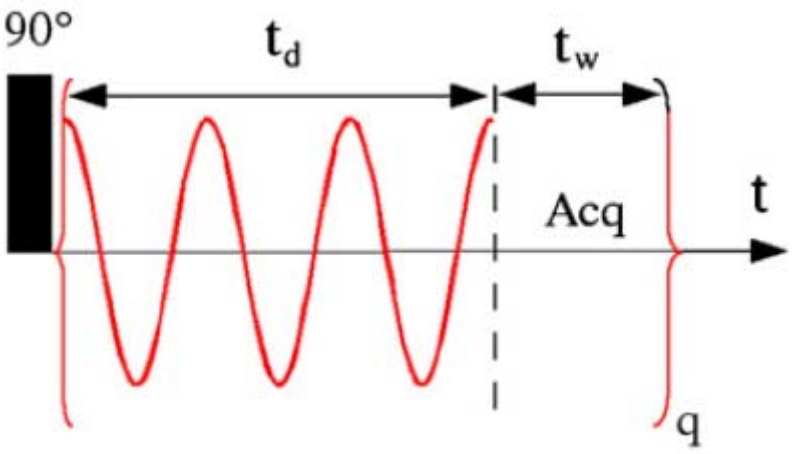

Fig.4.4 ^{1}H wSAM$_3$ pulse sequence. t_d is the time of the homo-nuclear decoupling period and t_w is that of the sampling window.

Another possibility could have been to truncate the $CN_n^{N/2}(\alpha\bar{\alpha})$ or SAM_p unit to make room for observation window: $t_d + t_w = qT_R$. But then the effective Hamiltonian does not satisfy the selection rules anymore meaning that homo-nuclear dipolar couplings are not averaged out. Moreover, it has been shown that since homo-nuclear dipolar interaction is active during acquisition windows, it is important that windows are not rotor synchronized so that related dephasings compensate each other for successive windows. Indeed, the timing of the windows must be chosen such that the integrals of the rotor-modulation functions for successive windows compensate each other. In this way, the dipolar interaction during these windows is averaged after a given number of acquisition points and, hence, is not accumulating.[16]

The experiments were performed at B_0 = 9.4 T on a wide-bore Bruker spectrometer with commercialized probe and amplifiers. With our 2.5 mm MAS probe and AVANCE-II console, we were able to decrease the 'dead time' to 5-6 μs, which is a classical value at 400 MHz. We have observed that the resolution weakly depends on the t_w value. Therefore, in

order to increase the S/N ratio, we have chosen to sample 32 points at 20 MHz over 1.6 μs to obtain one data point in each window, thus leading to a global window time t_w = 6.6-7.6 μs.

In practice, we generated cosine pulse line-shapes on Bruker Avance II spectrometer, using so called Bruker 'fast shape-pulse' with time resolution of 350 to 450 ns depending on the spinning speed. This proved to be sufficient at ν_R = 30kHz MAS, but would be too large at ultra-fast MAS speeds. As an example, with SAM_4 at ν_R = 80 kHz, the time required for the rf-field amplitude to increase from zero to the maximum peak value is only of 781 ns and thus the rf steps must be very short (e.g. 25-50 ns) to avoid any pulse transient and to obtain a smooth modulation.

We show results on commercial glycine and adamantane used without purification. We used restricted samples to increase the rf-homogeneity.

Fig.4.5 compares re-scaled spectra of glycine using MAS only and several optimized high-resolution sequences, $wC14_2^7(\alpha\bar{\alpha})$, $wSAM_{3.5}$ and $wPMLG5_{pp}^{\bar{xx}}$, recorded at ν_R = 31.74 kHz and also $wPMLG5_{pp}^{\bar{xx}}$ recorded at ν_R = 14.3 kHz. Even at ν_R = 31.74 kHz, the MAS spectrum only presents one main resonance with one shoulder (Fig.4.5a). The $wC14_2^7(\alpha\bar{\alpha})$ spectrum displays the three resonances corresponding either to the NH_3^+ (≈ 9 ppm) or to the CH_2 (≈ 3 and 4.5 ppm) (Fig.4.5b). However, a small zero peak appears at the carrier frequency (1 ppm). This zero-peak disappears when using a super-cycled sequence, which means changing the sign of the rf irradiation after every sampling period (Fig.4.5c). The disappearance of this zero-peak means that it cannot be an RRF line, and this peak may thus be related to pulse transients and/or to the fact the sequence does not correspond to a pure z-rotation. The same effect is observed with the $wSAM_{3.5}$ sequence (Fig.4.5d,e). We have also recorded $wPMLG5_{pp}^{\bar{xx}}$ spectra at ν_R = 31.74 kHz (Fig.4.5f) and ν_R = 14.3 kHz (Fig.4.5g). Both

spectra do not show zero peak, and they present nearly the same resolution, which means that this sequence may certainly be used at faster spinning speeds. By comparing spectra in Fig.4.5b-g, one observes that the resolution of CH_2 resonances is nearly identical in all spectra recorded at ν_R = 31.74 kHz (Fig.4.5b-f), but slightly better with wPMLG5$\bar{}^{xx}_{pp}$ recorded at 14.3 kHz (Fig.4.5g). Better resolved 1D spectra of glycine have been published with wPMLG5$\bar{}^{xx}_{mm}$, but they were recorded at B_0 = 14.1T,[22] and it must be kept in mind that the resolution is at least proportional to the magnetic field if we take into account truncation of the ^{1}H-^{1}H Hamiltonian due to chemical shift differences. Moreover, going to higher fields allows decreasing the window period.

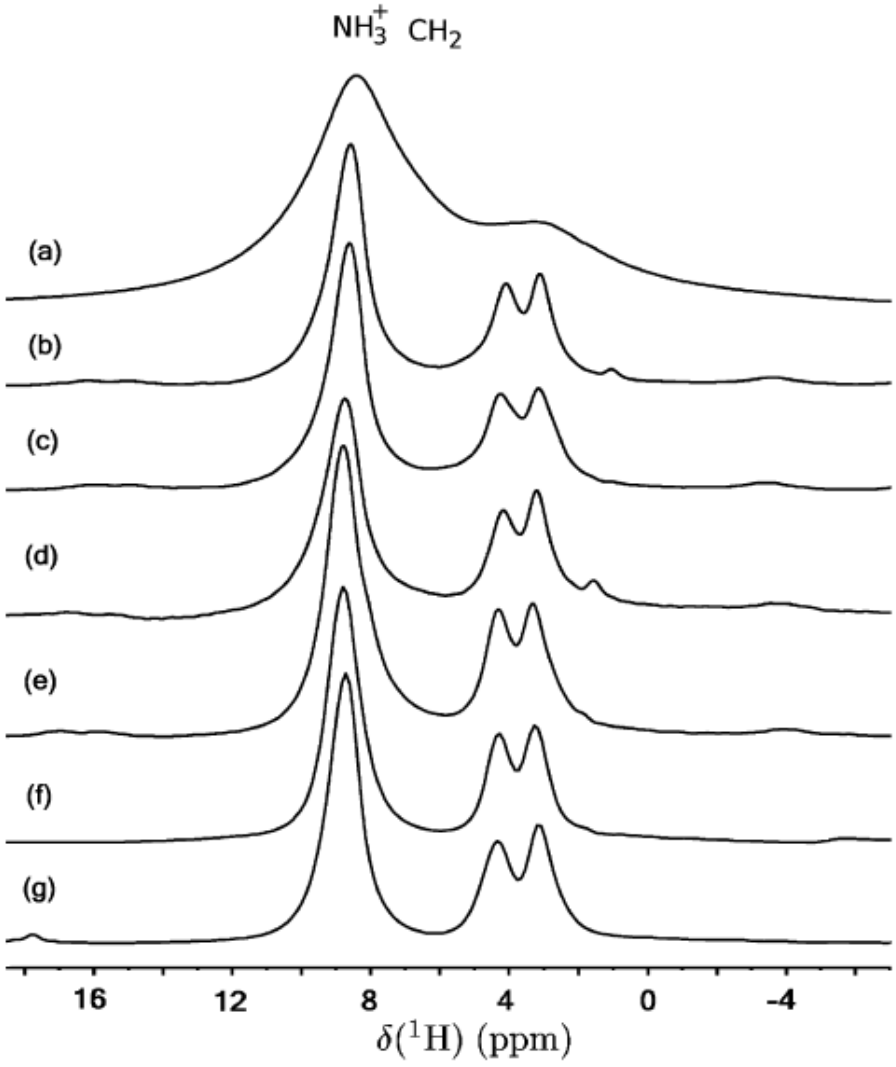

Fig.4.5 1D ^{1}H spectra of glycine at B_0 = 9.4 T. (a) one pulse MAS spectrum, (b) $wC14_2^7(\alpha\bar{\alpha})$, (c) super-cycled $wC14_2^7(\alpha\bar{\alpha})$, (d) $wSAM_{3.5}$, (e) super-cycled $wSAM_{3.5}$, (f,g) $wPMLG5_{pp}^{\bar{xx}}$. Spectra (b-g) have been rescaled : $\kappa \approx 0.70$ (b-e) and $\kappa \approx 0.46$ (f,g). ν_R = 31.74 (a-f) or 14.3 (g) kHz. t_w = 7.6 µs. ν_1 = 120 (b,c), 170 (f), 80 (g) kHz. ν_{1peak} = 140 kHz (d,e).

Synchronization requirements can be viewed on glycine in Fig.4.6. Keeping constant the spinning speed (ν_R = 31.74 kHz), SAM modulation frequency is altered quite significantly. The sampling window is introduced after every three (Fig.4.6a) or seven (Fig.4.6b) rf modulation periods. We observe the best resolution at the synchronization rule, which corresponds either to $\nu_{mod}/3 = \nu_R$, or in the time domain $t_d = T_R$, for $wSAM_3$ (Fig.4.6a),

or to $\nu_{mod}/3.5 = \nu_R$, or in the time domain $t_d = 2T_R$, for $wSAM_{3.5}$ (Fig.4.6b). These results and SIMPSON[31] simulations confirm that $wCN_n^{N/2}(\alpha\bar{\alpha})$ and $wSAM_p$ units must last multiple of T_R or $2T_R$, according to p or N/2n are integer or half-integer, respectively. However, as observed in Fig.4.6, this condition is not too narrow, which means that $wCN_n^{N/2}(\alpha\bar{\alpha})$ and $wSAM_p$ sequences are robust with respect to spinning speed stability.

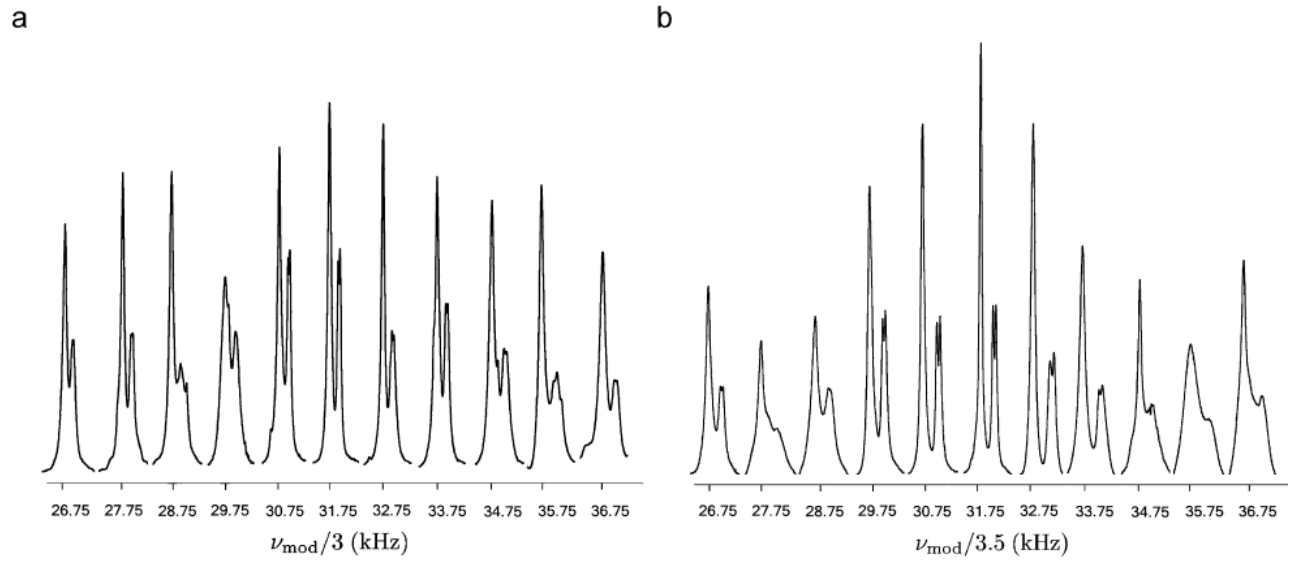

Fig.4.6 Glycine. ^{1}H wSAM spectra versus $\nu_{mod}/3$ (a) or $\nu_{mod}/3.5$ (b). $B_0 = 9.4$ T, $\nu_R = 31.74$ kHz, $\nu_{1peak} =$ 120 (a) or 140 (b) kHz, $t_d = 3/\nu_{mod}$ (a) or $7/\nu_{mod}$ (b), $t_w = 7.6$ µs.

We have tested on glycine several $wCN_n^{N/2}(\alpha\bar{\alpha})$ and $wSAM_p$ pulse sequences. $wC6_2^3(\alpha\bar{\alpha})$, $wC10_2^5(\alpha\bar{\alpha})$, $wSAM_{1.5}$ and $wSAM_{2.5}$ perform poorly as they are too close to the p = N/2n = 1 or 2 conditions that re-introduce CSA and dipolar interactions. Indeed, even if CSA and dipolar interactions are symmetry-forbidden at 1st-order AHT for $C6_2^3(\alpha\bar{\alpha})$, $C10_2^5(\alpha\bar{\alpha})$, $SAM_{1.5}$ and $SAM_{2.5}$ sequences, the magnitude of 2nd-order AHT terms is often increased in the vicinity of conditions which lead to finite first-order terms.[33] This means that homo- and hetero-nuclear dipolar interactions are partly re-introduced for these conditions. On the contrary, $wC16_3^8(\alpha\bar{\alpha})$, $wC6_1^3(\alpha\bar{\alpha})$, $wC14_2^7(\alpha\bar{\alpha})$, $wC8_1^4(\alpha\bar{\alpha})$, $SAM_{2.67}$, SAM_3, $SAM_{3.5}$

and SAM_4 performed similarly successfully. The only difference is that $wC16_3^8(\alpha\bar{\alpha})$ and $SAM_{2.67}$ minimum cycle spans over $3T_R$, and $wC14_2^7(\alpha\bar{\alpha})$ and $wSAM_{3.5}$ over $2T_R$, as compared to T_R for other sequences. However, optimal rf field value is proportional to N/2n (Eq.4.5) and p (Eq.4.6) and hence $wC6_1^3(\alpha\bar{\alpha})$ and $wSAM_3$ are the best compromise in terms of resolution, available spectral width ($SW = 1/(T_R + t_w)$ for $wSAM_3$ and $wSAM_4$, $SW = 1/(2T_R + t_w)$ for $SAM_{3.5}$ and $SW = 1/(3T_R + t_w)$ for $SAM_{2.67}$) and required rf field. It must be noted that the rf power leading to the optimal resolution in windowed $CN_n^{N/2}(\alpha\bar{\alpha})$ or SAM_p experiment is larger by a factor of $(1+t_w/t_d)$ than in the windowless experiment. The additional power seems to compensate for acquisition window times when no rf is sent.

4.4 Simulation

We have simulated with SIMPSON, optimized SAM_3 spectra, that could be obtained at ν_R = 65 kHz on a four-spin system. The SAM_3 spectrum, shown in Fig.4.7b, does not present any zero or image peak or RRF line. However, we have not introduced any pulse transient in the simulations, and it must be reminded that at this speed this hypothesis may only be approximated experimentally with a modern console using very fast electronics. By comparing $wSAM_3$ (Fig.4.7b) and MAS only (Fig.4.7a) spectra, one observes that the two resonances at 8.2 and 9.0 kHz, which are submitted to a moderate ^1H-^1H coupling and are already well resolved by MAS alone, are only slightly more resolved by SAM_3 decoupling. On the contrary, the two overlapping resonances at the same chemical shift (4 kHz), which are only partially narrowed by MAS alone, are much more narrow when using SAM_3 decoupling.

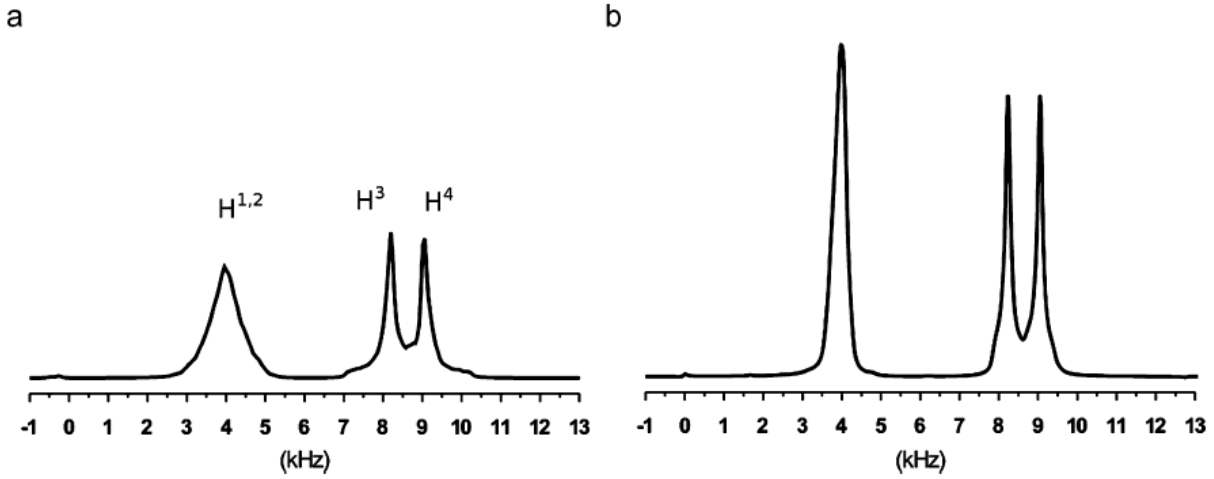

Fig.4.7 SIMPSON simulation of a four-spin system at ν_R = 65 kHz, and with REPULSION-320 and 15 gamma values powder averaging. The off-resonance frequencies of the protons are $\Delta\nu^{1,2}$ = 4 kHz, $\Delta\nu^3$ = 8.2 kHz, $\Delta\nu^4$ = 9 kHz. The carrier frequency is at 0 kHz. The dipolar coupling constants are $b_{1,2}$ = 30 kHz, $b_{1,3} = b_{1,4} = b_{2,3} = b_{2,4} = b_{3,4}$ = 10 kHz. (a) MAS spectrum. (b) wSAM$_3$ spectrum with $t_d = T_R$, t_w = 5 μs and ν_{1peak} = 240 kHz (to account for the window time). A line-broadening of 100 Hz has been introduced in the spectra.

4.5 Conclusions

We have shown that $CN_n^{N/2}(\alpha\bar{\alpha})$ and SAM$_p$ methods provide at ν_R = 30-65 kHz, enhanced ^{1}H resolution with respect to MAS only spectra. The best decoupling methods correspond to $C16_3^8(\alpha\bar{\alpha})$, $C6_1^3(\alpha\bar{\alpha})$, $C14_2^7(\alpha\bar{\alpha})$, $C8_1^4(\alpha\bar{\alpha})$, SAM$_{2.67}$, SAM$_3$, SAM$_{3.5}$ and SAM$_4$ schemes. These methods introduce very few false lines, provided the decoupling periods last qT$_R$ ($C6_1^3(\alpha\bar{\alpha})$, $C8_1^4(\alpha\bar{\alpha})$, SAM$_3$ or SAM$_4$), 2qT$_R$ ($C14_2^7(\alpha\bar{\alpha})$ or SAM$_{3.5}$), or 3qT$_R$ ($C16_3^8(\alpha\bar{\alpha})$ or SAM$_{2.67}$). Globally, $C6_1^3(\alpha\bar{\alpha})$ and SAM$_3$ seem the best compromise in terms of resolution, available spectral width and required rf-field. It has also been shown that the spinning speed stability is not an issue with these methods. It is remarkable that $CN_n^{N/2}$ and SAM$_p$ optimization is straightforward, and this is certainly related to the fact these sequences are rotor-synchronized (t_d = qT$_R$, 2qT$_R$ or 3qT$_R$). $CN_n^{N/2}(\alpha\bar{\alpha})$ method can be adapted to all

spectrometers, but SAM_p requires at ultra fast MAS a console with fast electronics that must be able to define the cosine line-shape without transients. Moreover, as all other ^1H high-resolution methods, $CN_n^{N/2}(\alpha\bar{\alpha})$ and SAM_p necessitate efficient NMR probe which generates large and homogeneous rf field over the sample. A very recent article has shown that $PMLGn_{mm}^{\bar{x}x}$ and zDUMBO sequences could also be used at ultra-fast MAS (ν_R = 65 kHz), with a rotor period shorter than the rf cycle time.[32] Following these results, it appears that the main advantage of $CN_n^{N/2}(\alpha\bar{\alpha})$ and SAMp over $PMLGn_{mm}^{\bar{x}x}$ and zDUMBO may be the much weaker rf-power required by the first methods: e.g. the rms rf-value required by $SAM_{2.67}$ is only 2.17 times the spinning speed (Eq.4.6). This may be a decisive advantage at ultra-fast spinning speeds (ν_R = 65-70 kHz). However, a detailed comparison of all present 1D methods with z-rotation ($CN_n^{N/2}(\alpha\bar{\alpha})$, SAM_p, zDUMBO and $PMLGn_{mm}^{\bar{x}x}$) is still to be done versus magnetic field (B_0 = 9.4-23.5 T) and spinning speed (ν_R = 10-70 kHz) in terms of resolution, robustness, and required rf-power.

At last, it should be pointed out that SAM is rotor-synchronized decoupling sequence while PMLG and DUMBO are not. Rotor-synchronized decoupling sequence is very important for t_1 dimension, because we always need to rotor synchronize t_1 dimension in 2D experiment under MAS condition, and SAM will be very useful in DQ-SQ experiment which will be described in the next chapter.

References

1. A.E. McDermott, F.J. Creuzet, A.C. Kolbert, R.G. Griffin, High-resolution magic-angle-spinning NMR spectra of protons in deuterated solids, *J. Magn. Reson.* 98 (1992) 408-413.

2. B.J. vanRossum, G.J. Boender, H.J.M. deGroot, High magnetic field for enhanced proton resolution in high-speed CP/MAS heteronuclear ^{1}H–^{13}C dipolar-correlation spectroscopy, *J. Magn. Reson*. 120 (1996) 274-277.

3. M. Lee, W.I. Goldburg, Nuclear magnetic resonance line narrowing by rotating rf fields, *Phys. Rev. A* 140 (1965) 1261-1271.

4. B.C. Gerstein, R.G. Pembleton, R.C. Wilson, L.M. Ryan, High resolution NMR in randomly oriented solids with homonuclear dipolar broadening: combined multiple pulse NMR and magic angle spinning, *J. Chem. Phys*. 66 (1977) 361-362.

5. J.S. Waugh, L.H. Hubert, U. Haeberlen, Approach to high resolution NMR in solids, *Phys. Rev. Lett.* 20 (1968) 180-183.

6. W.K. Rhim, D.D. Elleman, R.W. Vaughan, Enhanced resolution for solid state NMR, *J. Chem. Phys.* 58 (1973) 1772-1773; Analysis of multiple pulse NMR in solids, *J. Chem. Phys.* 59 (1973) 3740-3749.

7. D.P. Burum, W.K. Rhim, Analysis of multiple pulse NMR in solids III, *J. Chem. Phys.* 71 (1979) 944-956.

8. D.P. Burum, M. Linder, R.R. Ernst, Lower-power multiple line narrowing in solid-state NMR, *J. Magn. Reson*. 44 (1981) 173-188;

9. M. Howhy, P.V. Bower, H.J. Jakobsen, N.C. Nielsen, A high-order and broadband CRAMPS experiment using z-rotational decoupling, *Chem. Phys. Lett*. 273 (1997) 297-303.

10. D. Sakellariou, A. Lesage, P. Hodgkinson, L. Emsley, Homonuclear dipolar decoupling in solid-state NMR using continuous phase modulation, *Chem. Phys. Lett*. 319 (2000)

253-260.

11. B. Elena, G. de Paepe, L. Emsley, Direct spectral optimisation of proton-proton homonuclear dipolar decoupling in solid-state NMR, *Chem. Phys. Lett*. 398 (2004) 532-538.
12. E. Vinogradov, P.K. Madhu, S. Vega, High-resolution proton solid-state NMR spectroscopy by phase-modulated Lee-Goldburg experiment, *Chem. Phys. Lett.* 314 (1999) 443-450.
13. M. Mehring, J.S. Waugh, Magic-Angle NMR experiments in solids, *Phys. Rev*. B5 (1972) 3459-3471.
14. A. Bielecki, A.C. Kolbert, M.H. Levitt, Frequency-switched pulse sequences: homonuclear decoupling and dilute spin NMR in solids, *Chem. Phys. Lett.* 155 (1989) 341-346.
15. M.H. Levitt, A.C. Kolbert, A. Bielecki, D.J. Ruben, Proton line-narrowing in solids with frequency-switched pulse sequences, *Solid State NMR*. 2 (1993) 151-163.
16. S. Hafner, H.W. Spiess, Multiple-pulse assisted line-narrowing by fast magic-angle spinning, *Solid state NMR*. 8 (1997) 17-24.
17. P.K. Madhu, X. Zhao, M.H. Levitt, High-resolution ^{1}H NMR in the solid state using symmetry-based pulse sequences, *Chem. Phys. Lett*. 346 (2001) 142-148; S. Paul, R.S. Thakur, P.K. Madhu, ^{1}H homonuclear dipolar decoupling at high magic-angle spinning frequencies with rotor-synchronized symmetry sequences, *Chem. Phys. Lett*, in press.
18. A. Brinkmann, M. Eden, M.H. Levitt, Synchronous helical pulse sequences in magic-angle spinning nuclear magnetic resonance : Double quantum recoupling of multiple-spin systems, *J. Chem. Phys.* 112 (2000) 8539-8554.
19. M. Leskes, P.K. Madhu, S. Vega, Proton line narrowing in solid-state nuclear magnetic resonance: new insights from windowed phase-modulated Lee-Goldburg sequence, *J.*

Chem. Phys. 125 (2006) 124506.

20. L. Bosman, P.K. Madhu, S. Vega, E. Vinigradov, Improvement of homonuclear dipolar decoupling sequences in solid-state nuclear magnetic resonance utilising radio frequency imperfections, *J. Magn. Reson.* 169 (2004) 39-48.
21. A. Vega, Controlling the effects of pulse transients and RF inhomogeneity in phase-modulated multiple-pulse sequences for homonuclear decoupling in solid-state proton NMR, *J. Magn. Reson.* 170 (2004) 22-41.
22. M. Leskes, P.K. Madhu, S. Vega, A broad-banded z-rotation windowed phase-modulated Lee-Goldburg pulse sequence for ^{1}H spectroscopy in solid-state NMR, *Chem. Phys. Lett.* 447 (2007) 370-374.
23. E.K. Paulson, C.R. Morcombe, V. Gaponenko, B. Dancheck, R.A. Byrd, K.W. Zilm, Sensitive high-resolution inverse detection NMR spectroscopy of proteins in the solid state, *J. Am. Chem. Soc*. 125 (2003) 15831-15836.
24. V. Agarwal, A. Diehl, N. Skrynnkov, B. Reif, High-resolution ^{1}H detected ^{1}H, ^{13}C correlation spectra in MAS solid-state NMR using deuterated proteins with selective ^{1}H, ^{2}H isotopic labelling of methyl groups, *J. Am. Chem. Soc*. 128 (2006) 12620-12621.
25. Y. Ishii, J.P. Yesinowski, R. Tycko, Sensitivity enhancement in solid-state ^{13}C NMR of synthetic polymers and biopolymers by ^{1}H NMR detection with high-speed magic angle spinning, *J. Am. Chem. Soc*. 123 (2001) 2921-2922.
26. D.H. Zhou, G. Shah, M. Cormos, C. Mullen, D. Sandoz, C.M. Rienstra, Proton-detected solid-state NMR spectroscopy of fully protonated proteins at 40 kHz magic-angle spinning, *J. Am. Chem. Soc*. 129 (2007) 11791-11801.
27. E. Vinogradov, P.K. Madhu, S. Vega, Strategies for high-resolution proton spectroscopy in solid-state NMR, *Top. Curr. Chem.* 246 (2004) 33-90.
28. O. Lafon, B. Hu, Q. Wang, J. Trebosc, J.P. Amoureux, to be submitted.

29. R. Fu, S.A. Smith, G. Bodenhausen, Recoupling of heteronuclear dipolar interactions in solid-state MAS NMR by simultaneous frequency and amplitude modulation, *Chem. Phys. Lett.* 272 (1997) 361-369.

30. B. Hu, J. Trebosc, J.P. Amoureux, Comparison of several hetero-nuclear dipolar recoupling NMR methods to be used in MAS HMQC/HSQC, *J. Magn. Reson*. In press.

31. M. Baks, J.T. Rasmussen, N.C. Nielsen, *J. Magn. Reson*. 147 (2000) 296.

32. M. Leskes, S. Steuernagel, D. Schneider, P.K. Madhu and S. Vega, Homonuclear dipolar decoupling at magic-angle spinning frequencies up to 65 kHz in solid-state nuclear magnetic resonance, *Chem. Phys. Lett.* 466 (2008), 95–99.

33. A. Brinkmann, M. Eden, *J. Chem. Phys.* 120(2004),11726.

Chapter 5. Double-quantum spectroscopy

Many applications of solid-state Nuclear Magnetic Resonance (NMR) to molecular structure determination are based on dipole-dipole couplings between nuclei since they encode important information on the spatial proximity of atoms through their dependence on the inverse cube of the inter-nuclear distance. A wide variety of dipolar recoupling methods exist for the exploitation of dipole-dipole couplings in the presence of magic-angle spinning (MAS). A particularly important class of recoupling techniques restores the dipole-dipole coupling between spins of the same isotopic type.[1-4] Such homonuclear dipolar recoupling methods may be classified according to the rotational spin rank of the recoupled dipolar Hamiltonian. In particular, double-quantum (DQ) homonuclear recoupling has a number of important applications, including suppression of signals from isolated spins,[5] two-dimensional DQ-SQ correlation spectroscopy,[6-10] high-order multiple-quantum excitation in solids,[11] and the estimation of inter-nuclear distances[12] and torsional angles.[13]

The focus here is on DQ homonuclear recoupling of ^{1}H nuclei, which are increasingly exploited in the solid state because of the high sensitivity and the high natural abundance of this isotope.[8-10] Furthermore, the efficiency of current homonuclear decoupling sequences precludes the use of small ^{1}H-^{1}H J couplings (typically less than 10 Hz whereas the ^{1}H line-widths span hundreds of Hz) to create DQ coherences (DQC).

The ^{1}H DQ homonuclear recoupling sequences that have been mostly used so far are the BAck to BAck (BABA),[14,15] and the (CN_n^ν, RN_n^ν) symmetry-based[16,17] schemes. For slow spinning speeds ($\nu_R \leq$ 15-20 kHz), POST-C7,[18,19] $C9_1^4$,[9] $R14_2^6$[20] and SR26[21] sequences can be used. However, the required rf-field amplitude is proportional to the spinning speed for symmetry-based sequences, e.g. $\nu_1 = 9\nu_R$ for $C9_1^4$, which means that these sequences are hardly usable at fast MAS speeds, due to probe rf-limitations.

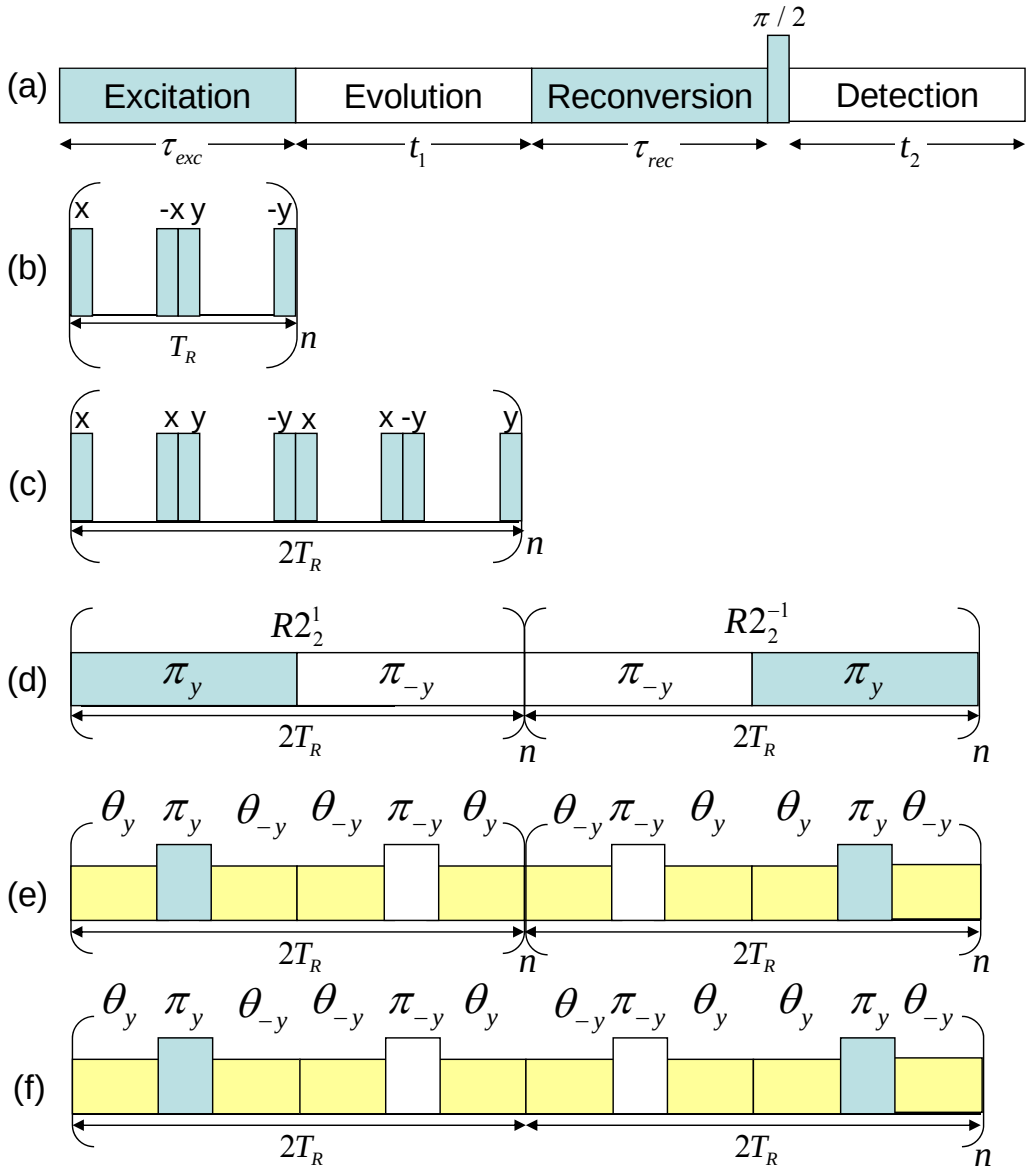

Fig.5.1. (a) General scheme of DQ experiments. Following are pulse sequences for SQ ↔ DQ excitation or reconversion: (b) BABA-1, (c) BABA-2, (d) super-cycled version of $R2_2^1(\pi)$, (e) SPIP and (f) SPIP. BABA sequences use π/2 pulses. The basic SPIP or SPIP' element lasts one T_R and consists in one π pulse sandwiched by the two spin-lock parts (θ_y and θ_{-y}). The super-cycling can be performed in two ways: (e) SPIP consists of n blocks of $2T_R$ each belonging to $R2_2^1$ symmetry class followed by n blocks of $2T_R$ each, belonging to $R2_2^{-1}$ symmetry class; (f) SPIP' consists of n blocks of $4T_R$ each belonging to $R2_2^1 R2_2^{-1}$.

BABA[14,15,22] sequence has been to date the method of choice for ^{1}H DQ recoupling at fast or ultra-fast MAS frequencies (ν_R > 30 kHz). The original BABA sequence,[14] denoted BABA-1 in this article, spans over one rotor period and consists of two evolution periods bracketed by two 90° pulses (see **Fig.5.1b**). BABA-1 has a short cycle time but it is very sensitive to resonance offsets and chemical shift anisotropy (CSA). Partial compensation of these unwanted interactions can be achieved by super-cycling pulse phases over two rotor periods, as shown in **Fig.5.1c**. This variant, denoted BABA-2, display a higher robustness with respect to resonance offsets than BABA-1. However, the performance of BABA sequences is relatively poor in cases of large chemical shift differences. This precludes the observation of DQ-SQ correlations between ^{1}H nuclei at high static magnetic field (see **Fig.5.7**). In addition, in between the pulses, the proton magnetization is submitted to losses due to flip-flop terms (T'_2), which can lead to a large signal decrease. Last, in the case of strong ^{1}H-^{1}H interactions and slow or moderate spinning speeds, the magnitude of dipole-dipole interactions recoupled by both BABA sequences is too large compared to their cycle times, T_R or $2T_R$. In other words, the build up of DQC is too fast compared to the minimal sampling period of the recoupling intervals. This results in abrupt variations in the double-quantum efficiency as function of the recoupling intervals and in a reduction in the double-quantum-filtered signal amplitude (see **Fig.5.2**).

To solve these three problem, we propose a new robust and efficient pulse sequence that does not need large rf power and can be used for broadband DQ NMR spectroscopy in rotating solids, at both moderate and fast MAS speeds.

5.1. Theory and simulations

An ideal DQ recoupling sequence should have the following characteristics: (i) the double quantum efficiency should be as large as possible; (ii) the sequence should be usable at high spinning frequencies, in order to ensure high spectral resolution and sensitivity and to minimize spinning sidebands generated by CSA; (iii) the sequence should have minimal dependence on isotropic and anisotropic shielding; (iv) the rf field requirement should be compatible with usual probe specifications; and (v) the

magnitude of recoupled dipole-dipole interactions should be much lower than the maximal sampling frequency of the recoupling intervals.

(1). Symmetry-based recoupling

The design of recoupling pulse sequences is facilitated by the use of symmetry theory.[16,17] The new pulse sequence is originated from the $R2_2^1(\pi)$ symmetry -based sequence,[16,23,24] which is composed of a series of π pulses, each occupying one whole rotor period with the phase of adjacent pulses being shifted by π. One of its super-cycled version is represented in **Fig.5.1d**. Considering solely the homonuclear dipolar coupling between two like spins *j* and *k*, the $R2_2^1(\pi)$ sequence, based on these continuous π-pulses, corresponds to the following zero-order average Hamiltonian:[23]

$$\bar{H}_{R2_2^1} = b_{jk} f(\beta,\gamma)\{I_j^+ I_k^- + I_j^- I_k^+ - 4I_{jz}I_{kz} + I_j^+ I_k^+ + I_j^- I_k^-\} \qquad (5.1)$$

where b_{jk} is the dipolar coupling constant and $f(\beta,\gamma) = 3\sin 2\beta.\cos\gamma/(16\sqrt{2})$ is a function of the Euler angles, β and γ, randomly distributed in a powder, relating the inter-nuclear vector to the rotor frame. Consequently, the magnitude of the recoupled interaction depends on the Euler angle γ and the $R2_2^1$ sequence is not γ-encoded and hence the evolution time t_1 must be an integer multiple of rotor periods (T_R). In this respect, the $R2_2^1$ recoupling method is similar to BABA schemes. Moreover, it can be seen in Eq.5.1 that $R2_2^1$ sequence can excite both zero- and double-quantum coherences from longitudinal polarization. However, only the DQ part of this Hamiltonian is involved in DQ recoupling.

(2). Basic element

Besides the homonuclear dipolar coupling terms, the zero-order average Hamiltonian corresponding to $RM_M^{M/2}$ sequences also contains isotropic chemical shift (offset) and

CSA terms having spin quantum numbers $\{\lambda, \mu\} = \{1, \pm 1\}$. The sensitivity to offset irradiation can be decreased by increasing the rf amplitude. To that end, the original basic element, a soft continuous π pulse, was replaced by a strong rotor-synchronized π pulse (see **Fig.5.1e**), as previously done in HORROR recoupling.[25] Furthermore, it is well-known that spin-locking allows decreasing the effect of offset if the spin-lock field is sufficient. Therefore, two compensated spin-lock periods were added, one on each side of the central π pulse. Finally, the basic inversion element of the $R2_2^1$ sequence we used corresponds to a $\theta_y \pi_y \theta_{-y}$ composite pulse that provides a rotation of π about the rotating-frame y-axis. The resulting pulse sequence is denoted $R2_2^1(\theta_y \pi_y \theta_{-y})$. As $R2_2^1(\pi)$ and $R2_2^1(\theta_y \pi_y \theta_{-y})$ sequences belong to the same symmetry class, the symmetry allowed and forbidden terms are the same but differ in magnitude. In the case of $R2_2^1(\theta_y \pi_y \theta_{-y})$ sequence, the scaling factor depends on the π pulse length as well as the θ value.

(3). Super-cycle

The unwanted offset and CSA terms can be further suppressed in the zero-order average Hamiltonian by applying a super-cycle. In the same way as for DQ recoupling between quadrupolar nuclei **(Fig.5.1d)**,[23,26] we have chosen a super-cycle constructed by applying an overall phase shift of π from the middle of the recoupling sequence (see **Fig.5.1e**). For simplicity reasons, this sequence has been called Sandwiched PI Pulse (SPIP). The 2Q phase super-cycle eliminates the offset and CSA terms in the zero-order average Hamiltonian. As already observed in the case of quadrupolar nuclei,[23] SPIP recoupling scheme leads to better performance than the sequence displayed in **Fig.5.1f**, hereafter denoted SPIP'. The zero-order average Hamiltonian of SPIP contains ZQ and DQ homonuclear dipolar couplings as well as homonuclear *J* coupling. Contrary to the two previously published methods,[23,26] the $R2_2^1$-based irradiation was not sandwiched by two bracketing π/2 pulses. Indeed, bracketing the

sequence described in **Fig.5.1e** leads to a doubling of the double-quantum part of the zero-order average Hamiltonian (Eq.5.1).[23] This doubling has two negative effects: (i) it divides by two the optimum contact times, which may be a limitation when spinning slowly, and (ii) it increases largely the sensitivity to offset irradiation (see **Fig.5.5**).

(4). 1D DQ-filtered experiment and 2D DQ-SQ spectroscopy

The performances of SPIP sequence were tested by incorporating such recoupling in one-dimensional (1D) DQ-filtered experiments as well as 2D DQ-SQ sequence.

The 1D DQ-filtered sequence corresponds to the scheme of **Fig. 5.1a** when $t_1 = 0$. A DQ recoupling sequence is applied for an interval τ_{exc} in order to transform the longitudinal magnetization into DQC. A second recoupling period of duration τ_{rec} followed by $\pi/2$ pulse transforms the DQCs into observable transverse magnetization. Signals passing through DQCs are selected by a four-step phase cycle of the pulses used for exciting or reconverting the DQCs. This is called double-quantum filtering (DQF).[10] The build-up of DQCs may be estimated by acquiring DQ-filtered NMR signals as function of the intervals τ_{exc} and τ_{rec}. Different protocols can be used.[10,27,28] In the following, we will only describe the results obtained with the symmetric protocol, i.e. the two intervals τ_{exc} and τ_{rec} are both incremented but kept equal to each other : $\tau = \tau_{exc} = \tau_{rec}$. Nevertheless SPIP recoupling can also be used in DQF experiments with unequal recoupling times.

Although DQF experiments are useful to test the efficiency and the robustness of the SPIP recoupling, they only allow determining whether a spin species is subject to dipole-dipole couplings, but the identity of the other spins involved in the couplings remains unknown. In order to identify the two spin species forming a dipolar-coupled pair, the DQF experiment has to be extended to a 2D version. A commonly employed approach is 2D DQ-SQ spectroscopy. This sequence derives from 1D DQF experiment by inserting an incremented time period t_1 between the excitation and reconversion recoupling intervals, as depicted in **Fig. 5.1a**. Hence, the evolution of DQCs in t_1 is correlated with that of single-quantum coherences (SQC) in t_2 and the resulting 2D

spectra display DQ-SQ correlations. In a 2D DQ-SQ spectrum, the spins that are alike and close in space result in diagonal peaks with a slope of 2, and a pair of unlike spins results in a pair of cross-peaks at the sum of the two SQ frequencies along the DQ dimension. For instance, two unlike spins with SQ frequencies of ν_A and ν_B will give rise to two cross-peaks at a DQ frequency of $\nu_A + \nu_B$. The intensity of the cross-peaks is an indication of the strength of the dipolar coupling between the spins and in turn of the inter-nuclear distance. Applications of ^{1}H DQ spectroscopy in various systems have proved the utility of this approach.[6-8]

(5). Numerical simulations

In preparation for the experiments, we performed simulations with the SIMPSON software,[29] and the powder averaging was performed using 320 crystallites following the REPULSION algorithm.[30] Spinning speed, chemical shifts, dipolar couplings and rf and static fields are specified in the figure captions. From **Fig.5.2** to **Fig.5.5**, the vertical axes show the calculated DQF efficiencies defined as the ratio of the integral of DQ filtered spectra to the integral of 1D spectrum obtained after $\pi/2$-pulse excitation.[31] For simulations shown from **Fig.5.2** to **Fig.5.4**, the spin system consists of two protons with the same chemical shift. In these cases, the recoupling sequences were applied on-resonance.

Fig.5.2 compares the build-up of DQF efficiencies as a function of the excitation/reconversion time τ for three DQ recoupling schemes (BABA-1, BABA-2 and SPIP) incorporated in a DQF experiment at ν_R = 30 kHz. The dipolar coupling constant between the two protons was varied from b_{12} = –5 kHz to –25 kHz. It must be reminded that the τ values can only be multiples of 33 μs (T_R: BABA-1), 67 μs ($2T_R$: BABA-2), or 133 μs ($4T_R$: SPIP) (see **Fig.5.1**). At this speed, the maximum BABA efficiencies (≈ 25%) are only accessible for moderate dipolar interactions: $b_{12} \approx$ –17 kHz (BABA-1) or $b_{12} \approx$ –9 kHz (BABA-2) (**Fig.5.2a,b**). It must be noted that BABA-2 sequence appears more 'robust' than BABA-1 scheme, in the sense that the DQF efficiencies decrease more slowly than those of BABA-1 for recoupling times longer

than the optimum value. Therefore, the efficiency of BABA-2 can be larger at slower spinning speeds than that of BABA-1. However, experimentally, this advantage of BABA-2 may be counterbalanced by larger T'_2 losses since the maxima in DQF efficiencies are reached for twice longer recoupling times in the case of BABA-2 as compared to BABA-1. On the contrary, we obtain the same optimum efficiency (≈ 25%), but for much longer recoupling times with SPIP sequence **(Fig.5.2c)**, which means an easy setting up, even with slow spinning speeds. Actually, this advantage is due to the small scaling factor of the homonuclear dipolar interaction when $\theta_y\pi_y\theta_{-y}$ pulse is used as basic element. Furthermore, as SPIP is a windowless sequence, the irreversible losses during the long recoupling times arise only from $T_{1\rho}$ losses, which are smaller than T'_2 losses affecting BABA experiments. It must be mentioned that SPIP is only weakly sensitive to CSA. The maximum efficiency of SPIP (≈ 25%), is much smaller than that accessible with γ-encoded sequences, such as POST-C7 (≈ 70%).[18,19] However, it must be reminded that these sequences are not usable at fast MAS speeds ($\nu_R \geq$ 15-20 kHz), as opposed to SPIP.

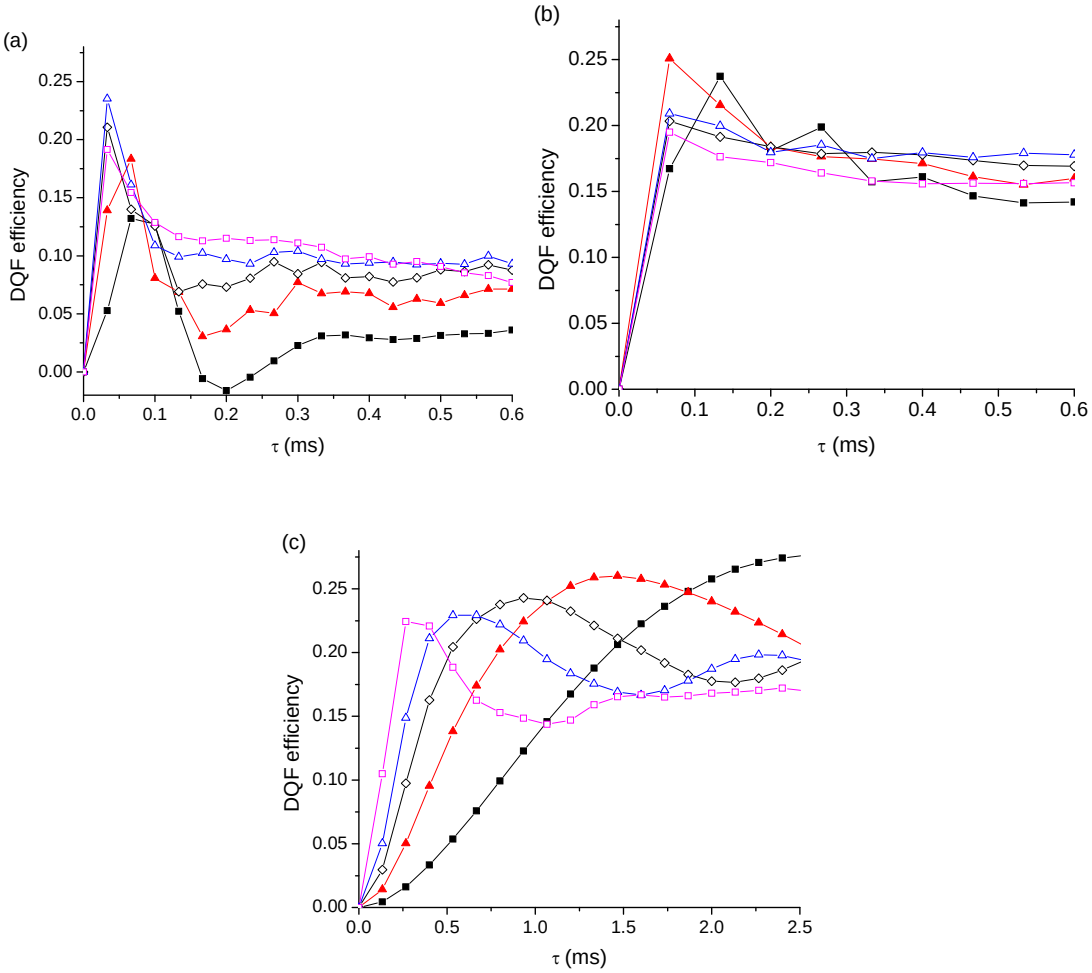

Fig.5.2. Calculated DQF efficiency as function of τ, for DQF experiment with different DQ recoupling schemes: (a) BABA-1 ($\tau = nT_R$), (b) BABA-2 ($\tau = 2nT_R$), (c) SPIP ($\tau = 4nT_R$). The spin system consists of two protons with the same chemical shift and the dipolar coupling constant between them is b_{12} = 5 (■), 9 (▲), 13 (◊), 17 (Δ), 25 (□) kHz. The recoupling sequences were applied on-resonance at ν_R = 30 kHz. For BABA-1 and BABA-2, the rf nutation frequency is ν_1 = 100 kHz, while for SPIP it is equal to $\nu_{1\pi}$ = 67.5 kHz for the central π pulse, and ν_{1SL} = 62 kHz for the spin-locking pulses. CSA of the two spins is equal to 4.4 kHz (η = 0.8) and 11.2 kHz (η = 0).

In **Fig.5.3** we have represented the DQF efficiency as function of τ for several amplitudes $\nu_{1\pi}$ of the central π pulses in SPIP recoupling, and for two spinning speeds: ν_R = 30 **(Fig.5.3a)** and 65 **(Fig.5.3b)** kHz. The maximum intensity first starts to increase with weak $\nu_{1\pi}$ values, and then becomes approximately constant as long as the π pulse amplitude is approximately at least twice the spinning speed.

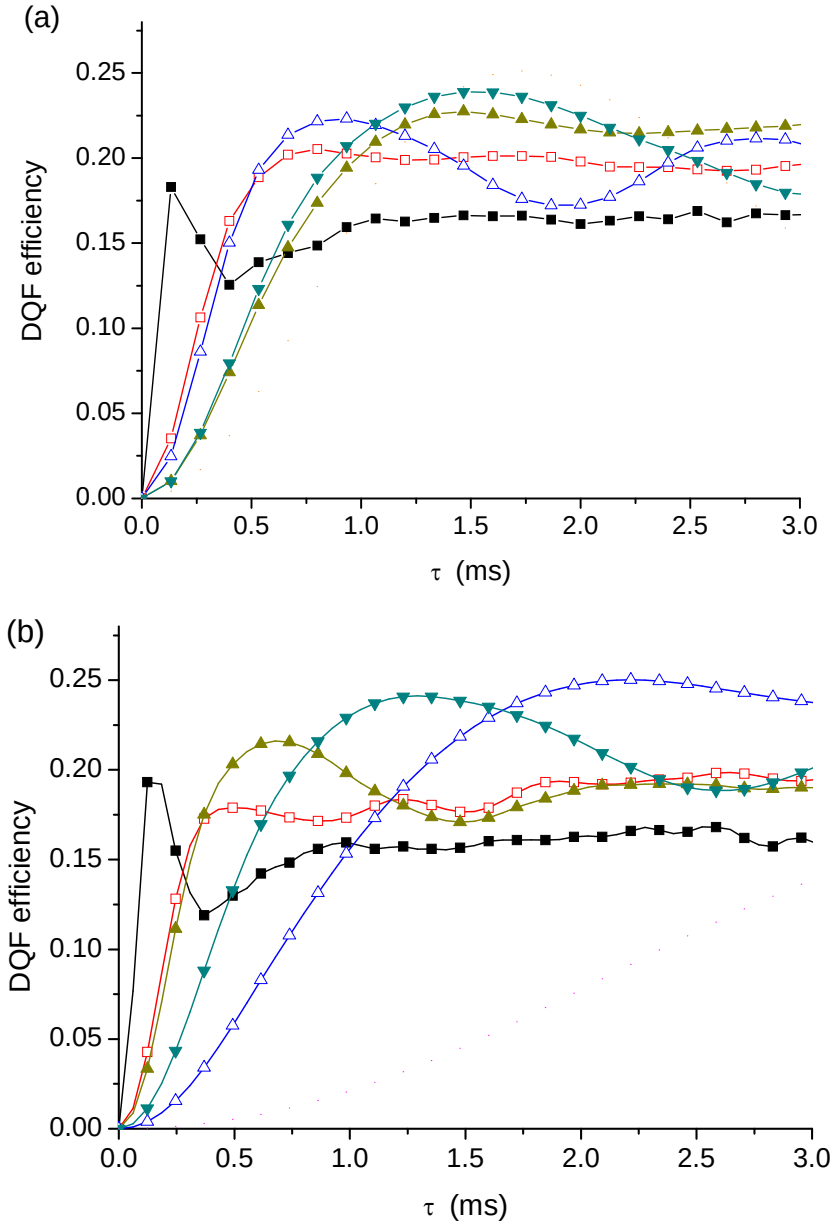

Fig.5.3. Calculated DQF efficiency as function of τ for DQF experiment with SPIP recoupling at two MAS speeds and varying the rf nutation frequency of the π-pulse : (a) ν_R = 30 kHz and $\nu_{1\pi}$= 45 (■), 60 (□), 75 (▲), 90 (Δ), and 105 (▼) kHz; (b) ν_R = 65 kHz and $\nu_{1\pi}$= 90 (■), 120 (□), 150 (▲), 180 (Δ), and 210 (▼) kHz. The spin system consists of two protons with the same chemical shift and the dipolar coupling constant between them is b_{12} = 11 kHz. The recoupling sequence is applied on-resonance and the rf nutation frequency for the spin locking pulses is fixed to ν_{1SL}= 0.7$\nu_{1\pi}$. CSA of the two spins is equal to 4.4 kHz (η = 0.8) and 11.2 kHz (η = 0).

In **Fig. 5.4**, we have represented the intensity of the spectra of the previous on-resonance two spin system with SPIP (**Fig. 5.1e** : two blocks lasting $2nT_R$ each) or SPIP' (**Fig. 5.1f** : n blocks lasting $2T_R$ each). These simulations show that SPIP

sequence **(Fig. 5.1e)** is much more efficient and much less CSA dependent than the SPIP' variant described in **Fig. 5.1f**. At large magnetic fields, this is important for ^{1}H and critical for nuclei experiencing large CSA, such as ^{31}P. This better robustness of SPIP recoupling as compared to SPIP' has been verified experimentally (not shown). Therefore, in the following, we will not consider the SPIP' sequence described in **Fig. 5.1f**.

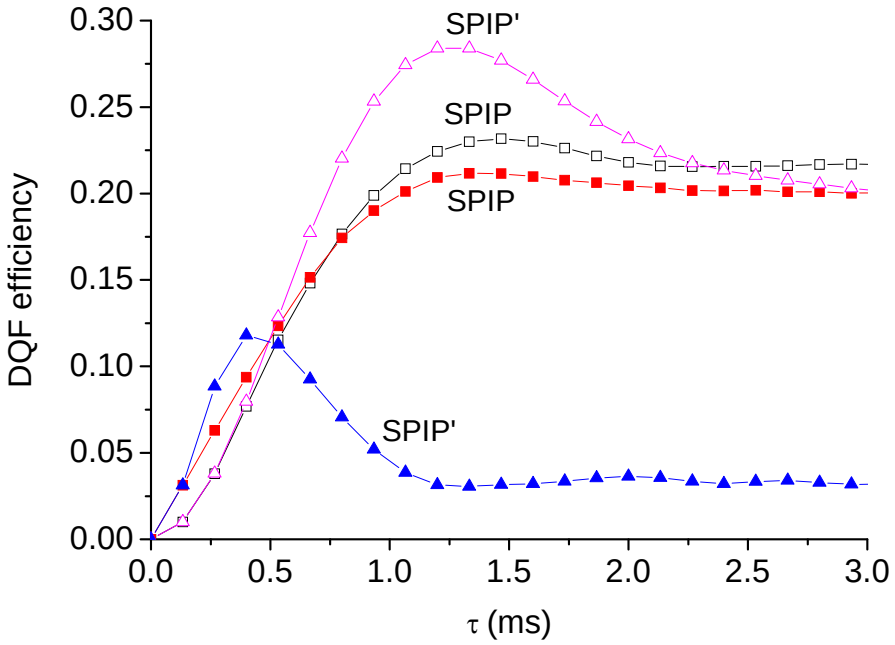

Fig.5.4. Calculated intensity of an on-resonance two spin-system versus τ, with b_{12} = 11 kHz, ν_R = 30 kHz. $\nu_{1\pi}$ = 75 kHz, ν_{1SL} = 52.5 kHz. The sequences are either that of **Fig.5.1e** (SPIP: squares) or that of **Fig.5.1f** (SPIP': triangles). A CSA has been introduced in the calculations: either 8 kHz (hollow) or 24 kHz (solid).

Fig.5.5 shows the calculated dependence of DQF efficiency as function of resonance offset for five recoupling sequences, BABA-1, BABA-2, SPIP and two of its variants: with either no spin-lock periods ($SPIP_{NSL}$) or with two bracketing 90° pulses ($SPIP_{BP}$) as in references (**23,26**). The simulations were performed for a spin system containing three protons and spinning at ν_R = 30 kHz. It may be observed that BABA-1, $SPIP_{NSL}$ and especially $SPIP_{BP}$ are quite sensitive to offset effects as opposed to the two other methods. BABA-2 is more sensitive to offsets and less efficient than SPIP. The difference in sensitivity would increase when taking into account irreversible

losses since they are more important for BABA-2 (T'_2) than for SPIP ($T_{1\rho}$). It must also be noted that the SPIP recoupling time leading to maximal DQF efficiency are seven times much longer with the spin lock periods (τ^{opt} = 933µs) than without (τ^{opt} = 133µs). This means that the scaling factor is c.a. seven times smaller in the first case than in the second case due to the change of the basic elements.

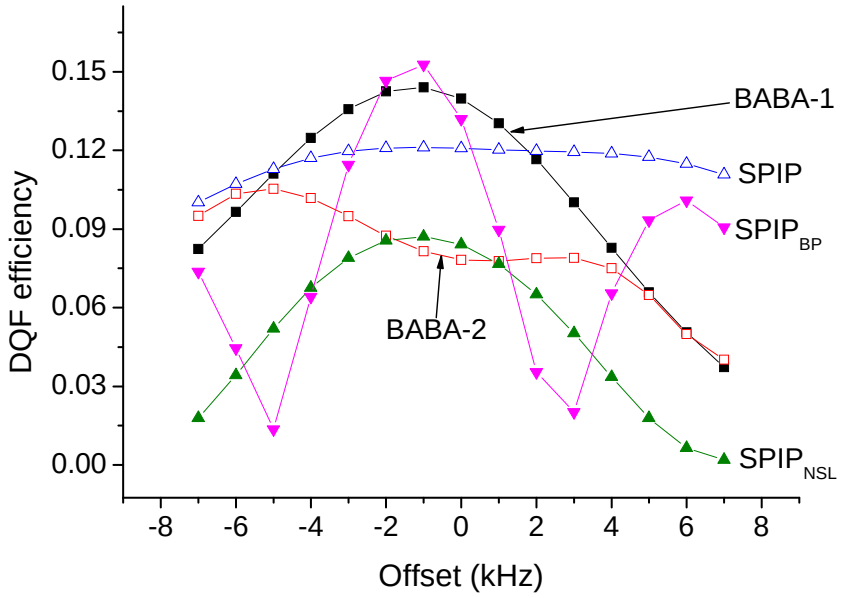

Fig.5.5. Calculated intensity of nucleus 1 in a three spin-system versus offset of this nucleus. Chemical shifts of nuclei 2 and 3 are at +2 and -3 kHz from that of nucleus 1. ν_R = 30 kHz, b_{12} = 11 kHz, b_{13} = 6.63 kHz, b_{23} = 6.75 kHz. BABA-1 (■, τ = 33.3µs), BABA-2 (□, τ = 66.6µs), SPIP (Δ, τ = 933µs), $SPIP_{NSL}$ (▲, τ = 133µs) and $SPIP_{BP}$ (▼, τ = 533µs). CSA (kHz)/η = 4.4/0.8, 11.2/0.58, 0/0 for nuclei 1, 2 and 3, respectively.

5.2. Experimental results and discussion

We have tested the SPIP and BABA experiments on three different samples: L-histidine.HCl.H_2O, NaH_2PO_4. and a phosphate compound The experiments on L-histidine.HCl.H_2O were performed on a narrow bore 18.8 T Bruker Avance-II spectrometer equipped with 3.2mm MAS probe spinning at ν_R = 23.6 kHz. Those on NaH_2PO_4 were performed on a wide bore 9.4T Bruker Avance-II spectrometer equipped with a 2.5mm MAS probe spinning at ν_R = 31.7 kHz. Those on the phosphate sample were performed with the same previous two probes at both 9.4 and 18.8 T.

We have tested on L-histidine.HCl.H_2O, the optimum spin-lock amplitude ν_{1SL} that can be observed when fixing the π pulse amplitude to $\nu_{1\pi}$ = 71 kHz **(Fig.5.6)**. This figure displays a large plateau, which means that the spin-lock value can remain quite moderate ($\nu_{1SL} \geq$ 35 kHz). Actually, simulations performed with different $\nu_{1\pi}$ and ν_R values have shown that this plateau always starts at moderate rf-values: c.a. $\nu_{1SL} \geq 0.5\nu_{1\pi}$.

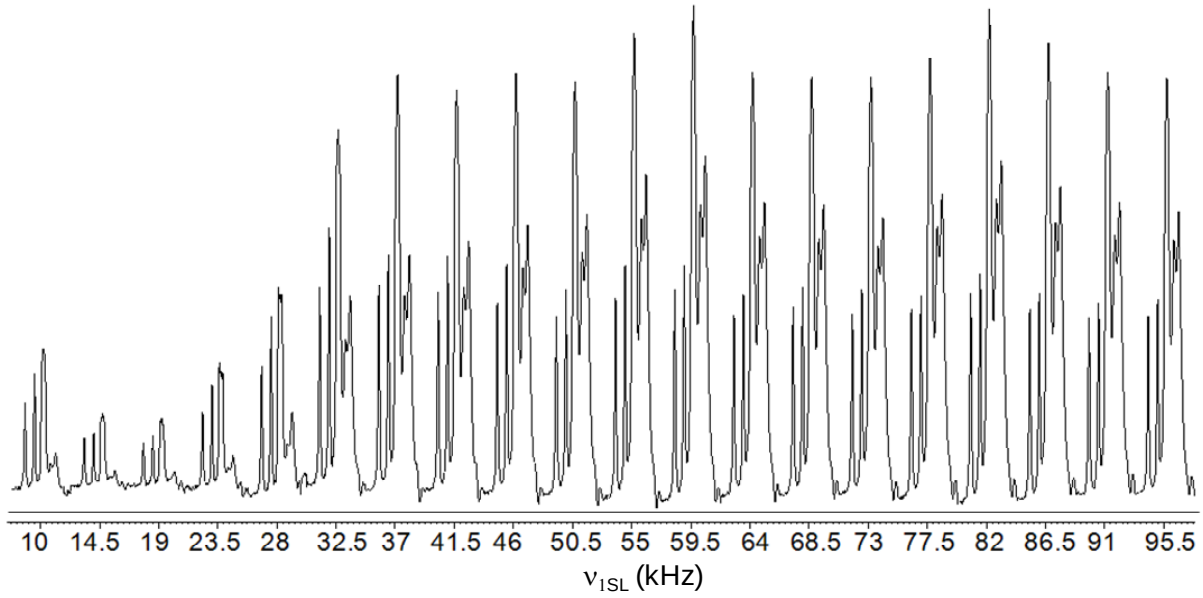

Fig.5.6. L-histidine.HCl.H_2O, 18.8 T, ν_R = 23.6 kHz. $\nu_{1\pi}$ = 71 kHz. Optimization of ν_{1SL} with SPIP sequence described in **Fig.5.1e**. 32 scans and recycling delay of 2s.

We have tested the offset sensitivity of L-histidine.HCl.H_2O for 4 different sequences: BABA-1 (**Fig.5.7a**), BABA-2 (**Fig.5.7b**), $SPIP_{NSL}$ (**Fig.5.7c**) and SPIP (**Fig.5.7d**). The experimental results confirm previous simulations concerning offset

irradiations (**Fig.5.5**): (i) BABA-1 is the most sensitive method to these effects, (ii) $SPIP_{NSL}$ and BABA-2 are less sensitive to offsets, but also less efficient on-resonance, and (iii) SPIP presents the great advantage of being insensitive to offsets and of providing a large efficiency identical that that of BABA-1 on resonance.

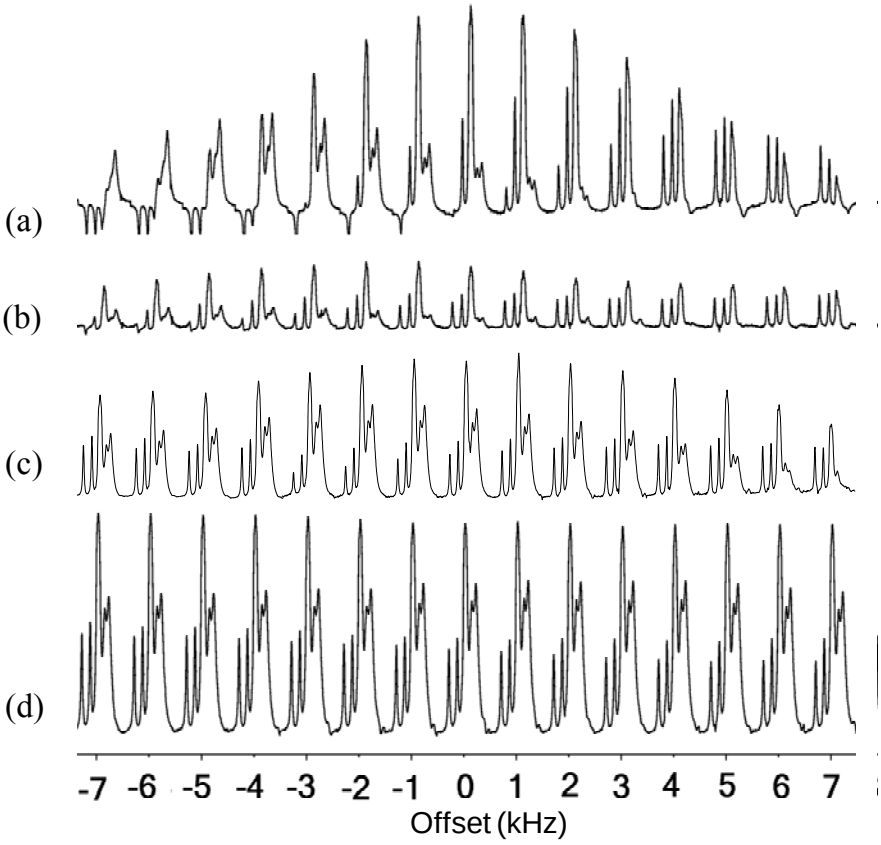

Fig.5.7. L-histidine.HCl.H_2O, 18.8 T, ν_R = 23.6 kHz. Offset effects. (a) BABA-1, $\nu_{1\pi}$ = 91 kHz, τ = 42.4 µs. (b) BABA-2, $\nu_{1\pi}$ = 91 kHz, τ = 84.8 µs. (c) $SPIP_{NSL}$, $\nu_{1\pi}$ = 71 kHz, τ = 170.8 µs. (d) SPIP, $\nu_{1\pi}$ = 71 kHz, ν_{1SL} = 59 kHz, τ = 169.5µs. 32 scans and recycling delay of 2s.

In **Fig.5.8**, we have represented three DQ-SQ spectra of L-histidine.HCl.H_2O, recorded with BABA-1 (**Fig.5.8b**), BABA-2 (**Fig.5.8c**) and SPIP (**Fig.5.8d**). By comparing the F_2 projections of **Fig.5.8b-d**, one observes that BABA-1 is the most sensitive method to offsets, as F_2 regions around -4kHz and +7kHz are quite attenuated. BABA-2 also presents this problem at $F_2 \approx$ -4kHz **(Fig.5.8c**), but moreover its on-resonance sensitivity is decreased by a factor of c.a. 3 with respect to that provided by BABA-1. This signal decrease is partly due to an increase of T'_2 losses as the recoupling time of BABA-2 ($\tau = 2T_R$ = 84.8 µs) is twice longer than that of BABA-1.

The SPIP spectrum (**Fig.5.8d**) shows an on-resonance signal intensity comparable to that of BABA-1, but without any offset attenuation. These results are completely in agreement with previous simulations. As a result, the number of correlations revealed by the DQ-SQ experiment is small in the case of BABA-2 (5 cross- and 2 auto-peaks), moderate with BABA-1 (7 cross- and 3 auto-peaks) and large with SPIP (10 cross- and 3 auto-peaks), which allows revealing long distance correlations. The SPIP spectrum is similar to that published by Madhu and co-workers,[9] who used the $C9_1^4$ DQ-SQ sequence, but it reveals more correlations (13 instead of 8) despite the fact that a PMLG decoupling method was used along F1 and F2 in ref [9], which increased the S/N ratio. Obviously, our spectra would have been quite improved by also using an homonuclear decoupling along F_1 and F_2.[32-34]

We have recorded several ^{31}P DQ-SQ spectra (not shown) on a phosphate sample which presents two phosphorous species, both submitted to a very large CSA of approximately 200 ppm. The BABA spectra recorded at 9.4 T with ν_R = 32 kHz, gave a poor S/N ratio, as opposed to those recorded with SPIP. The BABA spectra recorded at 18.8 T with ν_R = 20 kHz, gave no signal at all, and the efficiency observed on the SPIP spectra was not as good as that observed at 9.4 T. However, when taking off the spin-lock part of the sequence in Fig1e, the efficiency increased to c.a. 15%. The loss of efficiency observed with the initial SPIP sequence is related to the fact the rf-amplitude of the spin-lock parts was too small ($\nu_{1SL} \leq$ 100 kHz) to spin-lock efficiently such a large CSA ($\approx$ 60 kHz at 18.8 T).[35]

At last, we show (**Fig.5.9**) the SPIP DQ-SQ spectrum of NaH_2PO_4 recorded at 9.4T with Smooth Amplitude Modulation (SAM) homonuclear decoupling along F_1 and F_2.[34] There are four different proton species in this sample,[36] but two of them (H_3 and H_4) have very close chemical shifts.[37] All peaks are resolved in the 2D spectrum, and even on the 1D projections, and all diagonal and cross-peaks can be observed in this figure.

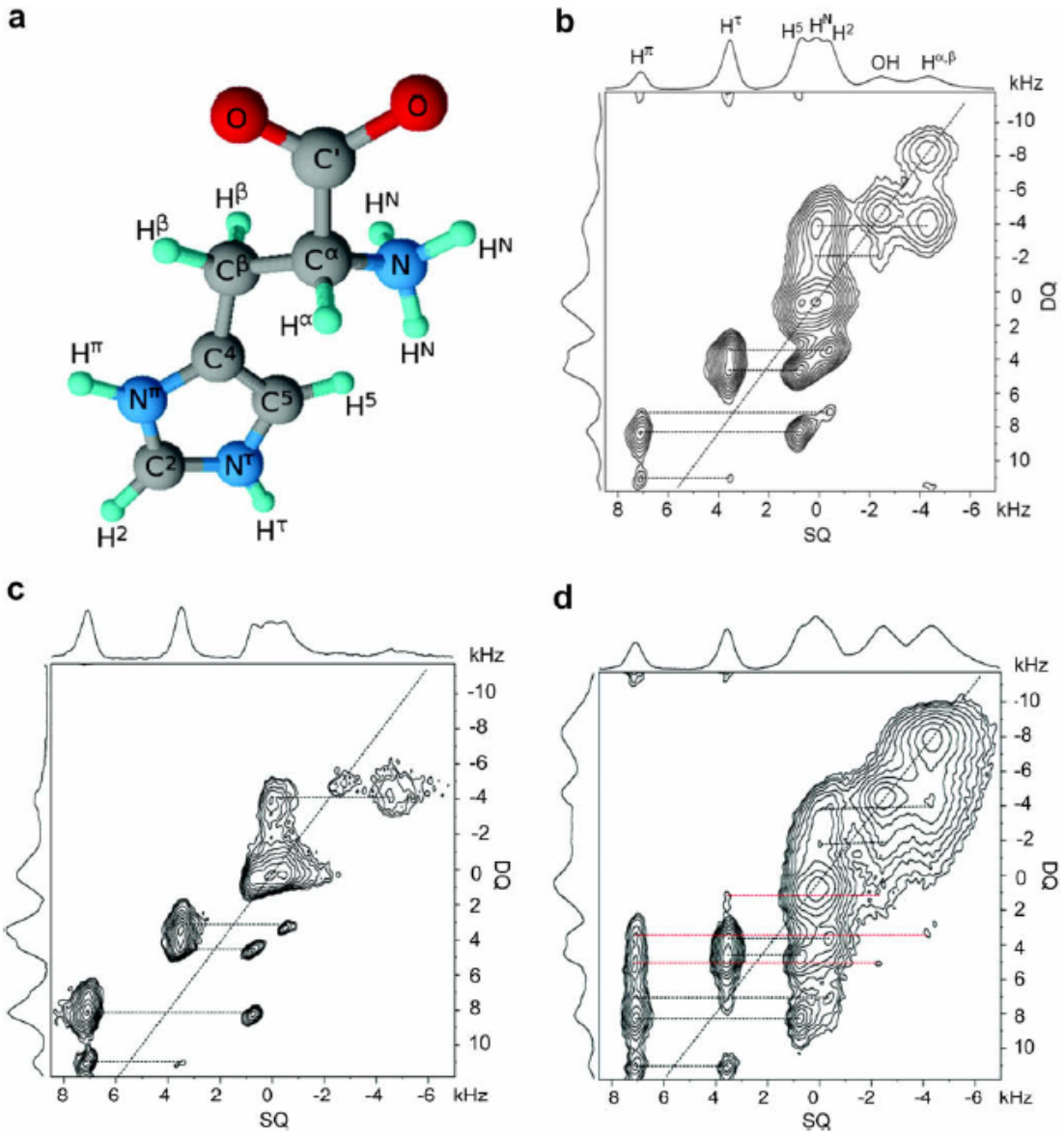

Fig.5.8. L-histidine.HCl.H_2O. (a) Molecular structure with atom labelling matching IUPAC recommendations. (b-d) 2D DQ-SQ spectra at 18.8 T and ν_R = 23.6 kHz, with same experimental specifications with 80 scans and recycling delay of 2s (3.5 hrs each). (b,c) BABA spectra with $\nu_{1\pi}$ = 91 kHz, (b) BABA-1 with τ = 42.4 μs; (c) BABA-2 with τ = 84.8 μs. (d) SPIP (**Fig.5.1e**) with $\nu_{1\pi}$ = 91 kHz, ν_{1SL} = 59 kHz, τ = 169.5 μs.

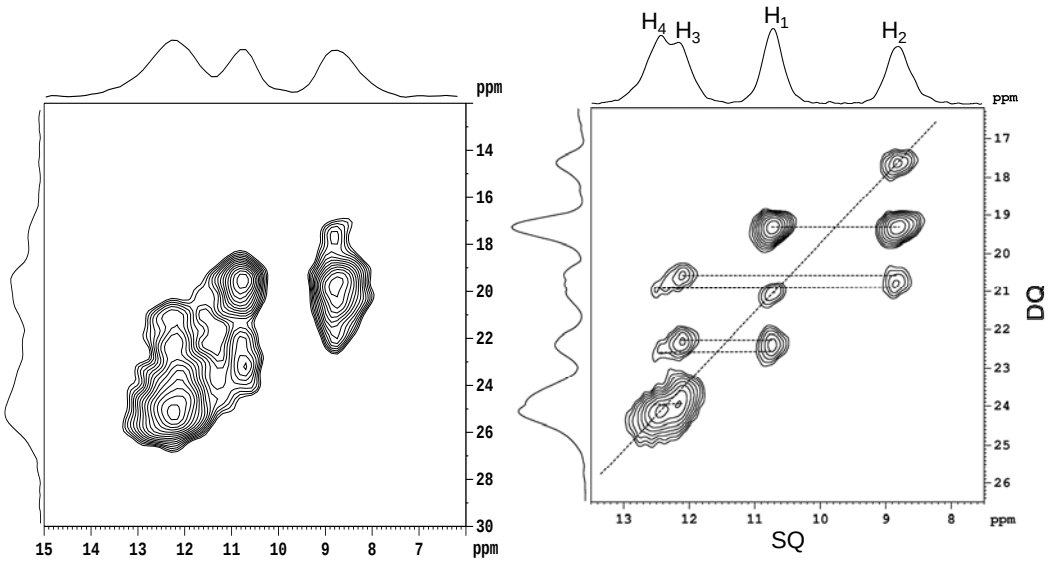

Fig.5.9. NaH_2PO_4. DQ-SQ 2D spectrum recorded at 9.4 T with SPIP, ν_R = 31.7 kHz, τ = 504 μs. $\nu_{1\pi}$ = 68 kHz, ν_{1SL} = 60 kHz. 64 scans and recycling delay of 1.5s. (left) SPIP without SAM (right) SPIP with SAM. $SAM_{3.5}$ was applied during t_1 and t_2 with ν_{1peak} = 121 kHz. Experimental time: 5.4 hrs.

5.3. Conclusion

We have developed a new simple pulse sequence, christened SPIP, based on the rotor-synchronized $R2_2^1$ sequence. We have demonstrated that SPIP can be applied at fast (ν_R = 31.7 kHz here) spinning speeds. Although this method may experience relaxation decay during long recoupling periods, it provides a very broad band and efficient DQ homonuclear dipolar recoupling method and it is thus more appropriate in high magnet fields than BABA sequences. The rf-amplitudes of the π pulse and spin-lock parts are moderate and do not have to fulfill stringent conditions. Therefore, the method is very robust and it does not require time-consuming optimization. SPIP recoupling may thus perform much better than BABA-1 and BABA-2 in protonated samples, such as proteins.

When the spinning speed is smaller than twice the frequency range of chemical shifts, folding of the resonances occurs along F_1. This may be avoided by introducing a π pulse in between the excitation and reconversion periods.[26] The position of this π pulse during the t_1 evolution time allows an easy scaling of all interactions in the indirect 2Q dimension, thus avoiding any possible folding.

Presently, the main limitation of all homonuclear dipolar methods is related to the dipolar truncation. This means that long-range correlations between two nuclei are not visible when one of these is also involved in a short-range correlation with a third-nucleus. A second limitation of these dipolar-based through-space methods is that unambiguous connectivity information can not strictly be ensured, as opposed to through-bond *J*-based methods. However, it is well-known that by a proper choice of a short dipolar recoupling time one may obtain the same results as with through-bond methods, at the expanse of the S/N ratio.

References

1. B.H. Meier, W.L. Earl, Excitation of multiple quantum transitions under magic angle conditions: adamantane, *J. Chem. Phys.* 85 (**1986**) 4905-4911.

2. B.H. Meier, W.L. Earl, Double-quantum filter for rotating solids, *J. Am. Chem. Soc.* 109 (**1987**) 7937-7941.

3. R. Tycko, G. Dabbagh, Measurement of nuclear magnetic dipole-dipole couplings in magic angle spinning NMR, *Chem. Phys. Lett.* 173 (**1990**) 461-465.

4. R. Tycko, G. Dabbagh, Double-quantum filtering in magic-angle-spinning NMR spectroscopy: an approach to spectral simplification and molecular structure determination, *J. Am. Chem. Soc.* 113 (**1991**) 9444-9448.

5. Y.K. Lee, N.D. Kurur, M. Helme, O.G. Johannessen, N.C. Nielsen, M.H. Levitt, Efficient dipolar recoupling in the NMR of rotating solids. A sevenfold symmetric radiofrequency pulse sequence, *Chem. Phys. Lett.* 242 (**1995**) 304-309.

6. S.P. Brown, I. Schnell, J.D. Brand, K. Müllen, H.W. Spiess, The competing effects of π-π packing and hydrogen bonding in a hexabenzocoronene carboxylic acid derivative: a ^{1}H solid-state MAS NMR investigation, *Phys. Chem. Chem. Phys.* 2 (**2000)** 1735-1745.

7. S. Pawsey, M. McCormick, S. De Paul, R. Graf, Y.S. Lee, L. Reven, H.W. Spiess, ^{1}H fast MAS NMR studies of hydrogen-bonding interactions in self-assembled monolayers, *J. Amer. Chem. Soc.* 125 (**2003)** 4174-4184.

8. S.P. Brown, Probing proton-proton proximities in the solid state. *Progress in Nuclear Magnetic Resonance Spectroscopy.* 50 (**2007)** 199-251.

9. P.K. Madhu, E. Vinogradov, S. Vega, Multiple-pulse and magic-angle spinning aided double-quantum proton solid-state NMR spectroscopy, *Chem. Phys. Lett.* 394 (**2004)** 423-428.

10. I. Schnell, Dipolar recoupling in fast MAS solid-state NMR spectroscopy, *Prog. Nucl. Magn. Reson. Spectrosc*. 45 (**2004**) 145-207.

11. M. Edén, M.H. Levitt, Excitation of carbon-13 triple-quantum coherence in magic-angle spinning NMR, *Chem. Phys. Lett.* 293 (**1998**) 173-179.

12. M. Carravetta, M. Edén, O.G. Johannessen, H. Luthman, P.J.E. Verdegem, J. Lugtenburg, A.Sebald, M.H. Levitt, Multiple-quantum ^{1}H MAS NMR studies of defect sites in as-made all-silica ZSM-12 zeolite, *J. Am. Chem. Soc.* 122 (**2000**) 6659-6663.

13. X. Feng, Y.K. Lee, D. Sandström, M. Eden, H. Maisel, A. Sebald, M.H. Levitt, Direct determination of a molecular torsional angle by solid-state NMR, *Chem. Phys. Lett.* 257 (**1996**) 314-320.

14. W. Sommer, D.E. Demco, S. Hafner, H.W. Spiess, Rotation-synchronized homonuclear dipolar decoupling, *J. Magn. Reson. Series A.* 116 (**1995)** 36-45.

15. M. Feike, D.E. Demco, R. Graf, J. Gottwald, S. Hafner, H.W. Spiess, Broadband multiple-quantum NMR spectroscopy, *J. Mag. Reson. - Series A.* 122 (**1996)** 214-221.

16. A. Brinkmann, M.H. Levitt, Symmetry principles in the nuclear magnetic resonance of spinning solids : heteronuclear recoupling by generalized Hartmann-Hahn sequences, *J. Chem. Phys.* 115 (**2001)** 357384.

17. M.H. Levitt, Encyclopedia of Nuclear Magnetic Resonance. Wiley, Chichester, **2002**, 165-196.

18. S. Li, A. Zheng, Y. Su, H. Zhang, L. Chen, J. Yang, C. Ye, F. Deng, Brϕnsted/lewis acid synergy in dealuminated HY zeolite: a combined solid-state NMR and theoretical calculation study, *J. Am. Chem. Soc.* 129 (**2007)** 11161-11171.

19. S.P. Brown, A. Lesage, B. Elena, L. Emsley, Probing proton-proton proximities in the solid-state: high-resolution two-dimensional ^{1}H-^{1}H double-quantum CRAMPS NMR spectroscopy, *J. Am. Chem. Soc.* 126, (**2004**) 13230-13231.

20. M. Carravetta, Y. Murata, M. Murata, L. Heinmaa, R. Stern, A. Tontcheva, A. Samoson, Y. Rubin, K. Komatsu, M.H. Levitt, Solid-state NMR spectroscopy of molecular hydrogen trapped inside an open-cage Fullerene, *J. Amer. Chem. Soc.* 126 (**2004)** 4092-4093.

21. M. Carravetta, A. Danquigny, S. Mamone, F. Cuda, O.G. Johannessen, I. Heinmaa, K. Panesar, R. Stern, M.C. Grossel, A. J. Horsewill, A. Samoson, M. Murata, K. Komatsu, M.H. Levitt, Solid-state NMR of endohedral hydrogen-fullerene complexes, *Phys. Chem. Chem. Phys.* 9 **(2007)** 4879-4894.

22. R. Graf, D.E. Demco, J. Gottwald, S. Hafner, H.W. Spiess, Dipolar couplings and

internuclear distances by double-quantum nuclear magnetic resonance spectroscopy of solids, *J. Chem. Phys.* 106 (**1997)** 885-895.

23. M. Eden, D. Zhou, J. Yu, Improved double-quantum NMR correlation spectroscopy of dipolar-coupled quadrupolar spins, *Chem. Phys. Lett.* 431 (**2006)** 397-403.

24. A. Brinkmann, M. Eden, Second order average Hamiltonian theory of symmetry-based pulse schemes in the nuclear magnetic resonance of rotating solids: application to triple-quantum dipolar recoupling, *J. Chem. Phys.* 120 (2004) 11726.

25. N.C. Nielsen, H. Bildsoe, H.J. Jakobsen, M.H. Levitt, Double-quantum homonuclear rotary resonance: efficient dipolar recovery in magic-angle spinning nuclear magnetic resonance, *J. Chem. Phys.* 101 (**1994)** 1805-1812.

26. G. Mali, G. Fink, F. Taulelle, Double-quantum homonuclear correlation magic angle spinning nuclear magnetic resonance spectroscopy of dipolar-coupled quadrupolar nuclei, *J. Chem. Phys*. 120 **(2004)** 2835-2845.

27. M. Carravetta, M. Eden, O.G. Johannessen, H. Luthman, P.J.E.Verdegem, J. Lugtenburg, A. Sebald, M.H. Levitt, Estimation of carbon–carbon bond lengths and medium-range internuclear distances by solid-state nuclear magnetic resonance, *J. Am. Chem. Soc.* 123 **(2001)** 10628–10638.

28. J. Schmedt, auf der Günne, Distance measurements in spin-1/2 systems by ^{13}C and ^{31}P solid-state NMR in dense dipolar networks, *J. Magn. Reson*. 165 **(2003)** 18–32.

29. M. Bak, J.T. Rasmussen, N.C. Nielsen, SIMPSON: a general simulation program for solid-state NMR spectroscopy, *J. Magn. Reson.* 147 (**2000)** 296-330.

30. M. Bak, N.C. Nielsen, REPULSION: a novel approach to efficient powder averaging in solid- state NMR, *J. Magn. Reson.* 125 (**1997)** 132-139.

31. P.E. Kristiansen, M. Carravetta, J.D. van Beek, W.C. Lai, M.H. Levitt, Theory and applications of supercycled symmetry-based recoupling sequences in solid-state NMR, *J. Chem. Phys.* 12 **(2006)** 234510–234519.

32. M. Leskes, P.K. Madhu, S. Vega, Supercycled homonuclear dipolar decoupling in solid-state NMR: toward cleaner ^{1}H spectrum and higher spinning rates, *J. Chem. Phys*. 128 **(2008)** 52309.

33. B. Elena, G. de Paepe, L. Emsley, Direct spectral optimisation of proton-proton homonuclear dipolar decoupling in solid-state NMR, *Chem. Phys. Lett*. 398 **(2004)** 532-538.

34. J.P. Amoureux, B. Hu, J. Trebosc, Enhanced resolution in proton solid-state NMR with very-fast MAS experiments, *J. Magn. Reson*. 193 **(2008)** 305-307.

35. L. Delevoye, B. Hu, O. Lafon, J. Trebosc, J.P. Amoureux, to be published.

36. R.N.P. Choudhary, R.J. Nelmes, K.D. Rouse, A room temperature neutron diffraction study of NaH_2PO_4, *Chem. Phys. Lett*. 78 **(1981)** 102-105.

37. L. Mafra, J.R.B. Gomes, J. Trebosc, J. Rocha, J.P. Amoureux, Resolution enhancement method to probe ^{1}H-^{1}H proximities in hydrogen-bonding networks in solids: employing 2D ^{1}H-^{1}H double-quantum CRAMPS NMR at very-fast MAS, *J. Magn. Reson*. in press.

Chapter 6. Direct and indirect covariance 2D spectroscopy

Up to now, 2D NMR frequency spectra have mostly been obtained by using a 2D Fourier transformation (2D-FT). Unfortunately, this method is very often experimentally time-consuming, as it requires a large number of acquisition points in the evolution time domain (t_1), especially with spectra presenting close resonances in liquids or in well-crystallized samples. Acquiring 2D spectra becomes especially time-consuming when the signal accumulated per unit of time is small, in case of experiments with weak efficiency, and/or nuclei with low-gamma, low natural abundance, or long relaxation times. To overcome this problem several methods have been proposed in liquids, but only few of them have been demonstrated in solids. In the case where 1D spectra have already been recorded, the previous knowledge of the positions and line-widths of the resonances can be used to speed up the acquisition of the 2D spectra. This leads to the ANAFOR data treatment in the time domain,[1] and to the HADAMARD-encoded multi-selective excitation in the frequency domain.[2] However, both methods have been mainly employed for samples presenting resolved lorentzo-gaussian resonances.

Here we show how the covariance method, which has been applied to liquids,[3] can also be employed in solid state NMR to get homo-nuclear correlation (HOMCOR) 2D spectra, without any previous knowledge of the positions and line-widths of the resonances, in a much faster way than the usual 2D-FT data treatment.

Besides, covariance methods can be applied to HETCOR NMR data to generate two HOMCOR indirect-covariance spectra.

6.1 The principle of covariance 2D spectroscopy

The principle of the covariance 2D can be viewed as a correlation of wave functions: if species 1 has a wave function $\cos(\omega^a t)$, and species 2 also have this wave function $\cos(\omega^b t)$; if $\omega^a = \omega^b$ then there is a cross-peak between species 1 and

species 2 in the covariance 2D spectrum; if $\omega^a \neq \omega^b$, then there is no cross-peak between species 1 and species 2.

6.2 Direct covariance 2D spectroscopy

(1) Theoretical background

Two-dimensional NMR spectroscopy correlates nuclear spin resonances in two dimensions, by following the scheme: preparation → evolution (t_1 or t_e) → mixing → detection (t_2 or t_d). A time-domain matrix signal $s(t_1,t_2)$, is typically collected as a set of N_1 FIDs in t_2, with evolution time t_1 that is increased from FID to FID in N_1 steps with a fixed increment.

In the case of the 2D-FT method, the digital resolution observed along F_1 is proportional to $1/N_1$. In the case of HOMCOR spectra, to achieve the same resolution along F_1 and F_2, hundreds (well-crystallized solids) to thousands (liquids) of t_1 steps are typically required. Obviously, this leads to time-consuming experiments. Moreover, in the case of amplitude-modulated experiments, to retrieve the correct sign of the resonances along F_1, either two different sets of 2D spectra must be acquired (States),[4] or a doubled F_1 spectral-width must be used (TPPI).[5]

The original covariance approach, called generalized 2D (GEN2D) spectroscopy, was applied successfully to the optical field, such as infrared, Raman, near-infrared and ultraviolet,[6-9] and then applied to diffusion NMR experiments.[10] Its name was then changed to covariance spectroscopy when applied to liquid-state 2D HOMCOR NMR experiments for structural analysis.[3, 11]

In the case of 2D-Cov, let us call t_e and t_d (instead of t_1 and t_2 with 2D-FT) the evolution and detection times of a homo-nuclear signal $s(t_e,t_d)$. After Fourier-transform with respect to t_d, this signal is converted in a mixed 2D matrix $S(t_e,\omega_d)$, from which only the real part is kept after phasing and apodization with respect to ω_d. The fact that the same phasing is mathematically used in 2D-Cov along the indirect dimension is a significant advantage in case of broad resonances where it

is often difficult to perform with 2D-FT. From this initial matrix, two slightly different homo-nuclear frequency matrices can be computed by covariance:

$$C(\omega_1,\omega_2)=\int S(t_e,\omega_1)\cdot S(t_e,\omega_2)dt_e \tag{6.1}$$

$$F(\omega_1,\omega_2)=\sqrt{C(\omega_1,\omega_2)} \tag{6.2}$$

These HOMCOR spectra are real and symmetric, and they are called covariance (C) and cross-correlation (F) spectra, respectively. It must be noted, that Eq.(6.2) corresponds to the square-root of a matrix, not of a number, whose computation can be speeded up by using a singular value decomposition method.[12] In the case of narrow resonances (spin-1/2 nuclei in well crystallized or liquid samples), the two representations are equally used. They provide similar resolutions, and the only difference is that the covariance representation emphasizes the peaks with large amplitudes. This is not the same in case of unresolved peaks and shoulders (broad resonances), and the line-shapes differ according to the representation. The cross-correlation ($F(\omega_1,\omega_2)$) spectrum is similar to that obtained with 2D-FT and the covariance ($C(\omega_1,\omega_2)$) spectrum to the power spectrum deduced from 2D-FT (Fig. 6.1).

In the covariance HOMCOR spectra, there are two types of resonances, which can be observed either as diagonal- or as cross-peaks. All resonances observed in the 1D spectrum always present in the 2D-Cov HOMCOR spectrum an auto-correlation diagonal peak with positive amplitude, since for $\omega_1=\omega_2$ we have $\int S^2(t_e,\omega_1).dt_e > 0$. (This peak arises from the multiplication by itself of the column corresponding to this peak (see. Eq.(6.1))). Therefore, the presence of a diagonal peak does not prove that this atom is actually connected to another equivalent atom. This is certainly the main limitation of the covariance method. On the contrary, a cross-peak emerges only if two different species are really connected.

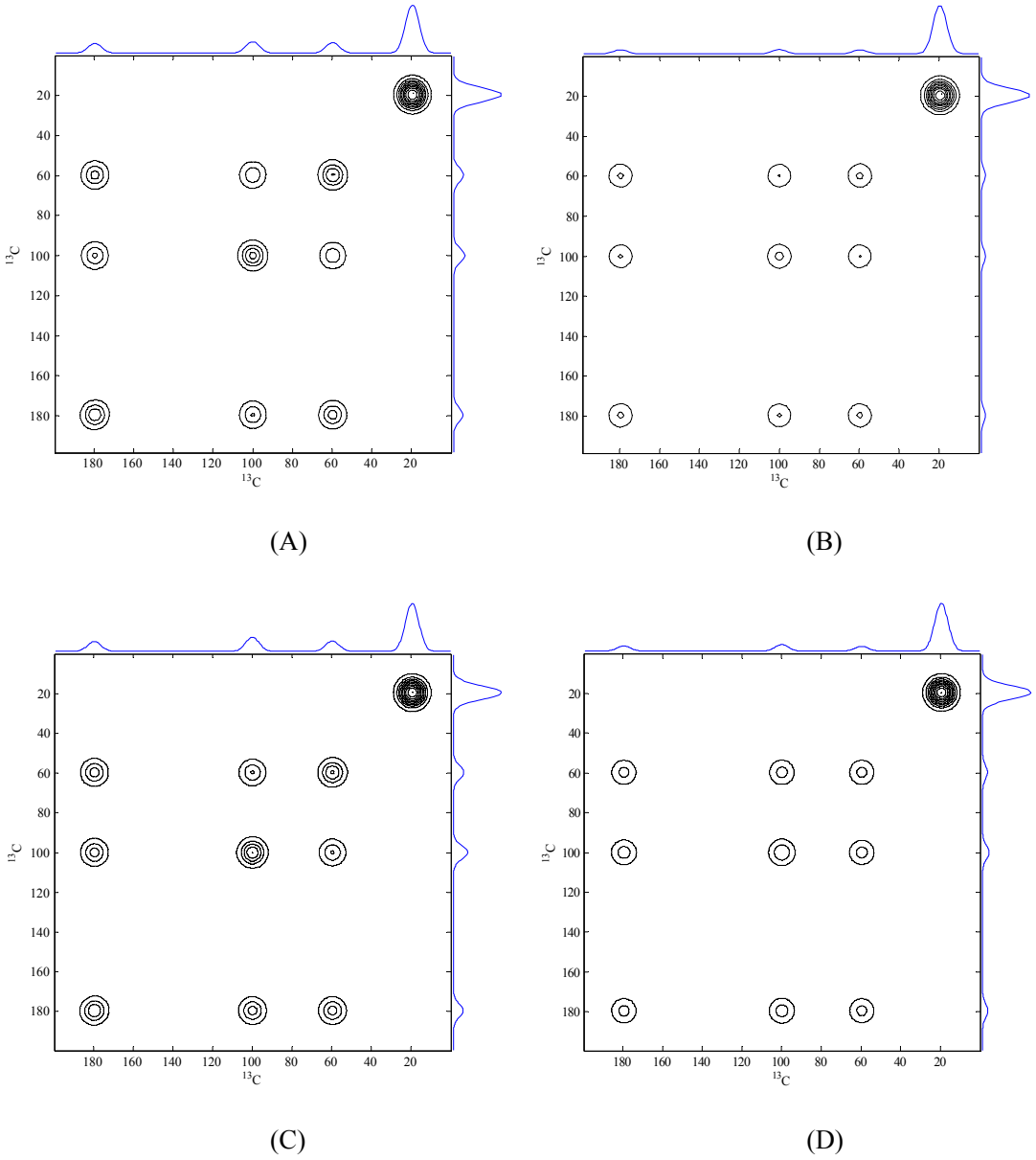

Fig. 6.1. Simulations of an RFDR experiment recorded with States on a sample with 4 different species: three spatially close each other, and one (with double intensity) not connected to the others. The FIDs have been treated with 2D-FT ((A) usual and (B) power spectra) and 2D-Cov ((C) $F(\omega_1,\omega_2)$ and (D) $C(\omega_1,\omega_2)$ spectra).

(2) Diagonal noise in covariance 2D spectra

Let us consider the noise of the 2D-Cov spectrum $C(\omega_1,\omega_2)$. This noise is generated from that observed on the two slices along ω_e: $S(\omega_1, t_e)$ and $S(\omega_2, t_e)$. When

ω_1 is very different from ω_2, it is clear from Eq. (6.1) that the multiplication of the two different stochastic noises can be randomly positive or negative, and thus the summation of the noise along t_e to obtain $C(\omega_1,\omega_2)$ is small and can also be randomly positive or negative. When ω_1 is equal to ω_2, the two slices along t_e are identical, so that their noises, and the product $S(\omega_1, t_e).S(\omega_2, t_e)$ is always positive, whatever may be the t_e value. Therefore, the summation of the noise along t_e in Eq.(6.1) has a maximum positive value onto the diagonal of covariance spectra. When $\omega_1 \approx \omega_2$, the summation of the noise along t_e is positive, but its amplitude decreases as noise along ω_1 and ω_1 get uncorrelated.

When the spectral-widths used along t_e are much smaller than the probe band-widths, the noise can be considered as constant in the 2D signal. The diagonal noise in all covariance-based 2D spectra has then a constant positive amplitude and line-shape. It is then easy to define several locations onto this diagonal where there is no resonance a priori, to verify that this noise-power ridge is constant and then to subtract it all along the diagonal. This simple method allows decreasing the correlated noise level close to the diagonal. This is especially important in solid-state NMR where S/N ratio is often small, if two resonance frequencies are close each other.

(3) ^{13}C Double-Quanta in Tyrosine

The ^{13}C double-quanta (DQ) experiment has been recorded at 9.4T on an uniformly ^{13}C enriched sample of tyrosine. Due to the TPPI acquisition, we have not been able to represent the results treated with 2D-FT in the same symmetrical way as those treated with covariance. The Post-C7 sequence has been used for creation and conversion of DQ coherences, which leads to a ^{13}C RF-field seven times larger than the spinning speed.[13] An efficient proton decoupling for ^{13}C resolution requires an additional factor of c.a. 2-3 for the proton RF-field with respect to ν_R.[14] Globally, these two factors resulted into a spinning speed limited to ν_R = 10kHz. This limited spinning speed leads to several sidebands, which are indicated by asterisks on the 2D spectra. The Tyrosine molecule is shown in Fig. 6.2A. The projection of the DQ spectrum shows that the ^{1}H decoupling was sufficient to partly resolve along F_2 the C_3

and C_5 resonances, which are only separated by c.a. 200 Hz, but not those related to $C_{2,6}$ (Fig. 6.2B). However, due to the truncated evolution time of 1.6 ms (125 t_1 steps of 12.5μs), C_3 and C_5 resonances are not resolved along F_1 with 2D-FT. It is important to note that no auto-correlation peaks are observable on the 'diagonal' (with slope 2) of this DQ experiment treated with 2D-FT (Fig. 6.2B).

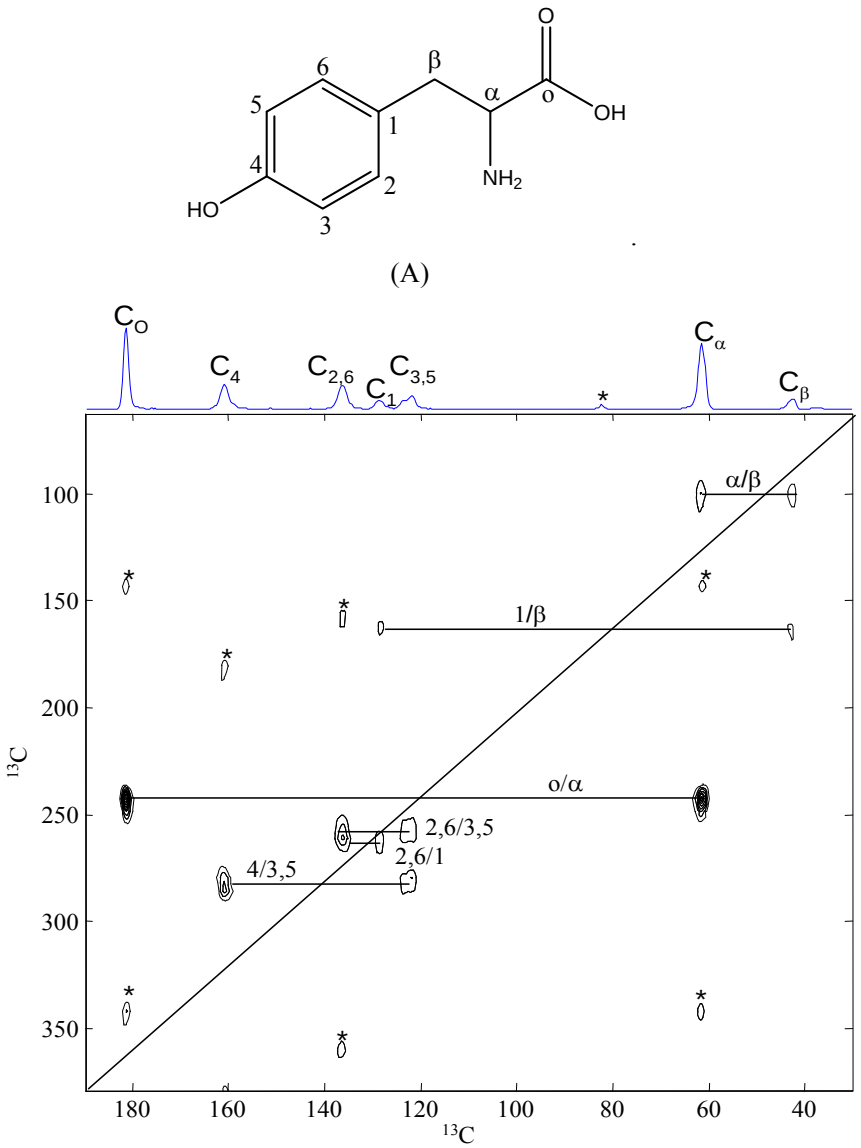

Fig. 6.2. Tyrosine. (A) Molecule. (B) ^{13}C Post C7 Double-Quantum spectrum. Spinning sidebands are indicated with ∗. B_o = 9.4T, ν_R = 10 kHz, proton decoupling has been performed with TPPM with 92.5 kHz RF-field.

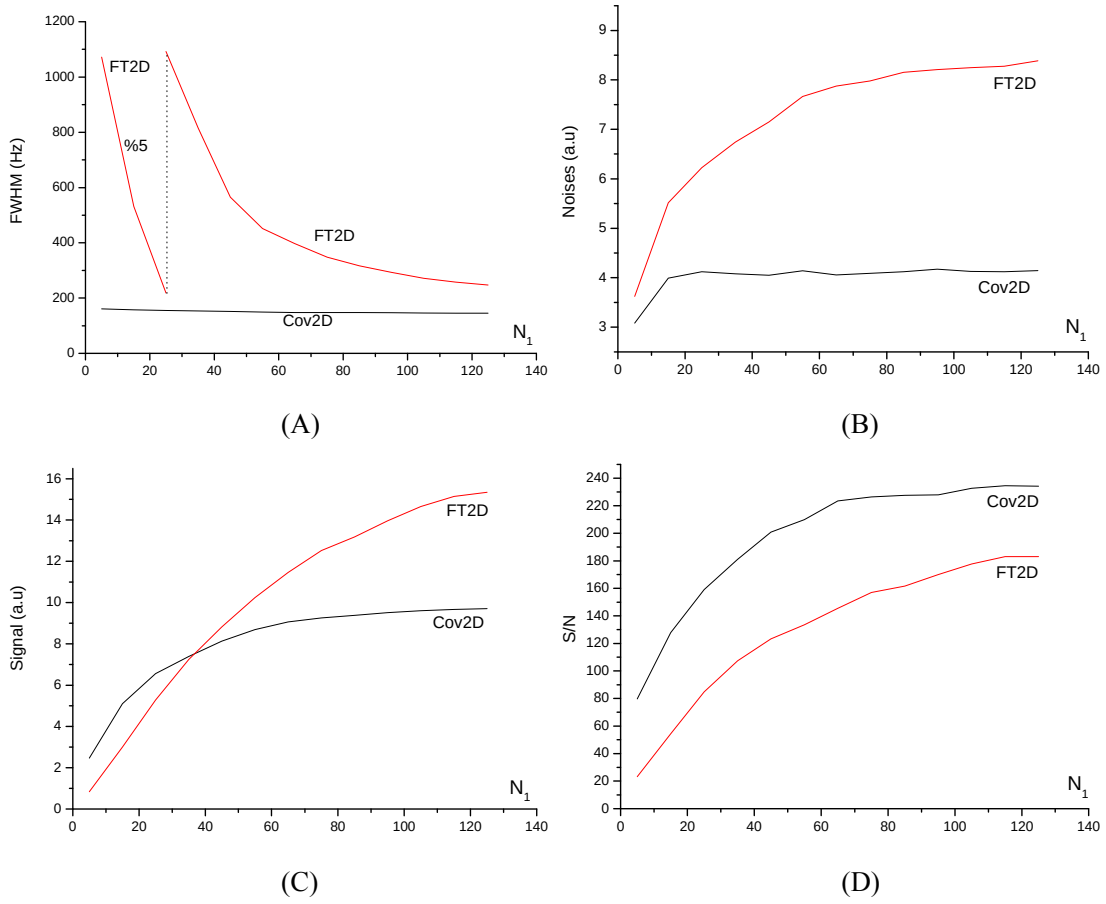

Fig. 6.3. Tyrosine: Analysis of the C_o-C_α cross-peak, versus N_1 the number of t_1 slices, observed in ^{13}C Post C7 spectra treated by $F(\omega_1,\omega_2)$ 2D-Cov (a) and 2D-FT (b). (A) Line-width along the indirect dimension in Hz, (B) Noise level (a.u), (C) Signal amplitude (a.u), and (D) S/N ratio.

In Fig. 6.3, we have represented the line-width (FWHM) along the indirect dimension, signal amplitude, noise level, and S/N ratio observed for the C_0-C_α cross-peak treated with 2D-Cov or 2D-FT, versus the number N_1 of t_1 steps used in the treatment.

It must be kept in mind that with 2D-Cov treatment, the resolution always remains the same along the two axes, due to the mathematical data-treatment. In the case of narrow resonances, such as those observed with tyrosine, the resolution is quasi N_1 independent, and the line-width only decreases from 159 Hz (N_1 = 5) to 143 Hz (N_1 = 125) (Fig. 6.3). It can also be observed that the 2D-Cov noise level is very weakly N_1 dependent (Fig. 6.3B), which means that it is mainly related to that observed in the 1D spectrum with the same spectral-width. Therefore, the evolutions

versus N_1 of the signal amplitude (Fig. 6.3C) and of the S/N ratio (Fig. 6.3D) are very similar. They display two different regimes: for small numbers of t_1 steps (< 40) one observes that they are proportional to $\sqrt{N_1}$, whereas for larger numbers a progressive saturation occurs.

With 2D-FT data-treatment, the resolution along F_2 is constant but the line-width along F_1 increases largely for insufficient t_1 steps (Fig. 6.3A). Even for $N_1 = 125$, one observes that the ultimate resolution is not yet obtained along F_1, due to truncated evolution time leading to wiggles and double-quantum relaxation larger than in the detection dimension (Fig. 6.3A). The noise level increases with N_1 (Fig. 6.3B), which means that it is related to that observed in the 1D spectrum and also to the number of indirect slices. This noise level never stops increasing with N_1, as every additional t_1 slice brings its own noise. The noise level is therefore much more important than that observed with 2D-Cov. Of course, in relation to the line-width (Fig. 6.3A), the signal amplitude (Fig. 6.3C) and the S/N ratio (Fig. 6.3D) increase largely with N_1. However, it must be noted that for longer evolution times ($N_1 >> 125$), the 2D-FT S/N ratio would start decreasing, because only noise would then be recorded. It is important to remark that the S/N ratio is much better with 2D-Cov than with 2D-FT. As an example, it is nearly the same with 2D-Cov and $N_1 = 25$ as with 2D-FT and $N_1 = 125$ in the case of the tyrosine spectra shown here. By analyzing in more detail the resolution and S/N ratio obtained with 2D-Cov, it can even be concluded that in this case of narrow resonances, it is completely equivalent to record 40 t_1 steps or only 10 t_1 steps with four times more scans, because it gives approximately the same line-width and the same S/N ratio.

The constant resolution with respect to N_1 is a significant advantage of 2D-Cov over 2D-FT. As an example, one can observe that the resolution is the same in Fig. 6.4A and B, which have been obtained with 2D-Cov treatment using either all the 125 t_1 steps or only the first 25 t_1 steps, respectively. By also taking into account the fact that the covariance treatment only requires a classical complex 2D acquisition (no States nor TPPI), this means that spectrum in Fig. 6.4B has been acquired ten times

faster than that in Fig. 6.2B, for similar S/N ratio (Fig. 6.3D) but twice better resolution (Fig. 6.3A).

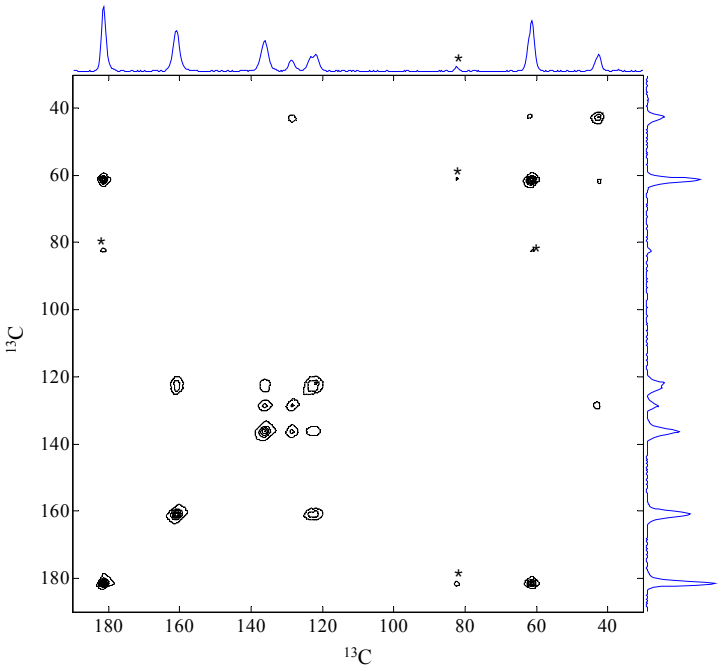

(A)

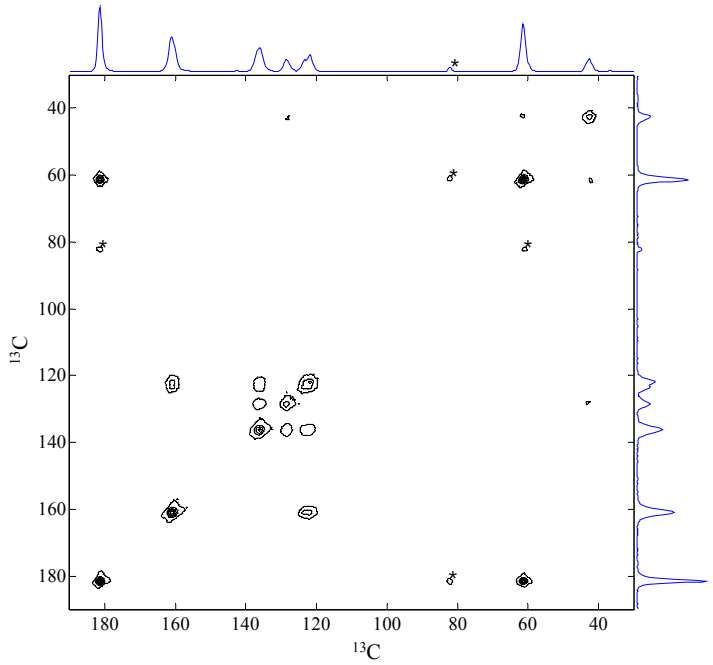

(B)

Fig. 6.4. Tyrosine: ^{13}C Post C7 spectra treated by $F(\omega_1,\omega_2)$ 2D-Cov with N_1 = 125 (A) or 25 (B)

In this case, the only drawback of the covariance treatment is related to the fact that one cannot 'trust' the diagonal peaks, which may appear due either to the mathematical treatment, or to close equivalent nuclei. Indeed, all other specifications are better than those for 2D-FT (line-width, S/N ratio and hence experimental time).

(4) ^{31}P RFDR of alumino-phosphates

The accuracy of the 2D-Cov method has also been demonstrated in the field of inorganic materials. The first example presented here is related to a phosphate binder. This class of phosphate materials is involved in a wide range of applications, which benefit from their high strength, abrasion resistance and high temperature stability. Basically, the binders are prepared through the thermal evolution of a metallic phosphate solution, giving rise to a mixture of phosphate compounds. The results reported here are related to the structure of a phosphate binder prepared from a commercial phosphate solution containing potassium and aluminum oxides. The ^{31}P RFDR experiment[15] was performed at 9.4 T with a 4 mm probe operating at 10 kHz spinning speed. The mixing time was set up to 32 ms. It has been recently shown that this value allows magnetization transfer between all phosphorus sites within one micro-crystallite and does not permit inter micro-crystallites transfer.[16, 17] We have used a States acquisition. In Fig. 6.5A,B are represented the usual 2D-FT spectra of this sample, obtained by treating either all 600 acquired FIDs or only the first 50 t_1 steps, respectively. The spectrum displayed in Fig. 6.5A is nearly symmetrical with respect to F_1 and F_2, but that shown in Fig. 6.5B is largely broadened along F_1, due to quite insufficient evolution time. This is not the case in Fig. 6.5C,D where the FIDs corresponding to the same evolution times have been treated with 2D-Cov. Spectra displayed in Fig. 6.5A,D are quite similar, but that of Fig. 6.5D required 24 (2*600/50) times less experimental time than that described in Fig. 6.5A : 4.5 hours instead of 106 hours with the usual 2D-FT data treatment. Moreover, in this example there is no drawback to using 2D-Cov instead of 2D-FT as both methods lead to uninformative diagonal peaks due to the RFDR transfer itself.

Since the mixing time value used to record the ^{31}P RFDR spectrum only allows intra micro-crystallite magnetization transfer, it can be deduced from the off-diagonal signals that the binder is constituted by two different phosphate compounds: a first phase which contains the two correlated phosphorus sites centered at -25 and -29 ppm and a second one constituted by the numerous correlated phosphate sites centered between 0 and -15 ppm. Additional experiments, including ^{31}P INADEQUATE, $^{27}Al[^{31}P]$ HMQC, $^{31}P[^{27}Al]$ CP-HETCOR and X-Ray diffraction, lead to the assignment of the first compound to $KAlP_2O_7$, whereas the second group of correlated phosphate is assigned to an unknown crystalline potassium alumino-phosphate compound whose structure is currently under investigation.

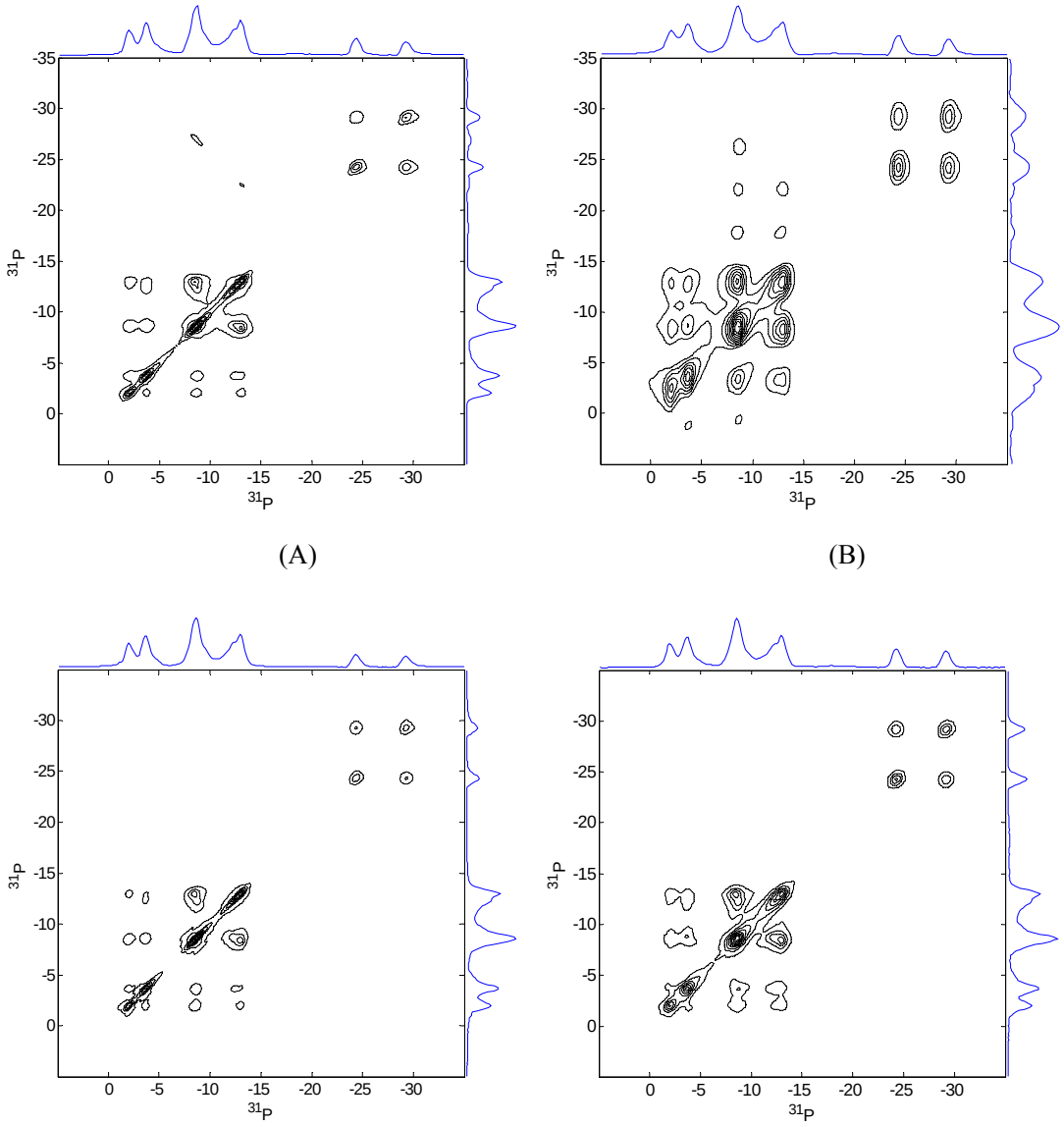

Fig. 6.5. Alumino-Phosphates: ^{31}P RFDR spectra treated either with 2D-FT with N_1 = 600 (A) or 50 (B) t_1 slices, or with $F(\omega_1,\omega_2)$ 2D-Cov with N_1 = 600 (C) or 50 (D) t_1 slices.

6.3 Indirect covariance 2D spectroscopy

Homo-nuclear scalar *J* coupling nuclear magnetic resonance (NMR) experiments are widely used methods for structural characterization of liquids [18], providing detailed information about the through-bond connectivity. These experiments have been well adapted under magic-angle spinning (MAS) for solid-state NMR of spin ½ nuclei [19, 20]. In the case of half-integer quadrupolar nuclei (with spin larger than ½), the first two- and three-dimensional (2D and 3D) through-bond homo-nuclear correlation (HOMCOR) experiments have been established in the solid-state only very recently [21, 22], because quadrupolar nuclei are difficult to deal with due to strong first- and second-order quadrupolar broadenings[23]. The methods, called homo-nuclear hetero-nuclear single-quantum correlation (H-HSQC), are two-step experiments, which explore first an aluminum-phosphorous transfer (Al→O→P) and then a second transfer back to aluminums (P→O→Al) [21]. In its 3D version, an evolution time on ^{31}P is introduced in between these two transfers [22]. Thus, on $AlPO_4$-14, these experiments provided information on through-bond correlations, 'relayed' through phosphorous atoms, between aluminum nuclei separated by four chemical bonds via two consecutive scalar ($^2J_{Al\text{-}O\text{-}P}$) couplings. However, this approach is not very efficient and it required a one-day (2D) and a seven-day (3D) acquisition on a 17.6 T spectrometer. Moreover, these experiments were performed with MAS quadrupolar averaging only, which does not provide high-resolution spectra due to second-order quadrupolar broadenings. Therefore, these experiments should be mainly reserved to very high-field spectrometers to decrease these second-order broadenings.

Here indirect covariance 2D approach is proposed, which generates a homo-nuclear correlation (HOMCOR) spectrum from a hetero-nuclear correlation (HETCOR) spectrum. This approach can save a lot of experiment time, which allows improving the resolution by introducing an MQMAS [24] or STMAS [25] high-resolution filter in case of half-integer quadrupolar nuclei. Therefore, in opposite to H-HSQC, the 2D-IC method does not require very high-magnetic fields to resolve the homo-nuclear cross-peaks of half-integer quadrupolar nuclei.

(1) Generalities

Let us start with a 2D hetero-nuclear (I,S) temporal signal with S observed spins: $s(t_1,t_2)$. After 2D-FT, this signal is converted in a 2D frequency matrix signal $S(\omega_I,\omega_S)$, from which only the real part is kept after phasing and apodization. From this initial matrix, two slightly different matrices can be computed by indirect covariance:

$$C(\omega_{I1},\omega_{I2}) = \int S(\omega_{I1},\omega_S)\cdot S(\omega_{I2},\omega_S)d\omega_S = S\cdot S^T \tag{6.3}$$

$$F(\omega_{I1},\omega_{I2}) = \sqrt{C(\omega_{I1},\omega_{I2})} = \sqrt{S\cdot S^T} \tag{6.4}$$

These HOMCOR I-spin spectra are real and symmetric, and they are called 'indirect' (through S-spins) covariance (C) and cross-correlation (F) spectra, respectively[26]. The spectral resolution of these indirect spectra is determined by the total evolution time in the HETCOR experiment. There are two types of resonance in the 2D HOMCOR spectra, which can be observed either as diagonal or cross peaks. None of them exist when the I species is not connected to any S species. As long as one I species is connected to at least one S species, there is a diagonal peak in the indirect spectra. Therefore, the presence of a diagonal peak does not prove that this I atom is connected, through S atoms, to another equivalent I atom. A cross-peak emerges when two different I resonances exhibit a connectivity with the same S resonance. Equations (6.4) also apply to S spins detected 'indirectly' through I nuclei. However, in opposition to the previous I indirect spectra, the spectral resolution of the S HOMCOR spectra can be very good, without any time-consuming experiment, as it is only determined by the analog-digital sampling resolution used in the HETCOR spectrum.

(2) Diagonal noise in covariance 2D spectra

Let us consider the noise of the 2D-IC spectrum $C_N(\omega_{I1},\omega_{I2})$. This noise is generated from that observed on the two hetero-nuclear slices along ω_S: $S_N(\omega_{I1},\omega_S)$ and $S_N(\omega_{I2},\omega_S)$. When ω_{I1} is very different from ω_{I2}, it is clear from Eq.(6.3) that the multiplication of the two different stochastic noises can be randomly positive or negative, and thus the summation of the noise along ω_S to obtain $C_N(\omega_{I1},\omega_{I2})$ (Eq.(6.3)) is small and can also be randomly positive or negative. When ω_{I1} is equal to ω_{I2}, the two hetero-nuclear slices along ω_S are identical, so that their noises, and the product $S_N(\omega_{I1},\omega_S).S_N(\omega_{I2},\omega_S)$ is always positive, whatever may be the ω_S value. Therefore, the summation of the noise along ω_S in Eq.(6.3) has a maximum positive value onto the diagonal of all (direct or indirect) covariance spectra. When $\omega_{I1} \approx \omega_{I2}$, the summation of the noise along ω_S is positive, but its amplitude decreases as noise along ω_{I1} and ω_{I2} get uncorrelated.

When the spectral-widths used along ω_I and ω_S are much smaller than the probe band-widths, the noise can be considered as constant in the 2D HETCOR signal. The diagonal noise in all covariance-based 2D spectra has then a constant positive amplitude and line-shape. It is then easy to define several locations onto this diagonal where there is no resonance a priori, to verify that this noise-power ridge is constant and then to subtract it all along the diagonal. This simple method allows decreasing the correlated noise level close to the diagonal. This is especially important in solid-state NMR where S/N ratio is often small, if two resonance frequencies are close

each other.

(3) Experimental

We have chosen to test the 2D-IC method in solids using a through-bond experiment on half-integer quadrupolar nuclei under high-resolution. We have used the MQ-*J*-HETCOR sequence [27, 28], which is a combination of the MQMAS method that refocuses second-order quadrupolar broadenings [24] and of the refocused INEPT that uses hetero-nuclear *J* transfers [29, 30]. To increase the S/N ratio, we have used its very recent SPAM (soft-pulse added mixing) version, which employs all coherence levels after the second hard-pulse to double the signal[31]. ^{27}Al-^{31}P SPAM-MQ-*J*-HETCOR spectra were acquired at 9.4 T on a Bruker Avance-II spectrometer equipped with a 4mm triple tuned (HXY) MAS probe at ν_R = 14 kHz. The RF-field amplitudes were of 50 kHz on the phosphorous INEPT part, and of 110 and 7 kHz for the hard and soft pulses, respectively, for the aluminum MQMAS part. To obtain the best resolution, we have used simultaneously two strong RF fields (80 kHz) during acquisition of the phosphorous FIDs: the first for a TPPM [32] proton irradiation, and the second for short-pulses at the aluminum frequency [33].

We have tested the 2D-IC approach on a powder sample of $AlPO_4$-14, which was also used to test the H-HSQC experiment [21, 22]. This sample was templated using isopropylamine and studied in the as-synthesized state. The structure is made of 4-, 6-, and 8-rings pores. Its space group is ***P*1** with an inversion center [34]. The unit cell composition corresponds to $Al_8P_8O_{32}(OH)^-_2$ for the framework, plus two protonated isopropylamine $(C_3H_{10}N)^+$ ions and two water molecules [34] that perform motions on the microsecond timescale in the 8-ring channels [35]. These molecular motions are the reason [35, 36] why we could not replace the quadrupolar MQMAS filter by the more efficient STMAS filter [37]. This AFN-type material forms a 3D channel system, made of alternating AlO_x (x = 4, 5, 6) and PO_4 polyhedrons, with 8-ring pores containing

four different P and four different Al sites [34, 35, 38-40]. However, even with our efficient $^{1}H/^{27}Al$ decoupling methods [33], the two phosphorous sites P_1 and P_4 are only partly resolved due to the medium field used (9.4 T). Each phosphorus is connected to four aluminum atoms via an oxygen atom as follows: P_1 ($1Al_1$, $2Al_2$, $1Al_3$), P_2 ($1Al_1$, $1Al_2$, $2Al_4$), P_3 ($1Al_1$, $2Al_3$, $1Al_4$) and P_4 ($1Al_1$, $1Al_2$, $1Al_3$, $1Al_4$) (Fig.6.6). Each aluminum is connected to four phosphorous atoms via an oxygen atom. However, Al_1 and Al_4 are also additionally connected to either one or two OH^- groups, respectively (Table 6.1).

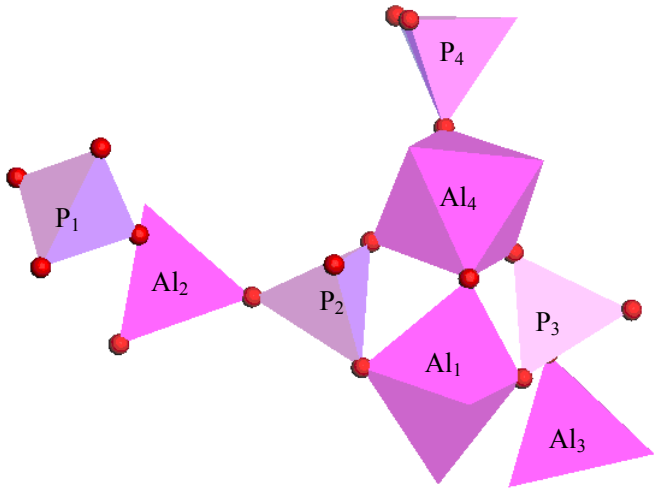

Fig.6.6. $AlPO_4$-14 structure in polyhedral mode

Table 6.1. Al-O-P-O-Al and Al-O-Al through-bond connectivities. To simplify the notation, the linking oxygen atoms have been omitted in the Al-O-P-O-Al description.

	Al_2-$P_{1,2,4}$-Al_1	Al_3-$P_{1,3,4}$-Al_1	Al_4-$P_{2,3,4}$-Al_1
Al_1-$P_{1,2,4}$-Al_2	Al_2-P_1-Al_2	**Al_3-$P_{1,4}$-Al_2**	Al_4-$P_{2,4}$-Al_2
Al_1-$P_{1,3,4}$-Al_3	**Al_2-$P_{1,4}$-Al_3**	Al_3-P_3-Al_3	Al_4-$P_{3,4}$-Al_3
Al_1-$P_{2,3,4}$-Al_4	Al_2-$P_{2,4}$-Al_4	Al_3-$P_{3,4}$-Al_4	Al_4-P_2-Al_4
Al_1-O_9-H^-			Al_4-$O_{9,9'}$-H^-

The quadrupolar coupling constants C_Q and asymmetry parameters η_Q of $Al_{1,2,3,4}$ are equal to 5.58, 4.08, 1.74 and 2.57 MHz and 0.97, 0.82, 0.63 and 0.7, respectively[38]. The complete ^{27}Al–^{31}P SPAM-MQ-*J*-HETCOR spectrum is shown in Fig.6.7. Although peaks P_1 and P_4 are adjacent, the three aluminums Al_1, Al_2 and Al_3 are really connected with these two phosphorous species simultaneously, and hence there will be no artificial cross-peak between these three aluminums in the ^{27}Al-^{27}Al *J*-coupled 2D-IC spectrum. Moreover, Al_4 connects to P_3 as Al_1 and Al_3 do, and Al_4 connects to P_2 as Al_2 does. Therefore, all ^{27}Al-^{27}Al cross-peaks will have true physical meaning in the *J*-coupled 2D-IC spectrum.

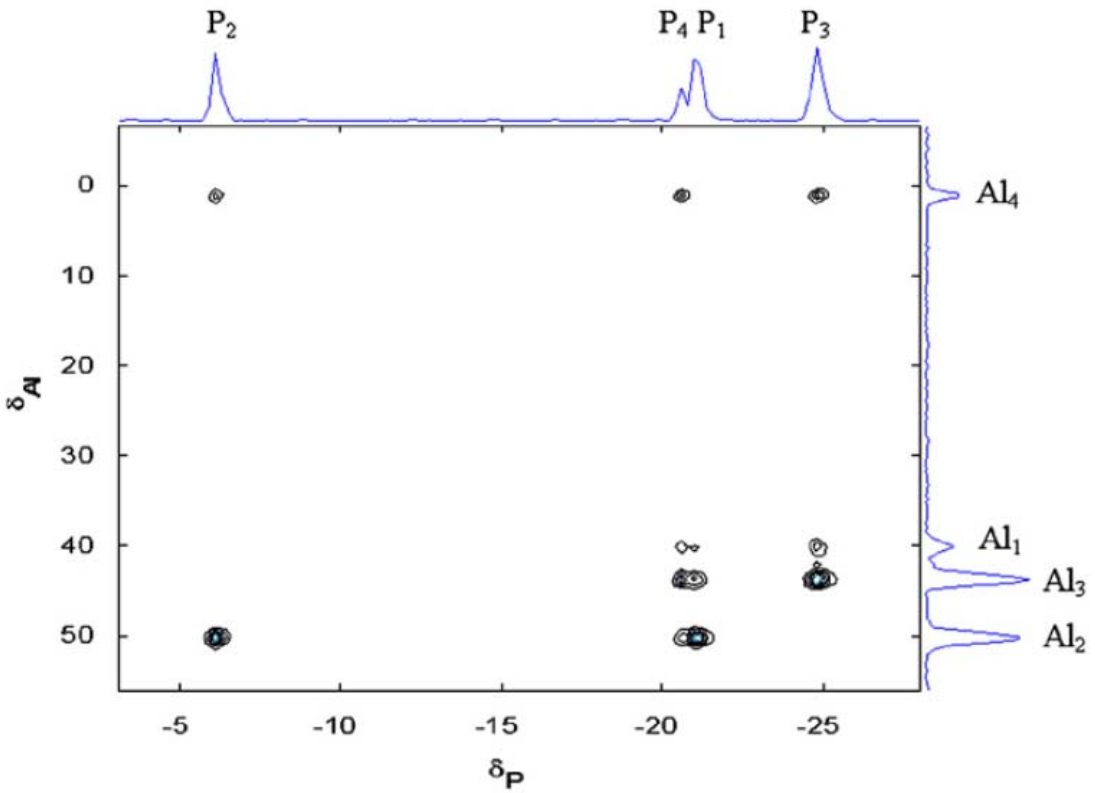

Fig.6.7. ^{27}Al-^{31}P SPAM-MQ-*J*-HETCOR spectrum of $AlPO_4$-14, with skyline projections, recorded with ^{1}H-TPPM and ^{27}Al multi-pulse decoupling. 96 scans were acquired for each of the 85 t_1 increments. When taking into account the hyper-complex acquisition method and a recycling delay of 250 ms, the experimental time is equal to 68 min.

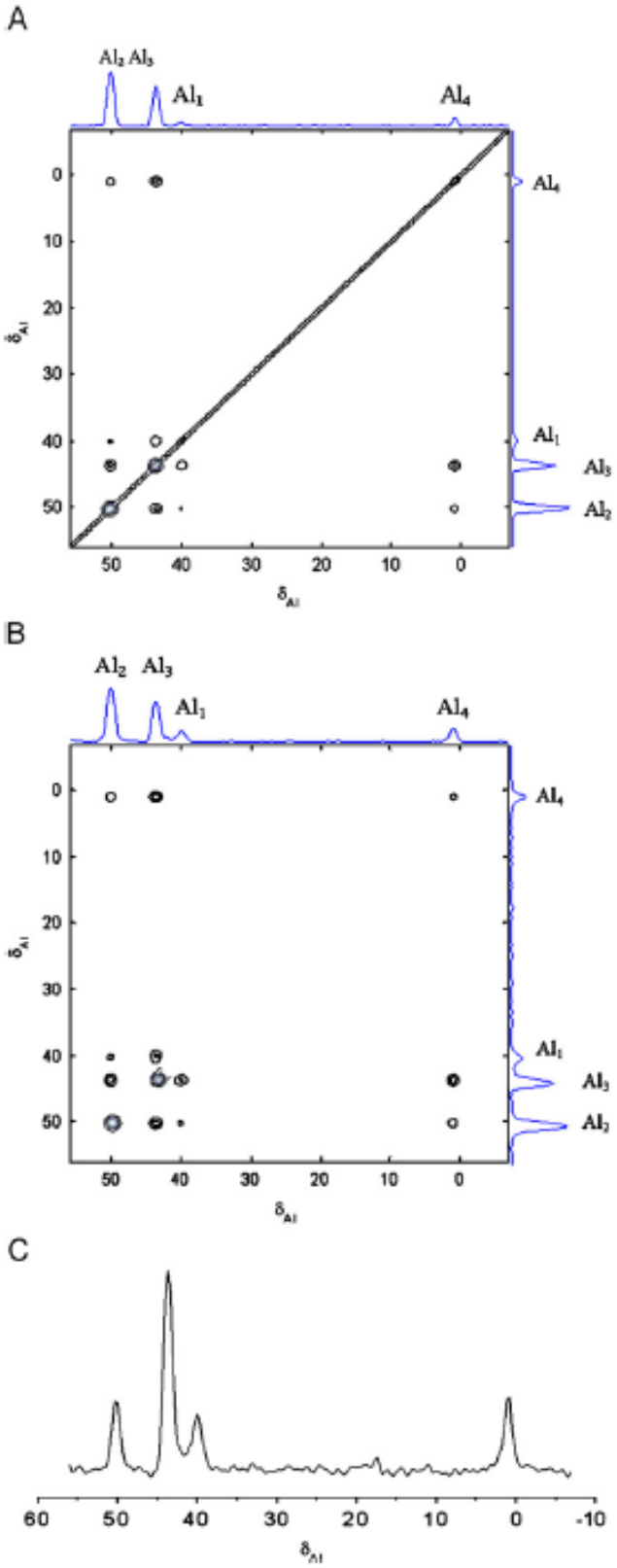

Fig.6.8. High-resolution ^{27}Al-^{27}Al *J*-coupled 2D-IC spectra of $AlPO_4$-14, with skyline projections, with (A) and without (B) the diagonal noises. (C) is a slice along the Al_3 peak (δ_{iso} = 44 ppm). S/N ratios are ≈ 64 and 23 for the diagonal and cross peaks, respectively.

(4) Indirect covariance 2D spectra

The ^{31}P-'detected' ^{27}Al-^{27}Al *J*-coupled 2D-IC spectrum, shown in Fig.6.8A, is generated from the ^{27}Al-^{31}P SPAM-MQ-*J*-HETCOR spectrum. There is a strong diagonal line in this figure, which is due to auto-correlated noise. After subtracting this noisy diagonal ridge, we have obtained the spectrum shown in Fig.6.8B. It can be observed that, due to the mathematical treatment we used, 2D-IC spectra displayed in Fig.6.8A,B are perfectly symmetrical. This is opposite to 2D-FT spectra (e.g. see cross-peaks Al_1-$P_{2,3,4}$-Al_4 and Al_4-$P_{2,3,4}$-Al_1 in Fig.3 of [21]), where losses act in a different way during the evolution (t_1) and acquisition (t_2) times.

Diagonal and cross peaks associated with sites Al_1 and Al_4 only are notably less intense than those associated with sites Al_2 and Al_3 (those associate with Al_1 are even hardly visible in Fig.6.8B). This was also the case with the H-HSQC experiment [21]. This effect is related to the fact that (Al_1, $P_{1,2,3,4}$) and (Al_4, $P_{2,3,4}$) peaks are weaker in the HETCOR spectrum than other peaks (Fig.6.7). Two possible factors may have contributed to this result. First, the efficiencies of the INEPT and MQMAS transfers decrease with increasing quadrupole interactions[28]. This decrease of efficiency applies to Al_4 and especially to Al_1. Second, this phenomenon may also be due to the fact that $^2J_{Al\text{-}O\text{-}P}$ couplings reduce when one aluminum atom coordinates with more atoms, and Al_1 and Al_4 are five and six-coordinated, respectively.

Let us compare our experimental results with those previously obtained with H-HSQC on the same sample. First, diagonal peaks, always have a positive sign in 2D-IC, whereas those with a physical meaning or due to incomplete transfer have

opposite signs in H-HSQC, which can lead to their global cancellation. Second, the *J*-coupled 2D-IC spectrum shows a very good sensitivity, which is demonstrated by selecting a slice along Al_3 (Fig.6.8C). The S/N ratio measured on the highest peak is equal to 64 with a 2D spectrum recorded at 9.4 T with only 96 scans. Third, the 2D-IC spectrum has also a very good resolution as it clearly separates all peaks, such as the (Al_2-$P_{1,4}$-Al_3) cross-peak and the (Al_3) diagonal peak, which were completely overlapping in the H-HSQC spectrum. Actually, the two (Al_2-$P_{1,4}$-Al_3) and (Al_3-$P_{1,4}$-Al_2) cross-peaks were overlapping with the two (Al_2 and Al_3) diagonal peaks, to give a single broad resonance in the H-HSQC experiment, in spite of the high-field used (17.6 T). The 2D-IC approach has also the last advantage that it can produce ^{31}P-^{31}P correlation spectrum, indirectly detected through ^{27}Al, from the same parent ^{27}Al-^{31}P HETCOR spectrum (Fig.6.9A). Globally, the initial ^{27}Al-^{31}P HETCOR spectrum can thus also be used to obtain ^{27}Al-^{27}Al and ^{31}P-^{31}P HOMCOR spectra, which altogether give the same information as the 3D H-HSQC method [22] in cases of such samples made of AlO_x and PO_4 polyhedrons, but much faster and under high-resolution. It is interesting to note that the ^{31}P-^{31}P *J*-coupled 2D-IC spectrum does not show the (P_2, P_3) cross-peaks, as related to the Al-P connectivities. In addition, the method has separated peaks P_1 and P_4, at only 9.4 T, which is demonstrated by selecting the slice along the P_2 peak (Fig.6.9B).

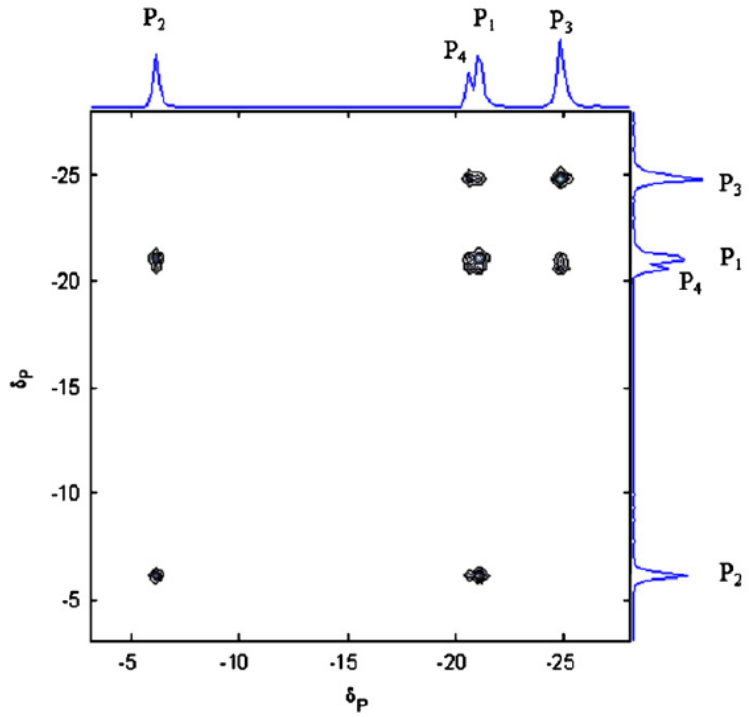

(A)

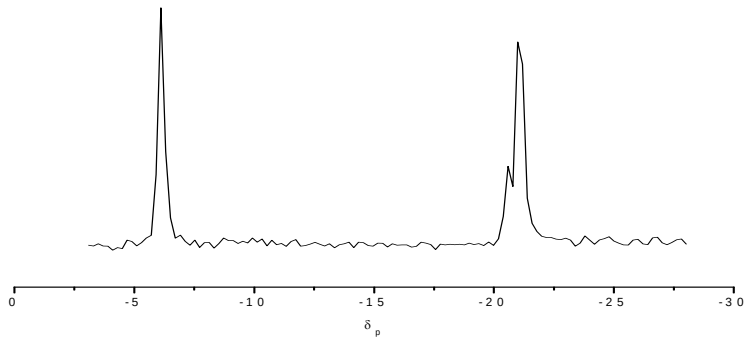

(B)

Fig.6.9. (A) ^{31}P-^{31}P *J*-coupled 2D-IC spectrum of $AlPO_4$-14 without any correlated diagonal noise. (B) is a slice in (A) along the P_2 peak (δ_{iso} = -5.8 ppm).

(5) Conclusions

Indirect-correlation (2D-IC) spectroscopy is easily implemented in solid-state NMR to generate HOMCOR spectra. We have demonstrated that the high-resolution 2D-IC *J*-coupled ^{27}Al-^{27}Al spectrum, generated from a MQ-*J*-HETCOR spectrum has

better resolution and sensitivity than the previous 2D HOMCOR H-HSQC spectrum[21]. The method provides the other advantage that it produces two kinds of HOMCOR spectra from a single HETCOR spectrum. However, it must be reminded that both methods (2D-IC and 2D H-HSQC) only provide *J*-coupled 'relayed' or 'indirectly detected' (through ^{31}P) through-bond connectivities. This means that their spectra can only be easily interpreted in case of 'polyhedral'-type materials, such as $AlPO_4$. In such compounds, they lead to the same information. Actually, they are only a different, but easier, way to interpret HETCOR results in the framework of homo-nuclear connectivities. Obviously, the 2D-IC tool can be extending to generate other high-resolution HOMCOR spectra, such as those related to through-space connectivities[27, 31].

References

1. Bodart, P. R.; Amoureux, J. P.; Taulelle, F., ANAFOR: application of restricted linear least-squares procedure to NMR data processing. *Solid. State. NMR* 2002, 21, 1-20.
2. Ashida, J.; Kupce, E.; Amoureux, J. P., Hadamard NMR spectroscopy in solids. *J. Magn. Reson.* 2005, 177, 474-480.
3. Bruschweiler, R.; Zhang, F., Covariance nuclear magnetic resonance spectroscopy. *Journal of Chemical Physics* 2004, 120, (11), 5253-5260.
   Hu, B. W.; Zhou, P.; Noda, I.; Zhao, G. Z., An NMR approach applicable to biomolecular structure characterization. *Analytical Chemistry* **2005,** 77, (23), 7534.
   Hu, B. W.; Zhou, P.; Noda, I.; Ruan, Q. X., Generalized two-dimensional correlation analysis of NMR and Raman spectra for structural evolution characterizations of silk fibroin. *Journal of Physical Chemistry B* **2006,** 110, (36), 18046.
4. States, D. J.; Haberkorn, R. A.; Ruben, D. J., A two dimensional nuclear Overhauser experiment with pure absorption phase in four quadrants. *J. Magn. Reson.* 1982, 48, 286–292.
5. Bax, A.; Freeman, R.; Kempsell, S. P., Investigation of C^{13}–C^{13} long-range couplings in natural-abundance samples. *J. Magn. Reson.* 1980, 41, 349–353.
6. Noda, I., Two-dimensional infrared spectroscopy. *J. Am. Chem. Soc.* 1989, 111, (21), 8116-8118.
7. Noda, I., Generalized 2-Dimensional Correlation Method Applicable to Infrared, Raman, and Other Types of Spectroscopy. *Appl. Spectrosc.* 1993, 47, (9), 1329-1336.
8. Noda, I., Determination of two-dimensional correlation spectra using the Hilbert transform. *Appl. Spectrosc.* 2000, 54, (7), 994-999.
9. Noda, I.; Dowrey, A. E.; Marcott, C.; Story, G. M.; Ozaki, Y., Generalized two-dimensional correlation spectroscopy. *Appl. Spectrosc.* 2000, 54, (7), 236A-248A.
10. Eads, C. D.; Noda, I., Generalized correlation NMR spectroscopy. *J. Am. Chem. Soc.* 2002, 124, (6), 1111-1118.

11. Bruschweiler, R., Theory of covariance nuclear magnetic resonance spectroscopy. *Journal of Chemical Physics* 2004, 121, (1), 409.
12. Trbovic, N.; Smirnov, S.; Zhang, F.; Bruschweiler, R., Covariance NMR spectroscopy by singular value decomposition. *Journal of Magnetic Resonance* 2004, 171, (2), 277.
13. Hohwy, M.; Jakobsen, H. J.; Eden, M.; Levitt, M. H.; Nielsen, N. C., Broadband dipolar recoupling in the nuclear magnetic resonance of rotating solids: A compensated C7 pulse sequence. *Journal of Chemical Physics* 1998, 108, (7), 2686.
14. Hohwy, M.; Rienste, C. M.; Jaroniec, C. P.; Griffin, R. G., Fivefold symmetric homonuclear dipolar recoupling in rotating solids: application to double-quantum spectroscopy. *J. Chem. Phys.* 1999, 110, 7983-7992.
15. Bennett, A. E.; Ok, J. H.; Griffin, R. G.; Vega, S., Chemical shift correlation spectroscopy in rotating solids: radio-frequency driven dipolar recoupling and longitudinal exchange. *J. Chem. Phys.* 1992, 96 8624-8627.
16. Hartmann, P.; Vogel, J.; Freidrich, U.; Jäger, C., Nuclear magnetic resonance investigations of aluminum containing phosphate glass-ceramics. *J. Non-Cryst Solids* 2000, 263&264, 94-100.
17. Tricot, G.; Delevoye, L.; Palavit, G.; Montagne, L., Phase identification and quantification in a devitrified glass using homo- and heteronuclear solid-state NMR. *Chem. Commun.* 2005, 42, 5289-5291.
18. Ernst, R. R.; Bodenhausen, G.; Wokaun, A., *Principles of Nuclear Magnetic Resonance in One and Two Dimensions*. Oxford University Press: 1990.
19. Lesage, A.; Bardet, M.; Emsley, L., Through-bond carbon-carbon connectivities in disordered solids by NMR. *Journal of the American Chemical Society* 1999, 121, (47), 10987.
20. Fayon, F.; Le Saout, G.; Emsley, L.; Massiot, D., Through-bond phosphorus-phosphorus connectivities in crystalline and disordered phosphates by solid-state NMR. *Chemical Communications* 2002, (16), 1702.
21. Deschamps, M.; Fayon, F.; Montouillout, V.; Massiot, D., Through-bond

homonuclear correlation experiments in solid-state NMR applied to quadrupolar nuclei in Al-O-P-O-Al chains. *Chemical Communications* 2006, (18), 1924.

22. Deschamps, M.; Massiot, D., Three-dimensional through-bond homonuclear-heteronuclear correlation experiments for quadrupolar nuclei in solid-state NMR applied to 27Al-O-31P-O-27Al networks. *Journal of Magnetic Resonance* 2007, 184, (1), 15-19.
23. Kundla, E.; Samoson, A.; Lippmaa, E., High-resolution NMR of quadrupolar nuclei in rotating solids. *Chem. Phys. Lett.* 1981, 83, 229-232.
24. Frydman, L.; Harwood, J. S., Isotropic spectra of half-integer quadrupolar spins from bidimensional magic-angle spinning NMR. *Journal of the American Chemical Society* 1995, 117, (19), 5367.
25. Gan, Z., Isotropic NMR spectra of half-integer quadrupolar nuclei using satellite transitions and magic-angle spinning. *Journal of the American Chemical Society* 2000, 122, (13), 3242.
26. Zhang, F.; Bruschweiler, R., Indirect covariance NMR spectroscopy. *Journal of the American Chemical Society* 2004, 126, (41), 13180.
27. Wiench, J. W.; Pruski, M., Probing through bond connectivities with MQMAS NMR. *Solid State NMR* 2004, 26, 51–55.
28. Amoureux, J. P.; Trebosc, J.; Wiench, J.; Pruski, M., HMQC and refocused-INEPT experiments involving half-integer quadrupolar nuclei in solids. *Journal of Magnetic Resonance* 2007, 184, (1), 1.
29. Morris, G. A., Sensitivity enhancement in 15N NMR: polarization transfer using the INEPT pulse sequence. *J. Am. Chem. Soc.* 1980, 105, 428-429.
30. Burum, D. P.; Ernst, R. R., Net polarization transfer via a J-ordered state for signal enhancement of low sensitivity nuclei. *J. Magn. Reson.* 1980, 39, 163-168.
31. Wiench, J. W.; Tricot, G.; Delevoye, L.; Trebosc, J.; Frye, J.; Montagne, L.; Amoureux, J. P.; Pruski, M., SPAM-MQ-HETCOR: An improved method for heteronuclear correlation spectroscopy between quadrupolar and spin-1/2 nuclei in solid-state NMR. *Physical Chemistry Chemical Physics* 2006, 8, (1), 144.
32. Bennett, A. E.; Rienstra, C. M.; Auger, M.; Lakshmi, K. V.; Griffin, R. G.,

Heteronuclear decoupling in rotating solids. *J. Chem. Phys.* 1995, 103, 6951-6958.

33. Delevoye, L.; Trebosc, J.; Gan, Z.; Montagne, L.; Amoureux, J. P., Resolution enhancement using a new multiple-pulse decoupling sequence for quadrupolar nuclei. *Journal of Magnetic Resonance* 2007, 186, (1), 94.
34. Broach, R. W.; Wilson, S. T.; Kirchner, R. M., Corrected crystallographic tables and figure for as-synthesized AlPO4-14. *Microporous Mesoporous Mater* 2003, 57, 211-214.
35. Antonijevic, S.; Ashbrook, S. E.; Biedasek, S.; Walton, R. I.; Wimperis, S.; Yang, H., Dynamics on the microsecond timescale in microporous aluminophosphate AlPO4-14 as evidenced by 27Al MQMAS and STMAS NMR spectroscopy. *J. Am. Chem. Soc.* 2006, 128, 8054-8062.
36. Ashbrook, S. E.; Antonijevic, S.; Berry, A. J.; Wimperis, S., Motional broadening: an important distinction between multiple-quantum and satellite-transition MAS NMR of quadrupolar nuclei. *Chem. Phys. Lett.* 2002, 364 634-642.
37. Trebosc, J.; Amoureux, J.-P.; Gan, Z. H., Comparison of high-resolution solid-state NMR MQMAS and STMAS methods for half-integer quadrupolar nuclei. *Solid State NMR* 2007, 31, 1-9.
38. Fernandez, C.; Amoureux, J. P.; Chezeau, J. M.; Delmotte, L.; Kessler, H., 27Al MAS NMR characterization of AlPO4-14. Enhanced resolution and information by MQMAS. *Micropor. Mat.* 1996, 6, 331-340.
39. Fyfe, C. A.; Altenschildesche, H. M. z.; Wong-Moon, K.; Grondey, H.; Chezeau, J. M., 1D and 2D solid state NMR investigations of the framework structure of As-synthesized AlPO4-14. *Solid. State. NMR* 1997, 9, 97-106.
40. Delevoye, L.; Fernandez, C.; Morais, C. M.; Amoureux, J. P.; Montouillout, V.; Rocha, J., Double-resonance decoupling for resolution enhancement of 31P solid-state MAS and 27Al-31P MQHETCOR NMR. *Solid State Nuclear Magnetic Resonance* 2002, 22, (4), 501-512.

Chapter 7. Applications of SAM and *D*-HMQC

In this chapter, we will discuss the applications of SAM and *D*-HMQC.

7.1. Applications of SAM decoupling in *D*-HMQC experiments

As shown in chapter 3, the *D*-HMQC pulse sequences can be applied to observe lower γ nuclei, such as ^{13}C or ^{14}N, through nearby high-γ isotopes, such as ^{1}H. Proton is an ideal spy nucleus because of its high gyromagnetic ratio and its high isotopic natural abundance. However, this combination generally entails strong homonuclear couplings among the protons. These homogeneous anisotropic interactions are not completely averaged out by the MAS, and hence, the ^{1}H-^{1}H strong dipolar couplings can reduce the sensitivity of *D*-HMQC experiments as well as the spectral resolution in both direct (F_2) and indirect (F_1) dimensions.

The enhancement of resolution in F_1 and F_2 dimensions requires the use of windowless and windowed homonuclear decoupling sequences in the t_1 and t_2 periods, respectively. We explore the use of SAM4 irradiation on the detected channel during t_1 and t_2. In the t_1 dimension, SAM4 was divided into two parts; each part includes half of SAM4. In the t_2 dimension, wSAM4 was applied.

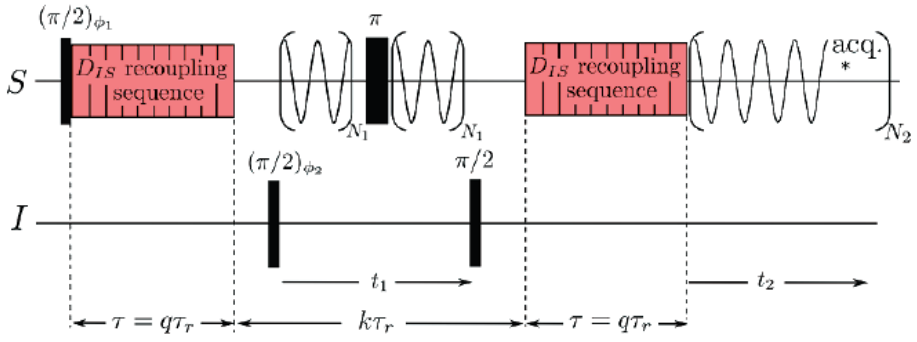

Fig. 7.1. Pulse sequences for D-HMQC experiments with SAM4 irradiations applied during t_1 and t_2 evolution periods, respectively.

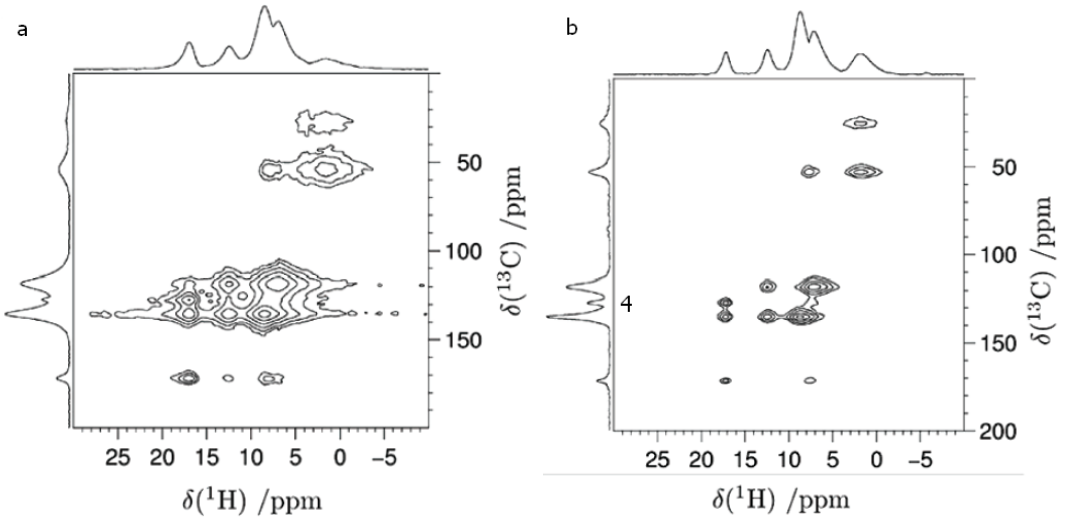

Fig. 7.2. Experimental 2D ^{1}H-^{13}C *D*-HMQC spectra of isotopically unmodified L-histidine.HCl at ν_R =31.746 kHz and B_0=9.4T. (a) and (b) were recorded without and with SAM4 decoupling, respectively. ^{13}C-^{1}H dipolar couplings were restored by applying $SR4_1^2$ recoupling to the detected ^{1}H channel.

Figure 7.2 shows the 2D ^{1}H-^{13}C *D*-HMQC spectra of isotopically unmodified L-histidine.HCl. The $SR4_1^2$ sequences were applied to the detected ^{1}H channel in order to suppress the D_{HH} dephasing during the recoupling time. Figure 7.2a shows the 2D *D*-HMQC spectra recorded without homonuclear decoupling, while Figure 7.2b displays the 2D *D*-HMQC spectrum obtained when applying SAM4 homonuclear decoupling during t_1 and t_2 periods, respectively. The comparison of Figure 7.2a and 7.2b clearly evidences that SAM4 homonuclear decoupling sequences allow improving the spectral resolution in both F_1 and F_2 dimensions. In particular, the C_4 signal is resolved in the F_1 projections of Figure 7.2b whereas it is hardly visible in the projections of Figure 7.2a. More quantitatively, the use of SAM4 decoupling yields a 3-fold decrease in line width of the carbon peaks, while the scaled-up line width of the proton peaks are divided by a factor of 2 when employing wSAM4 irradiation during the t_2 period. More theoretical details could be found in the ref [1].

7.2. Applications of *D*-HMQC in ^{14}N systems

Nitrogen is a nucleus of considerable chemical and biological importance. Despite the high isotopic abundance (99.63 %) of nitrogen-14 (spin I = 1), it has remained very difficult to study with nuclear magnetic resonance (NMR) spectroscopy. Thus, nitrogen NMR has been mostly limited to the less abundant isotope ^{15}N, hence requiring isotopic enrichment. The main difficulty in observing ^{14}N arises from the large quadrupole interaction, which results in broad NMR spectra of molecules in both liquid and solid states. In solutions, the broadening comes from very fast quadrupolar relaxation mechanisms.

In solid-state samples, the large electric quadrupole moment results in spectra having a width of several MHz wide due to the first-order quadrupole interaction. The ^{14}N MAS study of powdered solids has therefore been reduced to samples with quadrupole coupling constants of $C_Q \sim 1$ MHz or less.[2-5] Tycko et al.,[6-8] have demonstrated overtone NMR spectroscopy, where spectra are only influenced by the much smaller second-order quadrupole interaction. Because these transitions are only weakly allowed and require the use of a very large radio-frequency (rf) field, overtone methods result in poor sensitivity.

Recently, Gan has shown that the combination of dipolar recoupling and HMQC (called *D*-HMQC),[9,12,13] is suitable for the efficient indirect detection of ^{14}N via through-space dipolar couplings while Cavadini et al.[10,11] has yielded a method for the indirect detection of ^{14}N via a combination of scalar *J*-couplings and residual dipolar splittings (RDS). Siegel showed that a 3D ^{1}H-^{13}C-^{14}N correlation spectrum of ^{13}C enriched L-histidine.HCl.H_2O sample could also be obtained using *D*-HMQC with $SR4_1^2$.[14] The efficiency of ^{13}C-^{14}N-^{13}C transfer was very weak (4-5%) and the experiment lasted 85 hours on a 18.8 T spectrometer. In order to decrease the experimental time it would be desirable to acquire one ^{1}H-^{14}N and two ^{1}H-^{13}C through-space 2D HETCOR spectra instead of running a 3D experiment: the first

^{1}H-^{13}C with cross-peaks related to all carbons, and the second where cross-peaks are only related to those carbons close to nitrogen atoms.

A method to obtain ^{14}N-edited ^{1}H-^{13}C spectra has already been proposed with the Saturation-Pulse Induced Dipolar Exchange with Recoupling (SPIDER).[15] The SPIDER experiment is mainly suitable for slow spinning rates ($\nu_R \approx 5$kHz), which are not sufficient to cancel the ^{13}C chemical shift anisotropy (CSA) on high-field spectrometers. We propose here a new magic angle spinning (MAS) ^{14}N-edited method for ^{1}H-^{13}C through-space HETCOR spectra to obtain high resolution in both dimensions. We combine latest hetero-recoupling (Simultaneous Frequency and Amplitude Modulation: $SFAM_2$)[16,17] and homo-decoupling (Smooth Amplitude Modulation: SAM_3)[18] techniques along with a filter based on ^{13}C-^{14}N *D*-HMQC experiment.

The pulse sequence and coherence transfer pathway diagrams proposed to obtain high-resolution ^{14}N-edited ^{1}H-^{13}C 2D correlation spectra of powdered samples under MAS and rotor-synchronization are shown in **Fig.7.3**.

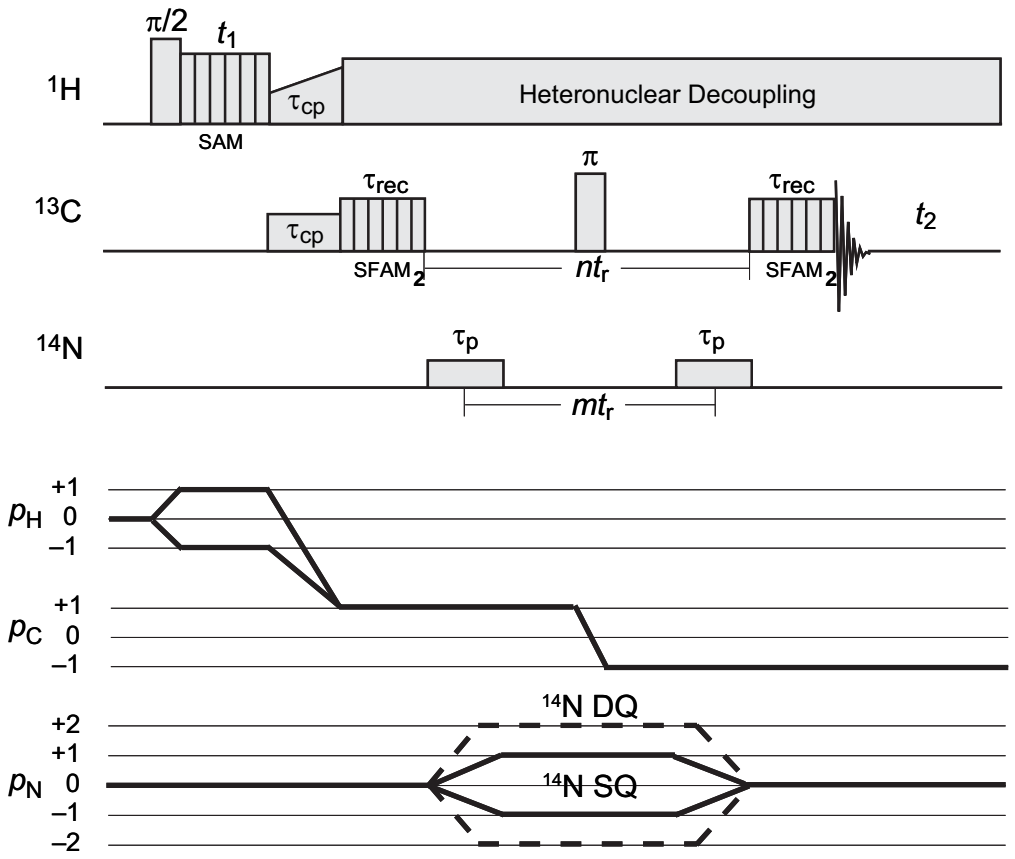

Fig.7.3. Pulse sequence and coherence transfer pathways for the ^{1}H-^{13}C CP HETCOR correlation NMR experiments implementing ^{14}N-editing via dipolar driven *D*-HMQC sequence. During the ^{14}N editing period it is possible to selectively choose single-quantum (SQ) (solid lines) or double-quantum (DQ) (dashed lines) ^{14}N coherences. Homo-nuclear ^{1}H decoupling sequences can be used during t_1, e.g., Smooth Amplitude Modulation (SAM),[18] in order to obtain high resolution ^{1}H spectra in the indirect dimension. Recoupling of dipolar interactions between ^{13}C and ^{14}N nuclei during the excitation and reconversion periods of *D*-HMQC can be achieved by Simultaneous Frequency and Amplitude Modulated ($SFAM_2$) pulses applied on ^{13}C nuclei.[17] The time between two blocks of $SFAM_2$ pulses should be equal to a multiple of the number of rotor periods (nt_r). It is also important to adjust the delay between the centers of the two nitrogen pulses to be equal to a multiple numbers of rotor periods (mt_r) with $n \geq m$. Efficient hetero-nuclear decoupling is required to prevent ^{1}H-^{13}C coherences to be created.

Our test sample, L-histidine.HCl.H_2O (98% ^{13}C enriched), was purchased from Cortecnet and used without further purification. It has three different nitrogen sites **(Fig.7.4a)**, the ammonium nitrogen is bonded to three protons (H^N) and one carbon (C^α), while N^π and N^τ nitrogens of imadazole ring are bonded to one proton and two carbons: (H^π, C^2/C^4), and (H^τ, C^2/C^5), respectively. The samples were packed in 3.2 mm zirconia rotors and spun at ν_R = 17.5 kHz in a Bruker triple resonance MAS probe at 18.8 T magnetic field (^1H, ^{13}C and ^{14}N Larmor frequencies of 800, 201 and 58 MHz respectively). Spectra were recorded using a Bruker Avance II console. Cross-polarization (CP) was used with $\nu_{1,1H}$ = 70 kHz and $\nu_{1,13C}$ = 52.5 kHz. The $SFAM_2$ scheme was used for ^{13}C-^{14}N recoupling with a carbon rf peak amplitude of $\nu_{1,13C}^{peak}$ = 40 kHz and the offset modulated in extent of 10 kHz. The ^1H homo-nuclear SAM decoupling scheme was used with three rf periods for the cosine amplitude modulation, with constant phase, during a single rotor period (SAM_3), varying the proton rf amplitude up to $\nu_{1,1H}^{peak}$ = 70 kHz.

2D ^1H-^{13}C HETCOR spectra of L-histidine, with homo-nuclear decoupling, are shown in **Fig.7.4**, after ^1H rescaling. Total correlation between ^1H and ^{13}C is obtained using the standard CP-HETCOR sequence and all the carbon atoms are observed in **Fig.7.4b** as expected. Using sequence in **Fig.7.3**, with the SAM_3 decoupling during t_1, we obtain one spectrum that displays only ^{13}C resonances that are in close proximity to ^{14}N nuclei **(Fig.7.4c)**. The weak efficiency of the ^{13}C-^{14}N-^{13}C transfer is observable by comparing **Figs.7.4b** and **7.4c**. Indeed, the S/N ratio is much lower in **Fig.7.4c** than in **Fig.7.4b**, in spite of 32 more transients. One observes: (i) that H^α + H^β peak observed at c.a. 1.5 ppm in **Fig.7.4b** has disappeared in **Fig.7.4c**, (ii) that the two peaks corresponding to H^2 + H^N + CH^5 in **Fig.7.4b** (6-9 ppm) simplify into a single H^N peak in **Fig.7.4c** (9 ppm), and (iii) that H^π (≈ 16 ppm) and H^T (≈ 12 ppm) peaks are emphasized in **Fig.7.4c** with respect to **Fig.7.4b**. Spectra shown in **Fig.7.4** are only slightly more resolved along the F_1 dimension

than those displayed without homo-nuclear decoupling (not shown). Indeed, they have been recorded at ν_R = 17.5 kHz, and the resolution gain is expected to be more pronounced at higher spinning rates (c.a. 60-70 kHz) as shown recently.[18] However, faster spinning speed would require larger ^{1}H decoupling rf amplitude that are not available on our probe. Indeed, we noticed that a minimum ratio $\nu_{1\text{-}1H}/\nu_R \approx 5$ is necessary to prevent ^{1}H-^{13}C coherence built up during $SFAM_2$ recoupling periods that leads to signal decrease through spin diffusion on the proton side, in addition to lower resolution on ^{13}C spectrum. More details could be found in ref [19].

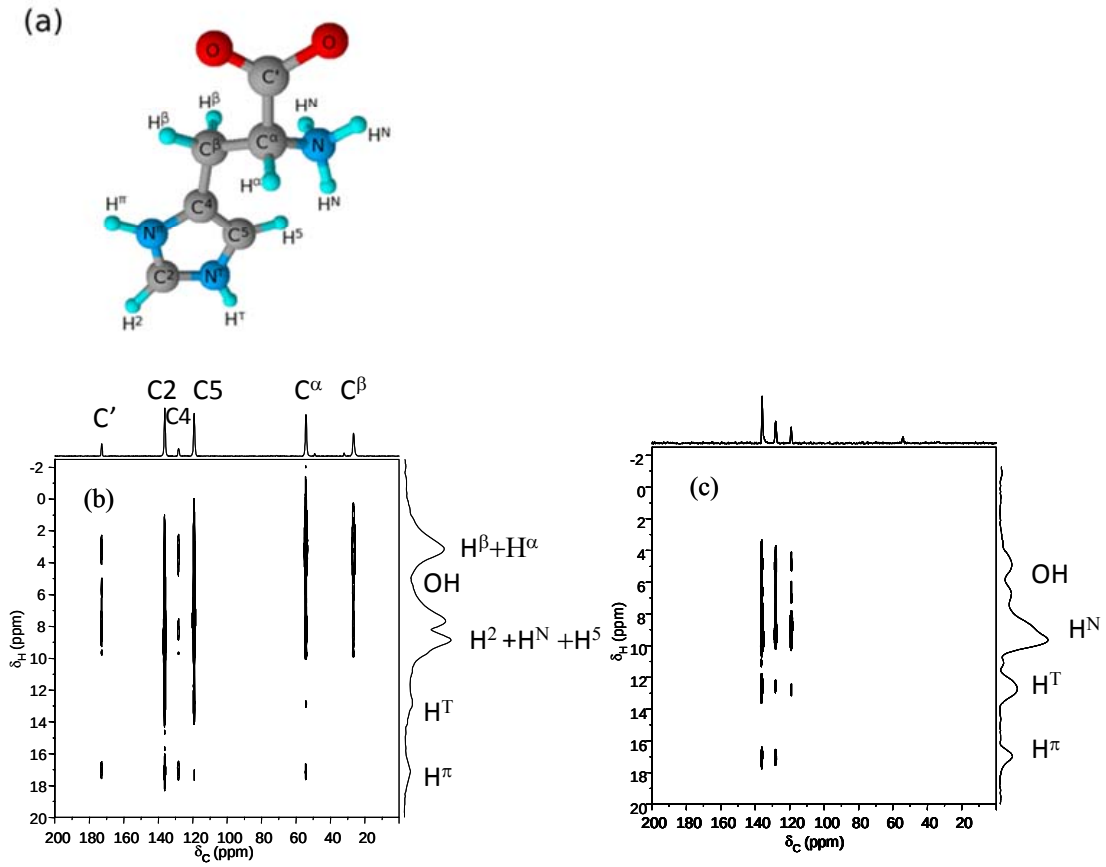

Fig. 7.4. (a) Molecular formula of L-histidine, and two-dimensional ^{1}H-^{13}C (b) CP HETCOR and (c) ^{14}N edited CP HETCOR NMR spectrum of polycrystalline L-histidine fully ^{13}C enriched. SAM_3 ^{1}H homo-nuclear decoupling scheme was applied during t_1 to record both spectra. Spectra (b,c) are acquired using a pulse sequence that selects pure SQ ^{14}N coherences during the *D*-HMQC step. Spectra are the result of averaging (b) 2 and (c) 64 transients for each of 30 t_1 increments with $\Delta t_1 = t_r = 57.1$ μs, with a relaxation interval of 5 s. The total experimental time has been of 10.6 (b) and 340 (c) min. The $SFAM_2$ recoupling intervals during excitation and reconversion wee $\tau_{rec} = 8t_r = 457$ μs, while the lengths of the two ^{14}N pulses were $\tau_p = 30$ μs. The rotor synchronization is achieved with n = 2 and m = 1. $B_0 = 18.8$ T with $\nu_R = 17.5$ kHz. ^{1}H-^{13}C CP-MAS : contact time = 500 μs, $\nu_{rf\text{-}1H} = 67.5$ kHz, $\nu_{1\text{-}13C} = 50$ kHz. ^{1}H decoupling : $\nu_{1\text{-}1H} = 80$ kHz. ^{13}C π and π/2 pulses : $\nu_{1\text{-}13C} = 50$ kHz.

7.3. Adiabatic pulse for *D*-HMQC

As discussed previously, *D*-HMQC combined with ^{14}N filtered pulses could be used to select ^{13}C nuclei in proximity to a nitrogen atom. However, this kind of experiment is not efficient due to the use of the two ^{14}N hard-pulses, which are too weak to irradiate correctly all atoms due to the large frequency spread (on the order of a few MHz) of powder pattern. However, it is well-known that this problem of very large frequency irradiation can be overcome by using an adiabatic pulse, and this principle has very recently been used by Z. Gan to acquire first-order ^{14}N quadrupolar spectra with ^{13}C detection under MAS.[20] In this experiment, the pair of ^{14}N short pulses of the HMQC experiment is replaced by a single adiabatic pulse, which partly reintroduces the ^{13}C-^{14}N dipolar interaction. The first-order ^{14}N quadrupolar spectra can be obtained by measuring the difference between ^{13}C signal intensities, with and without ^{14}N pulse, versus the ^{14}N frequency.

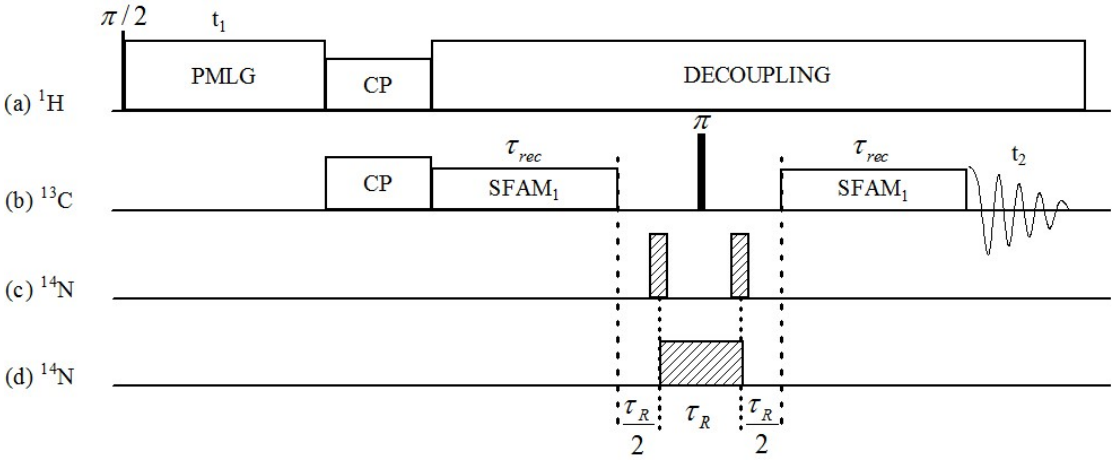

Fig 7.5. Pulse sequences for the ^{1}H-^{13}C heteronuclear correlation NMR experiments implementing ^{14}N-editing via dipolar driven *D*-HMQC sequence (a-c) or adiabatic ^{14}N change of states (a,b,d). The usual ^{1}H-^{13}C CP-HETCOR spectrum is obtained with no ^{14}N rf irradiation (S_0). In order to enhance ^{1}H resolution in the indirect dimension, homo-nuclear $PMLG5^{x\bar{x}}_{mm}$ decoupling sequence has been used during t_1.[21] Recoupling of ^{13}C-^{14}N dipolar interactions is achieved by $SFAM_1$ irradiations applied on ^{13}C nuclei.

We use here this adiabatic pulse to detect carbons that are close to nitrogen atoms and the pulse sequences are shown in **Fig.7.5**. Two ^{1}H-^{13}C 2D experiments must be performed: one with (S_1) and the second without (S_0) ^{14}N irradiation. S_0 corresponds to the classical ^{1}H-^{13}C dipolar HETCOR spectrum and $S_0 - S_1$ to the ^{14}N edited one.

According to Gan's communication, a ^{14}N pulse longer than one rotor period can generate a ν_R modulation of ^{14}N signal.[20] For ^{14}N edition, we verified experimentally that the ^{14}N pulse length is not critical. The 2D spectra of **Fig.7.6c** and **6d** were acquired with a pulse duration of one rotor period, but similar results were obtained for other multiples of the rotor period. The ^{14}N rf amplitude is the only critical parameter of the experiment. Its value must be sufficiently strong to introduce significant spin state changes during the very brief level-crossing related to the MAS modulation of the first-order quadrupolar coupling. A saturation occurs with a very large rf-field, but the value of optimal ^{14}N rf amplitude exceeds most of the time the probe specifications.[20] Therefore, there is no parameter to optimize for the ^{14}N pulse, as its amplitude has only to be fixed to its maximum accessible value; 50kHz for our probe.

The ^{1}H-^{13}C spectra have been recorded at 9.4T with a Bruker AVANCE-II console, and a 4 mm rotor. Due to limited spinning speed (ν_R = 13 kHz), we have used the $PMLG5^{x\bar{x}}_{mm}$ sequence during t_1 to obtain a ^{1}H high-resolution spectrum,[21] with an rf amplitude of 99 kHz. The ^{13}C-^{14}N dipolar recoupling sequence must be sent on a spin-1/2 nucleus,[17] and thus on the ^{13}C nucleus in this experiment. We have used the simultaneous frequency and amplitude modulation ($SFAM_1$) recoupling sequence, which is one of the most interesting heteronuclear recoupling method.[17] For $SFAM_1$, the carrier frequency, $\Delta\nu_{0,13C}(t)$, and the amplitude, $\nu_{1,13C}(t)$, of the rf field are modulated cosinusoidally and sinusoidally, respectively, with a

frequency equal to ν_R.[17]As the $SFAM_1$ sequence is γ-encoded, the dipolar recoupling periods must be rotor-synchronized.

For comparison with the previous experiments, we have used histidine, which has three different nitrogen sites all covalently bonded to at least one ^1H and one ^{13}C. The ammonium nitrogen is bonded to three protons (H^N) and one carbon (C^α), while N^π and N^τ nitrogens of imadazole ring are bonded to one proton and two carbons: (H^π, C^2/C^4), and (H^τ, C^2/C^5), respectively **(Fig.7.6a)**. We have quantified the efficiency of the ^{13}C-^{14}N dephasing process related to this adiabatic pulse. Due to the moderate ^{14}N quadrupole interactions ($C_Q \approx 1.1$MHz), we observed a large efficiency, $(S_0 - S_1)/S_0$, which was equal to 0.80 (C^2), 0.40 (C^4), 0.60 (C^5), and 0.56 (C^α), for the 4 carbons that are connected to a nitrogen atom. The very large efficiency for C^2 may be related to the fact this atom is connected to two nitrogen atoms. For the same experimental time, the present efficiency is c.a. 3-4 times larger than with the previous *D*-HMQC method. Adiabatic transfers are much less sensitive to the frequency offset than hard pulses and this sensitivity gain would thus increase with C_Q values, provided the ^{14}N rf field is sufficient. ^1H-^{13}C spectra shown in **Figs.7.6c and 7.6d**, have been recorded with a long CP contact time to enhance the S/N ratio, and therefore they do not display any selectivity with respect to protons. This selectivity can be obtained with shorter CP contact times, at the expanse of experimental time. In addition to these two spectra, we have also recorded the complementary ^1H-^{14}N *D*-HMQC spectrum of this sample. We have used a high-field spectrometer (18.8 T) and a flip-flop filter SAM4 (See chapter 7.1) during t_1, which lead to a very good resolution along ^{14}N **(Fig.7.6b)**.

We have also recorded the ^{14}N-edited ^1H – ^{13}C spectrum of another isotopically unmodified amino acid, L-glutamine, within an experimental time of 25 h on a 9.4 T spectrometer (**Fig.7.7**). More details can be found in ref [23].

By analyzing simultaneously the three 2D high-resolution spectra, the complete structural analysis of histidine is easy to achieve, and corresponds to the

previous analyses. It must be reminded that the three spectra have been recorded: (i) with an isotopically unmodified sample, (ii) on a moderate field (9.4T) spectrometer for ^{1}H-^{13}C spectra, and (iii) in a reasonable time (18 hrs altogether). We believe that this new method can be extended easily to larger biomolecules, especially by using high-field spectrometers to enhance the ^{1}H and ^{13}C resolution.

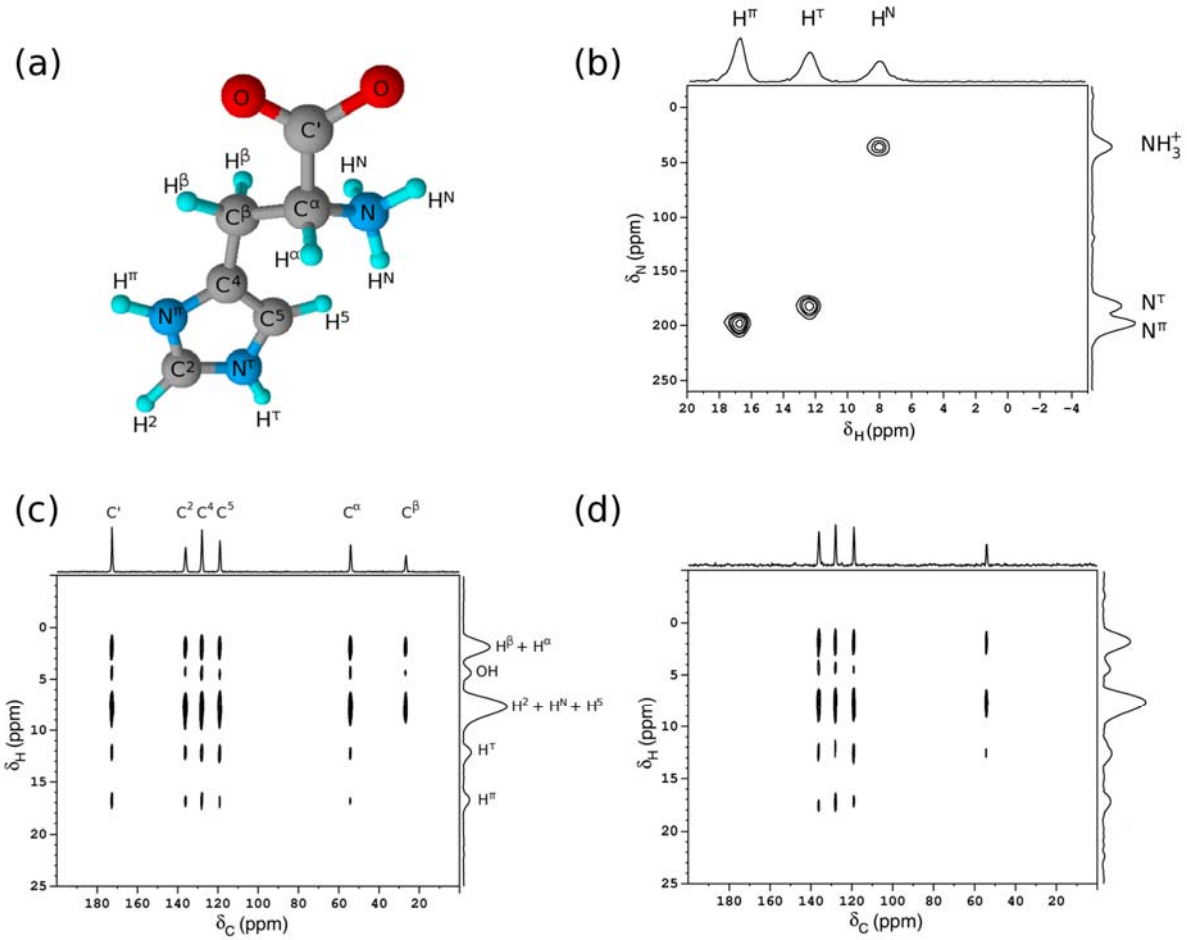

Fig 7.6. (a) Molecular structure of L-histidine. The atom labeling matches IUPAC recommendations. (b) 2D ^{1}H-^{14}N *D*-HMQC spectrum of L-histidine. ^{1}H axis has been rescaled. A smooth amplitude modulation $(SAM_4)^{22}$ flip-flop filter with ν_1=86 kHz was sent on protons during t_1 to enhance the ^{14}N resolution. B_0 = 18.8 T, ν_R = 20 kHz, $\nu_{1\text{-}14N}$ = 44 kHz. (c-d) CP-HETCOR spectra with: (c) all (S_0) or (d) ^{14}N-edited (S_0-S_1) ^{1}H-^{13}C cross-peaks of L-[U-^{13}C]-histidine.HCl.H_2O. *PMLG5*$^{x\bar{x}}_{mm}$ decoupling scheme was applied during t_1 with $\nu_{1,1H}^{peak}$ = 99 kHz and τ_p=1.4 µs. ^{1}H axis has been rescaled. Spectra are the result of averaging 112 transients for each of 120 t_1 increments with Δt_1 = 70 µs, with a recycle time of 2s. The total experimental time for the two spectra has been of 17.8 hrs. The $SFAM_1$ scheme was used for ^{13}C-^{14}N recoupling with τ_{rec} = 888 µs, $\nu_{1,13C}^{peak}$ = 41 kHz and $\Delta\nu_{0,13C}$ = 20 kHz. ^{1}H-^{13}C CP-MAS: contact time = 2 ms, $\nu_{1\text{-}13C}$ = 54 kHz, the power of ^{1}H is optimized with tangent-ramped shape. B_0 = 9.4 T, ν_R = 13.51 kHz, $\nu_{1\text{-}14N}$ = 50 kHz. ^{1}H decoupling : $\nu_{1\text{-}1H}$ = 86 kHz. ^{13}C π and π/2 pulses: $\nu_{1\text{-}13C}$ = 50 kHz.

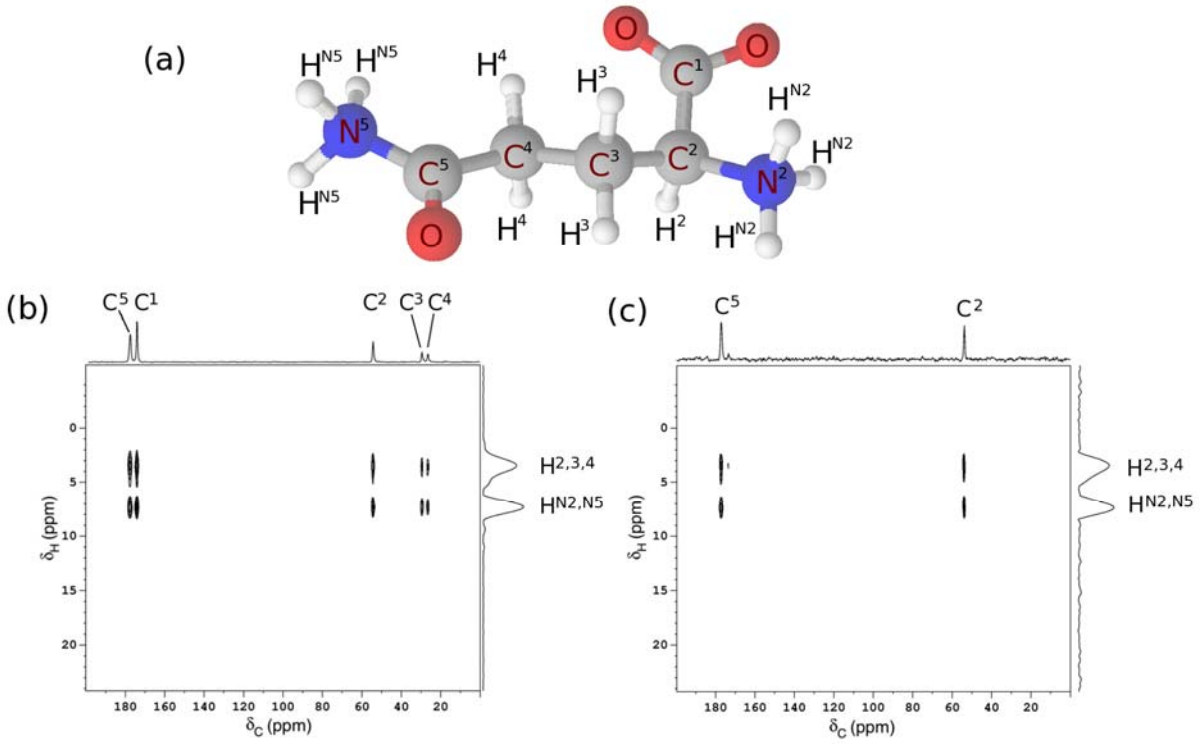

Fig.7.7 L-glutamine. (a) Molecular structure with atom labelling matching IUPAC recommendations. (b,c) CP-HETCOR spectra with : (b) all (S_0) or (c) ^{14}N-edited (S_0-S_1) ^{1}H-^{13}C cross-peaks. *PMLG5*$^{x\bar{x}}_{mm}$ decoupling scheme was applied during t_1 with $\nu_{1\text{-}1H}$ = 99 kHz and τ_p = 1.4 µs. ^{1}H axis has been rescaled. Spectra are the result of averaging 320 transients for each of 70 t_1 increments with Δt_1 = 70 µs, with a recycle time of 2s. The total experimental time for the two spectra has been of 25 hrs (320*70*2*2 sec). The $SFAM_1$ scheme was used for ^{13}C-^{14}N recoupling with τ_{rec} = 814 µs, $\nu^{peak}_{1,13C}$ = 41 kHz and $\Delta\nu_{0\text{-}13C}$ = 20 kHz. ^{1}H-^{13}C CP-MAS: contact time = 2.5 ms, $\nu_{1\text{-}13C}$ = 54 kHz, the power of ^{1}H is optimized with tangent-ramped shape. B_0 = 9.4 T, ν_R = 13.51 kHz, $\nu_{1\text{-}14N}$ = 50 kHz. ^{1}H decoupling : $\nu_{1\text{-}1H}$ = 86 kHz. ^{13}C π and π/2 pulses: $\nu_{1\text{-}13C}$ = 50 kHz.

References

[1] Olivier Lafon, Qiang Wang, Bingwen Hu, Filipe Vasconcelos, Julien Tre´bosc, Sylvain Cristol, Feng Deng, and Jean-Paul Amoureux, Indirect detection via spin-1/2 nuclei in solid state NMR spectroscopy : application to the observation of proximities between protons and quadrupolar nuclei. *J. Phys. Chem. A. http://pubs.acs.org/doi/abs/10.1021/jp906099k.*

[2] T. Giavani, H. Bildsoe, J. Skibsted, H.J. Jakobsen, A solid-state ^{14}N magic-angle spinning NMR study of some amino acids, *J. Magn. Reson.* 166 **(2004)** 262-272.

[3] G. Jeschke, M. Jansen, High-resolution ^{14}N solid-state NMR spectroscopy, *Angew. Chem. Int*. Ed. 37 **(1998)** 1282-1283.

[4] A.K. Khitrin, B.M. Fung, ^{14}N nuclear magnetic resonance of polycrystalline solids with fast spinning at or very near the magic angle, *J. Chem. Phys.* 111 **(1999)** 8963-8969.

[5] H.J. Jakobsen, A.R. Hove, R.G. Hazell, H. Bildsøe, J. Skibsted, Solid-state ^{14}N MAS NMR of ammonium ions as a spy to structural insights for ammonium salts, *Magn. Reson. Chem*. 44 **(2006)** 348-356.

[6] R. Tycko, S.J. Opella, High-resolution nitrogen-14 overtone spectroscopy: an approach to natural abundance nitrogen NMR of oriented and polycrystalline systems, *J. Am. Chem. Soc.* 108 **(1986)** 3531-3532.

[7] R. Tycko, S.J. Opella, Overtone NMR spectroscopy, *J. Chem. Phys.* 86 **(1987)** 1761-1774.

[8] R. Tycko, P.L. Stewart, S.J. Opella, Peptide plane orientations determined by fundamental and overtone nitrogen-14 NMR, *J. Am. Chem. Soc.* 108 **(1986)** 5419-5425.

[9] Z. Gan, Measuring amide nitrogen quadrupolar coupling by high-resolution $^{14}N/^{13}C$ NMR correlation under magic-angle spinning, *J. Am. Chem. Soc.* 128 **(2006)** 6040-6041.

[10] S. Cavadini, A. Lupulescu, S. Antonijevic, G. Bodenhausen, Nitrogen-14 NMR spectroscopy using residual dipolar splittings in solids, *J. Am. Chem. Soc.* 128 **(2006)** 7706-7707.

[11] S. Cavadini, S. Antonijevic, A. Lupulescu, G. Bodenhausen, Indirect detection of nitrogen- 14 in solids via protons by nuclear magnetic resonance spectroscopy, *J. Magn. Reson.* 182 **(2006)** 168-172.

[12] Z. Gan, $^{13}C/^{14}N$ heteronuclear multiple-quantum correlation with rotary resonance and REDOR dipolar recoupling, *J. Magn. Reson.* 184 **(2006)** 39-43.

[13] Z. Gan, J.P. Amoureux, J. Trebosc, Proton-detected ^{14}N MAS NMR using homonuclear decoupled rotary resonance, *Chem. Phys. Lett.* 435 **(2007)** 163-169.

[14] R. Siegel, J. Trebosc, J.P. Amoureux, Z. Gan, 3D ^{1}H-^{13}C-^{14}N correlation solid-state NMR spectrum, *J. Magn. Reson*. 193 (2008), 321-325.

[15] K. Schmidt-Rohr, J.D. Mao, Selective observation of nitrogen-bonded carbons in solid-state NMR by saturation-pulse induced dipolar exchange with recoupling, *Chem. Phys. Lett*. 359 **(2002)** 403-411.

[16] R. Fu, S.A. Smith, G. Bodenhausen, Recoupling of heteronuclear dipolar interactions in solid-state MAS NMR by simultaneous frequency and amplitude modulation, *Chem. Phys. Lett.* 272 **(1997)** 361-369.

[17] B. Hu, J. Trebosc, J.P. Amoureux, Comparison of several hetero-nuclear recoupling NMR methods to be used in MAS HMQC/HSQC. *J. Magn. Reson*. 192 **(2008)** 112.

[18] J.P. Amoureux, B. Hu, J. Trebosc, Enhanced resolution in proton solid-state NMR with very-fast MAS experiments, *J. Magn. Reson*. **2008,** 193, (2), 305.

[19] Jean-Paul Amoureux, Julien Trébosc, Bingwen Hu, Nicholas Halpern-Manners, Sasa Antonijevic, High-resolution 14N-edited 1H – 13C correlation NMR experiment to study biological solids, Journal of Magnetic Resonance 194 (2008) 317 – 320.

[20] Z. Gan, Measuring nitrogen quadrupolar coupling with 13C detected wide-line 14N NMR under magic-angle spinning, Chem. Comm. (2008) 868-870.

[21] M. Leskes, P.K. Madhu, S. Vega, A broad-banded z-rotation windowed phase-modulated Lee- Goldurg pulse sequence for 1H spectroscopy in solid-state NMR, Chem. Phys. Lett. 447 (2007) 370-374.

[22] J.P. Amoureux, B. Hu, J. Trébosc, Enhanced resolution in proton solid-state NMR with very-fast MAS experiments, J. Magn. Reson. 193 (2008) 305-307.

[23] Jean-Paul Amoureux, Qiang Wang, Bingwen Hu, Olivier Lafon, Julien Trébosc, Rapid analysis of isotopically unmodified amino acid by high-resolution 14N-filtered 1H-13C correlation NMR spectroscopy, Chem. Commun., 2008, 1–4.

Chapter 8. SPIP and its variations

8.1. Application of SPIP in ^{19}F system

^{19}F nucleus has the advantage of a spin quantum number equal to ½, a high gyromagnetic ratio ($\gamma_{19F} = 0.94\gamma_{1H}$) and a 100% natural isotopic abundance, leading to a very high Nuclear Magnetic Resonance (NMR) receptivity. Moreover, the ^{19}F isotropic chemical shifts (δ_{iso}) span over a wide frequency range (≈ 800 ppm) giving a high spectrum sensitivity to variations of the local environment of the fluorine atoms.[1] Therefore, ^{19}F solid-state NMR has been employed to investigate the structure of a broad range of materials, including fluorinated organic compounds, fluoropolymers, ^{19}F-labeled membrane active peptides as well as inorganic fluorides.[1-7]

^{19}F–^{19}F proximities in the solid state can be probed by two-dimensional (2D) homonuclear correlation (HOMCOR) spectra.[5-7] In 2D HOMCOR experiments, the frequencies of the peaks on the two axes are related to resonance frequencies of nuclei of the same type; e.g. fluorine-fluorine frequencies here. Since ^{19}F-^{19}F direct dipolar couplings are more than 30 times larger than ^{19}F-^{19}F indirect *J*-couplings (^{1}J-couplings only go up to 230 Hz), coherence transfer between nearby ^{19}F nuclei has only been achieved through the dipolar interaction (*D*-HOMCOR).[5-7] Indeed, the use of ^{19}F–^{19}F *J*-couplings requires ultra-fast magic-angle spinning (MAS) and efficient broadband ^{19}F–^{19}F homonuclear decoupling schemes. The selected coherences during the t_1 indirect evolution period of 2D *D*-HOMCOR experiments are generally single-quantum (SQ) or double-quantum (DQ) coherences and these two protocols have been both used to record ^{19}F *D*-HOMCOR spectra.[5-7] The DQ-SQ correlation method presents the great advantage over the SQ-SQ correlation experiment to allow the observation of through-space connectivities between species whose resonances have very close, or even identical, isotropic chemical shifts.[8] Especially, DQ-SQ ^{19}F *D*-HOMCOR experiments have proved to be an essential tool for the assignment of intricate ^{19}F solid-state NMR spectra.[6,7]

DQ-SQ MAS *D*-HOMCOR experiments require the use of adapted DQ dipolar recoupling techniques. In the case of ^{19}F, such recoupling is challenging owing to the NMR characteristics of this nucleus. First, the ^{19}F NMR spectra may exhibit a large spread of isotropic chemical shifts. Second, the chemical shift anisotropy (CSA) of ^{19}F nucleus is typically in order of 100 ppm. Furthermore, the magnitude of isotropic chemical shift and CSA linearly increases with the static magnetic field, B_0. For instance, at B_0 = 18.8 T, a shielding of 100 ppm is equal to 75 kHz, which is comparable with the magnitude of the

radiofrequency (rf) field. However, the use of high magnetic fields is highly desirable in the case of ^{19}F NMR, since it can lead to substantial benefits in terms of sensitivity and spectral resolution. This is due to the fact that the broadening of the ^{19}F resonances in MAS spectra arises mainly from residual ^{19}F homonuclear couplings and, hence, is independent of the magnetic field while the separation between the ^{19}F resonances increases with the magnetic field. These strong dipolar couplings lead also to fast decay of ^{19}F coherences in the absence of applied rf field and may result in a reduction of signal intensity in the *D*-HOMCOR spectra. The resolution can be further enhanced and the dephasing time lengthened by employing high MAS frequencies ($\nu_R \geq 30$ kHz). Moreover, fast MAS minimizes the spinning sidebands related to ^{19}F CSA. In the case of 2D DQ-SQ *D*-HOMCOR, small rotor period (T_R) also offers the advantage of a proper sampling of the DQ-coherence (DQC) build-up curves and large indirect dimension spectral widths, when using non γ-encoded recoupling sequence.[9]

From the above discussion, we may conclude that an ideal ^{19}F DQ homonuclear dipolar recoupling sequence should have the following properties: (i) the sequence must be robust to offset and CSA, (ii) it should work at ultra-fast MAS, and (iii) the magnitude of the recoupled dipolar interactions must be lower than the sampling frequency of the DQC build-up curve in order to maximize signal intensity. Few recoupling sequences fulfill these three conditions. Most of the usual symmetry-based recoupling techniques cannot be utilized at fast MAS since they require rf nutation frequency much larger than the MAS frequency.[9] Double Quantum coherences between ^{19}F nuclei have been excited by using Back-to-Back (BABA) scheme.[6,7,10] However, BABA sequences present some drawbacks for ^{19}F homonuclear dipolar recoupling. Actually they work well at fast MAS but are very sensitive to offset and CSA. This limitation of BABA sequences was illustrated recently by ^{19}F *D*-HOMCOR experiments on fluoroaluminates.[7] For such material, the spread of resonances is so large ($\Delta\delta_{iso}$ = 122.8 ppm in $Ba_3Al_2F_{12}$) that BABA sequences only allowed recording limited regions of the 2D DQ-SQ ^{19}F *D*-HOMCOR spectra, even at moderate magnetic field (B_0 = 7 T). As a result, only six of the eight ^{19}F resonances were unambiguously assigned in $Ba_3Al_2F_{12}$.

To circumvent this drawback, we propose the use of a recently-introduced recoupling method, the Sandwiched PI Pulse (SPIP)[11] sequence, in order to excite ^{19}F DQCs. The SPIP sequence is a rotor-synchronized symmetry-based experiment with continuous rf irradiation in order to decrease the losses with spin-lock periods. We demonstrate that this sequence, which can be employed at ultra-fast MAS, displays high robustness to offset and CSA. Therefore,

we have been able to record ^{19}F *D*-HOMCOR spectra of fluoroaluminates $Ba_3Al_2F_{12}$ at high magnetic field (B_0 = 18.8T) with large spectral width and high spectral resolution.

The high robustness of SPIP to offset and CSA has allowed recording DQ-SQ ^{19}F spectra, even when the range of isotropic chemical shift exceeds 100 ppm. This is illustrated by the study of $Ba_3Al_2F_{12}$. For this compound, the isotropic chemical shift difference between the ^{19}F resonances is $\Delta\delta_{iso}$ = 122.8 ppm (i.e. $\Delta\nu_{iso}$ = 92.5 kHz at 18.8 T), while $|\delta_{aniso}|$ values are spread from 70 to 105 ppm.[12] The structure of $Ba_3Al_2F_{12}$ is built up from rings formed by four AlF_6^{3-} octahedra sharing adjacent corners, and involves eight inequivalent F sites: two bridging (F1,F2), two free (F3,F4) and four non-bridging (F5-F8) of multiplicity 4, 4, and 8, respectively.[13] **Fig.8.1** shows the DQ-SQ ^{19}F spectrum of this compound. Compared to the spectrum of $Ba_3Al_2F_{12}$ shown in Ref. [7], this spectrum presents a significant gain in spectral resolution. Furthermore, as the SPIP sequence is more robust to offset and CSA than BABA, we were able to acquire the full spectrum in a single experiment. This last improvement allows detecting cross-peaks between lines 1 or 2 and 7 or 8, which permit completing the assignment of the ^{19}F MAS spectrum. Actually the lines 1 to 6 have already been unambiguously assigned to their respective crystallographic sites.[7] However, the spectrum in Ref. [7] did not allow determining whether the lines 7 and 8 should be assigned to the free fluorine ions F3 or F4. The spectrum of **Fig.8.1** shows that the line 7 correlates to the line 2, which corresponds to the F2 site, whereas the line 8 does not. Moreover, the shortest F2-F4 and F2-F3 distances are equal to 3.33 and 4.42 Å, respectively.[14] Therefore, the lines 7 and 8 are assigned to sites F4 and F3, respectively. This final line assignment based on the DQ-SQ *D*-HOMCOR spectrum slightly differs from that proposed by Body et al. from a ^{19}F isotropic chemical shift calculation using a semi-empirical superposition model, but is in full agreement with DFT calculations[15] performed using the GIPAW[16] (gauge including projector augmented wave) method suitable for periodic systems. As previously discussed, this demonstrates that such experiments are essential for correct line assignments and assessment of calculation results.[7] The ^{19}F DQ-SQ spectrum of $Ba_3Al_2F_{12}$ exhibits correlation peaks for all ^{19}F–^{19}F proximities shorter than 4.66 Å except for F2-F3 (4.42 Å) and F2-F2 (4.43 Å) proximities. Actually, besides these two correlation peaks, only the correlation peaks F1-F3 and F1-F4 are missing since they correspond to a polarization transfer through longer-range distances ($r_{F1,F3}$ = 4.95 Å, $r_{F1,F4}$ = 4.99 Å). Here again, the variation of correlation peak intensities agrees approximately with the relative ^{19}F–^{19}F distances. More details can be found in ref [17].

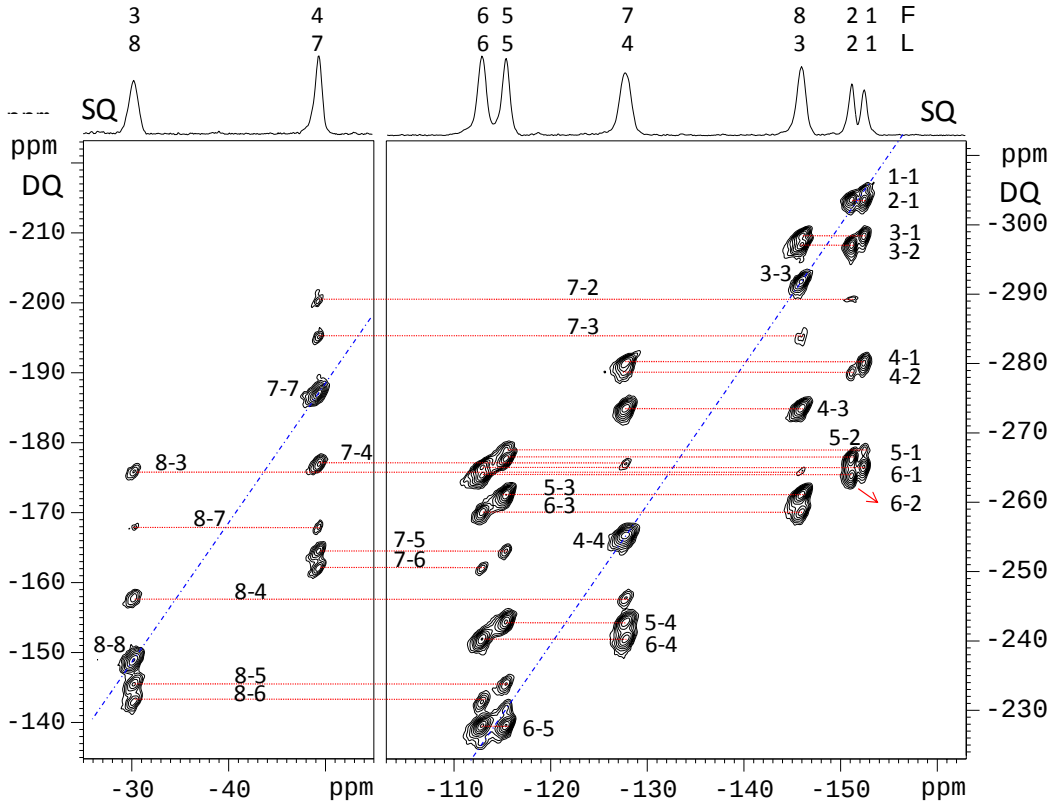

Fig.8.1. 2D ^{19}F DQ-SQ *D*-HOMCOR MAS spectrum of $Ba_3Al_2F_{12}$ recorded at 18.8 T with ν_R = 66.666 kHz. SPIP sequence is applied during $\tau_{exc} = \tau_{rec}$ = 240 µs = 16T_R. The rf nutation frequencies of the π pulses and the spin lock pulses of SPIP is equal to $\nu_{1\pi}$ = 120 kHz and ν_{1SL} = 100 kHz. 160 t_1 increments with 48 scans each were acquired with a recycling delay of 4 s, leading to a total experiment time of 9 h. The full spectrum has been acquired in a single experiment but for the sake of readability, only the spectral regions displaying correlation peaks are presented. The sum of the 2D spectrum is represented on top with the numbering of the lines (L) and species (F). The L5-L5 and L6-L6 auto-peaks are not indicated in the figure; they are small, but visible. Due to the folding along F_1, the vertical scaling on the right is only correct for the pairs of correlation peaks both situated in the right square of the spectrum. The vertical scaling on the left, which is correct for the pairs of correlation peaks with one peak in the left part and one peak in the right part, has been obtained by adding 88.5 ppm (ν_R/ν_0) to the right vertical scaling. For the three other peaks ((8,8), (8,7), (7,7)), the correct F_1 value can be obtained by adding 88.5 ppm to this left vertical scaling.

8.2. $BR2_2^1(\tau\pi\tau)$: SPIP variation for ^{31}P with very large CSA

Solid-state ^{31}P nuclear magnetic resonance (NMR) benefits from the favorable nuclear properties of this spin-1/2 isotope, characterized by a high gyromagnetic ratio ($\gamma_{31P} = 0.40\gamma_{1H} = 1.61\gamma_{13C}$) and a 100% natural isotopic abundance. In solids and mesophases, the chemical shift anisotropy (CSA), which is in the order of 100 – 200 ppm, provides additional information on the symmetry of the ^{31}P sites.

Up to now, ^{31}P recoupling schemes were mainly applied at moderate static magnetic fields ($B_0 \leq 11.7$ T). Higher magnetic fields can lead in principle to substantial benefits in terms of sensitivity and resolution. However, the magnitude of the CSA, in Hz, is proportional to B_0. As a result, ^{31}P nuclei in phosphate groups can experience CSAs as large as 81 kHz at 23.5 T (the largest magnetic field presently commercially available), when δ_{aniso} = 200 ppm. In that case, the magnitude of ^{31}P CSA is comparable with that of the radiofrequency (rf) fields and is much larger than the ^{31}P–^{31}P dipolar interactions, which do not exceed 1.8 kHz in magnitude.[18] Therefore, large ^{31}P CSAs can interfere with the homonuclear recoupling sequences and they may decrease the excitation efficiency of 2QCs.[19] The robustness of the recoupling sequences to resonance offset is generally less critical, since in most of phosphorous-containing samples, such as phosphate glasses, the phosphorous atoms occupy similar sites and the offset range is limited to about 20 ppm, i.e. 8.1 kHz at 23.5 T in these compounds.

In the case of ^{31}P nuclei, homonuclear 2QCs have been created under MAS condition by using BABA,[20] [fp-RFDR],[21] and RN_n^ν or CN_n^ν symmetry-based sequences,[22] such as POST-C7.[23] These recoupling methods allow to obtain 2D 2Q-1Q *D*-HOMCOR experiments (**Fig. 8.2a**) and to estimate the ^{31}P–^{31}P inter-nuclear distances.

The BABA sequences (**Fig. 8.2b**) can be employed at high MAS rates but are sensitive to CSA.[20] Even the use of a super-cycle spanning four rotor periods does not permit a total elimination of the CSA during BABA recoupling schemes. The symmetry-based sequences allow for a better compensation of CSA, but most of them can not be employed at high MAS frequencies owing to the need for large rf fields. For instance, POST-C7 requires the nutation frequency to be 7 times the sample spinning frequency. Such high rf power for extended time periods of tens of ms is not compatible with probe rf-limitations and can lead to the unwanted heating of high water and salt content samples, such as bio-molecules.

The SPIP recoupling sequence, depicted in **Fig.8.2c**, was introduced in order to recouple the ^{1}H–^{1}H dipolar couplings at high MAS frequency. It is constructed from the $R2_2^1$ symmetry-based sequence employing a composite π pulse $\mathcal{R} = \theta_0\pi_0\theta_{180}$ as basic element. The basic $R2_2^1$ symmetry achieves both 0Q and 2Q homonuclear dipolar recoupling but does not suppress all offset and CSA terms in the first-order AHT. These unwanted CSA and offset terms can be removed by applying a block super-cycle, which consists in an overall phase shift of rf pulses from the middle of the τ_{exc} and τ_{rec} delays.

The substitution of the θ pulses in SPIP by windows leads to the recoupling sequences $BR2_2^1(\tau\pi\tau)$ depicted in **Fig.8.2d**. This sequence originating from the $R2_2^1$ symmetry employs a windowed basic element $\mathcal{R} = \tau–\pi_0–\tau$. The delay τ is adjusted so that the basic element $\mathcal{R}$ lasts one rotor period. The block super-cycle is identical to that of SPIP, and hence the sequence is called $BR2_2^1(\tau\pi\tau)$ in the following. Therefore, $BR2_2^1(\tau\pi\tau)$ sequence provides 0Q and 2Q dipolar recoupling, while suppressing the unwanted CSA and offset terms to first-order.

The [fp-RFDR] sequence is depicted in **Fig.8.2e**. The usual version of fp-RFDR is constructed from $R4_4^1$ symmetry with an overall 45° phase shift and employs the same basic element $\mathcal{R} = \tau–\pi_0–\tau$ as $BR2_2^1(\tau\pi\tau)$.[9] This symmetry achieves 0Q dipolar recoupling and removes the CSA and offset interferences to first-order. The unwanted terms can be further suppressed by using super-cycle, such as XY-8 and XY-16. [9] The fp-RFDR sequence with XY-16 super-cycle corresponds to the symmetry $\left(R4_4^{-1}R4_4^1\right)2^1 = \left(R4_4^{-1}R4_4^1\right)_0\left(R4_4^{-1}R4_4^1\right)_{180}$ with an overall 45° phase shift, while the XY-8 super-cycle corresponds to $\left(R4_4^{-1}R4_4^1\right)_{45}$. The insertion of bracketing π/2-pulses at the beginning and at the end of fp-RFDR yields the [fp-RFDR] scheme and allows for the excitation of 2QCs.

Here the pulse fraction f is introduced, which is depending on the relative durations between the pulses and the windows.

$$f = \begin{cases} 4\tau_{\pi/2}/T_R & \text{for BABA} \\ \tau_\pi/T_R & \text{for SPIP, } BR2_2^1(\tau\pi\tau), [\text{fp - RFDR}] \end{cases}$$

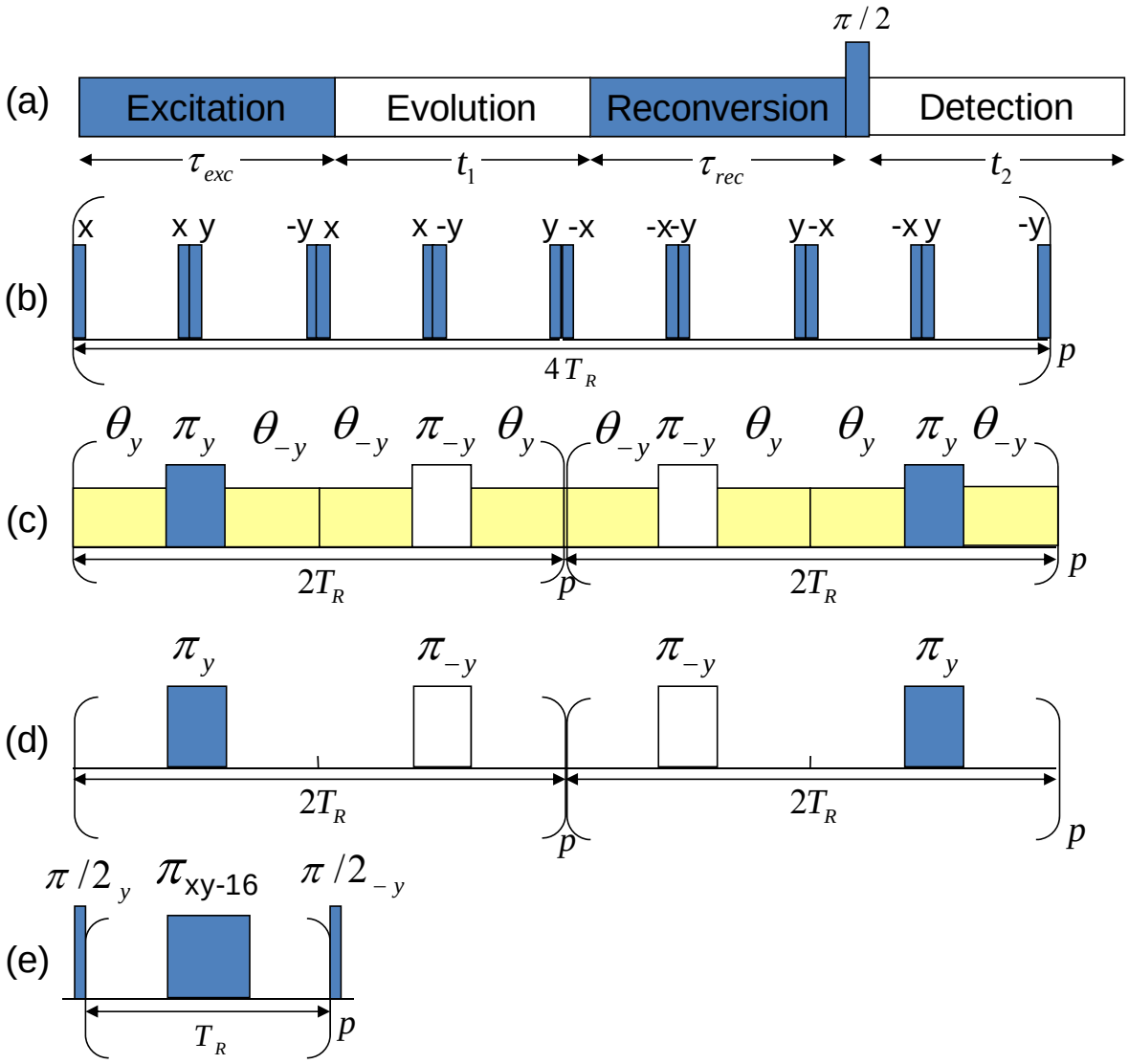

Fig.8.2 (a) General scheme of 2Q-1Q spectroscopy. Basic cycle of: (b) BABA-4, (c) SPIP, (d) $BR2_2^1(\tau\pi\tau)$, (e) [fp-RFDR]. The XY-16 super-cycle consists in (x,y,x,y), (y,x,y,x), (-x,-y,-x,-y) and (-y,-x,-y,-x).

We have tested the BABA-4, SPIP, $BR2_2^1(\tau\pi\tau)$ and [fp-RFDR] experiments on $Na_3P_3O_9$. The experiments were performed on three (2.35, 9.4 and 18.8 T) Bruker Avance-II spectrometers equipped with 2.5 (9.4 and 18.8 T) or 3.2 (2.35 T) mm MAS probes.

Sodium trimetaphosphate, $Na_3P_3O_9$, was synthesized as described in reference [24] including partial ^{17}O enrichment. It crystallizes in the orthorhombic *Pmcn* space group with four formula units per unit cell.[24] The basic unit of $Na_3P_3O_9$ is composed of two crystallographically distinct sodium sites, two phosphorous sites, and six oxygen sites. The ^{31}P MAS spectra exhibit two resonances P_1 at −16.0 ppm and P_2 at −18.8 ppm, in a 1:2 ratio, in good agreement with crystallographic data. The ^{31}P-^{31}P inter-nuclear distances and dipolar interactions are equal to: d_{11} = 410, $d_{22} \approx d_{12} \approx$ 289 pm, i.e. $b_{11}/(2\pi)$ = −283, $b_{22}/(2\pi) \approx b_{12}/(2\pi) \approx$ −812 Hz. The basic anionic unit is composed of a ring of three phosphate groups **(Fig.8.3d).** Following the conventional notation, all phosphate entities in $Na_3P_3O_9$ are noted Q^2 because they are connected to two other phosphate groups. The CSAs of these two ^{31}P species, evaluated from their sideband patterns, are approximately equal to $\delta_{aniso} \approx$ 155 (P_1) and 165 (P_2) ppm. At 18.8 T, these broadenings are very large and equal to 50 (P_1) and 53 (P_2) kHz.

The 1D 2QF spectra of $Na_3P_3O_9$, recorded with ν_R = 30 kHz at 18.8 T are represented in **Fig.8.3a**. The signal is about five times weaker with SPIP and BABA-4 than with [fp-RFDR] and $BR2_2^1(\tau\pi\tau)$. These results evidence the higher robustness of [fp-RFDR] and $BR2_2^1(\tau\pi\tau)$ to CSA. In order to test the influence of the CSAs, we performed the same 1D experiments on $Na_3P_3O_9$ at lower fields, 9.4T **(Fig.8.3b)** and 2.35T **(Fig.8.3c)**, which means that the CSAs were scaled down (in Hz) by a factor of two and eight, respectively with respect to 18.8T. At 9.4T, we used the same spinning speed of 30 kHz, which means that the only difference between experiments performed at 9.4 and 18.8 T resides in the CSAs. We do not have a 2.5mm probe operating at 2.35 T, and the spinning speed was thus limited to 20 kHz with a 3.2mm probe. One observes a merging of the efficiencies of BABA-4, $BR2_2^1(\tau\pi\tau)$ and [fp-RFDR], with decreasing CSAs. However, SPIP signal remains weak at 2.35 T, owing to long recoupling time and hence large irreversible losses.

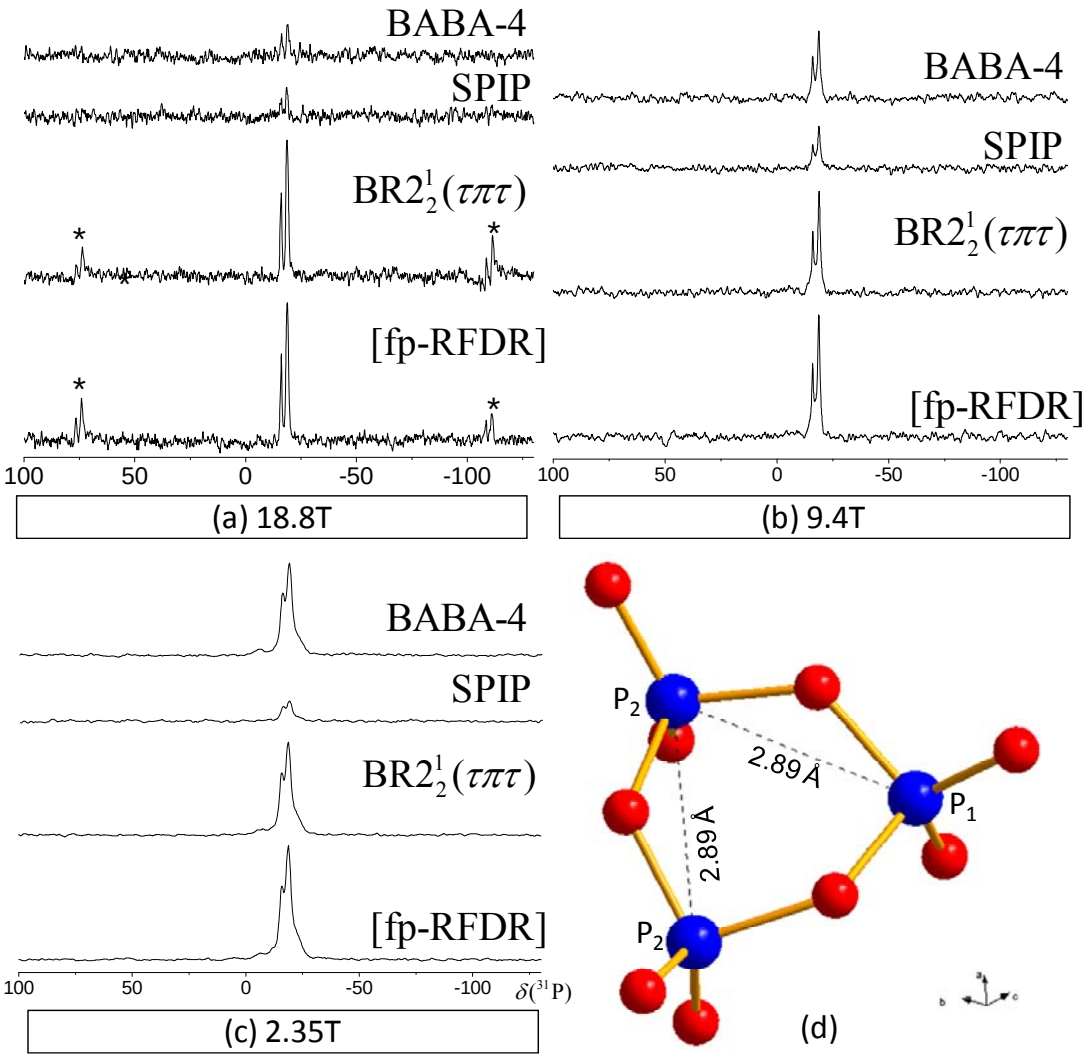

Fig.8.3 ^{31}P 1D 2QF spectra of $Na_3P_3O_9$ sample employing various B_0 fields and recoupling sequences: BABA-4, SPIP, BR2$^1_2(\tau\pi\tau)$, and [fp-RFDR]. (a) Spectra at B_0 = 18.8T and ν_R = 30 kHz. The $\tau_{exc} = \tau_{rec}$ and *f* values are equal to 400 μs and 0.46 for BABA-4, 2666 μs and 0.23 for SPIP, 1333 μs and 0.23 for BR2$^1_2(\tau\pi\tau)$, 1066 μs and 0.23 for [fp-RFDR]. The rf-field of hard π/2 pulse is 84 kHz. (b) Spectra at B_0 = 9.4T and ν_R = 30 kHz. The $\tau_{exc} = \tau_{rec}$ and *f* values are equal to 533 μs and 0.48 for BABA-4, 2133 μs and 0.275 for SPIP, 1600 μs and 0.275 for BR2$^1_2(\tau\pi\tau)$ and [fp-RFDR]. The rf-field of hard π/2 pulse is 84 kHz. (c) Spectra at B_0 = 2.35T and ν_R = 20 kHz. The $\tau_{exc} = \tau_{rec}$ and *f* values are equal to 551 μs and 0.30 for BABA-4, 3310 μs and 0.15 for SPIP, 2100 μs and 0.15 for BR2$^1_2(\tau\pi\tau)$ and [fp-RFDR]. The rf-field of hard π/2 pulse is 66 kHz. The stars in (a) indicate spinning sidebands.

Two opposite effects can be observed when increasing the magnetic field (**Fig.8.3a-c**): the S/N ratio decreases and the resolution is enhanced. The first effect is related to the very long T_{1z} relaxation time of phosphorous magnetization, which increases with the magnetic

field (≈ 200, 600, 1000 seconds at 2.35, 9.4, 18.8 T, respectively). With such long relaxation times, accumulations were performed on full rotor samples with initial pre-saturation followed by a constant delay of Δt. We have used similar delays in all experiments (Δt ≈ 50 s), which leads to a decrease of the S/N ratio with increasing field. Moreover, the sample volume at 2.35 T was c.a. 3 times larger than that used at 9.4 and 18.8 T, which also leads to a much better S/N ratio at that field. The second effect is related to the resolution 'enhancement' observed with increasing magnetic field. This enhancement stems from the line-width nature of $Na_3P_3O_9$. This well-crystallized compound shows very narrow chemical shift distribution. Moreover, ^{31}P is submitted to $^2J_{POP}$ that ranges between 10 to 30 Hz.[25] Finally, one can observe a very complex $^1J_{PO}$ multiplet structure ($^1J_{PO}$ coupling is around 120 Hz in this compound) mostly restricted around the base of the resonance because of partial ^{17}O enrichment. We have estimated the two resonance line-widths avoiding the $^1J_{PO}$ coupling multiplet, and observed line-widths of c.a. 55 ± 5 Hz, 65 ± 5 Hz, 150 ± 10 Hz for P_1 and 55 ± 5 Hz, 175 ± 15 Hz, 300 ± 20 Hz for P_2, at 2.35, 9.4 and 18.8 T respectively. Therefore, we can deduce that at 2.35 T the two line-widths are dominated by the scalar ^{31}P-^{31}P triplets due to $^2J_{POP}$ couplings (**Fig.8.3d**), and hence that the chemical shift distribution is limited to c.a. 0.20 (P_1) and 0.50 (P_2) ppm. At 9.4 T, these values correspond to the P_1 line-width, but the P_2 resonance must also be broadened by another process, certainly incoherent. At 18.8 T, a larger incoherent broadening is observed for both species. Globally, by comparing the ratio between the line-widths and the fields, we observe a significant resolution enhancement when going from 2.35 to 9.4 T, but only the bases of the resonance are better resolved between 9.4 and 18.8 T spectra (**Fig.8.3a** and **Fig.8.3b)**.

We have also measured on $Na_3P_3O_9$ the offset sensitivity of the two most efficient sequences, namely [fp-RFDR] and $BR2_2^1(\tau\pi\tau)$, at three magnetic fields, 18.8T (**Fig.8.4a**), 9.4T (**Fig.8.4b**) and 2.35T (**Fig.8.4c**). The offset full-width at half-height (FWHH) of $BR2_2^1(\tau\pi\tau)$ is always at least the double of that observed for [fp-RFDR]: FWHH($BR2_2^1(\tau\pi\tau)$)/FWHH([fp-RFDR]) 18/46, 38/80, and 68/200 ppm, as shown in **Fig.8.4 a,b,c**, respectively. For most samples, this chemical shift range is quite sufficient below 9.4T, but may be slightly too small at 18.8T, especially for [fp-RFDR].

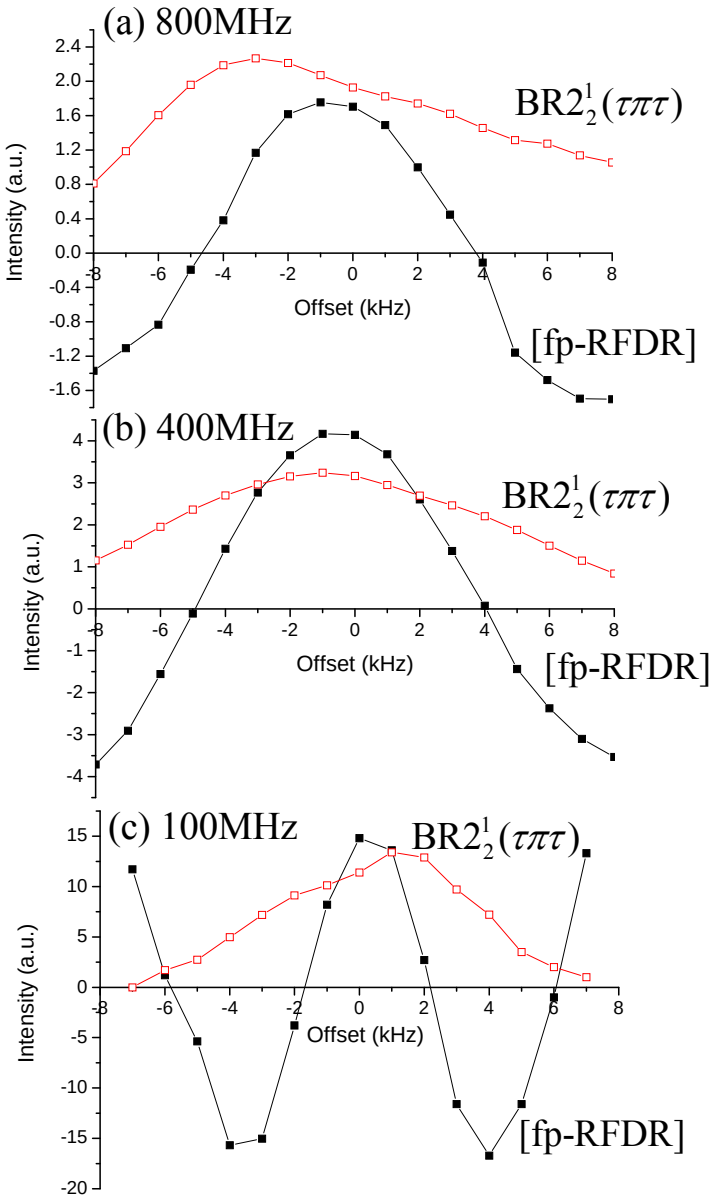

Fig.8.4 ^{31}P 1D 2QF signal in $Na_3P_3O_9$ sample, as a function of the offset irradiation, observed when using [fp-RFDR] and $BR2_2^1(\tau\pi\tau)$ sequences, with ν_R = 30kHz and B_0 = 18.8 T (a) or 9.4 T (b) and ν_R = 20 kHz and B_0 = 2.35 T (c). The intensity is given in arbitrary units (a.u.). The other experimental parameters are those given in Fig.8.3 caption.

We have recorded the 2D 2Q-1Q $BR2_2^1(\tau\pi\tau)$ spectrum of $Na_3P_3O_9$ at 18.8 T and ν_R = 30 kHz **(Fig.8.5)**. Under MAS, the two ^{31}P resonances are well resolved without overlapping. The NMR parameters of these ^{31}P species have been deduced from the spinning sideband patterns: {δ_{iso} (ppm), δ_{aniso} (ppm), η} = {-16.0, -155, 0.06} for P_1; and {-18.8, -165, 0.1} for P_2. Chemical shift separation between the two species is small (2.8 ppm), but both species are

submitted to a large CSA: 50 and 53 kHz at 18.8T, for P_1 and P_2 respectively. The spinning speed was thus insufficient to avoid sidebands in the spectrum (**Fig.8.3a**). The 2–2 auto-peak exhibits a large signal, whereas that for 1-1 is small, in agreement with the dipolar coupling constants: $b_{11}/(2\pi)$ = -283Hz and $b_{22}/(2\pi)$ =-810Hz values.

Above all, we have demonstrated that a new simple pulse-sequence, $BR2_2^1(\tau\pi\tau)$, can be applied for double-quantum NMR experiments on spin-1/2 nuclei submitted to very large CSAs. The method, which is a modified version of the rotor-synchronized SPIP sequence, is efficient and robust to both CSA and offset. In the same way as [fp-RFDR], $BR2_2^1(\tau\pi\tau)$ uses finite π pulses the amplitude of which is moderate and does not require stringent conditions. The main difference between the two sequences resides in the much more robust behaviour of $BR2_2^1(\tau\pi\tau)$ with respect to off-resonance irradiation. More details can be found in ref [26].

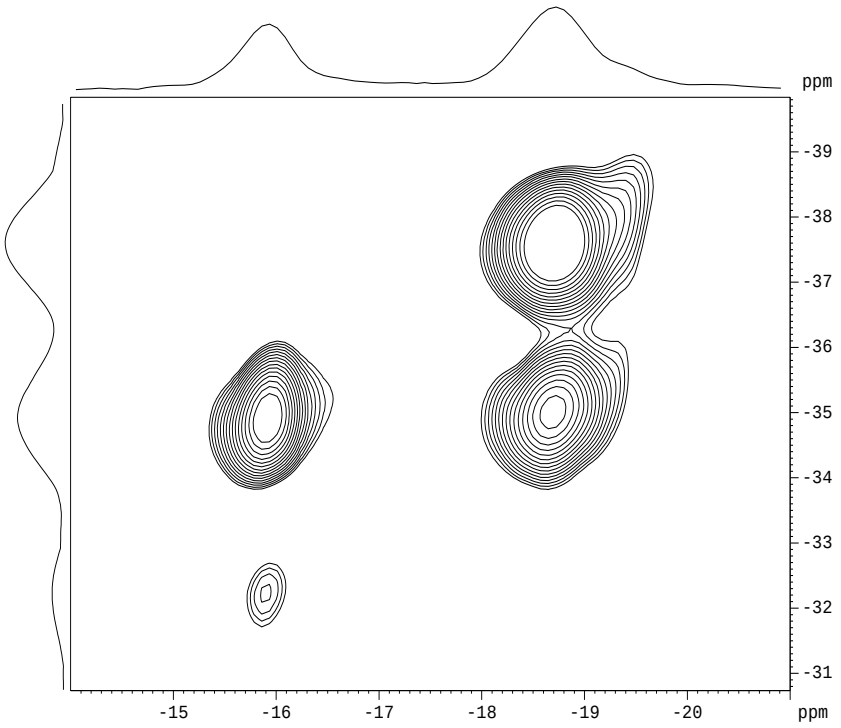

Fig.8.5 ^{31}P 2D 2Q-1Q *D*-HOMCOR spectrum of $Na_3P_3O_9$ recorded at 18.8 T with ν_R = 30 kHz. The dipolar recoupling sequence is $BR2_2^1(\tau\pi\tau)$ with $\tau_{exc} = \tau_{rec}$ = 1333 μs and f = 0.23. The rf nutation frequency of π/2 pulses is 84 kHz. This spectrum only represents a restricted region without any sidebands. The number of scans is 16, recycling delay is Δt = 90 s, 50 points in t_1 dimension with Δt_1 = 200 μs. The total experimental time is 20 h. The contour levels are separated every 5 %.

8.3. $BR2_2^1$: SPIP variation for quadrupolar nuclei

Most of homonuclear recoupling schemes are dedicated to the case of spin-1/2 nuclei, while homonuclear dipolar recoupling of quadrupolar nuclei under MAS is difficult because of the intricate nuclear spin dynamics of the quadrupolar nuclei in the presence of rf fields and sample rotation. Rotary resonance recoupling (R^3) techniques and especially the HORROR condition[27] have been demonstrated for recoupling of quadrupolar nuclei.[28-31] The HORROR condition, which selectively reintroduces the homonuclear dipolar interaction, is obtained for a spin-*S* when the rf amplitude ν_1 fulfills:

$$\nu_1 = \nu_R/(2S + 1) \quad (1)$$

where ν_R is the MAS frequency. Recently, it was shown that symmetry-based pulse sequences display superior rf error tolerance than the HORROR recoupling.[32-35] These symmetry-based pulse sequences were incorporated into 2D experiments, which correlate 2Q-coherences (2QCs) with the respective CT single-quantum (1Q) coherences within each spin pair.

Fig. 8.6a depicts the pulse scheme, which has been mainly employed so far to record 2D 2Q-1Q correlation spectra on half-integer quadrupolar nuclei.[30,33,35] Homonuclear 2QCs were excited by partly zero-quantum (0Q) recoupling sequences that were bracketed by two CT-selective $\pi/2$-pulses. These bracketing $\pi/2$-pulses achieve the conversion of the 0Q recoupling sequences into 2Q schemes. The bracketed recoupling methods allow the excitation of 2QCs from longitudinal magnetization. The excited 2QCs are subjected to a CT-selective π-pulse, which is phase-cycled to eliminate all 2QC involving a single nucleus through its satellite transitions (**Fig.8.6c**).[30] The 2QCs are reconverted into longitudinal CT polarization by repeating the excitation pulse sequence with a phase-shift of $\pi/2$. Finally the CT-selective $\pi/2$ read pulse creates observable 1Q coherences. Maximal sensitivity is obtained when the excitation and reconversion delays are equal. These delays are denoted τ in the following.

For 1D 2QF experiment, the CT-selective π-pulse is inserted between two equal short delays.[33] For 2D 2Q-1Q spectra, the delays around the central CT-selective π-pulse are set to unequal incremented time periods, qt_1 and $(1 - q)t_1$.[30] The position of the CT-selective π-pulse allows scaling the chemical and quadrupolar shifts in the indirect dimension F_1, such that the scaled CT 2QC frequency is $(1 - 2q)(\nu_j + \nu_k)$, where ν_j and ν_k are the CT 1Q frequencies of the connected two species. Furthermore, as the homonuclear recoupling sequences are not γ-encoded,[9,27] the t_1 evolution period must be incremented in steps of integer number of rotor period, T_R, thus leading to a limited spectral width in F_1.[33] However, any folding in F_1 can be avoided by using an appropriate scaling, i.e. an appropriate q value.

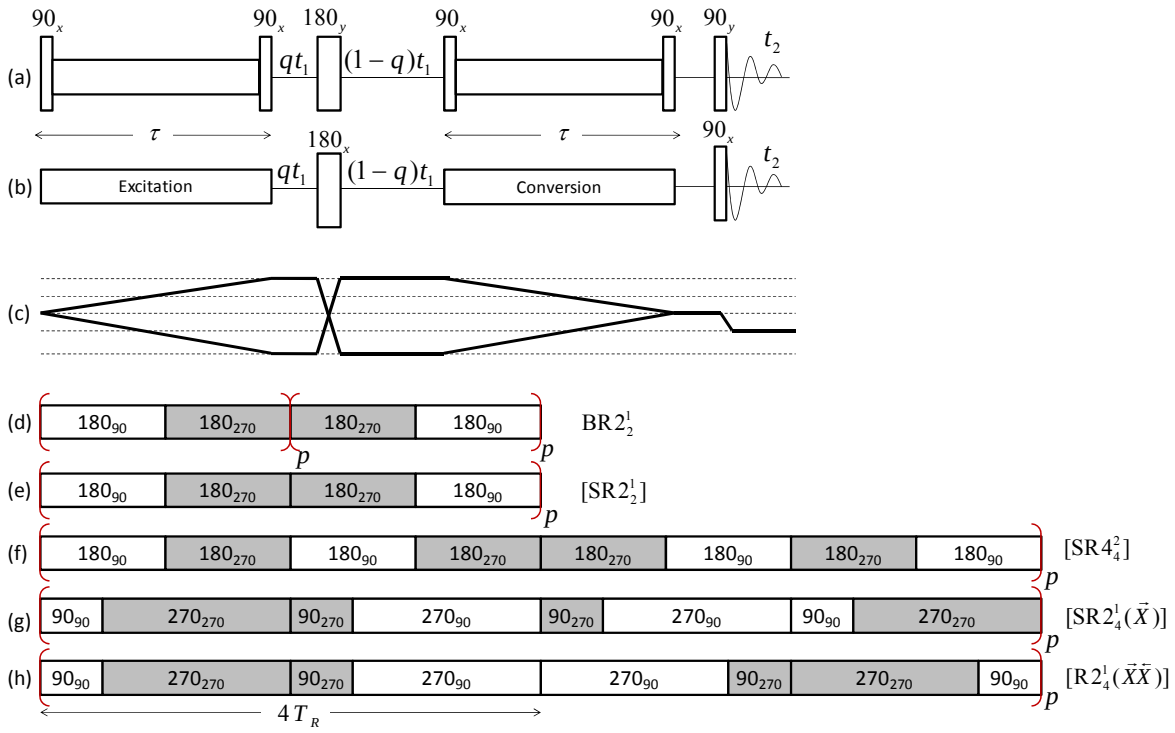

Fig.8.6. 2Q-1Q pulse sequences using bracketed (a) or un-bracketed (b) homo-nuclear dipolar recoupling schemes. All rf pulses depicted in the figure are CT-selective. The selected coherence transfer pathway is shown in (c). The DQ single-spin signal is cancelled by the CT-selective π pulse and only spin-pair DQ coherences result in observable signal. The *q* parameter is used to scale *all* interactions in order to avoid folding of the resonances along the F_1 dimension. Recoupling schemes used in this article with either sequence (b): $BR2_2^1(\pi)$ (d), or sequence (a) : $[SR2_2^1(\pi)]$ (e), $[SR4_4^2(\pi)]$ (f), $[SR2_4^1(\vec{X})]$ (g) or $[R2_4^1(\vec{X}\bar{\vec{X}})]$(h). They use either simple (d-f), or composite (g,h) π pulses. Phases are equal to 90° or 270°, according to the pulse is shown in white or grey. The recoupling schemes use two types of super-cycling: (d) all the $R2_2^1$ blocks half of the recoupling time, and then all the $R2_2^{-1}$ blocks the second half, or (e-h) a succession of $SRN_n^{N/2}$ blocks that last either $4T_R$ (e) or $8T_R$ (f-h).

To limit the number of rf pulses in quadrupolar channel in order to increase the sensitivity, we employ sequences that achieve 2Q recoupling but does not require any bracketing π/2-pulse.[33] This possibility was first demonstrated by Edén and co-workers when introducing $R2_2^1$ recoupling methods but was not further exploited.[33] The corresponding pulse scheme for 2D 2Q-1Q spectroscopy of half-integer nuclei is depicted in **Fig.8.6b**. Timing and phase cycling are identical to those used for the sequence of **Fig.8.6a**. Hence the coherence transfer pathways are still those displayed in **Fig.8.6c**.

Several RN_n^ν symmetries were tested for the dipolar recoupling of half-integer quadrupolar nuclei. RN_n^ν are composed of N/2 $R_\phi R_{-\phi}$ inversion cycle pairs, where R is an inversion element of duration nT_R/N and ϕ indicates an overall phase shift of νπ/N. Here, R

either represents a simple π_0-pulse (**Fig.8.6d-f**) or the composite inversion pulses $\vec{X} = (\pi/2)_0(3\pi/2)_\pi$ (**Fig.8.6g,h**) and $\bar{\vec{X}} = (3\pi/2)_\pi(\pi/2)_0$ (**Fig.8.6h**), which are both internally compensated to resonance offsets and rf errors.

$RN_N^{N/2}$ (π or $\vec{X}$) and $R2_4^1$ (π or $\vec{X}$) pulse sequences (**Fig.8.6d-h**) generate a dipolar average Hamiltonian (AH) between homonuclear spins *j* and *k*, which comprises both 0Q and 2Q operators. The recoupling sequences described in **Fig.8.6d-h** provide both 0Q and 2Q recoupling and the corresponding AH is equal to:

$$H = b_{jk} f(\beta_R,\gamma_R)\{\ S_j^+S_k^+ + S_j^-S_k^- - 4S_{jz}S_{kz} + \ S_j^+S_k^- + S_j^-S_k^+\ \} \qquad (2)$$

In the above equation, b_{jk} is the dipolar coupling constant and $f(\beta_R,\gamma_R) = 3\sin(2\beta_R).\cos\gamma_R /(16\sqrt{2})$ is a function of Euler angles (β_R,γ_R) describing the orientation of the inter-nuclear vector in the rotor-fixed frame. Eq.2 shows that $RN_N^{N/2}$ and $R2_4^1$ schemes can be incorporated in the pulse sequences of **Fig.8.6b**, since the 2Q terms, $S_j^+S_k^+ + S_j^-S_k^-$, enable direct excitation of 2QC from longitudinal magnetization. $RN_N^{N/2}$ and $R2_4^1$ symmetries do not suppress all shielding terms.[33,35] However, these undesirable AH terms can be suppressed by the $SRN_n^\nu = RN_n^\nu RN_n^{-\nu}$ phase inversion super-cycle, while the average dipolar Hamiltonian is not affected and hence Eq.2 remains valid.[9,36,37] As discussed in Ref. 33 and 37, the super-cycled sequences $SRN_N^{N/2}$ and $SR2_4^1$ can also be incorporated in the pulse sequence of **Fig.8.6a** in order to convert the 0Q operators into pure 2Q operators. These $\pi/2$-bracketed sequences are denoted $[SRN_N^{N/2}]$ and $[SR2_4^1]$ in the following. Their AH is equal to:

$$[H] = 2b_{jk} f(\beta_R,\gamma_R)\{S_j^+S_k^+ + S_j^-S_k^-\} \qquad (3)$$

disregarding the quadrupolar interaction.

We investigate the unbracketed $R2_2^1$ sequence employing a super-cycle, which consists in a phase inversion from the middle of the τ delay. This original super-cycle, depicted in

Fig.8.6d, better eliminates the offset and rf error dependence than the usual phase inversion super-cycle, $SR2_2^1 = R2_2^1 R2_2^{-1}$. It will be denoted $BR2_2^1$ in the following. In fact, $BR2_2^1$ is stemmed from SPIP, if we remove all spin-lock θ pulses from SPIP and expand π pulse in one rotor period. When the excitation and reconversion intervals span 4p rotor periods, the $BR2_2^1$ (π) sequence corresponds to $(R2_2^1)_p(R2_2^{-1})_p = R2p_{2p}^{p} R2p_{2p}^{-p}$ symmetry. The better performances of $BR2_2^1$ super-cycling compared to phase inversion super-cycling cannot be explained by the selection rules on the zero- and first-order AH and are not yet fully understood.[36] The detail explanation of super-cycling can be found in the appendix.

In preparation for the experiments, we performed simulations with the SIMPSON software,[38] and the powder averaging was performed using 168 crystallites following the REPULSION algorithm.[39]

We have chosen to use two identical sites with the same quadrupolar parameters, and hence the same powder line-shapes, but with symmetrical isotropic chemical shifts of ± Δ/2 with respect to the reference frequency. The gravity centers of these line-shapes are shifted from the isotropic chemical shift values by the quadrupolar induced shifts ($\nu_{QIS} < 0$), and they thus appear at ± Δ/2 + ν_{QIS}. The rf-carrier is defined with respect to the reference frequency through the off-resonance frequency (ν_{offset}), which means that the frequency differences between the rf irradiation and the isotropic chemical shifts (or the line-shape gravity centers) are equal to ± Δ/2 – ν_{offset} (or to ± Δ/2 – ν_{offset} + ν_{QIS}). The spinning speed was always fixed to ν_R = 15 kHz (except in **Fig.8.8d**), and the quadrupolar and dipolar parameters of the two-spin system are those of ^{23}Na in Na_2SO_4 for spin-3/2 nuclei (C_Q = 2.6 MHz, η_Q = 0.6, d_{12} = 318 pm, b_{12} = –259 Hz) and of ^{27}Al in $AlPO_4$ berlinite for spin-5/2 nuclei (C_Q = 4.07 MHz, η_Q = 0.43, d_{12} = 440 pm, b_{12} = –95 Hz). In both cases, the inter-nuclear vector was assumed aligned with the *z* principal axis of the quadrupolar tensor.

We ran simulations on a two-spin system, denoted S_1 and S_2 in the following. We detected the magnetization transferred from S_1 to S_2 during the 2QF experiment. It corresponds to one of the two cross-peaks between S_1 and S_2 CT transitions on the 2D 2Q-1Q spectrum. These simulations were done starting from S_1 longitudinal magnetization, i.e. the operator S_{1z}, and detecting only the −1Q coherence of spin S_2, which corresponds to the operator S_2^-. The transfer efficiency was then calculated in comparison to the signal from a CT-selective 90° pulse on S_2.

I. 'Diagonal'-peak, with $F_1 = 2(1\text{-}2q)F_2$, of two similar nuclei ($\Delta = 0$)

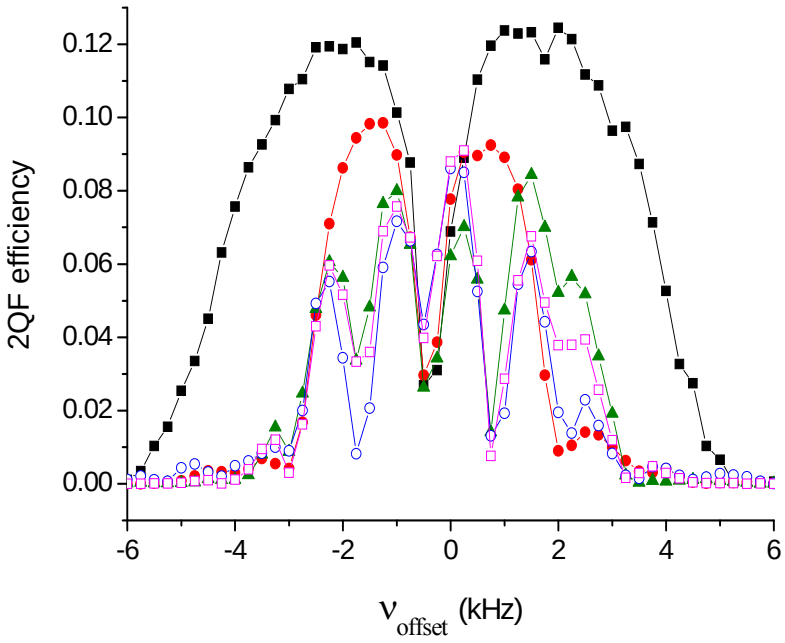

Fig.8.7. Simulations of 2QF efficiency of 'diagonal' peak ($\Delta = 0$) with $F_1 = 2(1-2q)F_2$, versus resonance offset, ν_{offset}, at Larmor frequency $\nu_0 = 208.6$ MHz and a MAS frequency $\nu_R = 15$ kHz. The spin system consists of two ^{27}Al nuclei ($S = 5/2$) with quadrupolar parameters, $C_Q = 4.07$ MHz and $\eta_Q = 0.43$. The dipolar coupling between them was $b_{12} = -95$ Hz. The rf nutation frequency for the recoupling sequence was fixed to $\nu_1 = 2.5$ kHz. The pulse lengths for the central π and the four bracketing $\pi/2$ pulses are 25 and 12.5 μs, respectively. Different homonuclear recoupling sequences were employed: black full squares (■): $\mathrm{BR}2_2^1(\pi)$ with $\tau = 2933$ μs, red full dots (●) : $[\mathrm{SR}2_2^1(\pi)]$ with $\tau = 2133$ μs, green full triangles (▲) : $[\mathrm{SR}4_4^2(\pi)]$ with $\tau = 2666$ μs, red empty squares (□) $[\mathrm{R}2_4^1(\vec{X}\bar{\vec{X}})]$ with $\tau = 2133$ μs, and blue empty dots (o) $[\mathrm{SR}2_4^1(\vec{X})]$ with $\tau = 2133$ μs.

We have first investigated the case of two nuclei with identical chemical shifts, $\Delta = 0$. The 2QF efficiency was calculated by numerical simulations as function of the offset, ν_{offset}, for all sequences described in **Fig.8.6**, and at static magnetic field 18.8 T. The obtained efficiencies correspond to those of auto-peaks situated on the diagonal of the 2D 2Q-1Q spectrum, which has a slope of $2(1 - 2q)$. For spin-3/2 nuclei (results not shown), all recoupling sequences are equivalent in terms of efficiency (around 16% for on-resonance irradiation, $\nu_{offset} = 0$) and robustness to offset. However, the efficiency of diagonal peaks is slightly less sensitive to offsets for $BR2_2^1(\pi)$ method. In contrast, for spin-5/2 nuclei, the $BR2_2^1$ method displays a higher efficiency and robustness to offset compared to the bracketed sequences. The larger 2QF efficiency for the un-bracketed method partly stems from the inability of the bracketing pulses to selectively rotate the central-transition polarization, since the rf pulses do not operate in the CT-selective regime for all crystallites and time points. An interesting phenomenon can also be observed in **Fig.8.7**: all sensitivity curves present a narrow dip for on-resonance irradiation. This dip is always observed, whatever may be the relative orientations of the two quadrupolar tensors and the inter-nuclear vector. We do not have presently any explanation for this effect. This dip entails that the carrier frequency must be set up in a frequency region devoid of resonance.

II Cross-peaks of two different nuclei ($\Delta \neq 0$)

We then simulated the case of two nuclei resonating at $\Delta = 5$ kHz from each other. The simulations were performed for spin-3/2 at 9.4 T (**Fig.8.8a**) and spin-5/2 at 18.8 T (**Fig.8.8b**). By comparing Fig. 8.7 and 8.8b, we observe that for spin-5/2 nuclei the maximum efficiency of bracketed sequences is roughly divided by a factor of two when increasing the chemical difference from $\Delta = 0$ to 5 kHz, whereas that of $BR2_2^1(\pi)$ is only slightly decreased. All experiments present one or several dips of sensitivity, which means that for sensitivity

reasons, the carrier frequency must be carefully optimized. However, globally, the $BR2_2^1$ sensitivity is much larger and much more robust to offset than bracketed sequences, especially for spin-5/2 nuclei. For spin-3/2 nuclei this chemical shift difference, Δ = 5 kHz, is often an upper limit for most nuclei (e.g. ^{23}Na or ^{11}B), even at high magnetic fields, but this value can be much larger for spin-5/2 nuclei. For example, it can amount to Δ = 10 kHz for the cross peaks between tetrahedral and octahedral ^{27}Al sites at 18.8 T. Thus we performed the same simulations, with the same spinning speed ν_R = 15 kHz, but we doubled the chemical shift difference: Δ = 10 kHz **(Fig.8.8c)**. It can be observed in this figure that the efficiencies obtained for bracketed sequences then become negligible. This is not the case with the $BR2_2^1$ sequence, and even if there are two large dips at $\nu_{offset} \approx$ 0.5 and -1.5 kHz, it always remains possible to get a reasonable efficiency (≈ 6-8 %) by optimizing the carrier frequency. These two dips disappear when increasing the spinning speed and thus the rf-field. In **Fig.8.8d**, simulated with Δ = 10 kHz and ν_R = 30 kHz, one observes for the $BR2_2^1$ sequence the same maximum efficiency as in **Fig.8.8c**, without the two dips. The spectral width is larger than in **Fig.8.8b** but the increase of isotropic chemical shift difference leads to a 30% decrease in the maximal 2QF efficiency. Simultaneously, the efficiency for the bracketed sequences remains very weak. The observation of 2Q-1Q cross-peaks of half-integer quadrupolar nuclei with large frequency separation thus requires the use of the $BR2_2^1$ sequence under fast MAS.

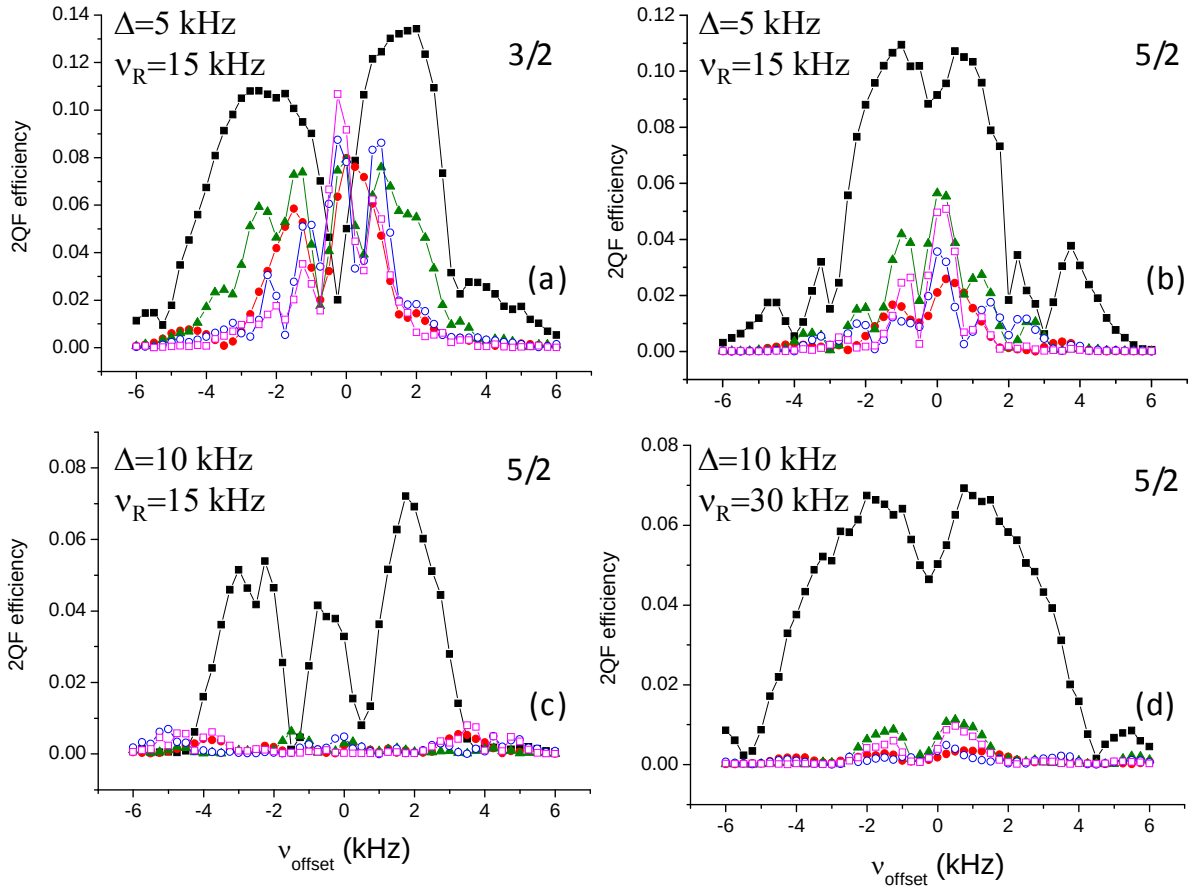

Fig.8.8. Simulations of 2QF efficiency of cross-peaks ($\Delta \neq 0$) versus resonance offset, ν_{offset}. (a) The spin system consists of two ^{23}Na nuclei ($S = 3/2$) with quadrupolar parameters C_Q = 2.6 MHz, $\eta_Q = 0.6$, and a dipolar coupling constant $b_{12} = -259$ Hz. The Larmor frequency was $\nu_0 = 105.8$ MHz and the MAS frequency $\nu_R = 15$ kHz. The frequency separation between the two sites was $\Delta = 5$ kHz. The rf nutation frequency for the recoupling sequence was ν_1 = 3.75 kHz. (b-d) The spin system consists of two ^{27}Al nuclei ($S = 5/2$), and its parameters are identical to those of Fig.8.7, except the frequency separation, the MAS frequency and the rf nutation frequency, which are as follows: (b) $\Delta = 5$ kHz, $\nu_R = 15$ kHz, $\nu_1 = 2.5$ kHz, (c) Δ = 10 kHz, $\nu_R = 15$ kHz, $\nu_1 = 2.5$ kHz, (d) $\Delta = 10$ kHz, $\nu_R = 30$ kHz, $\nu_1 = 5$ kHz. Symbols for the different recoupling schemes are identical to those defined for Fig.8.7.

In **Fig.8.9a** we have represented the 2Q-1Q 2D spectrum of as synthesized $AlPO_4$-14 recorded at 18.8 T and ν_R = 16 kHz, and using $BR2^1_2$ (π) for 2QC excitation and reconversion. This compound presents four different aluminum species:[40] two tetrahedral sites (Al_3 : δ_{cs} = 42.7 ppm, C_Q = 1.72 MHz, η_Q = 0.57; Al_2 : δ_{cs} = 43.5ppm, C_Q = 3.90 MHz, η_Q = 0.83), one pentavalent aluminum atom (Al_1 : δ_{cs} = 27.1 ppm, C_Q = 5.61 MHz, η_Q = 0.93) and

one octahedral site (Al_4 : δ_{cs} = –1.3 ppm, C_Q = 2.55 MHz, η_Q = 0.67), and in addition, our sample also presents an extra-framework impurity at –2 kHz. Along with Al-O-P-O-Al connectivities, which are common for all aluminophosphate molecular sieves, in $AlPO_4$-14 there are also some Al-O-Al connectivities due to edge sharing between AlO_6 octahedra and vertex sharing between AlO_5 and AlO_6 polyhedra. The corresponding distances are 290 pm for Al_4-O-Al_4 connectivity (b_{44} = –333 Hz) and 360 pm for Al_1-O-Al_4 connectivity (b_{14} = –174 Hz).[41] All other distances are much larger, and as an example they range over 430 to 480 pm (b_{23} = –73 to –102 Hz) between Al_2 and Al_3 nuclei.

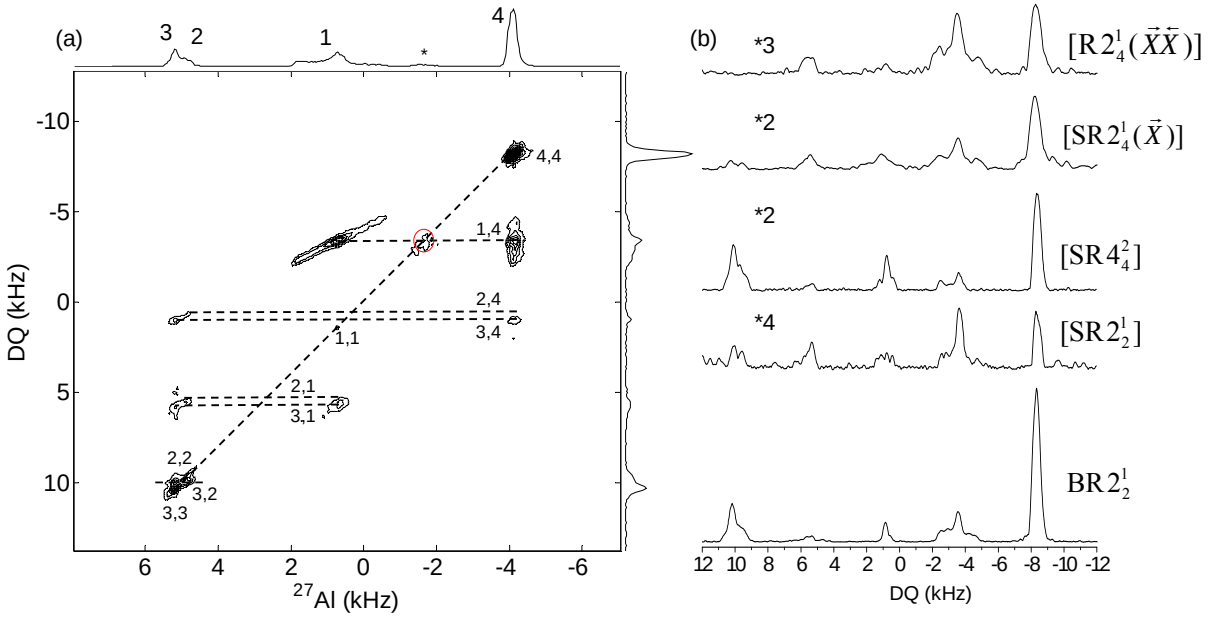

Fig.8.9. Experimental ^{27}Al correlation spectra of $AlPO_4$-14 at 18.8 T (ν_0 = 208.6 MHz) and ν_R = 16 kHz. (a) 2Q-1Q 2D spectrum using $BR2_2^1(\pi)$ for 2QC excitation. The parameter q has been fixed to 0.2, and the spectrum has been re-scaled in the F_1 dimension. The relaxation delay was 0.6s and the indirect dimension of each spectrum was acquired with 140 points each obtained with 192 scans. The total experimental time for each 2D spectrum was 4.5 hours. It can be decreased to 2 hours, without loss in S/N ratio, by using an initial hyper-secant CT enhancing. The impurity at c.a. -2 kHz is indicated by a star and its auto-peak is circled. The rf nutation frequencies were $\nu_1 \approx$ 2.67 kHz for the homonuclear recoupling sequence and 6.67 kHz for the CT-selective π and $\pi/2$ pulses. (b) Comparison of F_1 projections for the five homonuclear recoupling sequences described in Fig.8.6. The excitation time τ for $BR2_2^1(\pi)$, $[SR2_2^1(\pi)]$, $[SR4_4^2(\pi)]$, $[R2_4^1(\vec{X}\bar{\vec{X}})]$ and $[SR2_4^1(\vec{X})]$ are 1250, 750, 1000, 1000 and 1000 μs.

All peaks are easily distinguishable in this figure, even the cross-peaks between tetrahedral and octahedral sites ($Al_{2,3}$-Al_4), even if they are 540 pm apart ($b_{24} = b_{34} = -52$ Hz) and display a large difference in isotropic chemical shift ($\Delta \approx 10$ kHz). The F_1 projections of the five sequences described in **Fig.8.6** are compared in **Fig.8.9b**. This comparison points out the fact that the un-bracketed $BR2_2^1(\pi)$ method gives at least a two-fold sensitivity gain over all bracketed sequences. According to simulations, this sensitivity gain would increase at ν_R = 30-35 kHz (see **Fig.8.8d**). The Al_1 auto peak is hardly visible as it corresponds to long distances (670 pm and $b_{11} = -27$ Hz) and is certainly submitted to dipolar truncation with respect to the much larger dipolar interaction ($b_{14} = -174$ Hz) between the Al_1 and Al_4 sites. This dipolar truncation, which occurs in all 2Q-1Q and 1Q-1Q homo-nuclear dipolar methods, is one of the most important limitations of these methods.

Above all, we have demonstrated 2Q-1Q homo-nuclear correlation 2D experiments among the central transition of half-integer quadrupolar spins with an un-bracketed dipolar recoupling sequence based on the $R2_2^1$ rotor-synchronized and symmetry-based scheme initially developed for spin-1/2 nuclei. It must be noted that the super-cycling of this sequence differs from that used previously in the literature and yields higher efficiency and more robustness to rf-inhomogeneity and to offsets for auto- and cross-peaks. It allows the observation of cross-peaks that are separated by more than 10 kHz, provided the spinning speed is fast enough. More details can be found in ref [42].

References

[1] W.S. Brey, M.L. Brey, in *Encyclopedia of Nuclear Magnetic Resonance*, Wiley, Chichester, **1996**.

[2] J. Miller, *Prog. Nucl. Magn. Reson. Spectrosc.* **1996**, 28, 255-281.

[3] A.S. Ulrich, *Prog. Nucl. Magn. Reson. Spectrosc.* **2005**, 46, 1-21.

[4] S. Ando, R.K. Harris, U. Scheler, in *Encyclopedia of Nuclear Magnetic Resonance*, Wiley, Chichester, **2007**.

[5]M.L. Gilchrist, K. Monde, Y. Tomita, T. Iwashita, K. Nakanishi, A.E. McDermott, *J. Magn. Reson.* **2001**, 152, 1-6.

[6] C.D. Martin, S. Chaudhuri, C.P. Grey, J. B. Parise, *Am. Mineral.* **2005**, 90, 1522-1533.

[7] C. Martineau, C. Legein, J.Y. Buzaré, F. Fayon, *Phys. Chem. Chem. Phys*. **2009**, 11, 950-957.

[8] I. Schnell, *Prog. Nucl. Magn. Reson. Spectrosc.* **2004**, **45**, 145-207.

[9] M.H. Levitt, in *Encyclopedia of Nuclear Magnetic Resonance*, Wiley, Chichester, **2002**.

[10] W. Sommer, D.E. Demco, S. Hafner, H.W. Spiess, *J. Magn. Reson*. Series A. **1995**, 116, 36-45; M. Feike, D.E. Demco, R. Graf, J. Gottwald, S. Hafner, H.W. Spiess, *J. Magn. Reson*. **1996**, 122, 214-221.

[11] B. Hu, Q. Wang, O. Lafon, J. Trébosc, F. Deng, J.P. Amoureux, *J. Magn. Reson*. **2009**, 198, 41-48.

[12] M. Body, Ph.D. Thesis, Université du Maine, France, **2005**.

[13] V. Kaiser, D. Babel, *Z. Anorg. Allg. Chem*. **2004**, 630, 794-798.

[14] M. Body, C. Legein, J.Y. Buzaré, G. Silly, P. Blaha, C. Martineau, F. Calvayrac, *J.*

Phys. Chem. A **2007**, 111, 11873-11884.

[15] A. Zheng, S.B. Liu, F. Deng, *J. Phys. Chem. C* **2009**, 113 (33), 15018-15023.

[16](a) C.J. Pickard, F. Mauri, *Phys. Rev. B* **2001**, 63, 245101; (b) M. Profeta, M. Benoit, F. Mauri, C.J. Pickard, *J. Am. Chem. Soc.* **2004**, 126, 12628-12635.]

[17] Qiang Wang, Bingwen Hu,Franck Fayon, Julien Trébosc,Christophe Legein, Olivier Lafon, Feng Deng, Jean-Paul Amoureux, Double-quantum 19F-19F dipolar recoupling at ultra-fast magic angle spinning NMR: application to the assignment of 19F NMR spectra of inorganic fluorides, **Phys. Chem. Chem. Phys.**, 2009, **DOI:** 10.1039/b914468d

[18] A. Iuga, C. Ader, C. Gröger, E. Brunner, Applications of Solid-State 31P NMR Spectroscopy, Annu. Rep.NMR Spectrosc. 60 (2006) 145-189.

[19] J. Schmedt auf der Günne, Distance measurements in spin-1/2 systems by 13C and 31P solid-state NMR in dense dipolar networks, J. Magn. Reson. 165 (2003) 18–32.

[20] M. Feike, D. E. Demco, R. Graf, J. Gottwald, S. Hafner, H.W. Spiess, Broadband multiple-quantum NMR spectroscopy, J. Mag. Reson. - Series A. 122 (1996) 214-221.

[21] Y. H. Tseng, Y. Mou, C.Y. Mou, J.C.C. Chan, Double-quantum NMR spectroscopy based on finite pulse RFDR, Solid State NMR. 27 (2005) 266-270.

[22] A. Brinkmann, M. Edén, M. H. Levitt, Synchronous helical pulse sequences in magic-angle spinning nuclear magnetic resonance: Double quantum recoupling of multiple-spin systems, 112 (2000) 8539-8554.

[23] M. Hohwy, H.J. Jakobsen, M. Edén, M.H. Levitt, N.C. Nielsen, Broadband dipolar recoupling in the nuclear magnetic resonance of rotating solids: a compensated C7 pulse sequence, J. Chem. Phys. 108 (1998) 2686- 2694.

[24] F. Vasconcelos, S. Cristol, J.F. Paul, G. Tricot, J.P. Amoureux, L. Montagne, F. Mauri, L. Delevoye. 17O solid-state NMR and first-principles calculations of sodium

trimetaphosphate (Na3P3O9), tripolyphosphate ($Na_5P_3O_{10}$) , and pyrophosphate ($Na_4P_2O_7$), *Inorg. Chem.* 47 **(2008)** 7327.

[25] F. Fayon, G. Le Saout, L. Emsley, D. Massiot, Through-bond phosphorus–phosphorus connectivities in crystalline and disordered phosphates by solid-state NMR, Chem. Comm. 1702-1703 **(2002).**

[26]B. Hu, L. Delevoye, O. Lafon, J. Trébosc, J.P. Amoureux, Double-quantum NMR spectroscopy of ^{31}P species submitted to very large CSAs, Journal of Magnetic Resonance 200 (2009) 178–188.

[27] N. C. Nielsen, H. Bildsoe, H. J. Jakobsen, M. H. Levitt, Double-quantum homonuclear rotary resonance: Efficient dipolar recovery in magic-angle spinning nuclear magnetic resonance *J. Chem. Phys.* 101 (1994) 1805-1812.

[28]S. Wi, J.W. Logan, D. Sakellariou, J.D. Walls, A. Pines, Rotary resonance recoupling for half-integer quadrupolar nuclei in solid-state nuclear magnetic resonance spectroscopy, *J. Chem. Phys.* 117 **(2002)** 7024-7033.

[29] J. Painter, M.J. Duer, Double-quantum-filtered nuclear magnetic resonance spectroscopy applied to quadrupolar nuclei in solids, *J. Chem. Phys*. 116 **(2002)** 710-722.

[30] G. Mali, G. Fink, F. Taulelle, Double-quantum homonuclear correlation magic-angle sample spinning nuclear magnetic resonance spectroscopy of dipolar-coupled quadrupolar nuclei, *J. Chem. Phys*. 120 **(2004)** 2835-2845.

[31] G. Mali, V. Kaucic, Enhancing sensitivity or resolution of homonuclear correlation experiment for half-integer quadrupolar nuclei, *J. Magn. Reson.* 171 **(2004)** 48-56.

[32] M. Eden, H. Annersten, A. Zazzi, Pulse-assisted homonuclear dipolar recoupling of half-integer quadrupolar spins in magic-angle spinning NMR, *Chem. Phys. Lett*. 410 **(2005)**, 24-30.

[33] M. Eden, D. Zhou, J. Yu, Improved double-quantum NMR correlation spectroscopy of dipolar-coupled quadrupolar spins, *Chem. Phys. Lett*. 431 **(2006)** 397-403.

[34] M.R. Hansen, H.J. Jakobsen, J. Skibsted, Structural environments for boron aluminum in alumina-boria catalysts and their precursors from ^{11}B and ^{27}Al single- and double-resonance MAS NMR experiments, *J. Phys. Chem*. C112 **(2008)** 7210-7222.

[35] A.Y.H. Lo, M. Eden, Efficient symmetry-based homonuclear dipolar recoupling of quadrupolar spins : double-quantum NMR correlations in amorphous solids, *Phys. Chem. Chem. Phys.* 10 **(2008)** 6635-6644.

[36] A. Brinkmann, M. Eden, Second order average Hamiltonian theory of symmetry-based pulse schemes in the nuclear magnetic resonance of rotating solids: application to triple-quantum dipolar recoupling, *J. Chem. Phys.* 120 (2004) 11726-11745.

[37] A. Brinkmann, J. Schmedt auf der Günne, M. H. Levitt, Homonuclear Zero-Quantum Recoupling in Fast Magic-Angle Spinning Nuclear Magnetic Resonance, *J. Magn. Reson.* 156 (2002) 79-96

[38] M. Bak, J.T. Rasmussen, N.C. Nielsen, SIMPSON: a general simulation program for solid-state NMR spectroscopy, *J. Magn. Reson*. 147 **(2000)** 296-330.

[39] M. Bak, N.C. Nielsen, REPULSION: a novel approach to efficient powder averaging in solid-state NMR, *J. Magn. Reson*. 125 **(1997)** 132-139.

[40] C. Fernandez, J.P. Amoureux , C. Chezeau, L. Delmotte, A. Kessler, Al-MAS NMR characterization of $AlPO_4$-14. Enhanced resolution and information by MQMAS, *Microporous Materials*. 6 **(1996)** 331-340.

[41] R.W. Broach, S.T. Wilson, R.M. Kirchner, Corrected crystallographic tables and figure for as-synthesized $AlPO_4$-14, *Microporous Mesoporous Mater*. 57 **(2003)** 211-214.

[42] Q. Wang, B. Hu, O. Lafon, J. Trébosc, F. Deng, J.P. Amoureux, Double-quantum homonuclear NMR correlation spectroscopy of quadrupolar nuclei subjected to magic-angle spinning and high magnetic field, Journal of Magnetic Resonance 200 (2009) 251–260.

Appendix

1. SIMPSON simulation file for MP-CPMAS

```
spinsys {
   channels 1H 31P
   nuclei 1H 31P

   shift 1 0 0 0 0 0 0
   shift 2 0 0 0 0 0 0
   dipole 1 2 -400      0    0 0
}
par {
   method                    direct
   proton_frequency      400e6
   np                    2
   crystal_file          rep168
   start_operator        I1z
   detect_operator       I2p
   spin_rate             10000
   sw                    spin_rate
   gamma_angles    11
   verbose               1101
   use_cluster           1
   variable rfP          100000
   variable rfN          100000
   variable rfN90        100000
   variable rfNStrong 100000
   variable lRR          10
   variable rfRR         6000
   variable phP2         0
   variable pLfactor1.0
   variable count     10
   variable ph1       0
   variable pN180factor    1.0
   variable span 1
   variable nii  1
   variable powlist  ""
}
proc pulseq {} {
   global par
   maxdt 0.1
foreach pow $par(powlist) {
```

```
   set par(rfRR) [expr $pow]

   set pP [expr 1.0e6/$par(rfP)/4.0]
   set pN180 [expr 1.0e6/$par(rfN)/2.0/$par(pLfactor)]
   set pN180 [expr $pN180*$par(pN180factor)]
   set pN90 [expr 1.0e6/$par(rfN90)/4.0/$par(pLfactor)]
   set tr [expr 1.0e6/$par(spin_rate)]
   set tau1 [expr ($par(span)*1.0e6/$par(spin_rate)-$pN180)/2]
#    set tau2 [expr $tr-$pN90/2-$pN180/2]
   set tau2 [expr $tr]

set rfN3   [expr $par(rfN)*0.5]
reset [expr $pN90+$tau2]
pulse $tau1 0 0 $par(rfRR) 0
pulse $pN180 $par(rfN) 0 $par(rfRR) 0
pulse $tau1 0 0 $par(rfRR) 0
store 1


for {set i 1} { $i<=$par(count)} {incr i 1} {
      if ($i>1) {
            reset [expr $pN90+$tau2]
            prop 3
            prop 1
            store 3
      } else {
            reset [expr $pN90+$tau2]
            prop 1
            store 3
      }
}


reset [expr $pN90+$tau2]
   delay [expr 1.0e6/$par(sw)]
   store 999

reset
   pulse $pN90 $par(rfN90) $par(ph1) 0 0
   store 11
set ph90 [expr $par(ph1)+90]
reset
   pulse $pN90 $par(rfN90) $ph90 0 0
   store 12
```

```
reset [expr $pN90]
   delay [expr $tau2]
   store 22
reset [expr $pN90+$tau2]
   delay [expr $tr]
   store 23

   set nphalf [expr $par(np)]
for {set i 1} { $i<$par(nii)} {incr i 1} {
   if {$i>1} {
      reset [expr $pN90]
      prop 22

      prop 23
      store 22
   }
   }
   reset
   prop 11
   prop 3
   acq $nphalf 999


}
}

proc formatintbylen {int len} {
      set results ""
      append results $int
      set count [string length $results]
      while { $count<$len } {
            set results "0$results"

            incr count
      }
      return $results
}

proc main {} {
      global par

foreach rfNN { 100000    } {
```

```
foreach spin {10000 20000 40000} {
set v1 [expr 1.0]
set v2 [expr 1.0]
set cc [expr 50*$spin/10000]
for {set v [expr $v1]} {$v<=$v2} { incr v 1} {
for {set i [expr $cc]} {$i<=$cc} {incr i 2} {
   foreach j {0.2 0.3 0.4 0.667 0.7 0.8 0.9 0.95 1.05 1.1 1.2 1.3 1.4 1.6 1.7 1.8 } {
      set par(pN180factor) [expr $j]
            set par(span) [expr $v]
      set par(count)  [expr $i]
#     set par(rfRR)   [expr $power]
      set par(spin_rate) [expr $spin]
      set par(sw)     [expr $spin]
#     set par(sw1)    [expr $spin]
#     set par(rfN)    [expr $rfNN]
#     set par(rfN90) [expr $rfNN]

         set    par(powlist) ""
         set t    [expr $j/($v*1.0)]
         puts "=t=$t"
#set centerpower [expr    $spin*([expr $j]/[expr $v]/2)]
set power1 [expr round($spin*(0+$j/($v*1.0)/2.0))-500]
set power2 [expr round($spin*(0+$j/$v/2.0))+500]
for    {set power $power1} {$power<=$power2} {set power [expr $power+100]} {
      set    par(powlist) "$par(powlist) $power"
}

set power1 [expr round($spin*(1-$j/$v/2))-500]
set power2 [expr round($spin*(1-$j/$v/2))+500]
for    {set power $power1} {$power<=$power2} {set power [expr $power+100]} {
      set    par(powlist) "$par(powlist) $power"
}
set power1 [expr round($spin*(1+$j/$v/2))-500]
set power2 [expr round($spin*(1+$j/$v/2))+500]
for    {set power $power1} {$power<=$power2} {set power [expr $power+100]} {
      set    par(powlist) "$par(powlist) $power"
}
set power1 [expr round((2-$j/2/$v)*$spin)-500]
set power2 [expr round((2-$j/2/$v)*$spin)+500]
for    {set power $power1} {$power<=$power2} {set power [expr $power+100]} {
      set    par(powlist) "$par(powlist) $power"
}
set power1 [expr round((2+$j/2/$v)*$spin)-500]
set power2 [expr round((2+$j/2/$v)*$spin)+500]
```

```
for   {set power $power1} {$power<=$power2} {set power [expr $power+100]} {
      set   par(powlist) "$par(powlist) $power"
}

set par(ni) [llength $par(powlist)]


      set ioffset 0
      set iCq          3e6
      #set up Cq, QIS and offset
      set offset       $ioffset
      set Cq           $iCq
      set eta    0
            set I             2.5
      set m            0.5
      set n       -0.5
      set nu           [resfreq 27Al $par(proton_frequency)]
      #Al's QIS
      #set                                    QIS                                    [expr
-pow(3.*$Cq/(2.*$I*(2.*$I-1)),2)*56./(5040.*$nu)*(3.+$eta*$eta)*($I*($I+1.)-3./4.)]
      set QIS   [expr
pow(3.*$Cq/(2.*$I*(2.*$I-1)),2)*56./(5040.*$nu)*(3.+$eta*$eta)*($m*($I*($I+1.)-3.*$m*$m)-$
n*($I*($I+1.)-3.*$n*$n))]
      set ObsFreq    [expr $offset+$QIS]
      puts stdout "=== ObsFreq=$ObsFreq====="
      #spectrum Observed Freq.

      set count 0
            foreach par(ph1) {90 270} {
                  set g [fsimpson    ]
            if {$count>0} {
                  fsub $f $g
                  funload $g
            } else {
                  set f $g
            }
            incr count
            } ;#phP2

      set ext "rfN="
      append ext [formatintbylen $rfNN 7]
      append ext ".spin="
      append ext [formatintbylen $spin 3]
      append ext ".span="
```

```
        append ext [formatintbylen $v 3]
        append ext ".nTR="
        append ext [formatintbylen $i 4]
        append ext ".PW180="
        append ext [formatintbylen $j 4]
        fsave $f $par(name).$ext.fid
          set r [fcreate -np $par(np) -sw $par(sw)]
          set ii 0
          foreach rf $par(powlist) {
        set ext2 [formatintbylen $rf 7]
            fextractFid $r $f [expr $ii*$par(np)+1] $par(np)
            fsave $r $par(name).$ext.rf=$ext2.fid
            incr ii
          }
        funload $r
        funload $f

}
}
}
}
}
}

proc fextractFid {r d n1 nt} { # r:dest_dataset d:from_dataset n1:first_point nt:total_points
 set i 1
 for {set n $n1} {$n<$n1+$nt} {incr n} {
   fsetindex $r $i [findex $d $n -re] [findex $d $n -im]
   incr i
 }
}
```

2. SIMPSON simulation file for *D*-HMQC with SFAM

```
spinsys {
   channels    13C 15N
   nuclei    13C 15N
   shift 1      0 0 0       0 0 0
   shift 2      0 0 0       0 0 0
   dipole 1 2 1000 0       0.0 0
}

par {
```

```
   method                    direct
   np                        120
   crystal_file        rep168
    start_operator        I1x
   detect_operator      I1p

   variable OFF       40000
   variable RF       40000
   variable NTrStep   1
   sw                        $spin_rate
   spin_rate                4000
   verbose        0000
   use_cluster              1
   gamma_angles 15
}

proc pulseq {} {
   global par
   maxdt 0.1
   set RF 50000
   set pid90 [expr 250000./$RF]
   set p90 0

   set RFN 50000
   set pidN180 [expr 500000./$RFN]
   set pN180 0
   set Tr [expr 1.0e6/$par(spin_rate)]

   set n 200
   set q 1
   set Tinc [expr 1.0*$Tr/($n)]
   set pi [expr atan(1.0)*4]
   set span 1
#
# calculate one SFAM rotor period
   reset
   for {set i 0} {$i<=$n-1} {incr i} {
      set                                    ph                                    [expr
($par(OFF)/($q*$par(spin_rate)*1.0)*sin($q*$par(spin_rate)*2.0*$pi*$i*(1e-6)*$Tinc)/(2*$pi))*
360.0]
        set amp [expr $par(RF)*sin($q*$par(spin_rate)*2.0*$pi*$i*(1e-6)*$Tinc)]
      if {$amp<0} {
         set amp [expr -$amp]
         set ph [expr $ph+180]
```

```
      }
      pulse $Tinc      $amp $ph 0 0
   }
   store 1

   reset
   for {set i 0} {$i <    [expr $par(NTrStep)/$span] } {incr i} {
      prop 1
   }
   store 10
# hmqc refocusing 180 pulses with 2 phases inversion for 2Q selection
   reset
   delay [expr $Tr-$p90/2]
   pulseid $pid90 0 0 $RF 0
   delay [expr $Tr-$p90/2-$pN180/2]
   pulseid $pidN180 $RFN 0 0 0
   delay [expr $Tr-$p90/2-$pN180/2]
   pulseid $pid90 0 0 $RF 0
   delay [expr $Tr-$p90/2]
   store    2
   reset
   delay [expr $Tr-$p90/2]
   pulseid $pid90 0 0 $RF 0
   delay [expr $Tr-$p90/2-$pN180/2]
   pulseid $pidN180 $RFN 0 0 0
   delay [expr $Tr-$p90/2-$pN180/2]
   pulseid $pid90 0 0 $RF 180
   delay [expr $Tr-$p90/2]
   store    3

#reference experiment (single echo)
#
   reset
#    prop 2
   acq
   reset
#    prop 3
   acq

for {set NTr 1} {$NTr < [expr $par(np)/2]} {incr NTr} {
# with phases 0 0
   reset
   prop 10
   prop 2
```

```
   prop 10
   acq
# with phases 0 180
   reset
   prop 10
   prop 3
   prop 10
   acq

# update prop 10 for next pulse length
   reset
   prop 10
   for {set i 0} {$i <    [expr $par(NTrStep)/$span] } {incr i} {
      prop 1
   }
   store 10

   }
}

proc main {} {
   global par


# loops of varying parameters
   foreach offres {0    } {
     puts "=off=$offres"
   foreach par(spin_rate) {20000 70000} {
     set File [open "$par(name).offres=$offres.spin=$par(spin_rate).res" w]
     set par(NTrStep) [expr 2*$par(spin_rate)/20000]
     puts "==spinrate=$par(spin_rate)"
   for {set par(OFF) 0 } {$par(OFF) <= 60000 } {set par(OFF) [expr $par(OFF)+ 5000] } {
         puts "====OFF=$par(OFF)"
   for {set par(RF) [expr 10000]} {$par(RF) <= [expr $par(spin_rate)*5]}    { set par(RF) [expr
$par(RF)+1000]} {
       puts "=====RF=$par(RF)"
       set f [fsimpson [list [list shift_1_iso $offres]]]
# calculate reference amplitude
       set refr [expr [findex $f 1 -re] + [findex $f 2 -re]]
       set refi [expr [findex $f 1 -im] + [findex $f 2 -im]]
          puts $File "\#reference is Re:$refr Im:$refi"
          puts $File "\#RF OFF spin_rate pSFAM Sr Si"
# do phase cycling and print amplitudes
       for {set i 3} {$i <= [expr $par(np)/2]} {set i [expr $i+2]} {
```

```
        set Sr [expr -([findex $f [expr $i] -re] - [findex $f [expr $i+1] -re])]
        set Si [expr -([findex $f [expr $i] -im] - [findex $f [expr $i+1] -im])]
          puts $File "$par(RF) $par(OFF) $par(spin_rate) [expr
1e6*($i-1)/2/$par(spin_rate)*$par(NTrStep)] $offres $Sr $Si [expr sqrt(($Sr)*($Sr)+($Si)*($Si))]"
      }
      funload $f
   }
   }
   puts $File ""
   flush $File
   close $File

   }
   #puts $File ""
#   close $File
   }
}
```

3. SIMPSON simulation file for SAM

```
spinsys {

   channels 1H
   nuclei 1H 1H 1H 1H
   dipole 2    1 -30000     0     0.00       0.00
   dipole 3    1 -10000     0    69.65     302.28
   dipole 3    2 -10000     0    69.65     122.28
   dipole 4    1 -10000     0    69.65     237.72
   dipole 4    2 -10000     0    69.65      57.72
   dipole 4    3 -10000     0    90.00     180.00
   shift 1 6000 5p 0.8 0 0 0
   shift 2 6000 5p 0.8 0 0 0
   shift 3 8200 10p 0.2 0 0 0
   shift 4 9000 10p 0.2 0 0 0
   }

par {
   spin_rate              65000
   np                       512
   crystal_file         rep320
   proton_frequency 400e6
   start_operator      Inz
   detect_operator    I1p+I2p
   variable rf           200000
```

```
    sw                      spin_rate
    variable theta      54.7356103172
    variable OFF        0
    variable RF 0
    variable q 1
    variable span 1
    verbose 1101
    use_cluster 1
    gamma_angles 1
}

proc pulseq {} {
    global par

    set pLG1 [expr 1.0e6/$par(rf)/360.0*90]
    set pP [expr 1.0e6/$par(rf)/360.0*180.0]
    set tsw [expr 1.0e6/$par(sw)]
    set d1 [expr ($tsw/6-$pP)/2]

    set n 200
    set q [expr $par(q)]
    set Tr [expr 1.0e6/$par(spin_rate)]
    set Tinc [expr 1.0*$Tr/($n)]
    set pi [expr atan(1.0)*4]
    set span [expr $par(span)]

    reset [expr $pLG1]
    set f1 [open "amp2Tr.txt" w]

    for {set i 0} {$i<=$n-1} {incr i} {
        set ph [expr ($par(OFF)/($q*$par(spin_rate)*1.0)*cos($q*$par(spin_rate)*2.0*$pi*$i*(1e-6)*$Tinc)/(2*$pi))*360.0]
        set amp 0
                set amp1 [expr $par(RF)*cos($q*$par(spin_rate)*2.0*$pi*$i*(1e-6)*$Tinc)]
            set amp [expr $amp+$amp1]
                set t2 [expr $span*$Tinc]
        set tt [expr $t2*($i+1)]
        puts $f1 "$tt,$amp"
       if {$amp<0} {
          set amp [expr -$amp]
          set ph [expr $ph+180]

       }
```

```
      pulse $t2      $amp $ph
      }
   close $f1
store 999

   reset
   pulse $pLG1 $par(rf) x
   acq $par(np) 999 x
}

proc main {} {
   global par
   foreach par(spin_rate) { 30000 } {
   foreach par(span) {1.0} {
   foreach par(q) {3 4 5} {

   for {set par(OFF) 0 } {$par(OFF) <= 0 } {set par(OFF) [expr $par(OFF)+ 10000] } {
#     for {set par(RF) [expr 0.95*$par(q)*$par(spin_rate)/$par(span)]} {$par(RF) <= [expr
1.25*$par(q)*$par(spin_rate)/$par(span)]}                { set par(RF) [expr
$par(RF)+0.02*$par(q)*$par(spin_rate)/$par(span)]} {
     for {set par(RF) [expr 0]} {$par(RF) <= 0}      { set par(RF) [expr
$par(RF)+0.02*$par(q)*$par(spin_rate)/$par(span)]} {

   set par(sw) [expr $par(spin_rate)/$par(span)]
    set f [fsimpson]

      fsave                                                                    $f
$par(name).SFAMq=$par(q).span=$par(span).spin=$par(spin_rate).RF=$par(RF).OFF=$par(OFF
).fid
      faddlb $f 300 0
      fft $f
      fphase $f -rp 270
      fsave                                                                    $f
$par(name).SFAMq=$par(q).span=$par(span).spin=$par(spin_rate).RF=$par(RF).OFF=$par(OFF
).spe
      funload $f
      }
      }
      }
     }

   }
  }
}
```

4. SIMPSON simulation file for SPIP

```
spinsys {
channels 1H
nuclei 1H 1H
shift 1 0p 5.5p 0.8 99.4 146.6 138.9
shift 2 0p 14p 0.0 -0.7 88.5 138.9
dipole 1 2 -11000 0 57.95 90.71
}

par {
  spin_rate             20000
  proton_frequency 800e6
  gamma_angles        11
  sw                          spin_rate/4
  np                          30
  crystal_file        rep320
  start_operator    I2z
  detect_operator I1p
  variable rfsl        spin_rate*1.57/2
  variable rf180        spin_rate*1.57/2
  verbose                1101
  use_cluster 1
  variable scale1
}

proc pulseq {} {
    global par
    set DEBUG 0
    maxdt      0.5
    matrix set 1 totalcoherence {2 -2}
    matrix set 2 totalcoherence {0}
    set tr              [expr 1.0e6/$par(spin_rate)]
    set pi                 [expr atan(1.0)*4]
    set d1   0
    set d2   [expr $tr*0.0]
    set rfsl        [expr $par(rfsl)]
    set rf180        [expr $par(rf180)]
    set k     [expr $par(scale)]
    set p180              [expr 1.0e6/$par(spin_rate)/$k]
    set pp              [expr ($tr-$p180-2*$d1-2*$d2)/2]

    set rf 1.0e5
```

```
   set p90 [expr 1.0e6/$rf/4.0]
if {$DEBUG>0} {
 puts "d1=$d2"
 puts "d2=$d2"
 puts "SL=$pp"
 puts "p180=$p180"
 }
  reset
     delay $d1
     pulse $pp $rfsl 0
     delay $d2
     pulse $p180 $rf180 0
     delay $d2
     pulse $pp $rfsl 180
     delay $d1
     store 3

  reset
     delay $d1
     pulse $pp $rfsl 180
     delay $d2
     pulse $p180 $rf180 180
     delay $d2
     pulse $pp $rfsl 0
     delay $d1
     store 4


  reset
     delay $d1
     pulse $pp $rfsl 90
     delay $d2
     pulse $p180 $rf180 90
     delay $d2
     pulse $pp $rfsl 270
     delay $d1
     store 33

  reset
     delay $d1
     pulse $pp $rfsl 270
     delay $d2
     pulse $p180 $rf180 270
     delay $d2
```

```
      pulse $pp $rfsl 90
      delay $d1
      store 44

   reset
   pulseid    $p90 $rf -y

   acq

   for {set i 1} {$i <$par(np)} {incr i} {
   reset
      for {set k 1} {$k <= $i} {incr k} {
      prop      33
      prop      44
      }
      for {set k 1} {$k <= $i} {incr k} {
      prop      44
      prop      33
      }
      filter 1

      for {set k 1} {$k <= $i} {incr k} {
      prop      33
      prop      44
      }
      for {set k 1} {$k <= $i} {incr k} {
      prop      44
      prop      33
      }
      #filter 2
      pulseid    $p90 $rf -y
      acq

  }
}



proc main {} {
   global par
   foreach dd {-5000    -9000 -13000 -17000 -21000 -25000} {
for {set iso 0} {$iso <=0} {incr iso 10} {
   for   {set   par(spin_rate)   30000}   {$par(spin_rate)   <=   30000}   {set   par(spin_rate)   [expr
$par(spin_rate)+ 35000] } {
```

```
    foreach par(scale) {5} {
    set par(rf180) [expr $par(spin_rate)/2.0*$par(scale)]
    set par(rfsl) [expr $par(rf180)*0.7]
#      for {set par(rf180) [expr 40000]} {$par(rf180) <= [expr 40000]} {set par(rf180) [expr $par(rf180)+ 2000] } {
#           for {set par(rfsl) [expr 10000]} {$par(rfsl) <= [expr 120000]} {set par(rfsl) [expr $par(rfsl)+ 10000] } {
            set par(sw) [expr $par(spin_rate)/4.0]
            set par(np) [expr round(15*$par(spin_rate)/10000)]

     set f [fsimpson [list [list shift_1_iso [expr $iso]] [list dipole_1_2_aniso [expr $dd]] ]]

     fsave                                                                                $f $par(name)-spinrate=$par(spin_rate)-k=$par(scale)-rf180=$par(rf180)-rfsl=$par(rfsl)-iso=$iso-dd=$dd.fid
            funload $f
# }
#}
}
}
}
}
}
```

5. Super-cycling

(1)$SR4_1^2$

First we consider the $R4_1^2$. According to the RN_n^v selection rules[1],

$$H^{(1)}_{lm\lambda\mu} = 0 \quad \text{if } mn - \mu v \neq \frac{N}{2} Z_\lambda \qquad .$$
$$Z_\lambda \in \{0, \pm 2, \pm 4, ...\} \text{ if } \lambda \text{ is even} \qquad (1)$$
$$Z_\lambda \in \{\pm 1, \pm 3, ...\} \quad \text{if } \lambda \text{ is even}$$

We can obtain the following selection scheme with home-made software (it can be required by emailing to bw.hu@yahoo.com).

λ(μ): homonuclear coupling

l(m) \ λ(μ)	-2	-1	0	1	2
-2	-	0	-	-4	-
-1	-	-	-	-	-
0	*	-	*	-	*
1	-	-	-	-	-
2	-	4	-	0	-

λ(μ): heteronuclear coupling and CSA

l(m) \ λ(μ)	-1	0	1
-2	-	-2	-
-1	-	-	-
0	*	-	*
1	-	-	-
2	-	2	-

λ(μ): isotropic chemical shift

l(m) \ λ(μ)	-1	0	1
0	2	-	-2

λ(μ): *J* coupling

l(m) \ λ(μ)	0
0	0

Scheme 1. Selection scheme of $R4_1^2$ (-,* denotes forbidden element; it should pointed out that zero value means un-forbidden element). Rows correspond to $\omega_{l,m}$, while columns $T_{\lambda,\mu}$.

According to the super-cycling theory[1], if there is a sequence $SM^{\chi} = (RN_n^{\nu})M^{\chi}$ and SM^{χ} is constructed by concatenation of *M* phase-shifted sequences S_p with an overall phase shift $2\pi p\chi / M$ (*p*=0,1,…,*M-1)*, the selection rules for $(RN_n^{\nu})M^{\chi}$ will be

$$H_{lm\lambda\mu}^{(1)} = 0 \ \text{, if } mn - \mu\nu \neq \frac{N}{2} Z_{\lambda} \ or \ \mu\chi \neq MZ$$
$$Z_{\lambda} \in \{0, \pm 2, \pm 4, ...\} \text{ if } \lambda \text{ is even} \qquad (2)$$
$$Z_{\lambda} \in \{\pm 1, \pm 3, ...\} \quad \text{if } \lambda \text{ is even}$$
$$Z \in \text{Integer}$$

Now we consider the $SR4_1^2 = R4_1^2 R4_1^{-2}$. It should be mentioned that although $SR4_1^2$ is concatenated $R4_1^2$ with $R4_1^{-2}$ and $SR4_1^2$ looks like phase inversion sequence, $SR4_1^2$ actually should be considered as $(R4_1^2)2^1$. This can be verified by expressing the two parts: $R4_1^2$ is $(180)_{90}(180)_{-90}(180)_{90}(180)_{-90}$, and $R4_1^{-2}$ is $(180)_{-90}(180)_{90}(180)_{-90}(180)_{90}$. Thus $R4_1^2$ can be considered as S_0, and $R4_1^{-2}$ can be considered as S_1 with 180º phase shift with respect to S_0.

Therefore, for $SR4_1^2 = (R4_1^2)2^1$, the additional selection rule will be $H_{lm\lambda\mu}^{(1)} = 0, \text{ if } \mu \neq 2Z$, and the corresponding selection scheme is shown in scheme 2. Apparently, $SR4_1^2$ sequence only allows the heteronuclear ($T_{1,0}^{IS} = \omega_{IS}^{'} I_z S_z$) and CSA ($T_{1,0}^{CSA} = \omega_{CSA}^{'} I_z$) interactions, while eliminating the homonuclear interactions and the effect of isotropic chemical shift. At last, the selection scheme of $R12_3^5$ is shown in the scheme 3 for comparison.

λ(μ): homonuclear coupling

		-2	-1	0	1	2
	-2	-	0	-	-4	-
	-1	-	-	-	-	-
l(m)	0	*	-	*	-	*
	1	-	-	-	-	-
	2	-	4	-	0	-

λ(μ): heteronuclear coupling and CSA

		-1	0	1
	-2	-	-2	-
	-1	-	-	-
l(m)	0	*	-	*
	1	-	-	-
	2	-	2	-

λ(μ): isotropic chemical shift

		-1	0	1
l(m)	0	-	-	-

λ(μ): *J* coupling

		0
l(m)	0	0

Scheme 2. Selection scheme of $SR4_1^2$, the red crossed circles will suppress the corresponding interactions according to the additional selection rules $\mu\chi \neq MZ$ in equation (2).

λ(μ): homonuclear coupling

l(m)	-2	-1	0	1	2
-2	-	-	-	-	-
-1	-	-	-	-	-
0	-	-	*	-	-
1	-	-	-	-	-
2	-	-	-	-	-

λ(μ): heteronuclear coupling and CSA

l(m)	-1	0	1
-2	-	-6	-
-1	-	-	-
0	-	-	-
1	-	-	-
2	-	6	-

λ(μ): isotropic chemical shift

l(m)	-1	0	1
0	-	-	-

λ(μ): *J* coupling

l(m)	0
0	0

Scheme 3. Selection scheme of $R12_3^5$.

(2) **BR2$_2^1$**

Because $\left(\mathrm{R}2_2^{\pm 1}\right)^p = \mathrm{R}2\,p_{2p}^{\pm p}$, the selection rules of $\mathrm{R}2\,p_{2p}^{p}\mathrm{R}2\,p_{2p}^{-p}$ are equivalent to $\mathrm{R}2_2^1\mathrm{R}2_2^{-1}$, and then we will only consider the selection rules of $\mathrm{R}2_2^1\mathrm{R}2_2^{-1}$.

First we consider $\mathrm{R}2_2^1$, and show its selection scheme in scheme 4.

λ(μ): homonuclear coupling

l(m)	-2	-1	0	1	2
-2	-2	-	-4	-	-6
-1	0	-	-2	-	-4
0	*	-	*	-	*
1	4	-	2	-	0
2	6	-	4	-	2

λ(μ): heteronuclear coupling and CSA

l(m)	-1	0	1
-2	-3	-	-5
-1	-1	-	-3
0	*	-	*
1	3	-	1
2	5	-	3

λ(μ): isotropic chemical shift

l(m)	-1	0	1
0	1	-	-1

λ(μ): *J* coupling

l(m)	0
0	0

Scheme 4. Selection scheme of $\mathrm{R}2_2^1$

Secondly we consider $R2_2^1R2_2^{-1}$ as $(R2_2^1)2^1$ with additional selection rule $H_{lm\lambda\mu}^{(1)}=0,\ \text{if}\ \mu\neq 2Z$, and show the corresponding scheme in scheme 5. It's clear from scheme 5 that $R2_2^1R2_2^{-1}$ only excites homonuclear DQ ($T_{2,\pm2}^{II}$) and ZQ ($T_{2,0}^{II}$) interactions while eliminating all the heteronuclear interactions, CSA and isotropic chemical shift effects. In bracketed version of DQ-SQ experiments (pulse sequence 90°-$R2_2^1R2_2^{-1}$-90°) we employ the ZQ part of $R2_2^1R2_2^{-1}$, while in un-bracketed version of DQ-SQ (pulse sequence $R2_2^1R2_2^{-1}$) we use the DQ part of $R2_2^1R2_2^{-1}$.

λ(μ): homonuclear coupling

l(m) \ λ(μ)	-2	-1	0	1	2
-2	-2	-	-4	-	-6
-1	0	-	-2	-	-4
0	*	-	*	-	*
1	4	-	2	-	0
2	6	-	4	-	2

λ(μ): heteronuclear coupling and CSA

l(m) \ λ(μ)	-1	0	1
-2	-3	-	-5
-1	-1	-	-3
0	*	-	*
1	3	-	1
2	5	-	3

λ(μ): isotropic chemical shift

l(m) \ λ(μ)	-1	0	1
0	-1	-	-1

λ(μ): *J* coupling

l(m) \ λ(μ)	0
0	0

Scheme 5. Selection scheme of $R2_2^1R2_2^{-1}=(R2_2^1)2^1$, the red crossed circles will suppress the corresponding interactions according to the additional selection rules $\mu\chi\neq MZ$ in equation (2).

References

[1] A. Brinkmann, M. Eden, Second order average Hamiltonian theory of symmetry-based pulse schemes in the nuclear magnetic resonance of rotating solids: Application to triple-quantum dipolar recoupling, Journal of Chemical Physics, **2004**, 120(24), 11726.